EXPERIMENTAL HYDRODYNAMICS AND SIMULATION
OF MANOEUVRING OF AN AXISYMMETRIC
UNDERWATER VEHICLE

FARHOOD AZARSINA
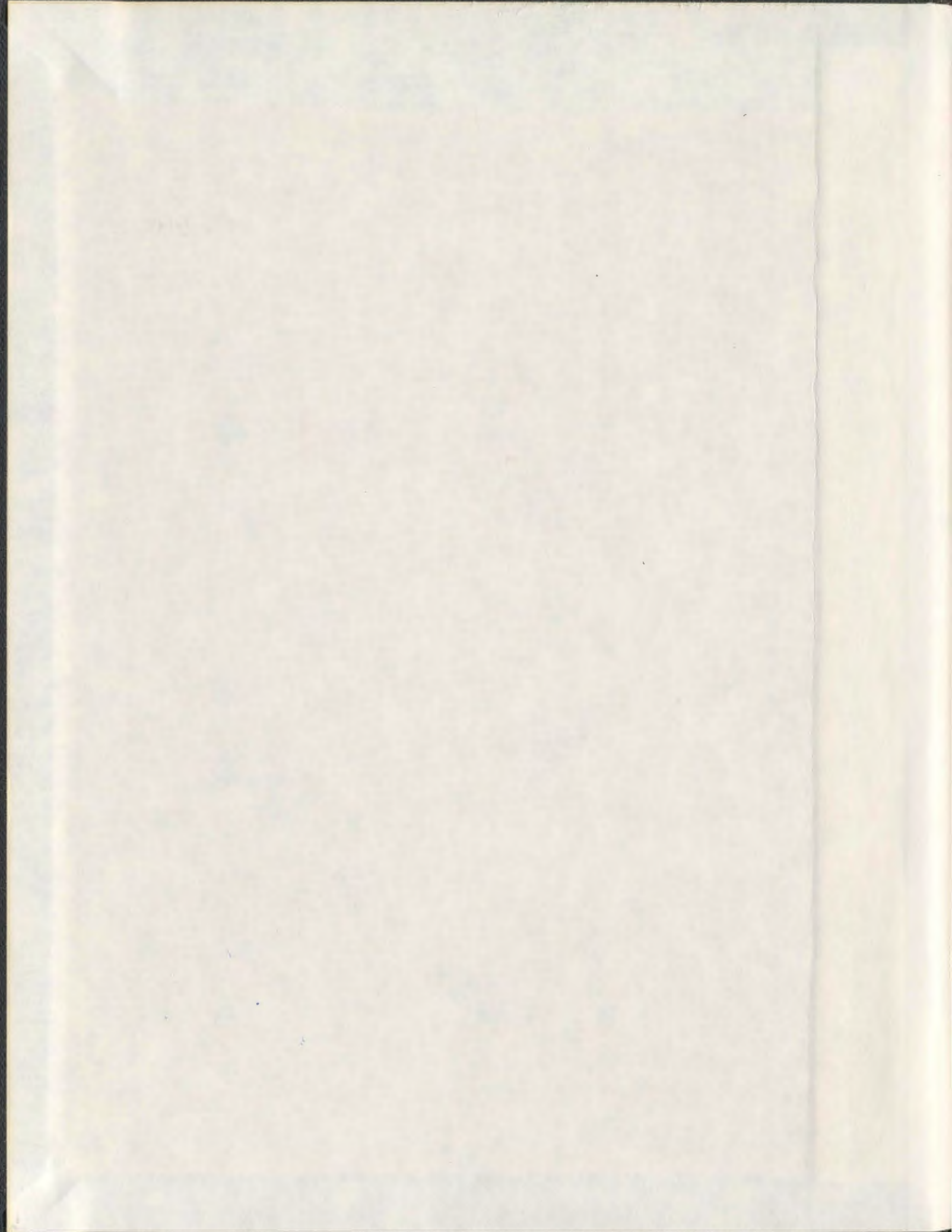
001311
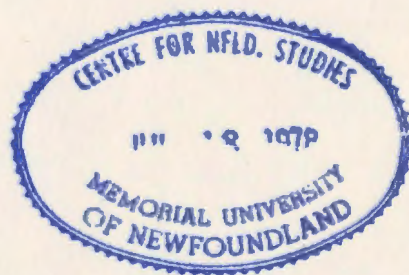
EXPERIMENTAL HYDRODYNAMICS AND SIMULATION

OF MANOEUVRING OF AN AXISYMMETRIC

UNDERWATER VEHICLE

by

© Farhood Azarsina

A thesis submitted to the

School of Graduate Studies

in partial fulfillment of the

requirements for the degree of

Doctor of Philosophy

Faculty of Engineering and Applied Science

Memorial University

April, 2009

St. John's   Newfoundland   Canada

Dedicated to my father: Mehdi, my mother: Nahid, and my brother: Farzad, who have been always incredibly supportive in spite of the physical distance between Tehran and St. John's.

Also dedicated to all my: Canadian, International and Iranian wonderful friends in St. John's, who made my single life during these years pleasant and memorable.

Farhood
April 2009
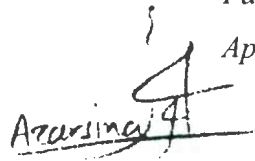
ABSTRACT

Experimental study of the hydrodynamics of an underwater vehicle requires state-of-the-art facilities, precise design of the experiment and careful analysis of the results. This thesis presents hydrodynamic observations resulting from experiments that were performed on a series of five bare-hull configurations of slender axisymmetric underwater vehicles and also reports a simulation code to predict the manoeuvring behaviour of a real underwater vehicle: *MUN Explorer*. The main aim is to find the correct form of the physically-based expressions for the hydrodynamic loads that are exerted on completely-submerged underwater vehicles during various manoeuvres and use this improved knowledge to obtain a better prediction of the manoeuvring of an underwater vehicle.

Straight-ahead resistance tests and static-yaw runs up to 20 degrees yaw angle for the axisymmetric bare-hull configurations that were performed in the 90 metre towing tank at the Institute for Ocean Technology, National Research Council, Canada, provided empirical formulae for the drag force, side force and turning moment that are exerted on such axisymmetric torpedo-shaped hull forms. The empirical formulae were then embeded in a numerical code to simulate the constant-depth planar manoeuvres of the *MUN Explorer* AUV. The simulation code was first calibrated using the sea-trials data, and then was used to study the turning manoeuvres and compare the simulation results with theoretical formulae based on the linearized equations of motion.

Dynamic captive-model tests including pure sway and pure yaw runs were the other part of the experiments on the five bare-hull configurations. The sway force that is exerted on

the bare-hull during lateral accelerations, according to the pure sway test data, was observed to have a variation over manoeuvring frequency and amplitude. Also, empirical formulae were proposed to estimate the magnitude and phase of the hydrodynamic loads: sway force and yawing moment that are exerted on the axisymmetric torpedo-shape bare-hull of an underwater vehicle during a rapid zigzag manoeuvre.

Finally, in order to obtain further insight into the origin and distribution of the hydrodynamic loads during underwater manoeuvres, pressure measurement experiments were proposed and as an initial step towards the aim of performing such measurements over the surface of an underwater vehicle, a re-analysis of the old airship data was presented. The re-analysis of the airship pressure test results provided an estimate of the normal pressures that may be experienced by an underwater vehicle during manoeuvres.

ACKNOWLEDGEMENTS

Table of Contents

List of Figures

---

[1] LDR: length-to-diameter ratio of the bare hull.

---

[2] RSM: response surface model

List of Tables

List of Abbreviations and Symbols[*]

A	Amplitude of the transverse distance that the PMM moves [m]
A_f	Frontal area of the bare-hull [m^2]
A_p	Planform area of the bare-hull [m^2]
AOA	Angle of attack [deg]
ANOVA	Analysis of variance
AUV	Autonomous underwater vehicle
a_y	Sway acceleration [m/s^2]
a_{y0}	Amplitude of the sway acceleration [m/s^2]
b	Span of the control surfaces [m]
C_D	Drag coefficient
C_L	Lift coefficient
C_M	Moment coefficient
CG	Centre of gravity [m]
CB	Centre of buoyancy [m]
CCD	Central Composite Design
c	Chord-length of the control surfaces [m]
D	Drag force [N]
DOE	Design of experiment
d	Maximum diameter of the bare-hull [m]

---

[*] List of symbols that were common within several chapters are given first, then the symbols which were used within a specific chapter only are given under each chapter.

F_x	Axial force [N]
F_y	Sway force [N]
F_{y0}	Sway force amplitude [N]
F'_{y0}	Non-dimensional sway force amplitude: $F_{y0}/(q \cdot A_p)$
L	Lift force [N]
l, LOA	Overall length of the bare-hull [m]
LDR	Length-to-diameter ratio for the bare-hull of an underwater vehicle
M_z	Yaw moment [N.m]
M_{z0}	Yaw moment amplitude [N.m]
M'_{z0}	Non-dimensional yaw moment amplitude: $M_{z0}/(q \cdot A_p \cdot l)$
N, n	Propeller revolution speed respectively: [rps] and [rpm]
PMM	Planar motion mechanism
p, q, r	Roll, pitch and yaw angular velocity [rad/s]
q	Dynamic pressure of the flow in water or air [Pa]
R	Radius of a turning circle manoeuvre [m]
RSM	Response surface model
r	Rate of turn during a turning manoeuvre [rad/s] or [deg/s] as indicated in the text
U	Speed of the underwater vehicle [m/s]
u, v, w	Surge, sway and heave velocity [m/s]
$u_{carriage}$	Towing speed [m/s]
v_0	Sway velocity amplitude of the PMM [m/s]

$\vec{\dot{v}}$	Acceleration vector [m/s^2] or [rad/s^2]
$\vec{v}$	Velocity vector [m/s] or [rad/s]
$\vec{v}_1$	Linear velocity vector [m/s]
$\vec{v}_2$	Angular velocity vector [rad/s]
β	Yaw angle of the PMM [deg]
β_0	Amplitude of yaw angle of the PMM and the underwater vehicle model [deg]
$\vec{\tau}$	The vector of forces and moments exerted on the rigid body [N] and [N.m]
φ_F	Phase lag between the sway force and sway velocity signals [rad]
φ_M	Phase lag between the yaw moment and the yaw angular acceleration signals [rad]
∇	The enclosed volume of the underwater vehicle's bare-hull [m^3]
ω	Frequency of the lateral oscillating manoeuvre [rad/s]

Chapter 2

k	Quadratic multiplier for the curve fits to the resistance test data
k_1 to k_6	Regression multipliers for drag, lift and moment coefficients
$A, B, C, ...$	The experiment factors
$[A], [B], ...$	Factor effects on the experiment response
$a, b, ab, ...$	Experiment runs in a 2-factorial design
α_0, α_1	Regression equation multipliers

Chapter 3

θ	Half the tilt angle of the force-velocity ellipse in the phase-plane plot [rad]

$M_{z,planes}$	Yaw moment that the rudders produce [N.m]
t_{Mz}	Time instant at which the hydrodynamic yaw moment that is exerted on the underwater vehicle is maximum [s]

Chapter 4

$F_{y0,d}$	Amplitude of the damping component of the sway force [N]
$F_{y0,i}$	Amplitude of the inertial component of the sway force [N]
$m_{apparent}$	Apparent mass of the vehicle–water system [kg]
b	Damping factor of the vehicle–water system [kg/s]

Chapter 5

K_1, K_2, K'	Surge and sway added mass coefficients and yaw added moment of inertia coefficient for an ellipsoid in potential flow
$F_{y,planes}$	Net sway force produced by the stern planes [N]
$M_{z,planes}$	Net yawing moment produced by the stern planes [N]
T	Propeller thrust force [N]
β	Drift angle [deg]
$\delta_1, \delta_2, \delta_3, \delta_4$	Stern-planes deflection angle [deg]
ξ	The installation angle of the stern control planes of the AUV

Chapter 6

x	Distance from airship nose [m]
$r(x)$	Radius of the airship bare-hull [m]
p_{total}	Total pressure measured at each orifice [Pa]
p_s	Static pressure along the centreline of the wind-tunnel test section [Pa]

p	Dynamic pressure measured at each orifice [Pa]
F_z	Normal force [N]
M_y	Pitching moment about an axis through the center of buoyancy (*CB*) [N.m]
θ	Airship pitch angle [deg]; positive nose up
φ	Airship surface slope along longitudinal generators [deg]; $\tan(\varphi) = dr/dx$
ω	Circumferential angle around the airship cross-sections [deg]; positive counterclockwise when looking aftward

CHAPTER 1

INTRODUCTION

1.1 General background

Underwater vehicles are being used increasingly in a variety of applications such as: survey, exploration, inspection, maintenance and construction, search and rescue, environmental and biological monitoring, military, undersea mining, and recreation. Underwater vehicles fall into two major categories: manned and unmanned. The costs and risks for the manned underwater vehicles are high and in recent past decades there has been an obvious trend toward unmanned vehicles. However, for the scientists who may want direct observation of the undersea world and for the tourist industry, manned vehicles are of use. Allmendinger [1990] provides an extensive introduction to most of the design aspects of manned underwater vehicles.

Unmanned underwater vehicles can be categorized as: towed, remotely operated (ROV) and autonomous (AUV). The towed and remotely operated vehicles are connected to the surface or a manned environment via a cable or tether. The towed vehicles are normally passive, i.e., they have no propellers and no active control systems. ROVs have thrusters and active control systems. They get energy supply, navigation commands, and they transfer data through the tethers. The high speed of communication allows real-time control of the vehicle. AUVs, instead, have no physical connection to the surface. Power supply, underwater communication, intelligent mission planning and control, underwater navigation and sensors are still challenging in the design and construction of an AUV.

Three classes of AUVs namely: 1) Research, 2) Industrial and 3) Military were introduced in the Code of Practice (CoP) edited by Dering [2000]. The major tasks of research and industrial AUVs are: 1) Oceanic process studies, such as study of the ocean circulation, decay processes, turbulence over sand banks, etc. 2) Routine observations, such as the study of CTD (Conductivity, Temperature and Depth) profiles. In these applications the AUV more likely replaces a surface vessel. 3) Survey tasks, such as bathymetric and sidescan sonar topographic survey. 4) Intervention tasks, such as the applications of AUVs in cybernetics and as other tools. The critical technologies for the development of the AUVs are: power supply, hydrodynamic design, navigation, artificial intelligence and robotics, communication and sensors [Dering, 2000].

The importance of studying AUV hydrodynamics is also emphasized as follows:

1- AUVs are the rapidly emerging class of underwater vehicles to explore the ocean.

2- Vehicle geometry should be efficient so as to minimize the hydrodynamic forces.

3- Stability and manoeuvrability of the AUV depend on its shape and the resulting hydrodynamic forces and moments.

4- Modeling and simulation of AUV motion are accurate if the hydrodynamics of the vehicle are precisely known. An accurate simulation (prediction) of the AUV motion is necessary for mission planning and control, which also improves the manoeuvring of the vehicle.

5- For obstacle avoidance, hovering and navigation in the restricted waters, AUVs perform manoeuvres with large angles of attack or high yaw and pitch rate of turns.

6- Also a better model for AUV manoeuvring reduces the operational risks.

2

1.2 Objective of the thesis

In this research, the main question is: what is the correct form of the physically-based expressions for the hydrodynamic loads that are exerted on completely-submerged underwater vehicles during various manoeuvres? Clearly, there are many parallels with the study of the aerodynamics of aircraft. However, for underwater vehicles, the vehicle weight is balanced by the buoyant force that is provided by the surrounding fluid, so in that sense underwater vehicles are more like airships than traditional winged aircraft. Also, the contribution of the hydrodynamic moment on the hull of an underwater vehicle is much greater than the contribution of the fuselage on a winged aircraft, so the traditional methods of computing the aerodynamic coefficients for aircraft do not immediately transfer to the computation of hydrodynamic coefficients for underwater vehicles [Nahon 1993, Jones et al. 2002].

For high-amplitude, high-rate manoeuvres, first-order Taylor-series expansion is insufficient to capture the higher-order non-linear dependence of the loads on the flow angle and the vehicle turning rate. For example, [Mackay et al. 2002] show that the transverse force has a non-linear variation with angle-of-attack; above an angle-of-attack of 10 degrees the stability-derivative-based prediction (slope through the data near the origin) underestimates the actual load by 50 percent or more. Therefore in the present research, employing mostly experimental methods, two extreme cases will be considered:

  (a) Large angles of attack encountered during hovering.

  (b) High-rate-of-turn manoeuvres encountered during obstacle-avoidance manoeuvres.

3

Two methods can be used for this study:

1) Measurement of the overall hydrodynamic loads with an internal balance.

2) Observations on the manoeuvring performance of a self-propelled vehicle.

This research is focused on the first method while the second method is the subject of parallel studies at Memorial University. For the first method, again there are two different possibilities:

1a) fixed-attitude (static) manoeuvres

1b) variable-attitude (dynamic) manoeuvres

To perform type (b), one uses a towing tank and a forced-oscillation apparatus such as the NRC-IOT Planar Motion Mechanism (PMM) or Marine Dynamic Test Facility (MDTF) [Williams et al. 2002]. Test results from both types of experiments are presented in this thesis and a new empirical formulation to model the hydrodynamic loads that are exerted on the bare hull of a slender axisymmetric underwater vehicle is proposed. Next, a simulation code based on the empirical formulae for the hydrodynamics of the bare hull is developed to simulate manoeuvring of the *MUN Explorer* AUV including control surfaces and the propulsion system.

In order to obtain further insight into the origin and distribution of the hydrodynamic loads during any manoeuvre, it is helpful to measure the distribution of pressures over the surface of the vehicle while these manoeuvres are taking place. The surface pressures can then be integrated and compared with the overall loads as measured simultaneously by the internal balance. Surface-pressure data exist from fixed-attitude experiments with an airship hull in a wind-tunnel [Freeman 1932b], but few data exist for surface-pressure

4

data on underwater vehicles, especially during high-rate and high-amplitude manoeuvres in water. This thesis also presents a re-analysis of the existing airship data which is the first step in design of the pressure experiments for an underwater vehicle.

1.3 Organization of the thesis

To obtain an answer for the main question of this research, experiments to measure the hydrodynamic loads that are exerted on the bare hull of a slender torpedo-shaped underwater vehicle during manoeuvres with large angles of attack and large rates of turn were performed. The overall hydrodynamic loads were measured with an internal balance during: i) fixed-attitude (static) manoeuvres and ii) variable-attitude (dynamic) manoeuvres. Then, the experimental data were studied and analyzed as follows:

1) Fixed-attitude tests: in chapter 2 empirical formulae are proposed for the drag, lift and moment coefficients of the bare hull of a slender axisymmetric underwater vehicle. Also, the concept of statistical design of experiment is introduced in chapter 2 and its possible application to design experiments for the study of underwater vehicle hydrodynamics is discussed.

2) Variable-attitude tests: a) in chapter 3, pure sway test results are analyzed to model the sway force that is exerted on the bare hull of a slender underwater vehicle during lateral accelerations; b) in chapter 4, response surface models are constructed for the pure yaw test results and a sample application of these models to predict the required deflection angle of the control planes to perform a rapid zigzag manoeuvre with the *MUN Explorer* AUV is illustrated.

5

Next, in chapter 5, a simulation code to predict the manoeuvring behaviour of the *MUN Explorer* AUV is developed. The empirical formulae for the drag, lift and moment coefficients for the slender torpedo-shaped bare hull of an underwater vehicle that were obtained in chapter 2, are used in the simulation code. Stern-planes of *MUN Explorer* which are in an X-configuration, are modeled as the active actuators to navigate the vehicle in a constant-depth planar manoeuvre. The propeller thrust force is modeled using the test results from straight-line sea-trials. Simulation results for turning manoeuvres are presented with more details.

Finally, in chapter 7, an initial step towards the aim of performing pressure measurement experiments over the surface of an underwater vehicle is presented. Re-analysis of the old airship data provides an estimate of the normal pressures that may be experienced by an underwater vehicle during manoeuvres.

1.4 Literature Review

Using both numerical simulations with a combination of the ANSYS and LS-DYNA finite element codes, and physical experiments with the Marine Dynamic Test Facility (MDTF), at the Institute for Ocean Technology, National Research Council, Canada (NRC-IOT), Curtis [2001] presented direct comparisons between numerical and experimental results in the study of underwater vehicle hydrodynamics. The focus of that study was more on the numerical simulation, and the experimental data were used to validate the numerical code. The bare hull of the DREA (Defense Research Establishment Atlantic) Standard Submarine was used for this purpose. Only the

6

numerical simulation of straight-ahead motion and its comparison to the experimental data was presented in that report [Curtis, 2001].

The Maritime Platforms Division within DSTO (Defence Science and Technology Organisation) of Australia was tasked with the development of models to determine the hydrodynamic coefficients of simple and complex submerged bodies as a function of their shape. The report by Jones et al. [2002] provides a discussion and evaluation of three methods for the calculation of these coefficients. Two of these methods were based on the techniques developed in the aeronautical industry: i) the U.S. Air Force DATCOM method which was applied by Peterson [1980] to underwater vehicles and ii) the Roskam method as was modified by Brayshaw [1999] for underwater vehicles. The third method was based on methods applicable to the calculation of the coefficients of single screw submarines and was developed at University College, London. Many semi-empirical relations to calculate the hydrodynamic coefficients are presented in the report by Jones et al. [2002], but most of them are only applicable over a small range of incidence angles and the effect of rate of change of angle is completely absent. One of the few studies on large non-linear angles of attack has been done by Finck [1976], which provides some additional techniques to use the DATCOM method in a non-linear range of angles of attack (AOAs).

A recent numerical study to predict hydrodynamic loads for underwater vehicles has been done by Boger and Dreyer [2006]. They added an overset mesh capability to the existing two and three-dimensional Reynolds-averaged Navier-Stokes (RANS) solvers, so as to enable the extension of traditional structured and unstructured solution methods in

7

computational fluid dynamics (CFD) to problems of greater geometric complexity, including better resolution of geometric details and the simulation of bodies in relative motion. The surface pressures and predicted forces and moments were shown to be in good agreement with measurements for the DARPA (Defence Advanced Research Projects Agency) SUBOFF and the ONR (Office of Naval Research) Body-1 submarine model. For DARPA SUBOFF the numerical and experimental data for static pressure along the bare hull were shown. For three-dimensional ONR Body-1 model, numerical and experimental results for hydrodynamic force and moment coefficients versus pitch angle were presented. Pitch angle varied from zero to 18 degrees [Boger and Dreyer, 2006].

CHAPTER 2

FIXED-ATTITUDE TESTS:

RESISTANCE AND STATIC-YAW EXPERIMENTS

2.1 Introduction

As part of an underwater vehicle study at the Institute for Ocean Technology, National Research Council of Canada, the bare hull of an underwater vehicle named "Phoenix" was tested in the open water 90 m Ice Tank. The original bare hull of the underwater vehicle "Phoenix", shown in Fig. 2.1, had an overall length of 1.641 metre and a diameter of 0.203 metre, that is, the original length-to-diameter ratio (*LDR*) was about 8.5:1. In anticipation that there would be a requirement to lengthen the vehicle in order to accommodate an increased payload or increased battery capacity, extension pieces were designed and fabricated that would permit testing hulls of the same diameter, 203 mm, but with *LDR* 9.5, 10.5, 11.5 and 12.5. Thus, a set of experiments was proposed that would investigate the manoeuvring characteristics of the hull-forms of *LDR* 8.5 to 12.5 [Williams et al. 2006]. Also the planar motion mechanism (PMM) in NRC-IOT was used to perform dynamic tests. The PMM was restricted to a maximum of 1.25 m sway amplitude, 0.65 [m/s] sway velocity and 60 [deg/s] yaw rate of turn.

In this chapter, test results for resistance and static yaw runs that were performed on the five bare hull configurations were analyzed and reported. In the resistance tests the model with zero heading (drift angle) is towed through the tank. In each run, the towing velocity goes from a stationary zero value to a constant value and then again back to zero. Having

the maximum acceleration is important so as to perform constant velocity towing through a longer distance. The second type of experiments analyzed was the static yaw tests. The vehicle, inclined with a yaw angle, was towed along the tank-x-axis. The yaw angle β was gradually increased through several runs to a maximum of 20 degrees.

Fig. 2.1 Bare hull model installed on the PMM using the two vertical struts

2.2 The model and test conditions

Three coordinate systems are used in this study: (i) Earth-fixed axis which is mainly used to indicate the heading of a free-running vehicle, (ii) body-fixed axis which is used to indicate the velocity, acceleration and force vectors of a free-running model, as well as the loads that are recorded with the internal balance for a captive model test, (iii) tank-fixed axis which may be used in the study of dynamic captive manoeuvring tests for example to describe the motions of the PMM mechanism. The Earth-fixed and body-fixed coordinates are shown in Fig. 2.2. Tank-fixed axis is defined with its x-axis along

the towing carriage and z-axis in vertical direction positive upward for testing surface vessels and positive downward for testing underwater vehicles.
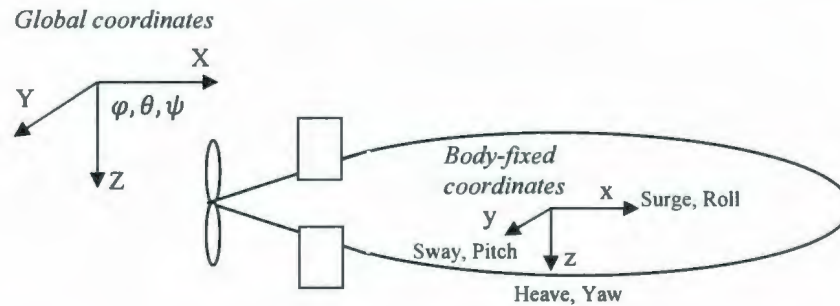
Fig. 2.2 Global and body-fixed coordinate systems for an underwater vehicle

Fig. 2.1 showed the model installed on the PMM using the supporting struts. The chord length of each faired strut was 176 mm and the maximum thickness of struts was 46 mm. Fig. 2.3 shows schematically the bare hull model mounted on the PMM: two vertical streamlined struts attach the internal balance to the PMM. Each strut passes through a hole in the skin of the upper surface of the mid-body section, thus there is no contact between either strut and the model itself. The distance between the free surface and the top of the upper surface of the bare hull was maintained at 1.09 m for all runs. The water depth was 2.18 m for all runs. So the ratio of the distance between the free surface and the top of the upper surface of the bare hull to the maximum hull diameter of 203 mm was almost 5.4. Similarly the ratio of the water depth to the maximum hull diameter was about 10.7. Within the interior of the model, the "ground" or "dead" portion of the balance is attached only to the two vertical struts. The "live" or "metric" portion of the balance is attached to two circular bulkheads within the mid-body section. With this attachment method the internal three-component balance measures only the

11

hydrodynamic loads (axial force, lateral force, yaw moment) which are exerted by the flow on the external surface of the model. Since neither strut is attached to the "live" portion of the balance, there is no load path from either strut to the model itself. The longitudinal spacing between the struts was 723 mm. Since there are two holes in the skin at the upper portion of the mid-body, the water which enters the model to fill the empty spaces within the model is referred to as the floodwater. During all lateral motions it is assumed that the floodwater moves as if it were a rigid body and that there is no empty space within the model for air to be trapped and thus no internal free surface where sloshing could occur.
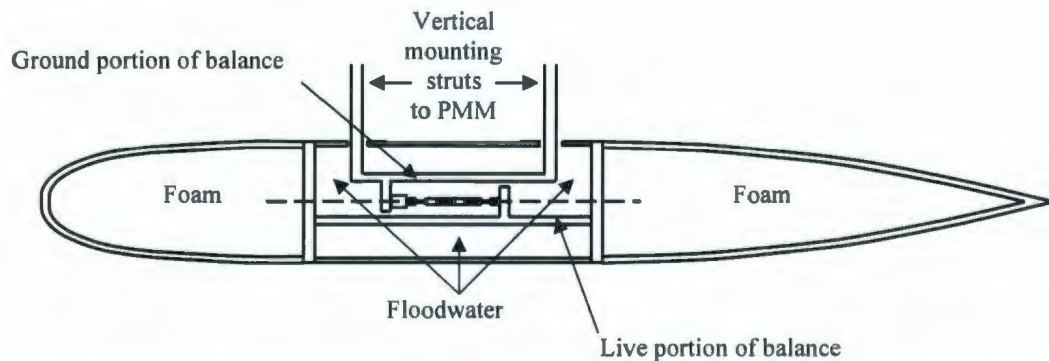
Fig. 2.3 A simplified diagram of the fully-submerged, fully-flooded Phoenix model mounted below the PMM; side view

In conclusion, due to the attachment method used in these experiments, the internal three-component balance measures only the hydrodynamic loads which are exerted on the exterior surface of the model, and not any effect of (a) hydrodynamic loads on the mounting struts, (b) floodwater "sloshing" within the mid-body, or, (c) any free surface. Table 2.1 and 2.2 show the details of the five bare hulls. Each of the five models was weighed by suspending the dry, empty model in air, and those masses are the values in

column #6 of Table 2.1 [Hewitt and Waterman, 2005]. Next all the joints of each model were taped closed so that the model was water-tight, then each model was filled with water until it overflowed; the mass of each flooded model when suspended in air is given in column #7 in Table 2.1. By subtraction, the mass of floodwater can be found, and this value for each model is given in column #8 of Table 2.1. The last two columns in Table 2.1 show respectively the dry and flooded moment of inertia of the five bare hulls. The yaw moment is reported about an axis through the centre of buoyancy (*CB*) [Hewitt and Waterman, 2005]. Table 2.2 shows the location of the *CB* for each model as both a distance from the nose [mm] and as a fraction of the overall length, reproduced from [Williams et al. 2006]. Also the wetted surface area and the volume of the hulls are presented in Table 2.2

Table 2.1 Mass and moment of inertias of the five Phoenix models

LDR	Maximum diameter [mm]	LOA [mm]	CG dry in air [mm] from nose	CG flooded in air [mm] from nose	Mass when dry in air [kg]	Mass when flooded in air [kg]	Mass of floodwater [kg]	Dry moment of inertia [kg.m^2]	Flooded moment of inertia [kg.m^2]
8.5	203	1724	734	847	24.3	49.2	24.9	3.52	8.82
9.5	203	1927	815	939	25.6	55.3	29.7	4.49	13.25
10.5	203	2130	912	1057	27.3	63.2	35.9	5.44	16.73
11.5	203	2333	1011	1159	28.2	70.1	41.9	6.73	21.84
12.5	203	2536	1118	1256	29.8	77.1	47.3	8.34	32.36

Table 2.2 Particulars of the five configurations tested; *MC* is the moment centre at the origin, *LCB* indicates the centre of buoyancy

LDR	LOA [mm]	MC (nose) [mm]	LCB (nose) [mm]	Ratio MC to LOA	Ratio LCB to LOA	Wetted surface area [m^3]	Enclosed volume [m^3]
8.5	1724	736	815	0.427	0.473	0.95	0.044
9.5	1927	838	915	0.435	0.475	1.08	0.051
10.5	2130	940	1017	0.441	0.477	1.21	0.057
11.5	2333	1041	1118	0.446	0.479	1.34	0.064
12.5	2536	1143	1220	0.451	0.481	1.47	0.070

2.3 Resistance runs

2.3.1 Modeling the axial force

Straight-ahead resistance runs were performed for the five bare hulls at fixed forward speeds of 1, 2, 3 and 4 m/s. All the resistance runs were performed for zero drift angle, that is, with each model aligned with the direction of towing. The axial force recorded during the resistance tests was modeled as a function of the towing speed and the bare hull LDR. Table 2.3 shows the quadratic multiplier k for the curve fits to the resistance test data as shown in Fig. 2.4. The axial force in straight-ahead motion is then modeled as:

$$F_x = k \cdot U^2, \text{ where: } k = 0.162 * LDR + 0.681 \tag{2-1}$$

which is valid in the range $8.5 < LDR < 12.5$, i.e. not for $LDR \rightarrow 0$.
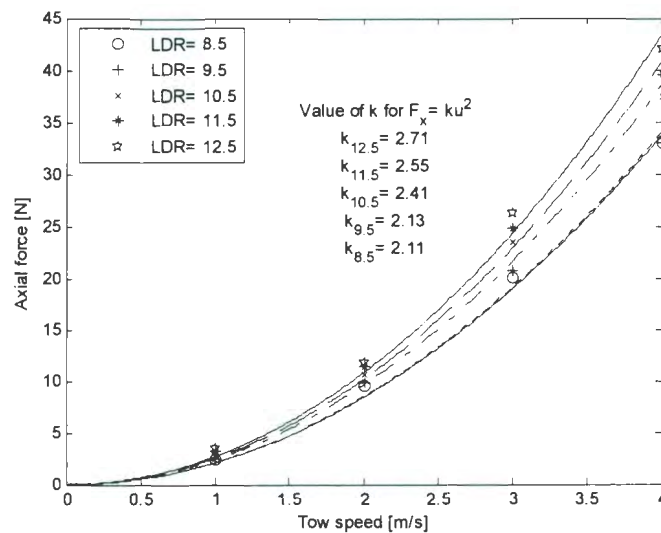
Fig. 2.4 Axial force versus tow speed for the five bare hulls; reproduced from [Williams et al. 2006]

14

Table 2.3 Quadratic multiplier for the curve fits to the resistance test data;

reproduced from [Williams et al. 2006]

LDR	8.5	9.5	10.5	11.5	12.5
k	2.11	2.13	2.41	2.55	2.71
R-sq	0.996	0.994	0.994	0.995	0.995

Although, this dimensional model captures the test data, it cannot be used to predict the resistance for the bare hull of another underwater vehicle of different size. If the non-dimensional axial force is defined by dividing the axial force by the frontal area times the dynamic pressure of the free-stream as follows:

$$F_x = C_x \cdot (\tfrac{1}{2}\rho U^2) \cdot \left(\tfrac{\pi d^2}{4}\right), q = \tfrac{1}{2}\rho U^2 \text{ and } A_f = \pi d^2/4 \qquad (2\text{-}2)$$

$$C_x = F_x/(q \cdot A_f), \qquad (2\text{-}3)$$

with fresh-water density $\rho = 1000$ [kg/m^3], then the axial force coefficient for the Phoenix bare hulls in straight-ahead motions also has a linear variation over the bare hull *LDR*, as follows:

$$C_x = 0.0117 * LDR + 0.038 \qquad (2\text{-}4)$$

Note that (2-4) was derived for tow speeds of 1 to 4 m/s and *LDR*s of 8.5 to 12.5, however due to the relatively simple hydrodynamics of the straight-ahead towing the model may be useful for small extrapolations outside the above ranges. The axial force could be also non-dimensionalized using the wetted surface area (WSA) or the volume of the bare hulls that were presented in Table 2.2; the resulting non-dimensional axial force based on the WSA and volume to the two-third are respectively shown in Figs. 2.5 and 2.6. Note that the quadratic multipliers k in Table 2.3 were used to calculate the values in Figs. 2.5 and 2.6, thus the data points are the same for all towing speeds under 4 m/s.

15

These results are valid for U < 4 m/s
For LDR 8.5, $0.78*10^6$ < Re < $6.2*10^6$
For LDR 9.5, $0.87*10^6$ < Re < $6.9*10^6$
For LDR 10.5, $0.96*10^6$ < Re < $7.7*10^6$
For LDR 11.5, $1.05*10^6$ < Re < $8.4*10^6$
For LDR 12.5, $1.14*10^6$ < Re < $9.1*10^6$
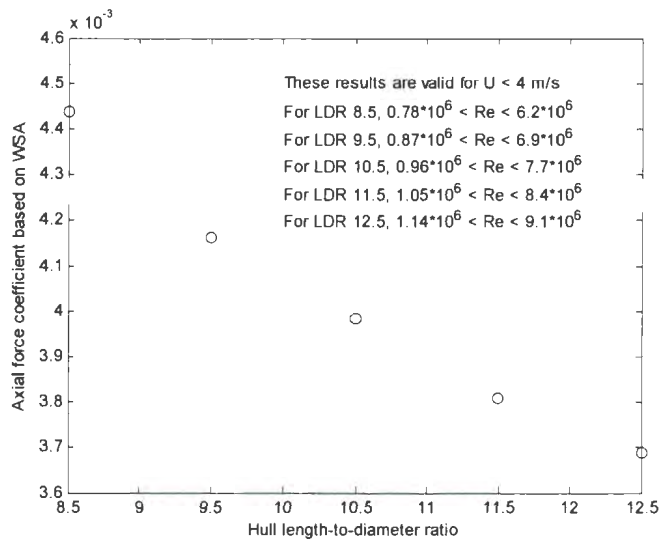
Fig. 2.5 Non-dimensional axial force based on the wetted surface area
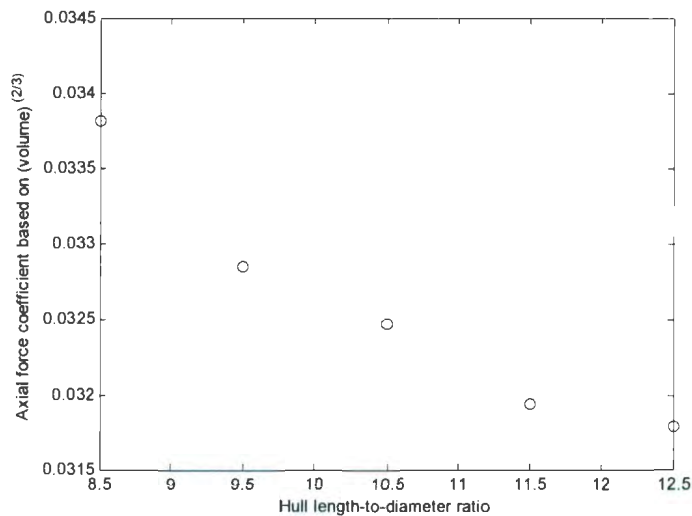
Fig. 2.6 Non-dimensional axial force based on the volume

If equation (2-4) is used to predict the axial force on the bare hull of the *C-SCOUT* AUV

which is 2.7 m long and 0.4 m in diameter [Curtis 2001], the axial force coefficient is

estimated to be 0.119. Substituting this value of C_x in (2-2) for various speeds U produces

the axial force as shown by solid line in Fig. 2.7. The predicted axial force for *C-SCOUT*

for forward speeds lower than 2 m/s is closely comparable to the resistance test data as were reported by Thomas [2003]. For larger forward speeds, since the bare *C-SCOUT* was tested relatively close to the water surface (centreline depth 2.2 body diameter), there is a large effect of wave-making resistance in the *C-SCOUT* test data.
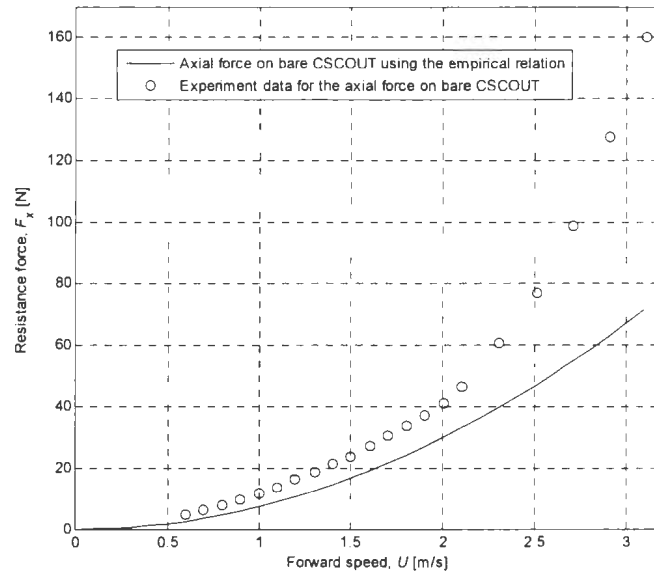
Fig. 2.7 Resistance force on bare *C-SCOUT*; eq. (2-4) compared to the test data

2.3.2 Uncertainty in the resistance tests

The uncertainty in the resistance tests data is characterized by measuring the mean value and the standard deviation of the axial force during the constant-speed portion of each run. The data were recorded at 50 Hz, thus e.g. if the constant speed was performed for 20 seconds there were 1000 data points to be averaged. Note that the usable length of the towing tank is 78 m and the maximum acceleration of the carriage is 0.5 m/s^2. Table 2.4 shows the mean value and the standard deviation for the axial force that were recorded for the bare hulls at different towing speeds. Number of samples for each run is also

shown in the last column in Table 2.4. The resistance curves are plotted including the error bars as shown in Fig. 2.8. The curve for **LDR 8.5** is placed on the correct velocity grids, then the curves for longer hulls were shifted sideways to the right by 0.05 m/s in order that the error-bars do not overlay each other. Note that the error-bars in Fig. 2.8 are of length equal to plus/minus one standard deviation.

Table 2.4 Uncertainty in the recorded axial force during resistance tests; speed in [m/s], force in [N]

$LDR = 8.5$			
U	F_x_mean	SD_F_x	No. of samples
1	2.49	3.56	696
2	9.32	4.77	697
3	20.02	7.66	574
4	32.96	8.26	238
$LDR = 9.5$			
U	F_x_mean	SD_F_x	No. of samples
1	2.49	4.51	2260
2	9.61	5.43	967
3	20.57	6.85	566
4	32.97	10.87	267
$LDR = 10.5$			
U	F_x_mean	SD_F_x	No. of samples
1	2.8	7.77	2510
2	10.48	7.02	1210
3	23.42	8.51	594
4	37.26	15.91	261
$LDR = 11.5$			
U	F_x_mean	SD_F_x	No. of samples
1	3.05	8.56	2405
2	11.13	4.92	1042
3	24.67	8.43	572
4	39.56	12.61	286
$LDR = 12.5$			
U	F_x_mean	SD_F_x	No. of samples
1	3.24	12.8	2415
2	11.49	3.39	1012
3	26.17	5.85	551
4	42.06	10.47	295

18
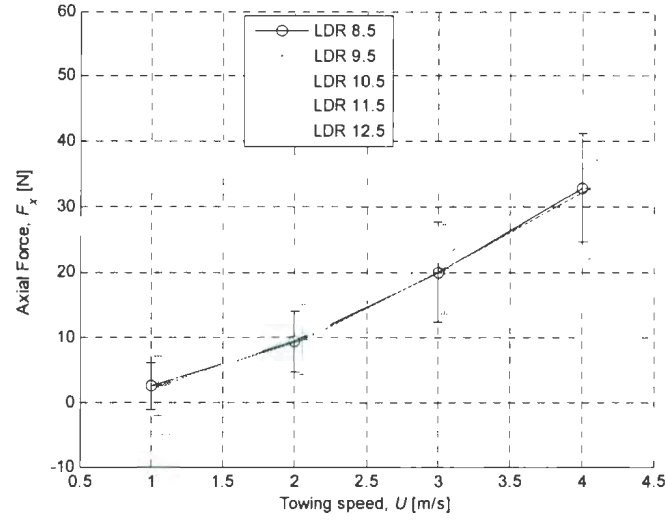
Fig. 2.8 Resistance curves and the corresponding error bars

2.4 Static yaw runs

All the static yaw runs were performed using a fixed sequence of yaw (drift) angles β from −2 to +20 degrees in steps of two degrees. All runs were performed at a fixed speed of 2 m/s. Figs. 2.9 to 2.11 show the axial force, lateral force and yawing moment data versus yaw angle of attack. As mentioned, the yaw moment is reported about an axis through the centre of buoyancy CB that was reported in Table 2.2. For the purpose of curve-fitting and modeling the data, it is more useful to derive the drag and lift forces by projecting the axial and lateral forces along and perpendicular to the flow, i.e., to define the drag and lift forces as follows:

$$D = F_x \cdot \cos(\beta) + F_y \cdot \sin(\beta) \tag{2-5}$$

$$L = F_y \cdot \cos(\beta) - F_x \cdot \sin(\beta) \tag{2-6}$$

Then, the drag, lift and yaw moment coefficients were defined as follows:

$$C_D = D/(q \cdot A_f), \tag{2-7}$$

19

$$C_L = L/(q \cdot A_f), \tag{2-8}$$

$$C_M = M/(q \cdot A_f \cdot l) \tag{2-9}$$

where $q = \frac{1}{2}\rho U^2$ and $A_f = \pi d^2/4$, and U is the towing speed which was 2 m/s for all

the static yaw runs. The resulting non-dimensional coefficients along with the curve fits

are shown in Figs. 2.12 to 2.14. Due to the length parameter in the denominator (2-9), the

yaw moment coefficient for all the bare hull configurations is about the same in Fig. 2.14;

while the dimensional yaw moment in Fig. 2.11 was larger for the longer models.
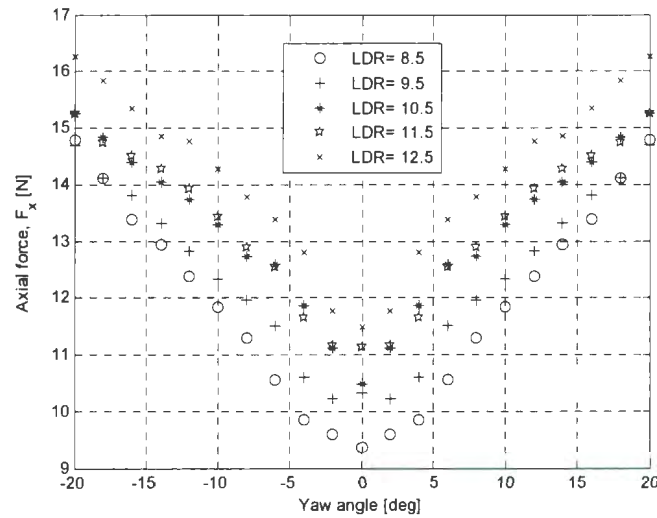
Fig. 2.9 Experimental data for the axial force in static yaw runs

20
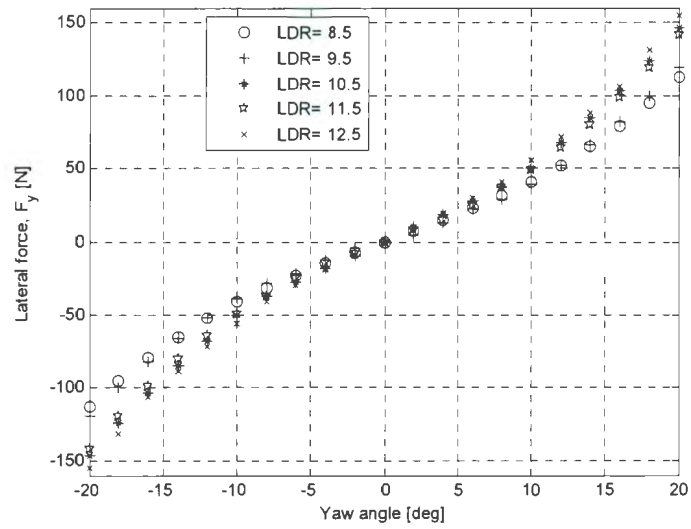
Fig. 2.10 Experimental data for the lateral force in static yaw runs
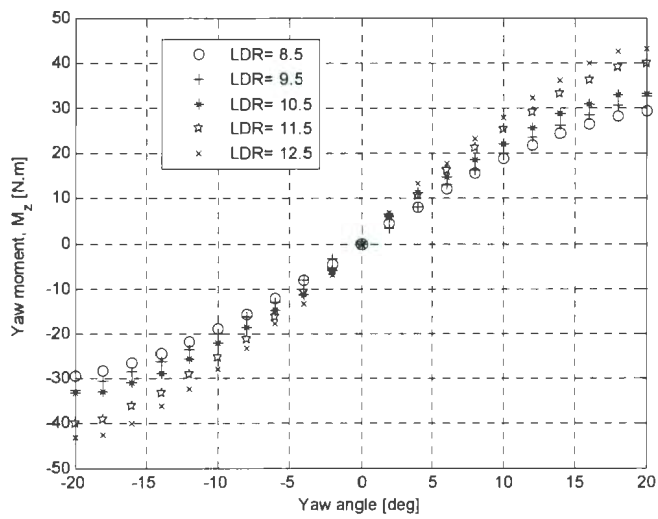
Fig. 2.11 Experimental data for the yawing moment about an axis through *CB* in static yaw runs

21
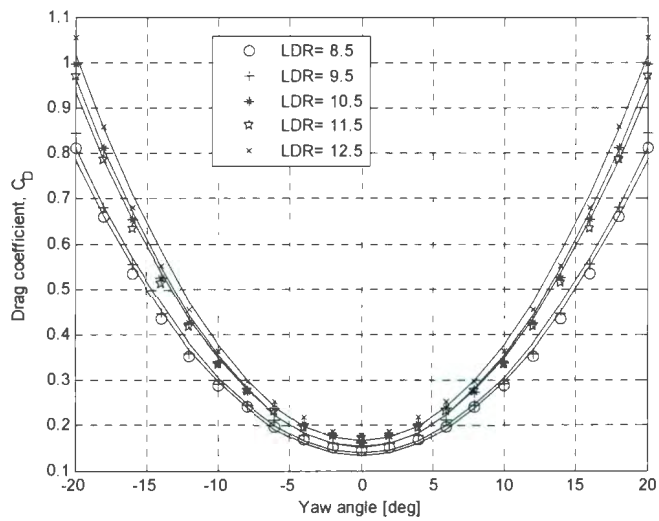
Fig. 2.12 Drag coefficient vs. yaw angle
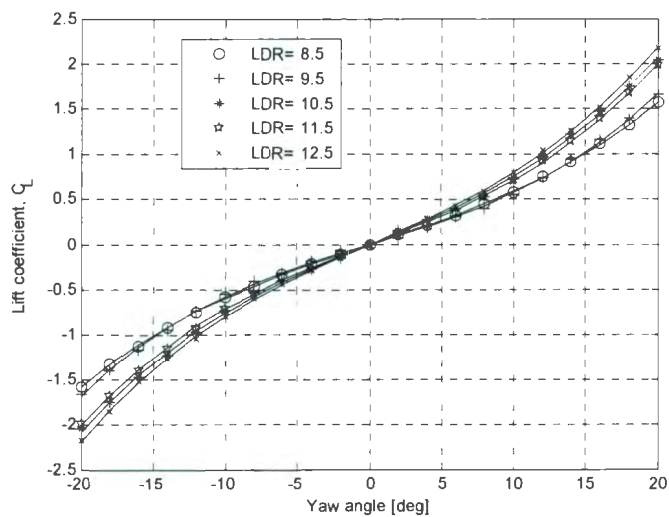
Fig. 2.13 Lift coefficient vs. yaw angle

22
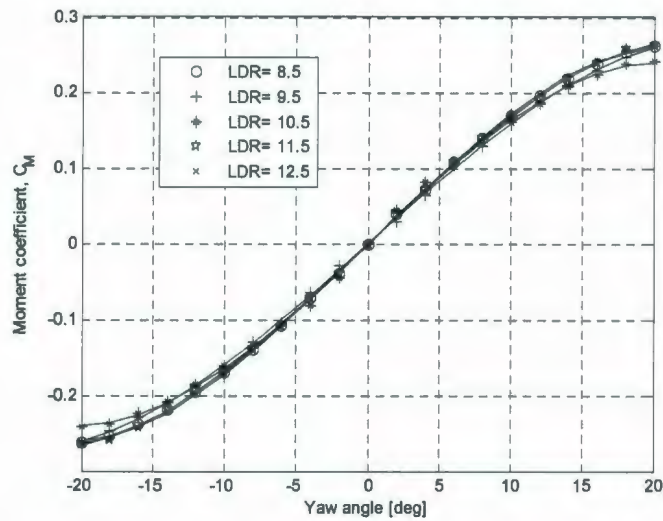
Fig. 2.14 Moment coefficient about an axis through *CB* vs. yaw angle

The drag coefficient data in Fig. 2.12 were fitted by quadratic polynomials which have no linear term, that is, an even second order polynomial of the form:

$$C_D = k_1\beta^2 + k_2 \tag{2-10}$$

Note that k_2 in (2-10) represents the drag force at zero yaw angle which is equal to the resistance force coefficient at the tow speed of 2 m/s. For the lift and moment coefficients cubic (third order) odd polynomials were fitted, that is:

$$C_L = k_3\beta^3 + k_4\beta \tag{2-11}$$

$$C_M = k_5\beta^3 + k_6\beta \tag{2-12}$$

Table 2.5 summarizes the curve-fit coefficients in (2-10) to (2-12) for drag, lift and moment coefficients for each configuration.

The constant value for the drag coefficient, third column in Table 2.5, is close to the axial force coefficient value that was modeled in equation (2-4) based on the resistance test results for tow speeds of 1 to 4 m/s instead of a single tow speed of 2 m/s. Thus, it is

23

beneficial to preserve the previous model for the constant value at zero yaw angle and add to that the quadratic term. Also, from second column in Table 2.5 and the curve fits in Fig. 2.12, the quadratic term for the drag coefficient can be averaged over the bare hull configurations. Therefore, the drag coefficient for the Phoenix hull can be modeled as:

$$1000 * C_D = 1.88\beta^2 + 11.7LDR + 38 \qquad (2\text{-}13)$$

which is valid in the range $8.5 < LDR < 12.5$, $1 < U < 4$ m/s, and $-20 < \beta < 20$ deg. Yaw angle in (2-13) is in degrees. Note that in deriving (2-13) it is assumed that the effect of yaw angle on the drag coefficient is the same for all forward speeds as it is for the speed of 2 m/s. Within a reasonable range of variation for the yaw angle and forward speed the above assumption is approximately correct. If the static-yaw runs were performed at different towing speeds this interaction effect between the yaw angle and forward speed could be studied [Azarsina et al. 2006].

Table 2.5 Thousand times the curve-fit coefficients for drag, lift and moment coefficients

for the bare hull configurations

LDR	$1000*C_D$		$1000*C_L$		$1000*C_M$	
	k_1	k_2	k_3	k_4	k_5	k_6
8.5	1.63	134.1	0.06	52.9	-0.01	18.2
9.5	1.68	139.5	0.09	48.3	-0.01	16.9
10.5	2.03	152.3	0.09	66.6	-0.01	17.9
11.5	1.95	153.4	0.10	61.7	-0.01	18.0
12.5	2.13	164.6	0.10	70.5	-0.01	18.6

For the Phoenix lift coefficient, the polynomial coefficients in Table 2.5 vary with length and can be approximated to have a closely linear increase for longer configurations. Thus, both the third order parameter k_3 and the linear parameter k_4 for the lift

24

coefficient, fourth and fifth columns in Table 2.5, are modeled by linear fits over LDR, as follows:

$$1000 * C_L = (0.007LDR + 0.011)\beta^3 + (4.87LDR + 8.85)\beta \qquad (2\text{-}14)$$

which is valid in the range $8.5 < LDR < 12.5$, $1 < U < 4$ m/s, and $-20 < \beta < 20$ deg. Yaw angle in (2-14) is in degrees. However, for the Phoenix yaw moment coefficient, the cubic and linear terms times 1000 in the last two columns Table 2.5 are almost the same, hence on average over all the bare hull configurations it is possible to write:

$$1000 * C_M = -0.01\beta^3 + 17.92\beta \qquad (2\text{-}15)$$

The empirical formulae in (2-13) to (2-15) are valid over ranges of the factors: LDR, yaw angle and forward speed of respectively: 8.5 to 12.5, -20 to 20 degrees and 1 to 4 m/s. These are the formulations which will be embedded in the simulations in chapter 5.

2.5 Design of experiments

2.5.1 Introduction

Statistical design of experiment (DOE) methodology was developed to make experimentation more efficient in terms of time and budget. First started in the agricultural sciences in the 1920s, DOE has gone through at least three industrial and academic eras and is now increasingly used in research and industry [Montgomery, 2001]. Basically, DOE is a methodology for systematically applying statistics to experimentation. DOE lets experimenters develop a mathematical model that predicts how input variables interact to create output variables or responses in a process or system. This method allows a large number of factors to be investigated in few

25

experimental runs and it was further developed to include fractional factorial designs, orthogonal arrays and response surface methodology.

Regular factorial design includes the following steps:

a)   Select the factors, i.e. decide which input variables are going to be studied;

b)   Determine the factor levels; that is, the range of values for each input variable.

c)   Identify the responses; what do we measure as the output?

d)   Perform the experiment with various combinations of factor levels to obtain the responses (outputs);

e)   Estimate the factor effects, i.e. perform the ANOVA (Analysis of Variance);

f)   Develop the model using important effects;

g)   Check if the model fits the responses well and if the assumptions of regression are valid;

h)   Analyze and interpret the results; and

i)   Use the model for prediction.

From the results, we can also determine if we should add or drop factors, change factor levels, redefine the responses, etc. until a suitable model of the process will be obtained. A major engineering application of the DOE is in manufacturing science and industry and other fields are becoming aware of its potential effectiveness. Many articles on the application of DOE in manufacturing, chemical and food science and technology can be found in [Statease website, 2008]. Among the few, [Morelli and Deloach, 2003] and

[Sutulo and Soares, 2002] can be mentioned as application of DOE in respectively aerodynamics and hydrodynamics. According to the highly non-linear manoeuvring mechanics, both the above references utilize the concept of subspaces and D-optimal design to model the responses through the whole range of definition of the factors. Reference [Chung et al. 2005] illustrates the vital need to have a well-designed experiment so as to reduce the number of runs.

A reverse design of experiment is applied using the available static-attitude test data and a response surface model is fitted to that portion of these data. It is desired to obtain answers for the following questions:

1.   Is it possible to combine the results of two sets of experiments, namely resistance and static yaw, and develop a model for the responses versus the important factors: velocity, length-to-diameter ratio and drift angle, as in

$$(F_x, F_y, M_z) = g(LDR, U, \beta)?$$
(2-16)

2.   According to the performed experiments and available data, how should an experiment for the study of the hydrodynamics of an underwater vehicle be designed so as to conserve time and cost?

2.5.2 Experiment factors

For the resistance tests the two factors are: towing velocity, U, and model dimensions, LDR; for the static yaw tests the factors involved are: yaw (drift) angle, β, and LDR. Tables 2.6 and 2.7 define the factors and their treatment levels for the two types of experiments. Shown in Tables 2.6 and 2.7, the resistance and static yaw tests respectively contribute $4*4 = 16$ and $5*12 = 60$ runs.

Table 2.6 Resistance tests: variables and factor levels

Factors	Levels
$A = LDR$	9, 10, 11 and 12
$B = U$ [m/s]	1, 2, 3 and 4

Table 2.7) Static yaw tests: variables and factor levels

Factors	Levels
$A = LDR$	8, 9, 10, 11 and 12
$B = \beta$ [deg]	-2 to 20 with step 2°

The experiments measured three responses: axial force, F_x, sway force, F_y, and yaw moment, M_z. It should be noted that:

- The variable LDR is common for both types of experiments.

- For the resistance test, the desired response is the axial force, F_x, and the two other responses (F_y and M_z) are expected to be zero.

- All treatment levels of the static yaw tests have been performed with the same forward velocity of 2 m/s.

In addition to the factors and responses (the main concern of the experimenter), there are several constraints that dominate the experiment design. The constraints are due to the facilities, environmental conditions and the experimenters. For instance, randomization is a basic requirement in the theory of the experiment design so as to cancel out the steady errors caused by unknown variables, however, installing and aligning the model on the towing carriage is a lengthy task, therefore, randomization over the variable LDR is practically impossible. Although, the randomization problem due to the presence of hard-to-change factors, can be solved using split-plot designs ([Montgomery, 2001],

28

[Kowalski and Potcner, 2003] and [Potcner and Kowalski 2004]), the data here are analyzed as if they were gathered randomly.

2.5.3 Analysis of test data using a statistical approach

The software "Design Expert™6.0.3" by Stat-Ease, Inc. was used to analyze the data. The ANOVA shows that in the resistance test, the velocity (U) is highly significant at the 10% significance level, whereas in the static yaw test, the yaw angle (β) is highly significant at the 10% significance level. None of the experiments result in a significant interaction effect between the two factors.

The 2^k factorial design is the special case of the general factorial design. In this case, there are k factors each used at two levels, usually called low level and high level, in order to make the combinations. As mentioned, ANOVA is used to test for the statistical significance. A factor that has a greater effect on the response is statistically more significant. The factor effect is defined as the change in the mean response when the factor is changed from low level to high level. For instance, if A and B are two factors in an experiment, the effect of A is evaluated as:

$$Term\ A1 = \text{Estimate of effect of } A \text{ at high } B = a_1 b_1 - a_0 b_1$$

$$Term\ A2 = \text{Estimate of effect of } A \text{ at low } B = a_1 b_0 - a_0 b_0$$

$$[A] = \text{Estimate of the effect of } A \text{ over all } B \qquad (2\text{-}17)$$

$$= (Term\ A1\ +\ Term\ A2)\ /2$$

The effect of B is evaluated in the same way. $[A]$ and $[B]$ are the main effects. Indices '0' and '1' consequently indicate the low and high level for each factor, e.g. $a_1 b_1$ is the response at the treatment combination in which both factors are in high level. There is

also an interaction effect between the two factors, which is named $[AB]$. Interaction is actually a form of curvature and describes the dependence of the effect of one factor on the level of the other factor. The interaction effect is calculated as:

$$[AB] = \text{Estimate of effect of } B \text{ on the effect of } A \qquad (2\text{-}18)$$

$$= (Term\ A1 - Term\ A2)\ /2$$

It should be noted that in the presence of large interaction effects, the main effects might not be meaningful.

Table 2.8 shows the sum of squares and contribution of the factors A, B and AB for the resistance experiments that is: model dimension (LDR), towing speed (U), and the interaction of them. Note that the sum of squares for any effect is directly proportional to the effect squared. Eliminating the interaction term AB, since it is the smallest contribution, and doing ANOVA for the factors A and B provides a significant model for the resistance test results as shown in Table 2.9. The significance level used was 10%. Although, from Table 2.9, factor A appears to be statistically significant, according to Table 2.8, it contributes less than 2% to the model. This shows that the dominant effect is the resistance of the nose and tail sections since the length of the constant-diameter mid-body accounts for less than two percent of the resistance.

Table 2.8 Sum of squares and contribution of terms for the selected model

Term	Sum Square	% Contribution
$A = LDR$	40.8	1.40
$B = U$	2840	97.8
AB	23.2	0.80

Table 2.9 ANOVA for the selected model for resistance test results

Source	Sum of squares	DF	Mean square	F-value	Prob > F	
Model	2881	6	480.3	185.9	< 0.0001	Significant
$A = LDR$	40.8	3	13.6	5.26	0.023	
$B = U$	2840	3	947.0	366.6	< 0.0001	
Residual	23.25	9	2.58			

Figs. 2.15 and 2.16 show the model interaction graphs. In Fig. 2.15, factor B (velocity) is the x-axis and different curves are drawn for different length-to-diameter ratios. In Fig. 2.16, factor A (length-to-diameter ratio) is the x-axis. For the resistance tests, as well as the static yaw tests, all regression assumptions were acceptable.
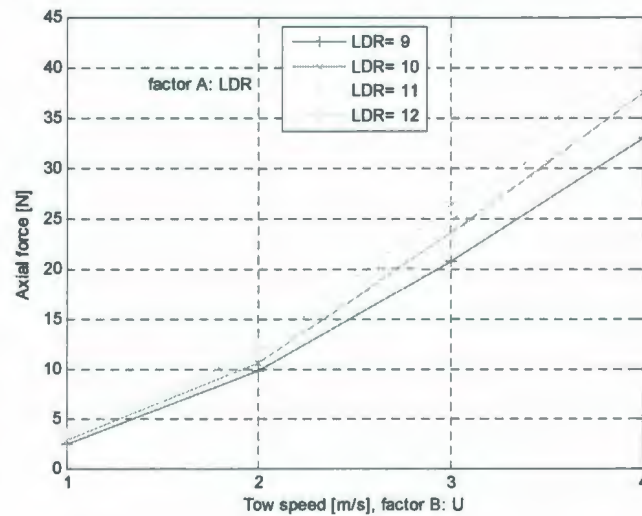
Fig. 2.15 Interaction graph for axial force; velocity on x-axis

31
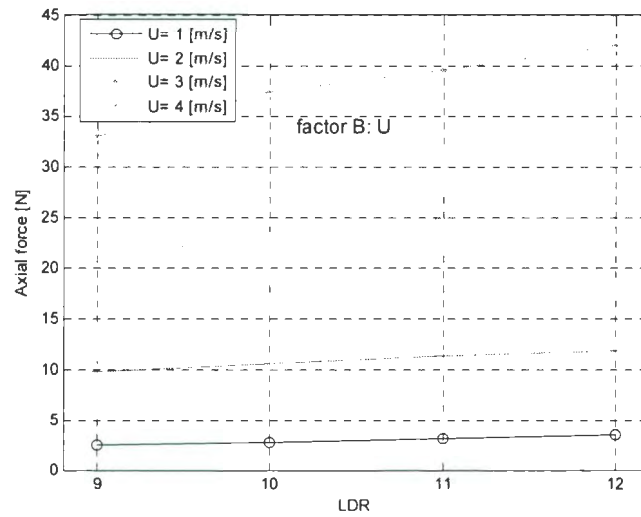
Fig. 2.16 Interaction graph for axial force; *LDR* on x-axis

2.5.4 Response surface models for the static yaw data

A regression model for a response, which depends on two factors, is a surface in 3D space. The response surface may be represented graphically using a contour plot or a 3D plot; this type of graphical representation is possible only when there are two factors. In the contour plot, lines of constant response are drawn in the plane of the two factors. In a 3D representation, the response is plotted in the third dimension. The Response Surface Model (RSM) can be a first-order model if the response is a linear function of the factors. If the response has curvature, then a higher order polynomial should be used. A second-order (quadratic) model is often able to capture the curvature [Myers and Montgomery 1995]. The general form of a quadratic regression for the response z versus the factors x and y is written as:

$$z = C_{xx}x^2 + C_{yy}y^2 + C_{xy}x \cdot y + C_x x + C_y y + C \qquad (2\text{-}19)$$

32

The available data for static yaw test included five levels for factor A (bare hull LDR) and 12 levels for factor B (yaw angle). Some of the available data can be used to develop a RSM. Central Composite Design (CCD) is a popular design to fit a response surface to the data [Montgomery, 2001]. A CCD was built in order to capture the static yaw experiment results. Fig. 2.17 shows the general scheme of design. The design points are shown as pairs of (LDR, β) values. The data shown in Table 2.10 were used for this purpose. In Fig. 2.17 the center-point has coordinates (LDR, β) of (10, 10) and axial-runs are the runs augmented in between the square two-level design; they have coordinates (8, 10), (12, 10), (10, 0) and (10, 20).
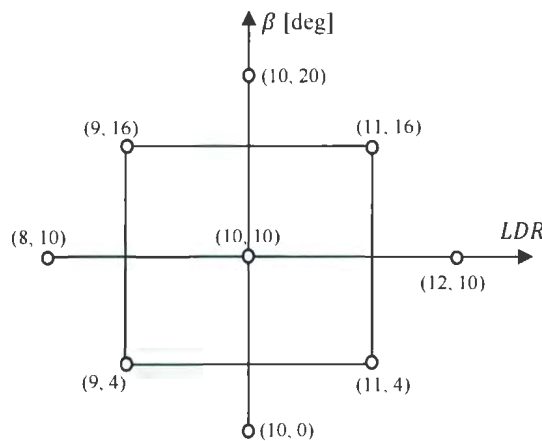
Fig. 2.17 Test set levels for the Central Composite Design

The process of fitting a RSM for sway force, axial force and yaw moment is similar. For the sway force data, the linear model was suggested; however, the quadratic terms were in the boundary of significance. The interaction term was negligible. Checking additional statistics for a second-order model revealed that including the quadratic terms will result in a more accurate but not redundant model. Table 2.11 shows the ANOVA for the

quadratic model. The model is significant but the interaction term AB and quadratic term A^2 can be omitted.

Table 2.10 Test data for the central composite design

Run	$A = LDR$	$B = \beta$ [deg]	F_x [N]	F_y [N]	M_z [N.m]
1	9	4	10.6	9.4	7.16
2	11	4	11.7	15.0	12.8
3	9	16	13.8	79.6	27.8
4	11	16	14.5	98.6	38.3
5	10	0	10.5	3.62	4.29
6	10	20	15.3	150.1	37.5
7	8	10	11.8	35.1	17.1
8	12	10	14.3	58.0	32.3
9	10	10	13.3	54.0	26.3

Table 2.11 ANOVA for the quadratic model for sway force during static yaw tests

Source	Sum of Squares	DF	Mean Square	F-value	Prob > F	
Model	17997	5	3599	41.4	0.006	Significant
A	412.6	1	412.6	4.75	0.118	
B	16561	1	16561	190.4	0.001	
A^2	3.9	1	3.90	0.04	0.85	
B^2	514.9	1	514.9	5.92	0.093	
AB	45.1	1	45.1	0.52	0.52	
Residual	260.9	3	87			
Correlation Total	18258	8				

Note that, in Table 2.10, the p-values (second last column) for AB and A^2 are evidently larger than 0.1, that is: outside the 10 percent significance level. For A and B^2 the p-values are near 10% and thus those terms were included in the final model. The model equation, written for the actual factors, after omitting the terms AB and A^2 is as follows:

$$F_y = -54.51 + 5.86(LDR) + 1.25(\beta) + 0.28(\beta)^2 \qquad (2\text{-}20)$$

where the yaw angle is in degrees. One can check if (2-20) fits the test data of Table 2.10. If the response surface captures the data with an acceptable accuracy, then the other

available data can be used to check for the predictive capability of the model. Fig. 2.18, showing sway force versus yaw angle for *LDR* equal to 8 and 12, is plotted to assess the predictive capability of the model. The asterisk and circle signs represent the experimental data, which are available for the yaw angle from −2 to 20 degrees, in steps of two degrees. The solid and dashed lines were fitted to the RSM generated data from (2-20) with the same step-size. There is a gap between the model prediction and test data at some yaw angles (e.g. at higher angles for the *LDR* 8 vehicle or lower angles for *LDR* 12).

As mentioned, the same procedure can be applied to the axial force and yaw moment. The models for the sway-force and yaw-moment include the quadratic term β^2, but the axial force model is a simple linear model. It is often convenient to convert the actual values of the test factors to coded levels. The coded factors are defined so that the low and high levels are minus one and plus one, respectively as defined in Table 2.12. The model equations written for the coded factors are:

$$F_x = 12.58 + 0.55(A) + 1.47(B) \tag{2-21}$$

$$F_y = 45.05 + 5.86(A) + 41.63(B) + 10.25(B)^2 \tag{2-22}$$

$$M_z = 24.22 + 3.88(A) + 10.61(B) - 1.51(B)^2 \tag{2-23}$$

where factor *A* is the bare hull *LDR* and factor *B* is the yaw angle, β. As was explained, equations (2-21) to (2-23) were derived by performing the analysis of variance over the static yaw test data for the axial force, lateral force and yawing moment and thus identifying the terms which have a significant effect on those responses.

Table 2.12 Actual and coded factors for the static yaw tests

β [deg]	0	4	10	16	20
A	-1	-0.6	0	0.6	1
LDR^3	8	9	10	11	12
B	-1	-0.5	0	0.5	1

Notice that (2-22) corresponds to (2-20); the former is written for the actual factors and the latter for the coded factors. With the coded factors one can exactly see which factor has a larger effect on the response because all factors have the same range of variation: -1 to 1.
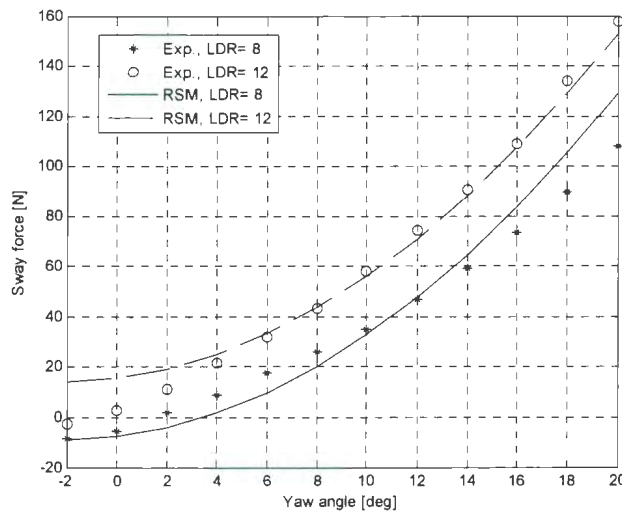
Fig. 2.18 Comparison of the experimental and RSM generated data

The RSM 3D demonstration for sway force F_y is shown in Fig. 2.19. Plot of contours of the sway force model is shown in Fig. 2.20. In fact, Fig. 2.20 is the bottom face of Fig. 2.19.

---

[3] Note that the models were actually 8.5 to 12.5 in length-to-diameter ratio but this section about DOE mainly focuses on the introduction of the concept of a statistical analysis of the test data.
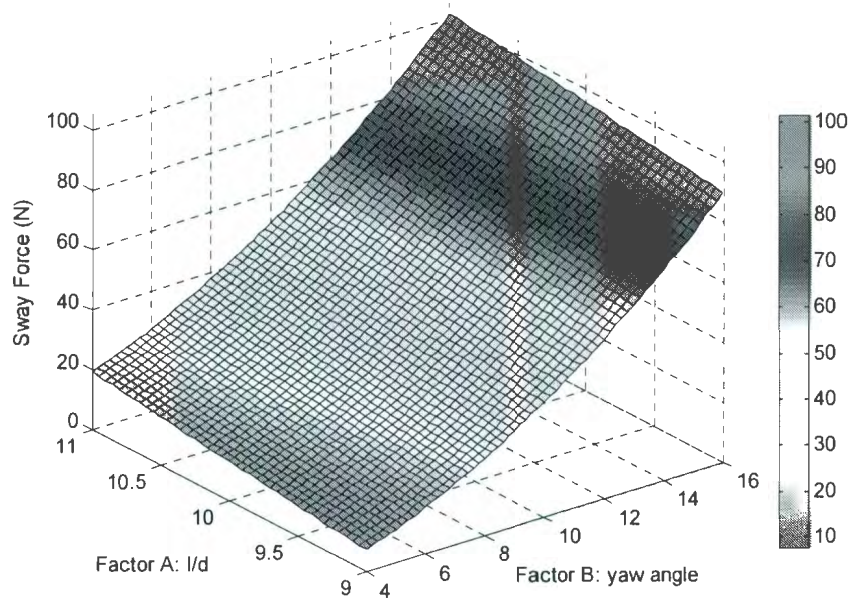
Fig. 2.19 Response surface model for sway force during static yaw tests
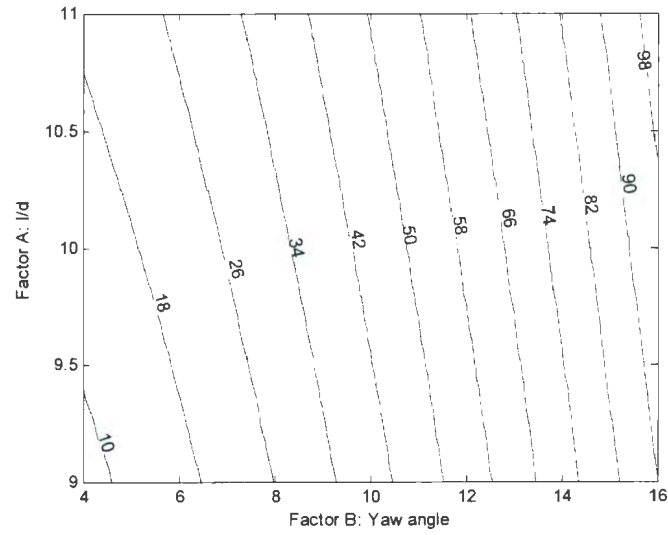
Fig. 2.20 Contours of the RSM for sway force [N]

2.5.5 Further discussion; the two crucial questions

As discussed in the previous sections, the general shape of the models for the magnitude of the hydrodynamic loads in resistance and static yaw tests respectively are given by the following equations:

$$\left(F_x,\ F_y, M_z\right) = f_1(LDR, U) \tag{2-24}$$

$$\left(F_x,\ F_y, M_z\right) = f_2(LDR, \beta) \tag{2-25}$$

The variability of the main response, axial force, in (2-24) versus velocity and dimension was shown in Figs. 2.15 and 2.16, and (2-25) is the compact expression for (2-21) to (2-23), after re-writing them for the actual factors. It should be noted again that:

a- The variable LDR is common for both experiments.

b- For the resistance test, the desired response is the axial force and two other responses (F_y and M_z) are expected to be zero.

c- In the resistance test, factor B (towing speed) was completely dominant. The magnitude of its effect and its contribution in the model was significantly higher than factor A (bare hull LDR).

d- In the static yaw test, factor B (yaw angle) was dominant.

e- None of the experiments concluded either a statistically (small F-value) or practically significant (large contribution) interaction effect.

f- From these experiments nothing can be concluded about the interaction of forward speed U and yaw angle β, because all the static yaw tests were performed with the same forward velocity of 2 m/s.

38

Therefore f_1 and f_2 have been already derived in (2-24) and (2-25), and there are some clues to answer the first question that was put before; equation (2-16) is repeated below:

$$\left(F_x, \ F_y, M_z\right) = g(LDR, U, \beta) \tag{2-26}$$

The objective function is g. In other words, a response surface model in the four-dimensional space is desired. If the three factors LDR, U and β are named consequently A, B and C, then the first-order (linear) regression equation for the objective function is of the form:

$$g = \alpha_0 + \alpha_1 A + \alpha_2 B + \alpha_{12} A * B + \alpha_3 C + \alpha_{13} A * C +$$

$$\alpha_{23} B * C + \alpha_{123} A * B * C \tag{2-27}$$

Equation (2-27) includes all the terms (i.e. main effects, two-factor interaction effects and the three-factor interaction effect) in the model, but some terms may not have a significant effect on the response. In case of a two–level factorial design, the coefficients are calculated as:

$$\alpha_0 = \text{overall average}, \ \alpha_1 = [A]/2, \ \alpha_2 = [B]/2, \ \alpha_3 = [C]/2, \ \alpha_{12} = [AB]/2,$$

$$\alpha_{13} = [AC]/2, \ \alpha_{23} = [BC]/2, \ \alpha_{123} = [ABC]/2, \tag{2-28}$$

In (2-28), $[A]$ is the effect of factor A, $[AC]$ is the interaction effect of factors A and C which represents the dependence of the effect of factor A on the level of factor C (or vice versa), and so on. Hence performing a 2^3 factorial design (two-levels for three factors), may give an appropriate approximation of the objective function. With the available data we have no information about α_{23} (interaction of the factors towing speed U and yaw angle β) and α_{123} (interaction of all three factors: bare hull LDR, towing speed and drift angle).

39

Now, an answer can be provided for the question: How an experiment (in the context of underwater vehicle hydrodynamics) should be designed in the future so as to conserve time and cost? To give an approximate quantity on the time and cost saving that could be made, noting the previous paragraph, with a 2^3 factorial design, performing only eight runs, we might obtain an approximation of the objective function g. Then, to check for the curvatures in the responses, the design could be augmented with axial runs to create a central composite design, which is a very effective design for fitting a second-order response surface model.

The full CCD for three factors is 14 runs plus the center-point runs. The center-point for instance, has coordinates (LDR, β) of (10, 10) in Fig. 2.17. Note that if we have performed the 2^3 design, only six axial runs plus the center-point runs should be augmented to it. Axial-runs have coordinates (8, 10), (12, 10), (10, 0) and (10, 20) in Fig. 2.17. It is usual to replicate the center-point runs. With e.g. three replications for the center-point the design totals to 17 runs. The present data for the resistance and static yaw tests totalled $16 + 60 = 76$ runs! The difference between the number of runs shows the time and cost saving.

2.6 Summary

In this chapter, experimental data for fixed-attitude manoeuvring experiments, i.e. resistance and static yaw tests, that were measured for a series of five axisymmetric bare hull models of the same diameter but of increasing length-to-diameter ratios of 8.5, 9.5, 10.5, 11.5 and 12.5 were presented and analyzed. Empirical formulae to predict the drag,

lift and moment coefficients for the bare hull of an axisymmetric underwater vehicle were proposed.

Next, from a statistical design of experiment (DOE) point of view, the effects of the main factors in each type of experiment were studied. Derivation of a unified response for the axial force, lateral force and turning moment that are exerted on the bare hull during fixed-attitude experiments was discussed. With a statistically designed experiment, the adequate regression equation, which gives the hydrodynamic loads versus the main factor effects and interaction effects, can be derived. Moreover, with a statistically designed experiment, the possible saving of time and cost in the experiments was suggested. As was illustrated for the present data, the number of runs for a statistically designed experiment is several times less than the regular one-factor-at-time experiment which means a great saving in time and cost.

CHAPTER 3

VARIABLE-ATTITUDE TESTS: PURE SWAY EXPERIMENTS

3.1 Introduction

Pure sway experiments on the five hull forms for an axisymmetric underwater vehicle were also performed in the 90 m towing tank at NRC-IOT in November 2005. These experiments used the towing carriage to move the vehicle along the tank x-axis, the PMM (Planar Motion Mechanism) to produce the oscillating lateral (sway) motions, and, an internal three-component balance to measure two hydrodynamic forces (axial, lateral) and the hydrodynamic yaw moment.

As was introduced in the previous chapter, the original bare hull model had a length-to-diameter ratio (*LDR*) of about 8.5:1. Extension pieces were added to the parallel mid-body to test hulls of the same diameter, 203 mm, but with *LDR* 9.5, 10.5, 11.5 and 12.5. The carriage forward velocity for all the runs was 2 m/s; in the pure sway runs the sway velocity of the PMM had smooth sinusoidal variations with amplitudes of about 0.55 m/s for most of the runs. The maximum and minimum sway motion amplitudes for the pure sway runs were 1.25 and 0.32 m; the maximum and minimum periods of oscillation were respectively about 14.3 and 3.5 s for all the bare hull configurations. Although some parts of the pure sway test results that were performed on five axisymmetric bare hull models in November 2005 were published in an earlier report in September 2006 [Williams et al. 2006], a more comprehensive analysis of the filtered data was necessary. Analysis of the resulting experimental data from the pure sway captive manoeuvring tests reveals a variation of the apparent mass with the oscillation amplitude and frequency.

3.2 Pure sway tests

One way to study the time-varying hydrodynamic loads which are experienced by a fully-submerged underwater vehicle is to perform captive-model forced oscillations with a device such as a Planar Motion Mechanism (PMM). In practice it is convenient (for programming of the drive motions, smoothness of the loads imposed on the PMM, and, for data-analysis purposes) to use sinusoidal motions. In a spatial coordinate system, such as a towing tank, a sinusoidal trajectory can be defined by the width of one cycle of the trajectory (cycle-width) and the amount of length of towing tank required to execute one cycle, the cycle-length. In the context of the motions of the PMM and the towing carriage, the cycle width is equivalent to twice the amplitude of the lateral (sway) motion A, and the cycle-length is equivalent to the product $T \cdot u_{carriage}$ where T is the period of the motion and $u_{carriage}$ is the constant carriage speed.

In a pure sway manoeuvre, the *CG* of the vehicle is moved through a sinusoidal path while the longitudinal axis of the vehicle is held parallel to the towing carriage's forward direction that is: the vehicle's yaw angle remains at zero during all the pure sway runs. As a result, the sway force and yaw moment measured on the vehicle during pure sway runs are larger than the loads in pure yaw runs. In this study the purpose of the pure sway experiments was to measure the sway force and yaw moment as functions of PMM lateral velocity and acceleration. In pure sway runs the body-fixed and global coordinates are parallel to each other; positive x, y and z-axes are respectively defined forward, to starboard and downwards. Assuming that time starts when the model passes the towing tank centerline in the positive y direction, sway displacement and velocity of the PMM

43

are as follow:

$$y = A \sin(\omega t) \tag{3-1}$$

$$v = v_0 \cos(\omega t) \tag{3-2}$$

where A and v_0 are the amplitude of the PMM sway displacement and velocity respectively, and v_0 is given by $A \cdot \omega$.

Differentiating (3-2) results in the PMM's and thus the model's sway acceleration as:

$$a_y = a_{y0} \cos(\omega t + \frac{\pi}{2}) \tag{3-3}$$

where a_{y0} is the amplitude of the sway acceleration of the PMM given by $A \cdot \omega^2$. Also, from the tests it is concluded that the sway force can be represented in the form:

$$F_y = F_{y0} \cos(\omega t + \varphi_F) \tag{3-4}$$

where F_{y0} is the amplitude of the sway force measured by the internal balance and φ_F is the phase lag between the sinusoidal sway force and sinusoidal sway velocity motions, that is, φ_F is the amount by which the PMM sway velocity leads the measured sway force. See Table 3.1 on pages 74 and 75 at the end of this chapter for the pure sway manoeuvring data. The raw time-series were filtered using the "filtfilt" function in MATLAB™ which does not use a frequency band to filter the signal, but it calculates a smoothed value at each time-instant by averaging n data points in the vicinity; in this analysis n was 20. Since, this filter processes the data twice, once in the forward direction and once in the reverse direction, no phase shift is introduced into the signal, which is of particular interest in the present method of analyzing the data where the phase shift between the PMM motion and the measured loads is of primary interest.

3.3 Data analysis

3.3.1 Manoeuvring frequency and amplitude

The manoeuvring amplitude versus frequency for all pure sway runs for the bare hull with *LDR* 8.5 is plotted in Fig. 3.1. For other bare hulls the amplitude and frequency are also the same as in Fig. 3.1. Since the tests were planned to have about the same sway velocity amplitude for most of the runs, $v_0 = A \cdot \omega$ is constant at about 0.55 [m/s], hence there is an inverse relationship between the amplitude A and frequency ω as can be seen in Fig. 3.1. However, as will be presented later, the sway frequency and amplitude are the two independent factors affecting the sway force amplitude and phase. There are two sets of runs with equal frequency but different amplitude. There is one single run of frequency about 0.44 rad/s and amplitude 0.7 m which has lower sway velocity amplitude that is about 0.3 m/s (Table 3.1).
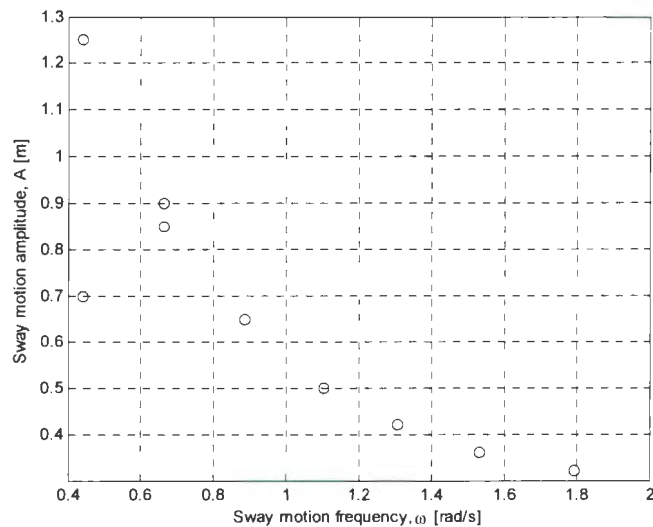
Fig. 3.1 Sway amplitude versus frequency for all runs for the bare hull with *LDR* 8.5

3.3.2 The sway force amplitude

It is simplest first to interpret the results for a single bare hull configuration, and then the effect of model size can be studied. Sway force amplitude versus sway frequency for *LDR* 8.5 is plotted in Fig. 3.2. It is clear that for the runs of equal frequency, the lower maximum sway velocity – that is the smaller manoeuvre amplitude – produces a smaller force. Next, the sway force amplitude is plotted against sway acceleration amplitude in Fig. 3.3. The run with the lowest maximum acceleration results in the smallest sway force amplitude. It is seen that the amplitude of the sway force increases with increasing amplitude of the sway acceleration.
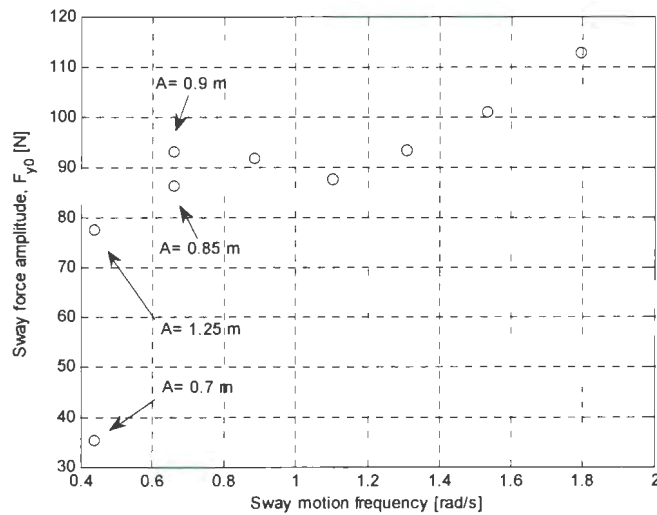
Fig. 3.2 Sway force amplitude versus sway frequency for the bare hull with *LDR* 8.5
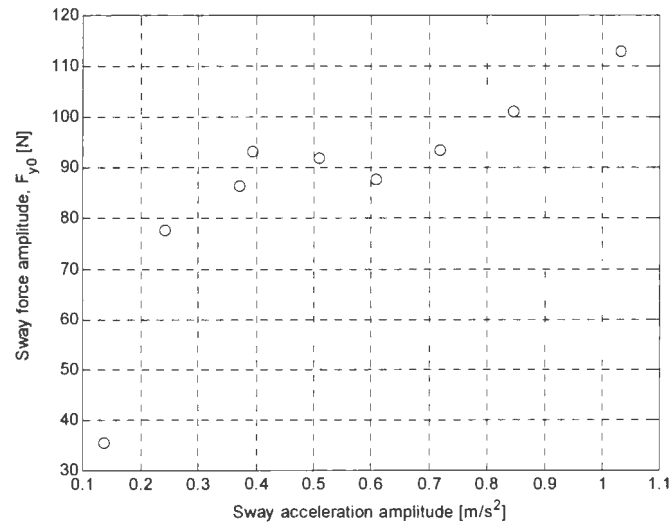
Fig. 3.3 Sway force amplitude versus sway acceleration

amplitude for the bare hull with *LDR* 8.5

3.3.3 Phase lag between the sway force and sway velocity signals

The values of the phase lag between the sway force and sway velocity signals (minus 90 degrees) as presented in Table 3.1 for the five bare hulls, are shown in Fig. 3.4. As the sway frequency, and thus the amplitude of the acceleration increase, the phase lag decreases. Also, the phase lag for longer bare hulls is smaller. As a result, one may anticipate that if this trend continues for higher frequencies that this phase lag will tend to zero.

47
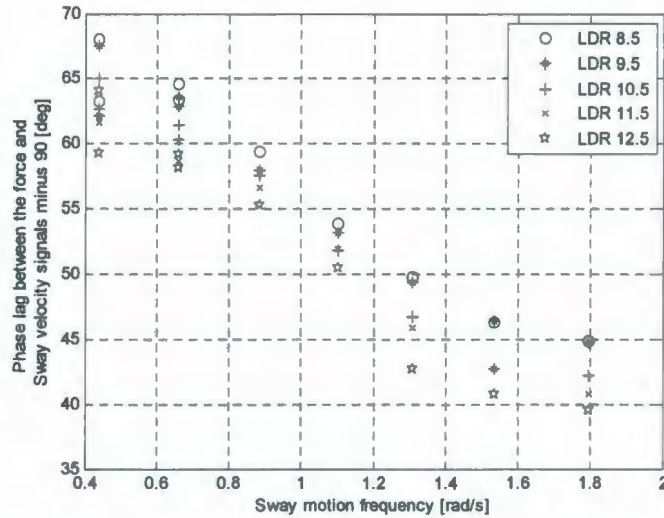
Fig. 3.4 Phase lag between the sway force and sway velocity signals (minus 90 degrees)

during pure sway runs

3.3.4 The inertial and damping terms

As was explained in chapter 2, it is assumed that the recorded hydrodynamic loads during these pure sway runs were not affected by any free-surface effect because of the large distance from the bare hull to the free surface. Also, it is assumed that the hydrodynamic loads due to the supporting struts did not affect the recorded signals (see Fig. 2.3). Thus, the recorded sway force signal is assumed to be solely due to the lateral accelerations of the bare hull models. As is shown in Table 3.1 on pages 74 and 75 and Fig. 3.4, the sway force signal has a phase lag of φ_F, larger than $\pi/2$, relative to the velocity signal. In Fig. 3.5 the sway velocity is shown by a vector pointing to the right, the sway acceleration vector points upward, and the sway force vector is shown in the second quadrant. Since with increasing time these vectors rotate in the clockwise direction, the velocity vector leads the sway force vector by the angle φ_F. Projecting this sway force vector along the

48

real and imaginary axes respectively produces (i) the damping component of the force vector, named $F_{y,d}$ which acts in phase with the velocity vector but in the opposite direction, and, (ii) the inertial component of the force vector, named $F_{y,i}$ which is in phase with the acceleration vector.
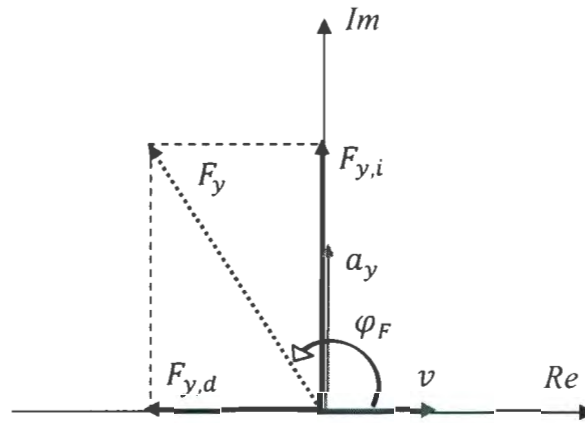
Fig. 3.5 Velocity, acceleration and force vectors in the complex plane

As shown in Fig. 3.5 the amplitude of the damping and inertial components of the sway force vector are derived as:

$$F_{y0,d} = -F_{y0} \sin\left(\varphi_F - \frac{\pi}{2}\right) \tag{3-5}$$

$$F_{y0,i} = F_{y0} \cos\left(\varphi_F - \frac{\pi}{2}\right) \tag{3-6}$$

According to the experimental data in Table 3.1, as the frequency increases (i) the magnitude of the sway force increases and (ii) the phase lag φ_F decreases, both of which result in a larger inertial component of the sway force.

3.3.5 The apparent mass versus manoeuvring frequency and amplitude

If the inertial component of the sway force vector in (3-6) is divided by the amplitude of the sway acceleration, the resulting parameter is the apparent mass of the system (the

flooded vehicle mass, reported in Table 2.1, plus the added mass of the surrounding water external to the vehicle), that is:

$$F_{y0,i}/a_{y0} = m_{apparent} \ [\text{kg}] \tag{3-7}$$

where a_{y0} is given by $A \cdot \omega^2$. The magnitude of the apparent mass from (3-7) is shown in Table 3.1 for all pure sway runs for all the bare hulls. The apparent mass for the bare hull with LDR 8.5 is plotted in Fig. 3.6 versus the sway acceleration amplitude. The same data are plotted versus the sway frequency ω and amplitude A in Figs. 3.7 and 3.8. The sway velocity amplitude for each data point is also shown in Figs. 3.6 to 3.8.
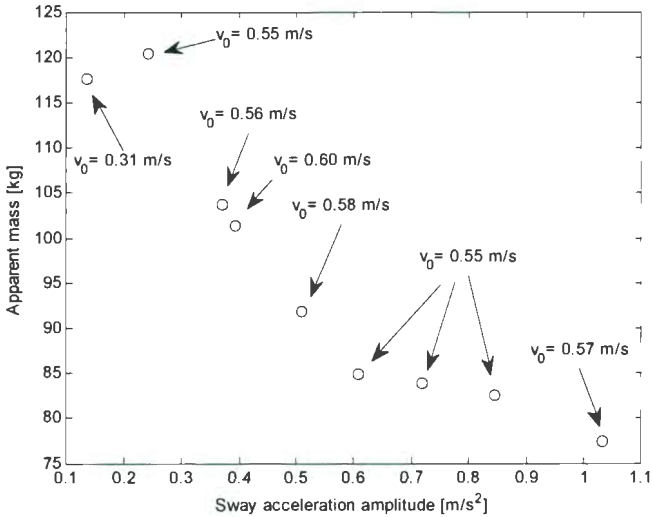
Fig. 3.6 Apparent mass of the bare hull with _LDR_ 8.5 versus sway

acceleration amplitude during pure sway runs

50
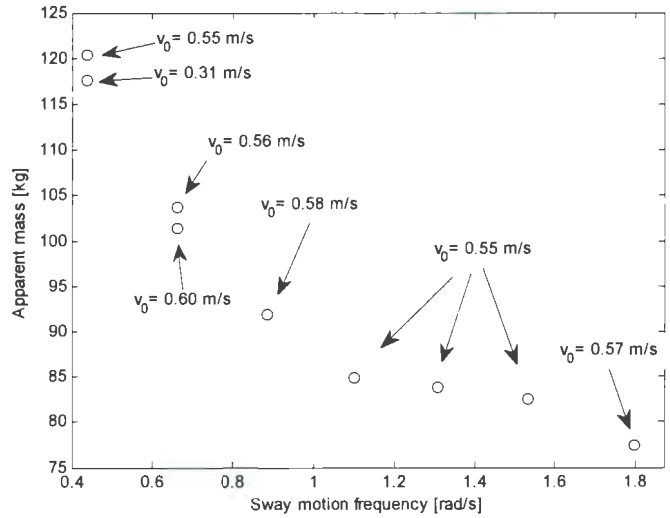
Fig. 3.7 Apparent mass of the bare hull with *LDR* 8.5 versus sway frequency

during pure sway runs
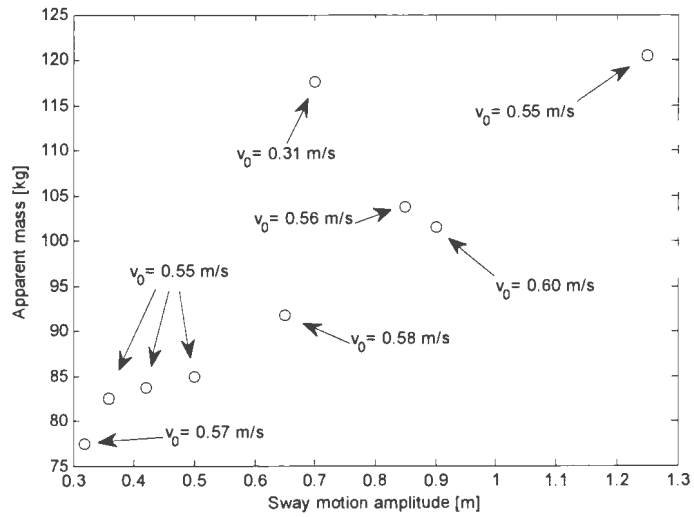
Fig. 3.8 Apparent mass of the bare hull with *LDR* 8.5 versus sway amplitude

during pure sway runs

51

Clearly seen for the *LDR* 8.5 data, the apparent mass resulting from these lateral acceleration manoeuvres is variable. From Figs. 3.8 to 3.10 the following conclusions can be made:

1. Fig. 3.6 shows that as the amplitude $A \cdot \omega^2$ of the sway acceleration increases, the apparent mass decreases.

2. Fig. 3.7 shows that as the frequency ω of the sway motion increases, the apparent mass decreases.

3. Fig. 3.8 shows that as the amplitude A of the sway motion increases, the apparent mass increases.

4. According to Fig. 3.6, the lateral velocity and acceleration have independent effects on the magnitude of the apparent mass, because the data with different sway velocity amplitudes do not lie along a curve. Since the velocity and acceleration amplitudes are respectively: $A \cdot \omega$ and $A \cdot \omega^2$, it can be concluded that the oscillation amplitude and frequency are in fact the two independent factors that are affecting the magnitude of the apparent mass besides the body geometry, that is:

$$m_{apparent} = f(A, \omega, geometry) \qquad (3\text{-}8)$$

5. In Fig. 3.7 for the same sway velocity 0.55 m/s, the three data-points which have frequencies higher than 1 rad/s result in almost the same apparent mass of about 85 kg.

6. According to Fig. 3.8, for the same sway motion amplitude, a lower sway velocity amplitude $A \cdot \omega$ results in larger apparent mass. Note that one should

avoid concluding from the two smallest frequency data-points in Fig. 3.7 that for the same frequency a larger amplitude of the sway velocity results in a larger apparent mass, because then the next pair of data-points in Fig. 3.7, which also have the same frequency suggest the contrary. Thus, again it is emphasized that for equal motion amplitude, according to Fig. 3.8, a sway manoeuvre with a longer period results in a larger apparent mass.

7. From Fig. 3.8 one should not conclude that the magnitude of the apparent mass will indefinitely increase as the amplitude of the sway motion increases. The apparent mass will reduce to the vehicle mass for large amplitudes. Because, for an arbitrary sway velocity amplitude, if the oscillation amplitude becomes too large, then the sway acceleration amplitude tends to zero. The reason is that the sway acceleration amplitude is as follows:

$$\omega = v_0/A, \text{ and } a_0 = A \cdot \omega^2 \rightarrow a_0 = v_0^2/A \qquad (3\text{-}9)$$

Thus, for an arbitrary sway velocity if the sway motion amplitude becomes too large, then the sway acceleration becomes so small that the inertial effects notably vanish.

8. The flooded vehicle mass for LDR 8.5 was measured to be about 49.2 kg (Table 2.1) by which amount the data in Figs. 3.6 to 3.8 should be shifted downward to show the added mass values; that is, the added mass for LDR 8.5 varies between about 28.3 to 71.2 kg depending on the sway frequency and amplitude.

3.3.6 The apparent mass versus the bare hull size

Next, Fig. 3.9 shows the apparent mass for the five bare hull configurations versus the sway frequency. The clear pattern is that for all configurations the magnitude of the apparent mass appears to tend asymptotically to a single value as the frequency increases. On the other hand, if the experimental data are plotted versus the bare hull LDR, as shown in Fig. 3.10, it is seen that there is effectively a linear increase in the magnitude of the apparent mass with increasing LDR, for all the combinations of sway frequency and amplitude shown.
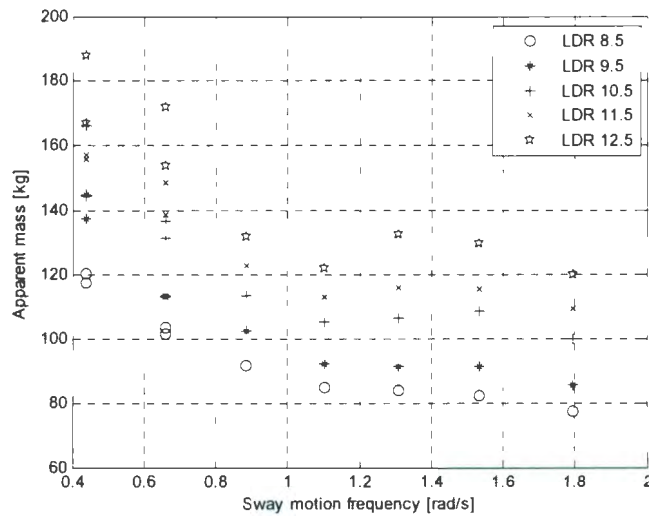
Fig. 3.9 Apparent mass versus sway motion frequency for all the bare hulls during pure sway runs
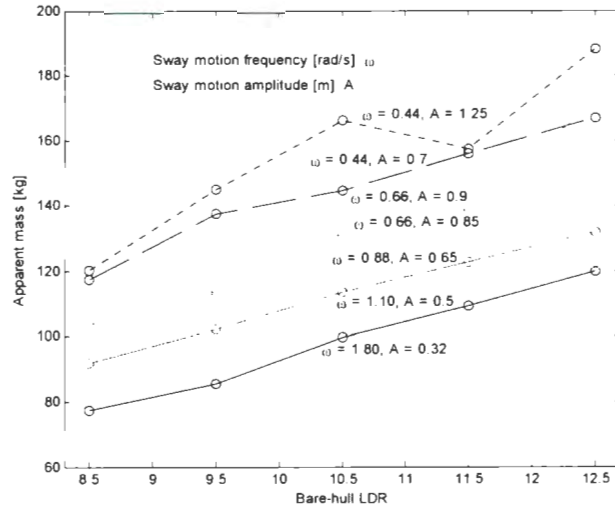
Fig. 3.10 Apparent mass versus bare hull *LDR* for several combinations of sway frequency and

amplitude during pure sway runs

3.3.7 The damping factor

Going back to Fig. 3.5 and equation (3-5), if the damping component of the sway force

vector is divided by the sway velocity amplitude the resulting value is a damping factor

which is often denoted by b, that is:

$$|F_{y0,d}|/v_0 = b \ \ [\text{kg/s}], \tag{3-10}$$

where: $v_0 = A \cdot \omega$. The magnitude of the damping factor from (3-10) is shown in column

#10 in Table 3.1 on pages 74 and 75 for all pure sway runs for all the bare hulls. Note that

the damping force acts in the opposite direction of the velocity vector but the damping

factor is defined to be positive. The damping factor derived by (3-10) has the dimension

of [kg/s] and the dimensional values are between about 100 to 180 [kg/s]. Fig. 3.11 shows

how the damping factor varies with the frequency of the sway motion. It is observed that

the damping factor is largest for the longest model.

55
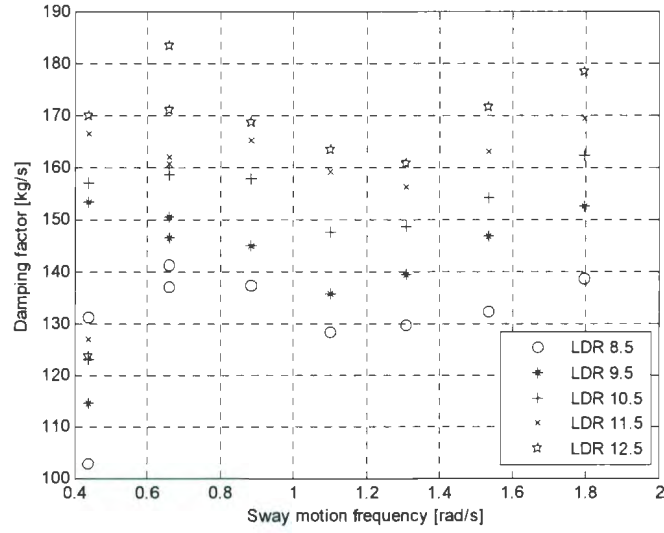
Fig. 3.11 Damping factor versus frequency of sway motion for all bare hulls

during pure sway runs

3.4 The sway force model

Using the rotating vector representation in Fig. 3.5, the sway force in a pure sway manoeuvre at time instant $t = 0$ can be modeled as follows:

$$F_{y(t=0)} = F_{y0,d} + i\, F_{y0,i} = -bv_0 + i(m_{apparent} a_{y0}) \qquad (3\text{-}11)$$

where i is the imaginary unit vector. Equation (3-11) is rewritten as follows:

$$F_{y(t=0)} = -bA\omega + i(m_{apparent} A\omega^2) \qquad (3\text{-}12)$$

Then the amplitude of the sway force is found to be:

$$F_{y0} = A\omega \left[b^2 + \left(m_{apparent}\omega\right)^2\right]^{(1/2)} \qquad (3\text{-}13)$$

and the amount by which the sway force lags the sway velocity is given by:

$$\varphi_F = \tan^{-1}\left(-m_{apparent}\omega/b\right) = \tan^{-1}\left(b/m_{apparent}\omega\right) + \frac{\pi}{2} \qquad (3\text{-}14)$$

56

In general, the magnitude of the apparent mass and the magnitude of the damping factor depend on the body geometry as well as the sway frequency and amplitude. The parameters for the sway force model in (3-13) and (3-14) can be obtained from the experimental data for each of the five models. The time variation of the sway force is obtained by substituting the force amplitude and phase lag from (3-13) and (3-14) into equation (3-4), that is: $F_y = F_{y0} \cos(\omega t + \varphi_F)$.

3.5 Uncertainty in the test results

The model that was constructed for the sway force during lateral acceleration manoeuvres can be checked for the uncertainty. The apparent mass was derived as the in-phase component of the sway force divided by the lateral acceleration of the PMM as follows:

$$m_{apparent} = \cos\left(\varphi_F - \frac{\pi}{2}\right) \cdot (F_{y0}/A\omega^2) \tag{3-15}$$

Equation (3-15) provides an explicit statement for the apparent mass versus the experimentally measured values: amplitude of the sway force F_{y0}, and the phase lag between the sway force and sway velocity signals φ_F, as well as the manoeuvring amplitude and frequency. Using (3-15), uncertainty in the prediction of apparent mass during the pure sway manoeuvres can be studied. There may be the following uncertainties in the pure sway experiments:

(1) The planar motion mechanism (PMM) is uncertain in performing the required amplitude and frequency. Since the manoeuvring frequency and amplitude, during a pure sway manoeuvre, are independent parameters, thus the test facility also may have independent uncertainties. Therefore, the test facility is $x_1\%$ uncertain

57

in performing the required sway amplitude and $x_2\%$ uncertain in performing the required frequency.

(2) The load cells are $x_3\%$ uncertain in measuring the magnitude of the sway force.

(3) The phase difference between the sinusoidal curve fits to the recorded signal for the sway force and the sway velocity signal, that is: φ_F, are read with $x_4\%$ uncertainty.

Also if it is assumed that: the command signals that are sent to the test facility (carriage and PMM) are transferred with 100% certainty, and the measured load values are transferred with 100% certainty through the recording channels, then the above three items are the main sources of uncertainty during the tests. Substituting those uncertainty sources into (3-15) results in:

$$m_{apparent} = \cos\left(x_4 * \varphi_F - \frac{\pi}{2}\right) \cdot (x_3 * F_{y0})/[(x_1 * A)(x_2{}^2 * \omega^2)] \qquad (3\text{-}16)$$

Assuming a confidence level of 98% for the PMM performance, i.e. $x_1 = 0.98$ and $x_2 = 0.98$, and a confidence level of 95% for the data analysis in reading the magnitude of the sway force and its phase difference, i.e. $x_3 = 0.95$ and $x_4 = 0.95$, then the apparent mass versus manoeuvring frequency for the bare hull model of LDR 8.5 is plotted with the error intervals as shown in Fig. 3.12. According to (3-16), the lower bars are resulting if the PMM sway amplitude and frequency are both larger than the recorded values in Table 3.1, and the amplitude of the sway force is smaller and its phase lag is larger than estimated in Table 3.1. The upper bars are resulting if the frequency and amplitude are smaller, the sway force is larger and the phase lag is smaller than their

58

values in Table 3.1 on pages 74 and 75. Note that there are two data points at frequencies 0.44 and 0.66 rad/s.
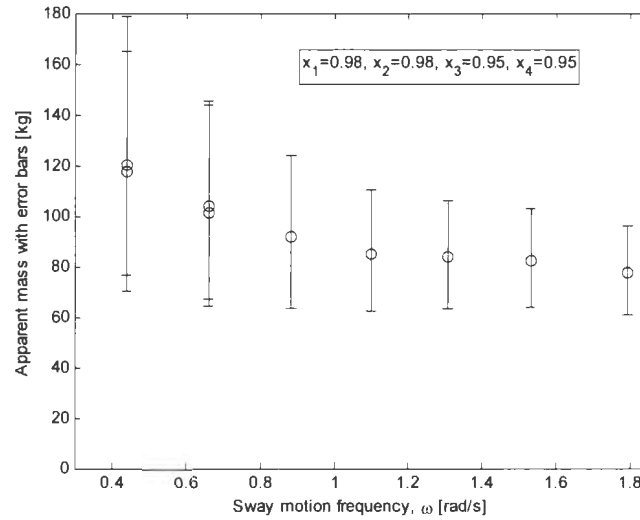
Fig. 3.12 Apparent mass of the bare hull LDR 8.5 during pure sway manoeuvres including the error bars

At this level of uncertainty for these parameters, still the trend of varying apparent mass versus the manoeuvring frequency does not lay within the uncertainty limits. The largest uncertainties in the data in Fig. 3.12 are about 40% lower and 50% upper limits which occur at the smallest frequency: the most rapid manoeuvre. However, the uncertainty in the test results for the apparent mass in Fig. 3.12 is rather large and is even larger if e.g. the uncertainty in reading the phase lag x_4 has been larger than 95% which is quite possible. Thus, further PMM experiments are suggested to clarify the phenomenon.

3.6 An improved design for future pure sway experiments

Observation of the pure sway test data revealed that the sway force vector, in addition to the body geometry, is a function of two independent variables (i) the amplitude of the

sway velocity $A \cdot \omega$, and, (ii) the amplitude of the sway acceleration $A \cdot \omega^2$, in a lateral harmonic manoeuvre. In other words, the sway motion amplitude A and frequency ω should vary independently during the experiments so as to acquire data-points at different levels of both sway velocity and sway acceleration. With the present test data, since the sway amplitude and frequency had an inverse relation for most of the runs, it is only possible to observe the sway force variation versus lateral acceleration for a particular sway velocity amplitude of about 0.55 m/s. With a statistical design of experiment, using the concept of response surface models, the tests can be designed starting with a basic two-level factorial scheme which is then augmented with axial and centre-point runs so as to capture the variation of the response, sway force, over the two test factors: (i) the amplitude of the sway velocity $A \cdot \omega$, and, (ii) the amplitude of the sway acceleration $A \cdot \omega^2$.

Fig. 3.13 proposes an example test plan which covers a range of 0.3 to 0.6 [m/s] for the sway velocity amplitude and a range of 0.1 to 0.8 [m/s^2] for the sway acceleration amplitude. In the figure the factor sway velocity varies horizontally, and the factor sway acceleration is along the vertical axis. The design has both axial runs which are outside the square-box, and face-centered runs which lie on the sides of the square. Such an experimental plan can capture the variation of the sway force over the manoeuvring frequency and amplitude. In Table 3.2 the proposed test runs are shown; for each run the manoeuvring frequency is obtained by dividing the acceleration amplitude by the velocity amplitude, and then the amplitude A of the sway displacement equals the amplitude of the sway velocity $A \cdot \omega$ divided by the sway frequency ω.

60
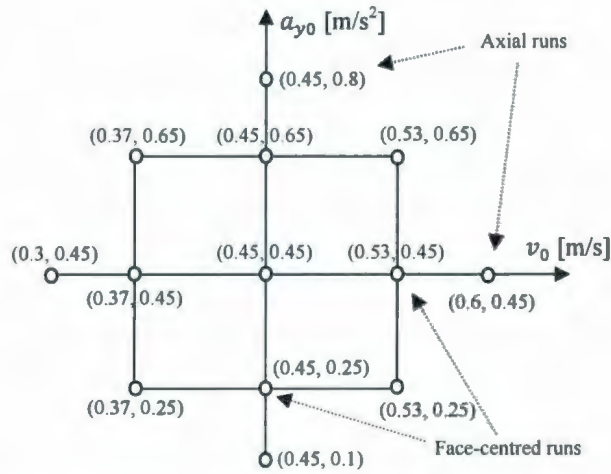
Fig. 3.13 Test runs: pairs of factor levels for the sway velocity and

sway acceleration amplitudes

Table 3.2 Test-plan proposed for future pure sway tests in order to cover both the manoeuvring

frequency and amplitude effects on the sway force response

Run No.	v_0 [m/s]	a_{y0} [m/s²]	$\omega = a_0/v_0$ [rad/s]	$A = v_0/\omega$ [m]
1	0.37	0.25	0.68	0.55
2	0.53	0.25	0.47	1.12
3	0.37	0.65	1.76	0.21
4	0.53	0.65	1.23	0.43
5	0.45	0.1	0.22	2.03
6	0.45	0.8	1.78	0.25
7	0.3	0.45	1.50	0.20
8	0.6	0.45	0.75	0.80
9	0.45	0.45	1.00	0.45
10	0.45	0.25	0.56	0.81
11	0.45	0.65	1.44	0.31
12	0.37	0.45	1.22	0.30
13	0.53	0.45	0.85	0.62

The centre-point run number 9 has the velocity and acceleration amplitude pair of (0.45

m/s, 0.45 m/s²) which corresponds to a frequency and sway motion amplitude of $(\omega, A) =$

(1 rad/s, 0.45 m). This run could be replicated three times so as to provide a measure of

61

the experimental repeatability. For example, with three replications for the centre-point run, the design scheme in Fig. 3.13 totals to 15 runs; to this if a study of the effect of the bare hull geometry is added, e.g. with three different bare hulls the test set totals to 45 runs which is equal number of runs as the present data.

3.7 Instantaneous lift and drag forces

During pure sway manoeuvres due to the combination of forward towing speed and PMM sway velocity, there is an apparent drift angle which produces apparent lift and drag forces on the model. Fig. 3.14 illustrates the apparent drift angle. Since the maximum sway velocity occurs when the model passes the centre-line, the apparent drift angle is a maximum at that time instant which is calculated as follows:

$$\beta = \tan^{-1}(v/u) \tag{3-17}$$

Towing speed u was 2 m/s for all runs and maximum sway velocity of the PMM was about $v = 0.56$ m/s for most of the runs which results in a maximum apparent drift angle of about 16 deg. Since the sway velocity during pure sway runs varies sinusiodally, the apparent drift angle also has a harmonic sinusoidal variation. The apparent drag and lift forces that are exerted on the vehicle due to the apparent drift angle are calculated as follows:

$$D = \tfrac{1}{2}\rho A_f U^2 C_D, \tag{3-18}$$

$$L = \tfrac{1}{2}\rho A_f U^2 C_L \tag{3-19}$$

where $A_f = \pi d^2/4$ and $U^2 = u^2 + v^2$. Drag and lift coefficients in the above formulae are functions of the apparent drift angle.
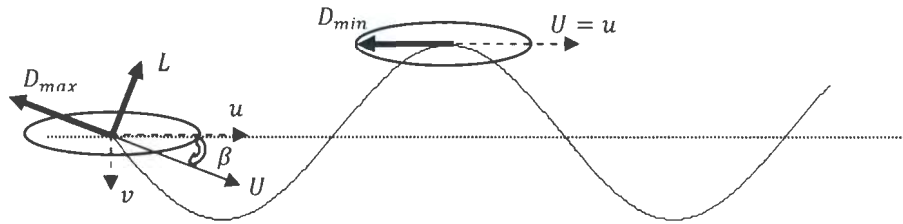
Fig. 3.14 Illustration of the apparent drift angle during pure sway manoeuvres and the resulting apparent drag and lift forces

As was explained in chapter 2, static yaw test results were used to model the drag and lift coefficients versus drift angle and LDR of the five bare hull configurations. The following models were obtained (equations (2-13) and (2-14)):

$$1000 * C_D = 1.88 \, \beta^2 + 11.7 \, LDR + 38 \qquad (3\text{-}20)$$

$$1000 * C_L = (0.007 \, LDR + 0.011)\beta^3 + (4.87 \, LDR + 8.85)\beta \qquad (3\text{-}21)$$

where the drift angle in (3-20) and (3-21) is in degrees. Thus, e.g. for a maximum apparent drift angle of 16 deg which occurs at the towing tank centre-line, the maximum drag and lift coefficients are respectively: 0.62 and 1.08 which are then vary sinusoidally during a pure sway run. The minimum apparent drift angle is zero at the instant at which the sway motion displacement is maximum, for which the lift coefficient from (3-21) is zero and the drag coefficient from (3-20) for respectively shortest to longest bare hulls (LDR 8.5 and 12.5) is about 0.14 to 0.18.

Hence, the apparent lift and drag forces which for each run vary sinusoidally with the same frequency as of the PMM, are maximum while the model passes the towing centre-line. The apparent drag force has a non-zero minimum, while the apparent lift force is zero at the maximum sway displacements as was illustrated in Fig. 3.14. The maximum

and minimum apparent drag forces as well as the maximum apparent lift force are shown in Table 3.1 at the end of this chapter.

Now, if the apparent drag and lift forces are projected along the towing x and y-axes, the axial and lateral forces due to these apparent drag and lift are calculated as follows:

$$F_{x,static} = D \cdot \cos(\beta) - L \cdot \sin(\beta) \tag{3-22}$$

$$F_{y,static} = L \cdot \cos(\beta) + D \cdot \sin(\beta) \tag{3-23}$$

The resulting amounts for the axial force and sway force from (3-22) and (3-23) at the maximum apparent drift angle which occurs at the towing centre-line are also shown in Table 3.1. In (3-22) and (3-23) the index "static" was added to indicate that these axial and sway forces were calculated using the previously introduced models for the drag and lift coefficients during static-yaw tests. Fig. 3.15 compares the sway force amplitude that is estimated using (3-23) to the sway force amplitude as was measured during pure sway tests at two extreme manoeuvring frequencies of 1.8 and 0.44 for the five bare hulls.

As is observed in Fig. 3.15 and Table 3.1, the sway force amplitude due to the apparent lift and drag forces as is calculated by (3-23), does not vary notably versus the manoeuvring frequency, while the sway force amplitude that was measured during pure sway manoeuvres varies significantly from a small value at low frequency to a large value at high frequency. This effect is due to the added mass phenomena. It appears that the pure sway test data at low frequency $\omega = 0.44$ [rad/s], shown by red squares, are very close to the estimated value due to the apparent instantaneous drag and lift forces.
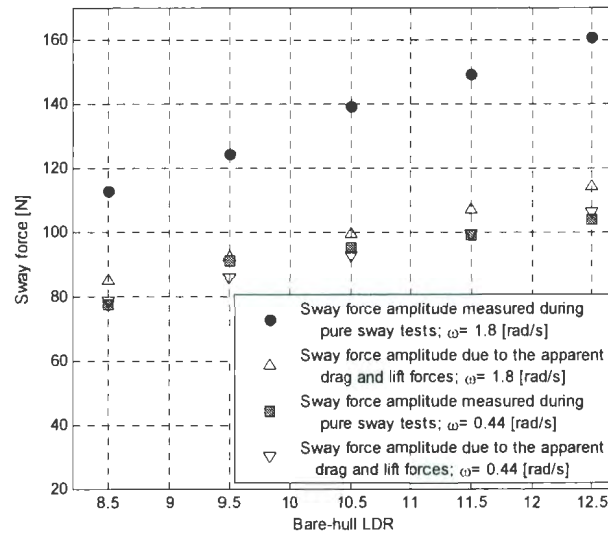
Fig. 3.15 Sway force amplitude at low and high frequencies for the five bare hulls:

pure sway test data compared to the estimated value in (3-23)

The axial force that was estimated by (3-22), as shown in Table 3.1, has a maximum value at the towing centre-line of about 20 N for the shortest model. However, at the sway motion amplitudes, where the apparent drift angle is zero, the estimated axial force which is equal to the minimum apparent drag force is about 10 N. The measured axial force signals during pure sway tests were not analyzed yet to verify such a sinusoidal variation in the axial force during pure sway manoeuvres due to the apparent drift angle.

3.8 Deriving the conventional sway coefficients from PMM tests

The application of the planar motion mechanism (PMM) to perform captive manoeuvring tests and the conventional approach to derive the hydrodynamic coefficients from those tests have been presented in sources such as [PNA, 1967], [Goodman, 1960] and [Bishop and Parkinson, 1970].

In a static yaw test the towing speed U is the total speed of the model, thus sway velocity of the model is:

$$v = -U \sin(\beta) \tag{3-24}$$

Therefore, slopes of plots of sway force and yaw moment curves versus drift angle give values for the derivatives Y_v and N_v. The slopes of those curves for the Phoenix bare hull with LDR 8.5 (Figs. 2.10 and 2.11) are: $Y_v \approx -110$ N/(m/s) and $N_v \approx -58$ N.m/(m/s). Non-dimensional derivatives are calculated for bare hull length: $l= 1.73$ m and towing speed: $U= 2$ m/s, dividing the force derivative by $\frac{1}{2}\rho U l^2$ and the moment derivative by $\frac{1}{2}\rho U l^3$ which results in $Y_v' = -0.037$ and $N_v' = -0.011$. A negative value for the moment derivative N_v means that the effect of the bow dominates. In the same manner for all the five hulls with length-to-diameter ratios 8.5 to 12.5 the non-dimensional force and moment derivatives are calculated from the static yaw test results as follows:

$$Y_v' = -[0.037, \ 0.029, \ 0.024, \ 0.02, \ 0.017] \tag{3-25}$$

$$N_v' = -10^{-3} * [11, 8.1, 6.0, 4.5, 3.5] \tag{3-26}$$

To derive the sway coefficients from the pure sway test results, the sway forces that are recorded by the fore and aft loadcells in the lateral direction respectively named F_1 and F_2 each are decomposed into in-phase and out-of-phase components relative to the sway displacement signal. Then it follows:

$$F_{in} = (F_1)_{in} + (F_2)_{in}, F_{out} = (F_1)_{out} + (F_2)_{out} \tag{3-27}$$

The amplitudes of the in-phase and out-of-phase forces according to the illustration in Fig. 3.5 are respectively equivalent to the inertia and damping components, i.e.: $|F_{in,0}| = F_{y0,i} = F_{y0} \cos(\varphi_F - \pi/2)$, and $|F_{out,0}| = F_{y0,d} = F_{y0} \sin(\varphi_F - \pi/2)$. Then the

oscillatory derivatives of the sway force with respect to the sway acceleration and sway velocity are respectively defined as follows [Bishop and Parkinson, 1970, equation (68)]:

$$\tilde{Y}_{\dot{v}} = m - (F_{y0,i}/a_{y0}) \tag{3-28}$$

$$\tilde{Y}_v = -F_{y0,d}/v_0 \tag{3-29}$$

where according to the previous sections, amplitudes of the lateral velocity and acceleration of the PMM during a pure sway run are $v_0 = A\omega$ and $a_{y0} = A\omega^2$. In fact, equations (3-28) and (3-29) are analogous to (3-7) and (3-10), i.e., the velocity derivative of the sway force $\tilde{Y}_v$ is equal to the damping factor b that was defined in section 3.3.7, and the acceleration derivative of the sway force $\tilde{Y}_{\dot{v}}$ is the flooded mass of the vehicle m minus the apparent mass $m_{apparent}$ (the flooded mass of the vehicle plus the added mass of water) that was defined in section 3.3.5. Obviously, this definition for $\tilde{Y}_{\dot{v}}$ is not quite straightforward for using in the equation of motion {see equation (66) in [Bishop and Parkinson, 1970]}.

If (3-28) and (3-29) are multiplied by the sway motion frequency with some algebra the sway coefficients are calculated as follows:

$$(m - Y_{\dot{v}})^{\frac{1}{2}} = \text{slope at the origin of } (F_{y0,i}/A)^{\frac{1}{2}}$$

$$\text{plotted versus frequency as shown in Fig. 3.16} \tag{3-30}$$

$$Y_v = \text{slope at the origin of } (F_{y0,d}/A)$$

$$\text{plotted versus frequency as shown in Fig. 3.17} \tag{3-31}$$

This approach was presented by van Leeuwen [1964] for a model of a surface vessel. Fig. 3.16 as stated in equation (3-30) was pllotted using the pure sway test data for the five

bare hull configurations and lines were fitted to the test data. The line slopes at the origin, i.e. $\omega \to 0$, are larger for longer hulls. Then, rearranging (3-30) and substituting the line slopes from Fig. 3.16 and the flooded mass of the vehicle from Table 2.1 into it, the sway force derivative $Y_{\dot{v}}$ is calculated for the five hulls. Those values divided by $\frac{1}{2}\rho l^3$ result in the non-dimensional acceleration derivative of the sway force which is as follows for the bare hulls of LDR 8.5 to 12.5 respectively:

$$Y_{\dot{v}}' = -10^{-3} * [6.9, 4.5, 4.6, 4.0, 3.4] \tag{3-32}$$

The non-dimensional mass of the underwater bare hulls of LDR 8.5 to 12.5 using the data in Table 2.1 are respectively $m' = 10^{-3} * [19.2, 15.4, 13.1, 11, 9.4]$.
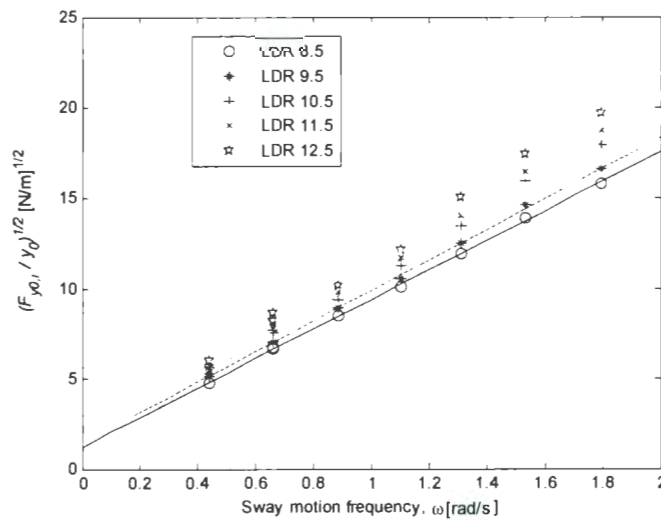
Fig. 3.16 The plot based on equation (3-30) to find the acceleration derivative of the sway force $Y_{\dot{v}}$

So it may be concluded that for a slender underwater bare hull the non-dimensional acceleration derivative of the sway force during a lateral acceleration manoeuvre has about one-third of magnitude of its non-dimensional mass. In fact, $Y_{\dot{v}}'$ is the no-dimensional added mass of the vehicle with a minus sign.

68

Fig. 3.17 as stated in equation (3-31) was plotted to derive the velocity derivative of the sway force Y_v. Then it is divided by $\frac{1}{2}\rho U l^2$ –at the towing speed of $U = 2$ m/s for all the runs– to conclude the non-dimensional sway force derivative with respect to the sway velocity for the five bare hulls of LDR 8.5 to 12.5 as follows:

$$Y_v' = -[0.046, \ 0.042, \ 0.035, \ 0.031, \ 0.028] \qquad (3\text{-}33)$$

Compared to the previously derived values of $Y_v' = -[0.037, \ 0.029, \ 0.024, \ 0.02, \ 0.017]$ in (3-25) that was from the static yaw test results for the five bare hulls, the above values in (3-33), although are in rough agreement, show that the velocity derivative of the sway force during a dynamic test, i.e. pure sway, is larger than predicted during static tests. So this may make the validity of deriving Y_v' from static yaw tests doubtful. Also van Leeuwen [1964] using (3-31) reported a non-dimensional sway force derivative Y_v' of about −0.02 for the surface vessel model which was 2.258 m long with a maximum breadth of 0.323 m thus a length-to-breadth ratio of about seven.
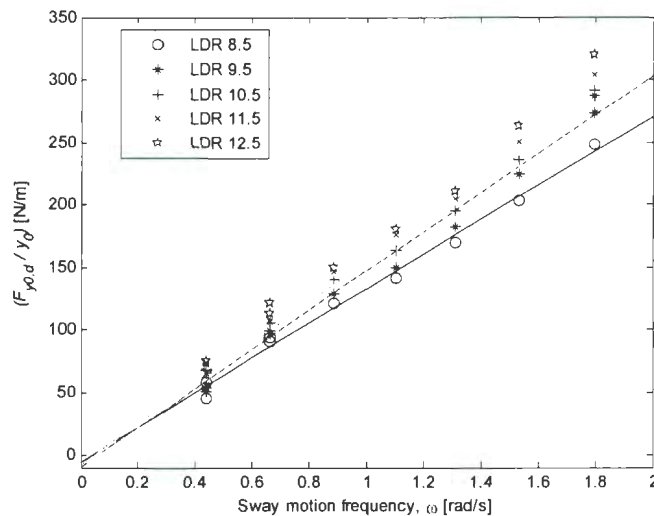
Fig. 3.17 The plot based on equation (3-31) to find the velocity derivative of the sway force Y_v

With the same approach as for the sway force, the yawing moment derivatives are calculated as follows:

$$\tilde{N}_{\dot{v}} = G_{in}/a_0, \tilde{N}_v = -G_{out}/v_0 \tag{3-34}$$

$$G_{in} = -M_{z0}\sin(\varphi_M - \pi), G_{out} = M_{z0}\cos(\varphi_M - \pi), \tag{3-35}$$

where M_{z0} is the amplitude of the yawing moment that was recorded during pure sway tests, and φ_M is the phase lag between the sinusoidal signal of the yaw moment and the sinusoidal signal of the sway velocity. The tests data for M_{z0} and φ_M are reported in Table 3.1 the last two columns on pages 74 and 75. The phase lag is very close to 180 degrees and the amplitude of the yaw moment is about 20 to 50 [N.m] for the five bare hulls (see Table 3.1). Using (3-34) and (3-35) the yaw moment derivatives $\tilde{N}_{\dot{v}}$ and $\tilde{N}_v$ (also called oscillatory coefficients in aeronautics [Bishop and Parkinson, 1970]) are calculated which are then non-dimensionalized respectively by $\frac{1}{2}\rho l^4$ and $\frac{1}{2}\rho U l^3$ as are plotted in Figs. 3.18 and 3.19. It is seen in Fig. 3.18 that the acceleration derivative of the yawing moment during a pure sway motion has a non-dimensional value $N_{\dot{v}}'$ close to zero which becomes negative as the manoeuvring frequency increases. A sinusoidal fit of type:

$$\text{Curve fit to } N_{\dot{v}}': a*\sin(bx+c) = 0.6*10^{-3}*\sin(1.9\omega + 8.26), \tag{3-36}$$

was crossed through all the data points in Fig. 3.18 which has an intercept of about $N_{\dot{v}}' \approx 0.5*10^{-3}$ at zero frequency. Van Leeuwen [1964] also reported a value of about 10^{-3} for $N_{\dot{v}}'$ with a similar variation versus manoeuvring frequency for the surface vessel model (see Fig. 9(b) in [Bishop and Parkinson, 1970]).
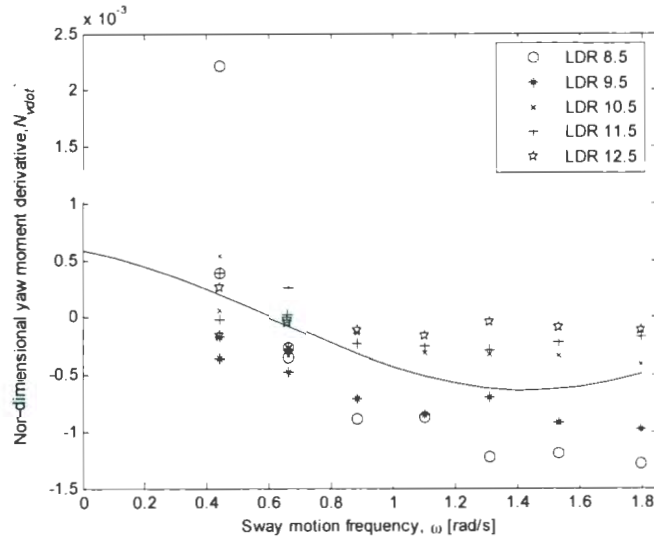
Fig. 3.18 Non-dimensional acceleration derivative of the yaw moment $N'_\dot{v}$ during pure sway tests

On the other hand, the velocity derivative of the yawing moment during a pure sway manoeuvre seems to be more significant. According to Fig. 3.19 the test data are about an average constant value for N'_v which are shown by solid lines for each LDR; it is seen that for longer hulls the non-dimensional derivative N'_v is smaller. If the constant average value is extended to $\omega \rightarrow 0$, then for the five bare hulls of LDR 8.5 to 12.5 it follows:

$$N'_v = -10^{-3} * [9.3, 7.7, 6.6, 5.7, 4.9] \tag{3-37}$$

Compared to the previously derived values of $N'_v = -10^{-3} * [11, 8.1, 6.0, 4.5, 3.5]$ in (3-26) from the static yaw test results, the above values in (3-37) show that the velocity derivative of the yaw moment during a dynamic test, i.e. pure sway, is somewhat different than predicted using the static tests.

71
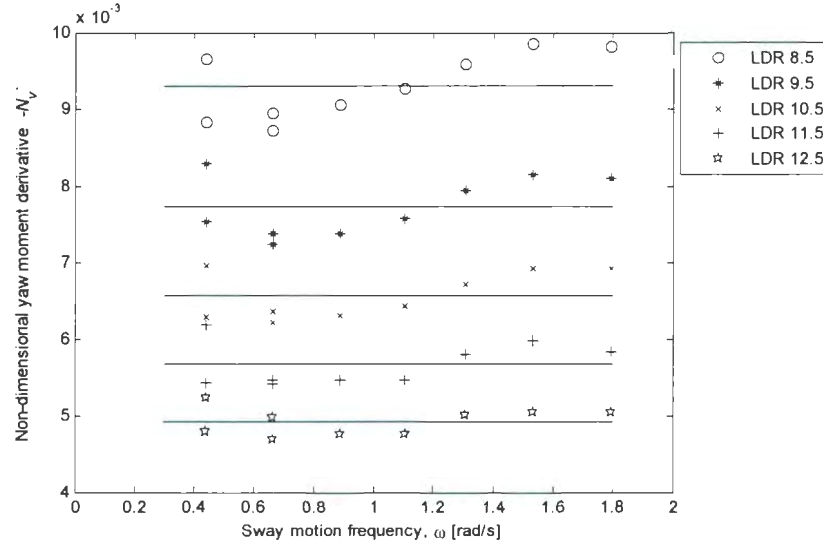
Fig. 3.19 Non-dimensional velocity derivative of the yaw moment N'_v during pure sway tests

Finally, it should be noted that although the values for hydrodynamic derivatives were derived in this section invariable with frequency, as suggested in previous sections of this chapter, there is a frequency effect on the amplitude and phase of the sway force and yaw moment during pure sway tests which should be studied more carefully with a better design of experiment as was roughly outlined in section 3.6.

3.9 Summary

This study presents test results that indicate how the sway force and yaw moment of the bare hull of an AUV varies during a lateral acceleration manoeuvre. In oscillating lateral motions such as the pure sway manoeuvres performed in these experiments, the value of the apparent mass depends on the manoeuvring frequency and amplitude as well as the body geometry. However, the presented results indicate that further experimental and analytical research is required to acquire an improved understanding of the apparent mass and damping phenomena in lateral acceleration manoeuvres.

The sway force that is exerted on the axisymmetric bare hull of an underwater vehicle during pure sway manoeuvres was modeled in the complex plane with its damping component in phase with sway velocity vector (but in the direction opposite to it), and its inertial component in phase with the sway acceleration vector. Then the amplitude and phase of the sway force were formulated versus the manoeuvring frequency and amplitude, the magnitude of the apparent mass and the magnitude of the damping factor of the system. As mentioned, it is shown that the magnitude of the apparent mass itself is a function of the body geometry, and the manoeuvring frequency and amplitude.

Also, the conventional method of analyzing the PMM test data was used to calculate the sway force and yawing moment derivatives. It was shown that the derivatives that are calculated using the dynamic test results compared to the same derivatives based on static yaw test results are rather different. Moreover, using the conventional method, still the frequency-dependency is observable in the test data during the dynamic manoeuvres.

An improved test-plan for future experimental work was also proposed in section 3.6 so that to perform the pure sway tests in a way that both the manoeuvring frequency and amplitude effects on the response sway force are independent variables instead of their product $A \cdot \omega$ being effectively held constant as is shown in the fifth column of Table 3.1 for the present experiments.

Table 3.1 Pure sway test results for the five bare hull series

Run No.	LDR	A [m]	ω [rad/s]	v_0 [m/s]	a_0 [m/s²]	F_{y0} [N]	$\varphi_F - 90$ [deg]	$m_{apparent}$ [kg]	b [kg/s]	D_{max} [N]	D_{min} [N]	L [N]	$F_{y,static}$ [N]	$F_{x,static}$ [N]	M_{z0} [N.m]	$\varphi_M - 180$ [deg]
1	8.5	0.32	1.8	0.57	1.03	112.8	44.9	77.5	138	43.5	8.9	75.9	85.0	20.8	29.6	11.4
2	8.5	0.36	1.53	0.55	0.85	101	46.3	82.5	132	40.7	8.9	71.2	79.4	20.3	28.3	9.1
3	8.5	0.42	1.31	0.55	0.72	93.3	49.7	83.8	130	40.5	8.9	70.8	79.0	20.3	27.4	8.2
4	8.5	0.5	1.1	0.55	0.61	87.5	53.9	84.9	128	40.7	8.9	71.1	79.3	20.3	26.4	5.1
5	8.5	0.65	0.89	0.58	0.51	91.8	59.4	91.8	137	43.6	8.9	76.1	85.1	20.8	26.8	4.3
6	8.5	0.7	0.44	0.31	0.14	35.4	63.3	117.6	103	18.6	8.9	31.8	34.3	13.6	15.3	-5.0
7	8.5	0.85	0.66	0.56	0.37	86.1	63.4	103.8	137	42.0	8.9	73.3	81.9	20.6	25.9	1.3
8	8.5	0.9	0.66	0.60	0.39	93.1	64.6	101.4	141	46.1	8.9	80.4	90.2	21.2	26.7	1.0
9	8.5	1.25	0.44	0.55	0.24	77.6	68	120.4	131	40.4	8.9	70.7	78.8	20.3	24.9	-1.0
10	9.5	0.32	1.8	0.57	1.03	124.3	44.8	85.5	152	44.3	9.7	83.3	92.3	19.6	34.1	11.8
11	9.5	0.36	1.53	0.55	0.85	111.8	46.4	91.2	147	41.5	9.7	78.1	86.3	19.3	32.7	9.5
12	9.5	0.42	1.31	0.55	0.72	100.9	49.4	91.3	139	41.3	9.7	77.7	85.8	19.2	31.5	6.4
13	9.5	0.5	1.1	0.55	0.61	93.4	53.2	92.1	136	41.5	9.7	78.0	86.2	19.3	30.2	6.8
14	9.5	0.65	0.89	0.58	0.51	98.2	58	102.2	145	44.4	9.7	83.5	92.5	19.6	30.6	4.7
15	9.5	0.7	0.44	0.31	0.14	39.9	62.2	137.6	115	19.4	9.7	34.9	37.4	13.9	18.3	1.1
16	9.5	0.85	0.66	0.56	0.37	92.5	62.9	113.5	146	42.8	9.7	80.5	89.0	19.4	29.8	2.4
17	9.5	0.9	0.66	0.60	0.39	99.9	63.6	113	150	46.9	9.7	88.2	97.9	19.8	30.9	1.4
18	9.5	1.25	0.44	0.55	0.24	91.2	67.4	145	153	41.2	9.7	77.5	85.7	19.2	29.7	0.5
19	10.5	0.32	1.8	0.57	1.03	138.9	42.2	99.8	162	45.1	10.4	90.7	99.6	18.3	38.8	6.5
20.	10.5	0.36	1.53	0.55	0.85	125.1	42.8	108.7	154	42.3	10.4	85.0	93.2	18.2	37.1	4.6
21	10.5	0.42	1.31	0.55	0.72	112	46.8	106.6	148	42.1	10.4	84.5	92.7	18.2	35.8	3.9
22	10.5	0.5	1.10	0.55	0.61	103.5	51.8	105.3	148	42.3	10.4	84.9	93.1	18.2	34.3	3.2
23	10.5	0.65	0.89	0.58	0.51	107.5	57.5	113.4	158	45.2	10.4	90.9	99.8	18.3	35.2	1.2
24	10.5	0.7	0.44	0.31	0.14	42.6	62.7	144.5	123	20.2	10.4	37.9	40.6	14.2	20.7	-2.1
25	10.5	0.85	0.66	0.56	0.37	102.4	61.4	131.6	160	43.6	10.4	87.6	96.1	18.3	34.6	2.1

74

Table 3.1 contd.

Run No.	LDR	A [m]	ω [rad/s]	v_0 [m/s]	a_0 [m/s^2]	F_{y0} [N]	φ_F-90 [deg]	$m_{apparent}$ [kg]	b [kg/s]	D_{max} [N]	D_{min} [N]	L [N]	$F_{y,static}$ [N]	$F_{x,static}$ [N]	M_{z0} [N.m]	φ_M-180 [deg]
26	10.5	0.9	0.66	0.60	0.39	108.6	60.3	136.7	158	47.7	10.4	96.1	105.7	18.3	35.9	1.7
27	10.5	1.25	0.44	0.55	0.24	95.1	65	166.2	157	42.1	10.4	84.4	92.5	18.2	33.4	-0.3
28	11.5	0.32	1.80	0.57	1.03	148.9	40.7	109.4	169	45.9	11.2	98.1	106.9	17.1	42.7	3.5
29	11.5	0.36	1.53	0.55	0.85	132.7	42.7	115.4	163	43.2	11.2	91.9	100.1	17.2	42	3.8
30	11.5	0.42	1.31	0.55	0.72	119.7	45.9	115.7	156	42.9	11.2	91.4	99.5	17.2	40.7	4.4
31	11.5	0.5	1.10	0.55	0.61	111.3	52	112.8	159	43.1	11.2	91.8	100.0	17.2	38.4	3.4
32	11.5	0.65	0.89	0.58	0.51	113.7	56.7	122.7	165	46.0	11.2	98.3	107.1	17.1	40.1	2.5
33	11.5	0.7	0.44	0.31	0.14	44.4	61.7	155.9	127	21.0	11.2	41.0	43.7	14.5	24.2	0.1
34	11.5	0.85	0.66	0.56	0.37	104.1	60.2	139	161	44.4	11.2	94.7	103.2	17.1	39.1	-0.3
35	11.5	0.9	0.66	0.60	0.39	112.7	58.7	148.6	162	48.5	11.2	103.9	113.4	16.9	41	-2.1
36	11.5	1.25	0.44	0.55	0.24	99.1	67.4	157.4	167	42.9	11.2	91.3	99.4	17.2	38	-2.1
37	12.5	0.32	1.80	0.57	1.03	160.7	39.6	120.1	178	46.7	11.9	105.5	114.3	15.8	47.3	2.8
38	12.5	0.36	1.53	0.55	0.85	144.8	40.8	129.6	172	44.0	11.9	98.9	107.0	16.1	45.5	1.9
39	12.5	0.42	1.31	0.55	0.72	130	42.8	132.7	161	43.8	11.9	98.3	106.4	16.1	45	0.8
40	12.5	0.5	1.10	0.55	0.61	116.6	50.5	122.1	163	43.9	11.9	98.7	106.8	16.1	43	2.8
41	12.5	0.65	0.89	0.58	0.51	118	55.3	131.9	169	46.8	11.9	105.7	114.5	15.8	44.8	1.5
42	12.5	0.7	0.44	0.31	0.14	44.2	59.3	167	124	21.7	11.9	44.1	46.9	14.8	26.4	1.0
43	12.5	0.85	0.66	0.56	0.37	121.3	58.2	172	183	45.2	11.9	101.9	110.3	16.0	45.6	0.1
44	12.5	0.9	0.66	0.60	0.39	118.4	59.2	154	171	49.4	11.9	111.7	121.1	15.5	45.6	0.3
45	12.5	1.25	0.44	0.55	0.24	103.8	64.1	188.1	170	43.7	11.9	98.1	106.2	16.1	43.1	-1.7

CHAPTER 4

VARIABLE-ATTITUDE TESTS: PURE YAW EXPERIMENTS

4.1 Introduction

Pure yaw tests are one of the most important and basic types of manoeuvring experiments to be performed on marine vessels. These manoeuvres are performed in captive model tests as a counterpart to zigzag manoeuvres which are performed in free running model tests, full-scale tests and also as validation checks for numerical manoeuvring codes. In the pure sway manoeuvre, the vehicle follows a sinusoidal path with a constant heading angle of zero, but in the pure yaw manoeuvre the vehicle's heading is always tangent to its path. In a zigzag manoeuvre compared to a pure yaw captive test, the vehicle has a small sway velocity which creates a small drift angle off its path.

In the literature, extensive studies are available for the pure yaw and zigzag tests especially for surface vessels. The recommendations of the ITTC for captive model tests cover most of the important requirements for the zigzag tests on surface vessels [24th ITTC, 2005]. There are many reported results from either one of the mentioned experimental methods, that is: captive, free-running or full-scale tests, but also numerical codes are recently used to perform PMM tests. By Hochbaum [2006] a set of virtual PMM test results using a RANS code based on a finite volume technique to simulate the flow around a twin-screw ship was presented.

A not very recent but valuable set of PMM tests were performed on the full-scale autonomous underwater vehicle MARIUS in the Danish Maritime Institute; some of the results were reported by Aage and Smitt [1994]. That paper utilizes SNAME standard

factors to define the non-dimensional parameters, and presents the test results in the form of hydrodynamic coefficients for surge, sway, heave, pitch and yaw directions. The AUV MARIUS is a flatfish type vehicle and therefore horizontal and vertical plane manoeuvres are different. A non-dimensional sway force coefficient Y'_v of about 0.04 and a non-dimensional yaw moment N'_r of about 0.01 were measured; however, it is not clear to which values of manoeuvring amplitudes and frequencies that the reported values correspond. The parameters Y'_v and N'_r in the notation of this thesis are respectively F'_{y0} and M'_{z0}, as will be introduced later.

In this project, as a part of the underwater technology studies, the pure sway and pure yaw experiments on a series of five hull forms for an underwater vehicle were performed in the 90 m towing tank at NRC-IOT. These experiments used the towing carriage to move the vehicle along x-axis, the PMM (Planar Motion Mechanism) to produce the oscillating lateral (sway) plus angular (yaw) motions, and, an internal three-component balance to measure two hydrodynamic forces (axial, lateral) and the hydrodynamic yaw moment.

It is desired to find the correct form of the physically-based expressions for the hydrodynamic forces and moments on a completely submerged underwater vehicle during high-amplitude, high-rate manoeuvres. It should be noted that the results of this research are valid for the planar manoeuvres for either horizontal or vertical planes, because these underwater bare hull series are bodies of revolution. Therefore, throughout this chapter sway and yaw motions are respectively equivalent to heave and pitch motions.

4.2 The experiment set up and the recorded data

The original bare hull model, as was shown in chapter two Fig. 2.1 when installed on the PMM, had a length-to-diameter ratio (LDR) of about 8.5:1. Extension pieces were added to the parallel mid-body to test hulls of the same diameter, 203 mm, but with LDR of 9.5, 10.5, 11.5 and 12.5. The centre of buoyancy (CB) of the model remained essentially the same distance aft of the origin of the internal balance. All the modules were free-flooding and no appendages were included in this hull-extension investigation. The carriage forward velocity for all the runs was 2 m/s; the PMM lateral velocity and yaw angle of the PMM had smooth sinusoidal variations with amplitudes of respectively about 0.5 [m/s] and 14 deg for all the runs; maximum and minimum sway motion amplitudes were 1.25 and 0.41 m; the maximum and minimum yaw rates were respectively about 17.4 [deg/s] for the shortest model in its short-period pure yaw motion, and, about 5.5 [deg/s] for the longest model in its long-period pure yaw manoeuvre. See Table 4.1 at the end of this chapter page 124 for the details of the pure yaw manoeuvres.

Fig. 4.1 shows the time period T for the pure yaw runs for the LDR 8.5 model, versus the ratio of the sway amplitude to vehicle diameter. Fig. 4.1 shows that the periods and amplitudes for the pure yaw runs were chosen such that the product of the amplitude and frequency was held the same for all runs. Note that in this study the purpose of the pure yaw experiments was to measure the sway force and yaw moment as functions of PMM angular velocity and acceleration.

The data points in Fig. 4.1 were read from either the PMM lateral velocity or its yaw angle recorded for each run. Fig. 4.2 shows a sample yaw angle signal for LDR 8.5 and

input values of $A= 0.51$ m and $T= 6.4$ s. Clearly seen in Fig. 4.2, there is an initial set-angle in the PMM yaw angle which has introduced a vertical shift to the recorded yaw angle, however, the yaw angle amplitude is 14 degrees as mentioned. As a result of this set-angle, the recorded loads have offsets as well, which were removed during the data analysis. The reason is that the model motion must begin from rest, so the software computes an initial set-angle which corresponds to the distance that is required for the PMM to accelerate the model to begin a manoeuvre with zero yaw attitude and the correct angular velocity.
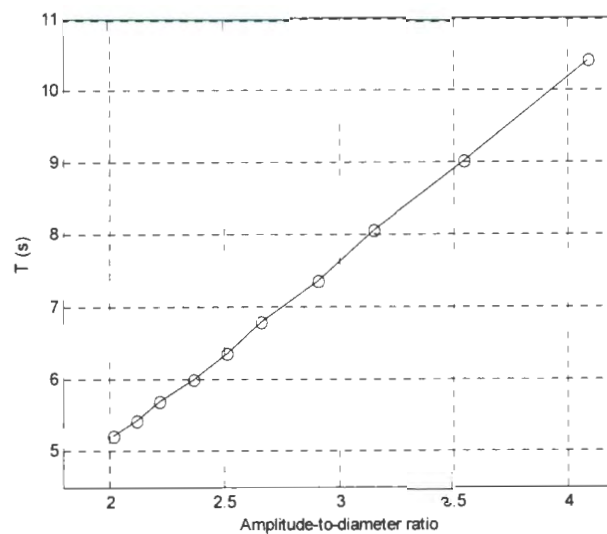
Fig. 4.1 Time period versus non-dimensional sway amplitude A/d; pure yaw runs for *LDR* 8.5
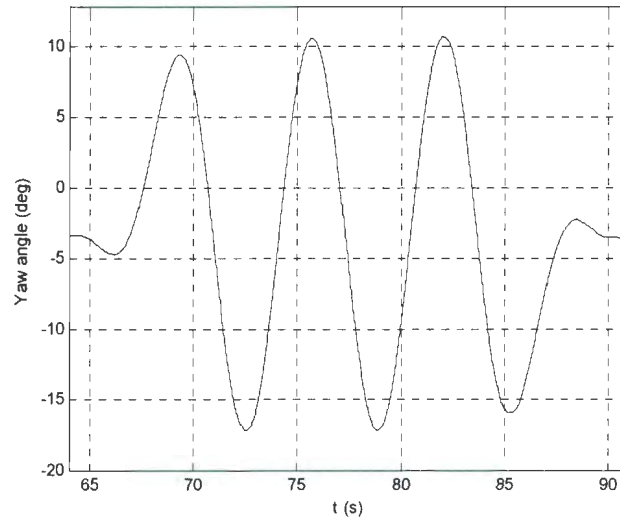
Fig. 4.2 Yaw angle signal for *LDR* 8.5 and input values of *A*= 0.51 m and *T*= 6.4 s

for a pure yaw manoeuvre

The main outputs are the axial force, F_x, the sway force, F_y, and the yaw moment, M_z.

Fig. 4.3 shows the original and filtered sway force, yaw moment and axial force signals

for a pure yaw manoeuvre with *LDR* 8.5, $A = 0.51$ m and $T = 6.4$ s. Fig. 4.4 shows a

close-up of the filtered sway force in Fig. 4.3. The three-component balance inside the

bare hull model uses a single loadcell to measure the axial force and two loadcells to

measure the lateral force; by summing the signals from the two lateral-force loadcells we

obtain the total lateral force, and, by differencing the signals from the two lateral-force

loadcells, we obtain the yaw moment. The three loadcells selected for the internal balance

must withstand many different loads: (i) the hydrodynamic loads during the manoeuvres,

(ii) the weight of the model in air when flooded with water, (iii) the inertial loads during

the acceleration and deceleration of the model, and, (iv) the inevitable bumps that occur

during installation and removal of the model. Thus the capacity of each loadcell is much

80

larger than that required to measure only the hydrodynamic loads. Also there are inevitable vibrations in the PMM due to flexibilities in the drive mechanism. Thus there is significant measurement noise on the loadcell signals as is indicated in Fig. 4.3. The raw time-series data were therefore filtered using the "filtfilt" function in MATLAB™7.1, since this filter does not introduce any phase shift into the signal.

For a high-frequency manoeuvre as in Figs. 4.2 and 4.3, there were one or two complete cycles in which several zero-crossing points, peaks and troughs are observable which are circled in Fig. 4.4, hence an average value for the maximum and minimum force and moment and the corresponding time period could be obtained from the data. However, for low-frequency (higher T) manoeuvres, hardly a complete cycle was performed due to the restricted length of the towing tank. For example, for LDR 10.5, $A = 1.19$ m and $T = 14.3$ s the data were captured for less than one complete cycle; this may affect the statistical reliability of the results. The approximate number of steady-state cycles for all pure yaw runs are shown in Table 4.1 column#8.
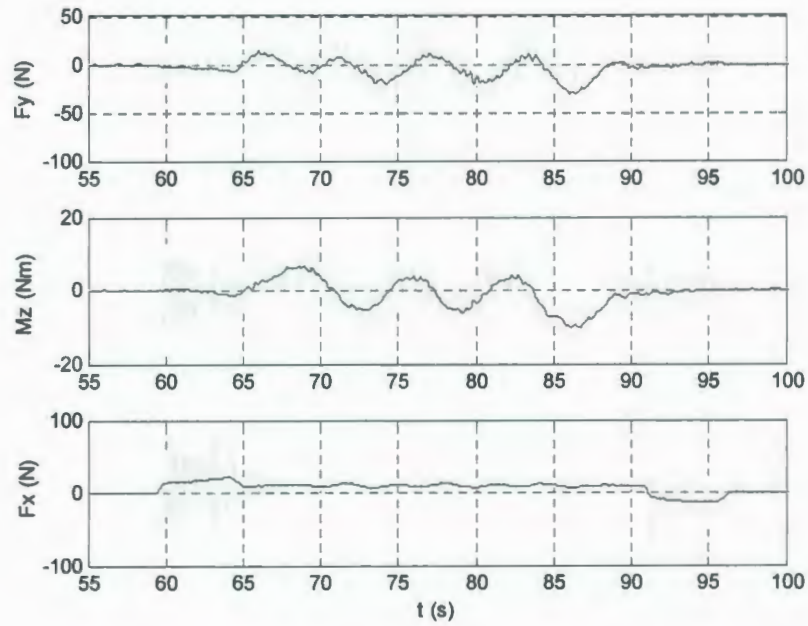
Fig. 4.3 The original and filtered sway force, yaw moment and axial force signals for a pure yaw

manoeuvre with *LDR* 8.5, $A = 0.51$ m and $T = 6.4$ s
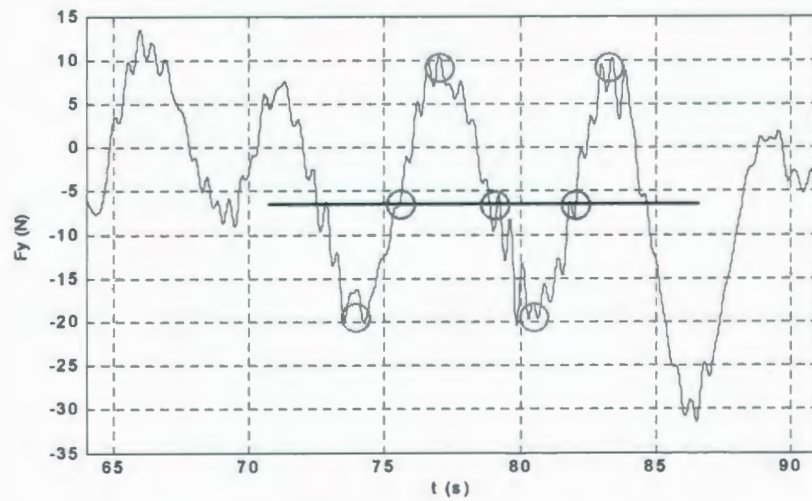
Fig. 4.4 Close-up of filtered sway force in Fig. 4.3; maximum, minimum and zero-

crossings circled during the steady-state portion of the manoeuvre

4.3 PMM motions during pure yaw tests

During a sea-trial, an overhead view of a spatially-sinusoidal trajectory allows us to view the cycle width and cycle length; these are analogous to the PMM sway amplitude and cycle length $T \cdot u_{carriage}$ in the towing tank. In designing the pure yaw manoeuvres, two constraints that had to be satisfied were due to physical limitations of the PMM (i) the maximum PMM lateral velocity cannot exceed 0.50 m/s, and, (ii) the maximum yaw rate cannot exceed 60 deg/s. The first of these requires that:

$$A \cdot \omega < 0.50 \text{ [m/s]} \tag{4-1}$$

or, which is equivalent, that:

$$T > 4\pi \cdot A \text{ [sec]} \tag{4-2}$$

A third constraint is the kinematic requirement that the longitudinal axis of the vehicle is everywhere tangent to the sinusoidal trajectory in the tank x-y coordinate system; this requires that

$$\beta_0 = \tan^{-1}(A \cdot \omega / u_{carriage}) \tag{4-3}$$

which is equivalent to

$$\beta_0 = \tan^{-1}\left[\frac{2\pi A}{T \cdot u_{carriage}}\right] \tag{4-4}$$

In these experiments, a constant carriage speed of 2 m/s was used. Combining these kinematic and dynamic constraints, the result is that:

$$\beta_0 < \tan^{-1}\left(\frac{1}{4}\right) \tag{4-5}$$

So the yaw amplitude will not exceed about 14 deg in any of these pure yaw manoeuvres. For small yaw amplitudes (4-4) can be approximated by:

83

$$\beta_0 = 2\pi A / (T \cdot u_{carriage}) \tag{4-6}$$

or

$$T = 2\pi A / (\beta_0 \cdot u_{carriage}) = 2\pi d \cdot (A/d) / (\beta_0 \cdot u_{carriage}) \tag{4-7}$$

If the carriage speed $u_{carriage}$ and yaw amplitude β_0 are held constant at 2 m/s and 14 deg respectively, then (4-7) provides a linear relation between the period T and the sway amplitude A or non-dimensional sway amplitude A/d.

The time-series for the PMM sway and yaw motions were plotted as in Fig. 4.2, for one or more cycles of motion; smooth sinusoids were fitted to the constant-amplitude portions of the time-series and values for β_0, T and A were extracted. These experimental values were plotted in Fig. 4.1 which confirmed the validity of the approximation (4-7). The relation in Fig. 4.1 can be represented by a straight line through the origin as follows:

$$A/T \approx 0.08 \text{ [m/s]} \tag{4-8}$$

or

$$A \cdot \omega \approx 0.5 \text{ [m$\cdot$ rad/s]} \tag{4-9}$$

which satisfies the requirement in (4-1) that the maximum PMM lateral velocity cannot exceed 0.50 m/s.

4.4 Analysis of data

4.4.1 PMM lateral velocity and yaw angle

The planar motion mechanism is programmed with the desired time-series of sway displacement and yaw angle as inputs. A sample of the yaw angle time-series was shown in Fig. 4.2. As mentioned, the desired values for the amplitude of the PMM lateral

84

velocity and its yaw angle were 0.5 m/s and 14 deg respectively. Hence the variables: PMM lateral velocity v and yaw angle β can be approximated as:

$$v = v_0 \sin(\omega_v t) \qquad (4\text{-}10)$$

$$\beta = \beta_0 \sin(\omega_\beta t) \qquad (4\text{-}11)$$

with $v_0 = 0.5$ m/s, and $\beta_0 = 14$ deg. The frequencies of the two motions, sway and yaw, must be identical, thus $\omega = \omega_v = \omega_\beta$, and in phase with each other, i.e., the vehicle in a pure yaw manoeuvre has the largest PMM lateral velocity and largest yaw angle as the vehicle crosses the centreline of the towing tank, and zero v and zero β at the extremes of the motion. Differentiating (4-10) and (4-11) gives the lateral acceleration of the PMM and yaw rate. Hence, the yaw rate of turning [deg/s] is:

$$\dot{\beta} = \beta_0 \omega \cos(\omega t) \qquad (4\text{-}12)$$

The amplitude of yaw rate of turn resulting from (4-12) is plotted versus non-dimensional sway amplitude A/d in Fig. 4.5 and also reported in column#7 of Table 4.1, page 124 for the five-hull series. As mentioned, the most abrupt manoeuvre $\dot{\beta} = 17$ deg/s was performed with the shortest vehicle, LDR 8.5, with $A = 0.41$ m and $T = 5.2$ s, and the least abrupt manoeuvre $\dot{\beta} = 5.8$ deg/s was performed with the longest vehicle, LDR 12.5, with $A = 1.25$ m and $T = 15.6$ s.
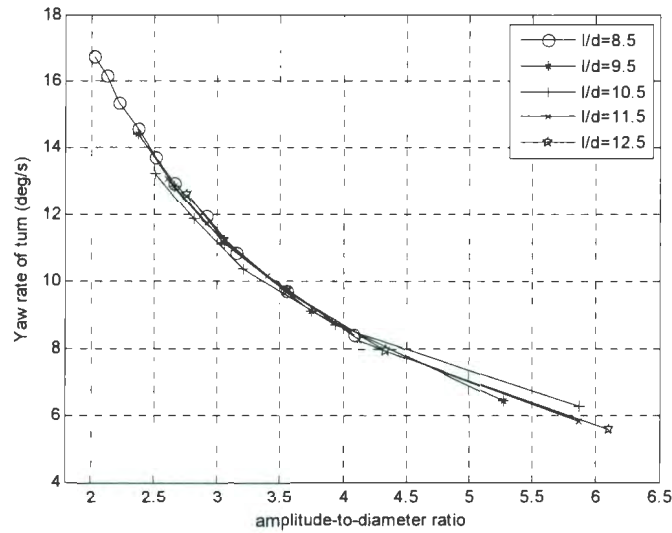
Fig. 4.5 Yaw rate of turn vs. sway amplitude A/d during pure yaw manoeuvres

4.4.2 Sway force and yaw moment amplitudes

The main responses to be studied in the pure yaw experiments are the sway force and yaw moment. The primary results are the maximum and minimum values of the lateral force F_y and yaw moment M_z. There is an offset (vertical shift) in the time-series of both responses, which, when removed, gives the amplitude of force and moment sinusoidal signals, named F_{y0} and M_{z0}. Figs. 4.6 and 4.7 are the plots of the amplitude of sway force and yaw moment versus the yaw rate of turn during the pure yaw tests. Note that, as shown in Table 4.1 at the end of this chapter, all the pure yaw manoeuvres were performed with the same amplitude of the lateral velocity of PMM at 0.5 m/s and the same amplitude of yaw angle of PMM at about 14.3 deg.
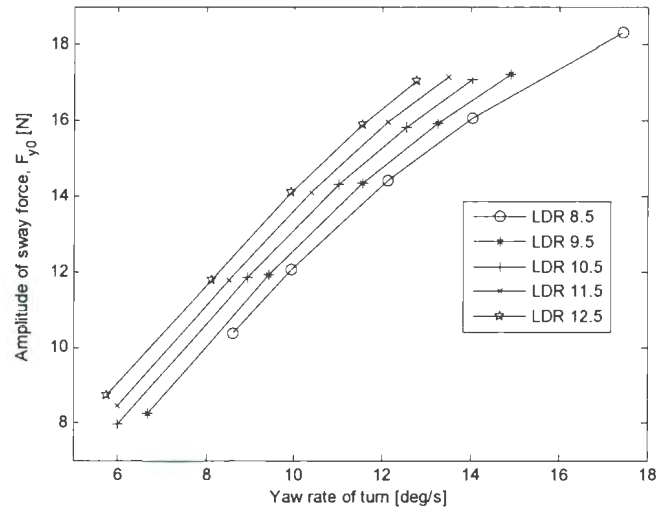
Fig. 4.6 Amplitude of the sway force vs. yaw rate of turn of the PMM
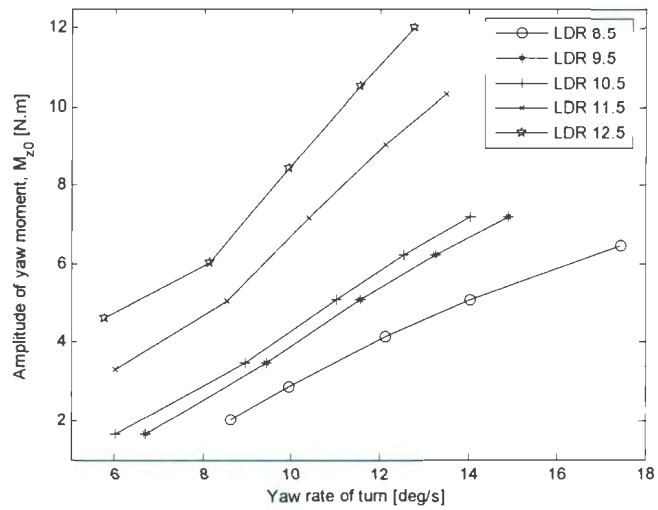
Fig. 4.7 Amplitude of the yaw moment vs. yaw rate of turn of the PMM

Similar graphs as in Figs. 4.6 and 4.7 are obtained if the amplitude of lateral acceleration of the PMM is on the x-axis instead of yaw rate of turn. Then, the amplitudes of sway force and yaw moment are non-dimensionalized as follows:

$$F'_{y0} = F_{y0}/(\tfrac{1}{2}\rho U^2 A_p) \tag{4-13}$$

$$M'_{z0} = M_{z0}/(\tfrac{1}{2}\rho U^2 A_p l) \tag{4-14}$$

where ρ is the water density, A_p is the rectangular planform area of the vehicle defined

as:

$$A_p = l \cdot d. \tag{4-15}$$

and U is the vehicle velocity evaluated as:

$$U^2 = u^2_{carriage} + v^2_0 \tag{4-16}$$

where $u_{carriage}$ is the towing speed of the carriage which was 2 m/s for all the pure yaw

runs, and v_0 is the amplitude of PMM sinusoidally-varying lateral velocity equal to 0.5

m/s for all runs, thus U in (4-16) is: $\sqrt{2^2 + 0.5^2} = 2.06$ m/s.

In (4-13) the non-dimensional sway force amplitude was defined as force divided by the

planform area. The vehicle is slender ($8.5 < LDR < 12.5$) and the hull series were

produced by increasing the length of the parallel mid-body, therefore the non-

dimensional sway force amplitude as defined in (4-13) gives an estimate of the maximum

sway force per unit length for a slender underwater vehicle of diameter d. For the non-

dimensional yaw moment amplitude in (4-14), planform area times length is in the

denominator so as to account for the axial variation of location of centre of effort within

the length of the vehicle (see Table 2.2). The centre of effort is the point which defines

the vertical axis about which the yaw moment is zero at each yaw angle. Detailed

definition of the centre of effort and curves of its variation versus static yaw angle for this

hull series was presented by Williams et al. [2006].

The amplitude of the non-dimensional sway force and yaw moment versus non-

dimensional sway amplitude A_l/d during pure yaw runs are plotted in Figs. 4.8 and 4.9

and also shown in Table 4.1 at the end of this chapter. Although the data points do not all lie on smooth curves, the trend is clear. In both these figures the short-period small-amplitude manoeuvres are in the top left-hand corner of the figure and the long-period high-amplitude runs are in the bottom right-hand portion.

The sway force per unit length (during pure yaw manoeuvres) is larger for the longer vehicles, but other than the large jump from the LDR 8.5 curve to the LDR 9.5, the difference between curves is less significant. Fig. 4.8 shows that as A/d increases F'_{y0} decrease, i.e., a large amplitude slow manoeuvre sustains less lateral force. The point is that for abrupt manoeuvres, e.g. obstacle avoidance, a quick small-amplitude manoeuvre might be required, hence the large lateral forces are unavoidable. This has implications for size of control surfaces required to produce the yaw moment necessary to produce these turning rates. Fig. 4.9 shows the same trend for the yaw moment, that is, as A/d increases, M'_{z0} decreases, and, the yaw moment per unit length (during pure yaw manoeuvres) is larger for the longer vehicles. Moreover, the manoeuvring frequencies for these pure yaw runs are readable on the top axis of Figs. 4.8 and 4.9. Again, showing the same point that: at large frequencies the amplitudes of non-dimensional sway force and yaw moment are larger.
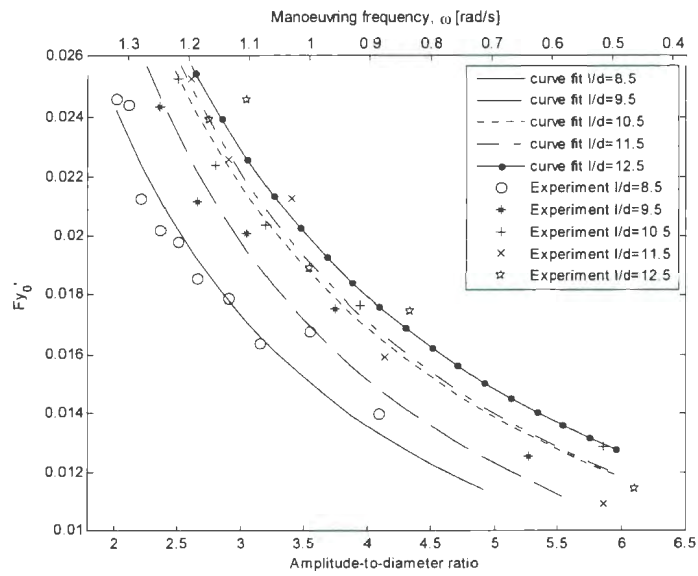
Fig. 4.8 Non-dimensional sway force amplitude vs. A/d during pure yaw manoeuvres
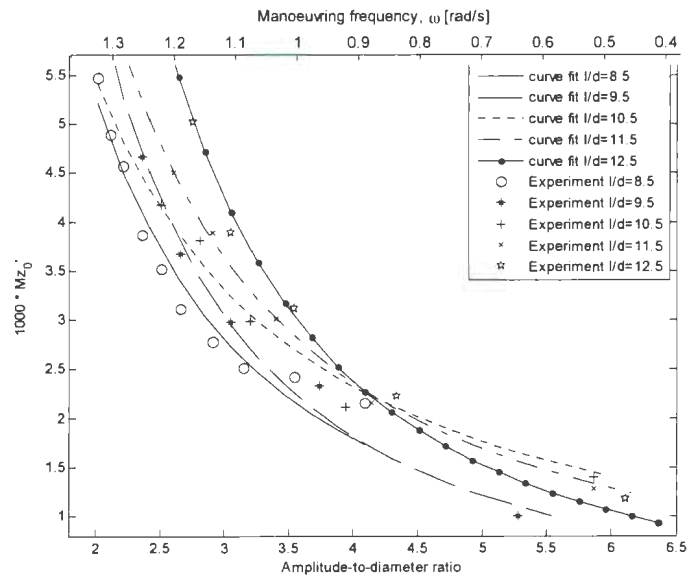
Fig. 4.9 Non-dimensional yaw moment amplitude vs. A/d during pure yaw manoeuvres

4.4.3 Phase difference between the hydrodynamic loads and the model motions

Again it should be emphasized that for the pure yaw manoeuvres the input signals to the PMM are the time-series of PMM lateral displacement and model heading angle. These two state variables are in phase and have equal frequency. Also, measurements reveal that the frequency of the hydrodynamic loads is the same as frequency of the state variables. Therefore the sway force is of the form:

$$\beta = \beta_0 \sin(\omega t) \tag{4-11}$$

$$F_y = F_{y0} \sin(\omega t - \varphi_F) \tag{4-17}$$

Fig. 4.10 shows the magnitude of φ_F phase lag between the sway force and yaw angle signals, in radians, versus A/d for pure yaw manoeuvres with this hull-series. The sinusoidal sway force is delayed by about $\pi/2$ radians relative to the sinusoidal yaw angle. Although, the data are scattered, there is a trend: the longer vehicle experiences a larger phase lag and for slower manoeuvres, larger A/d, the phase lag is larger. It should be noted that rather than the magnitude of the phase lag, we are more interested to know how far the data points are from the potential flow phase lag of $\pi/2$. In Fig. 4.10 a single curve indicates the trend for all hull lengths combined. The trend is closer to $\pi/2$ for larger sway amplitudes. The information from Figs. 4.8 and 4.10 may be combined and portrayed with a polar plot as in Fig. 4.11. The radius of the data points is the non-dimensional amplitude of the sway force F'_{y0} and the polar angle is the phase difference between the measured sway force and the yaw angle φ_F in (4-17).
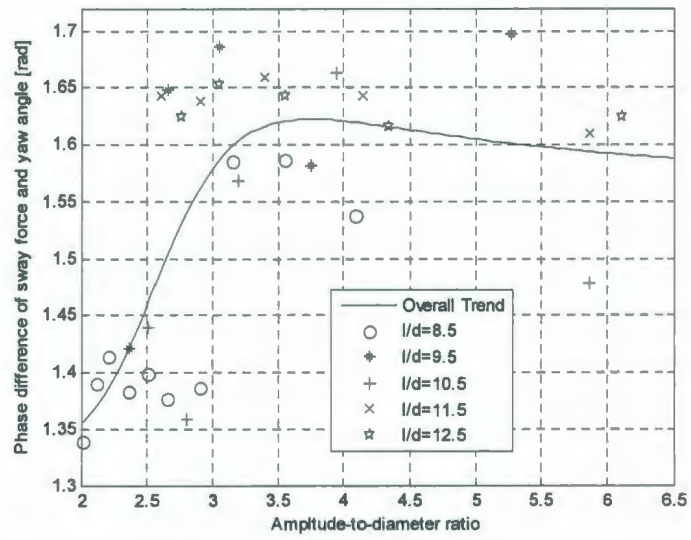
Fig. 4.10 Phase difference of the sway force and yaw angle signals vs. A/d

during pure yaw manoeuvres
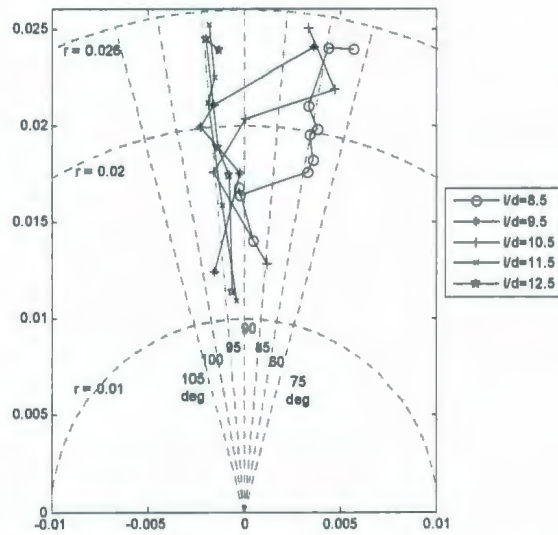
Fig. 4.11 Polar plot of the non-dimensional sway force amplitude for the hull-series

during pure yaw manoeuvres

Comparing Figs. 4.8 and 4.11, it is concluded that pure yaw manoeuvres with smaller amplitude (short-period manoeuvres), which result in overall larger forces, makes the deviation of the phase difference (from the potential value of $\pi/2$) larger. On the other hand, the phase difference for larger LDR is closer to the theoretical $\pi/2$ value.

The yaw moment M_z is computed from differencing the signals from the two lateral-force loadcells. Fig. 4.12 shows the phase lag between the yaw moment and yaw angular acceleration signals versus A/d for the hull-series. These data are presented in the last column in Table 4.1 on page 124 in degrees. Again the trend is that the larger hull LDR results in a larger phase difference, and for long-period manoeuvres (larger A/d) the phase lag is larger.
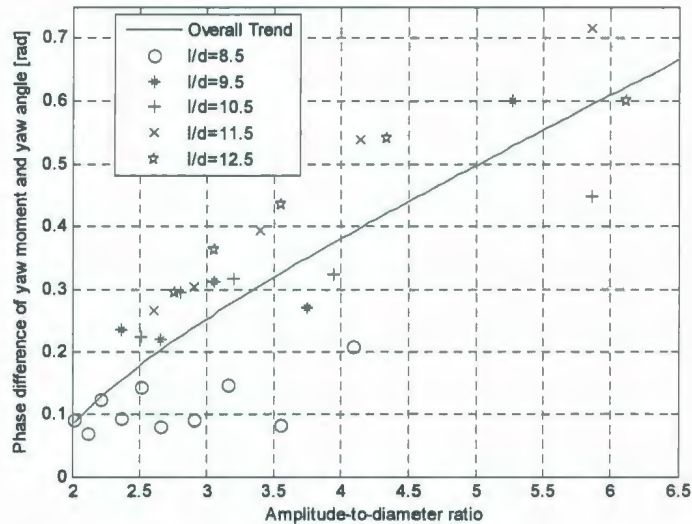
Fig. 4.12 Phase difference of the yaw moment and yaw angular acceleration versus A/d

during pure yaw manoeuvres

To better observe the phenomena, the yaw angle time-series along with the filtered yaw moment and filtered signals from the fore and aft lateral-force loadcells for a pure yaw

manoeuvre with LDR 8.5, $A = 0.51$ m and $T = 6.4$ s are shown in Fig. 4.13. The black line is the yaw angle, the blue line is the portion of F_y that is measured by the forward lateral-force loadcell the purple line is the portion of F_y that is measured at the aft lateral-force loadcell and the red line is the yaw moment. The forward portion of the sway force lags the yaw angle by about 1.0 s or $T/6$ and the aft portion of the sway force lags the yaw angle by about 2.1 sec or $T/3$. For this particular pure yaw run, shown in Fig. 4.13, the phase difference between sway force and yaw angle φ_F is about 80 degrees and between yaw moment and yaw angular acceleration φ_M is about 8 degrees[4]. This implies that in a rapid pure yaw manoeuvre with a relatively short vehicle the fore and aft components of the sway force have phase lags with respect to the yaw angle in such a way that the yaw moment tends to be nearly in phase with the yaw angular acceleration signal. According to Newton-Euler equation for a rigid body we know that:

$$M_z = I_{total} \cdot \ddot{\beta} \qquad (4\text{-}18)$$

where $\ddot{\beta}$ is the yaw angular acceleration and I_{total} is the sum of the hull moment of inertia and added moment of inertia of the surrounding fluid:

$$I_{total} = I_{hull} + I_{added} \qquad (4\text{-}19)$$

The heading angle and the yaw angular acceleration are π radians out of phase, hence (4-18) proposes that in a potential flow yaw moment and yaw angular acceleration are in phase. Using the experiment results Fig. 4.14 shows a polar plot of the yaw moment. The

---

[4] The values for φ_M in Table 4.1 were reported by Azarsina et al. [2007 b & c] as the phase lag between yaw moment and yaw angle signal, however, the values in Table 4.1 are actually the phase lags between the yaw moment and yaw angular acceleration. The values in Table 4.1 should be added to π radians to result in the phase lag between the yaw moment and yaw angle signals. This is because the yaw angular acceleration has π radians phase lag relative to the yaw angle.

radius of the data points is the non-dimensional amplitude of the yaw moment M'_{z0} and

the polar angle is the phase difference between the measured yaw moment and the yaw

angular acceleration φ_M.
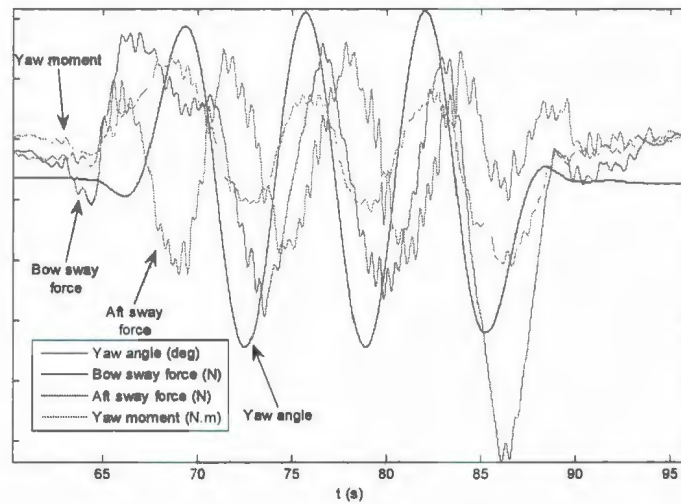
Fig. 4.13 Yaw angle, fore and aft lateral-force loadcell signals and yaw moment during a pure yaw

manoeuvre with LDR 8.5, $A = 0.51$ m and $T = 6.4$ s
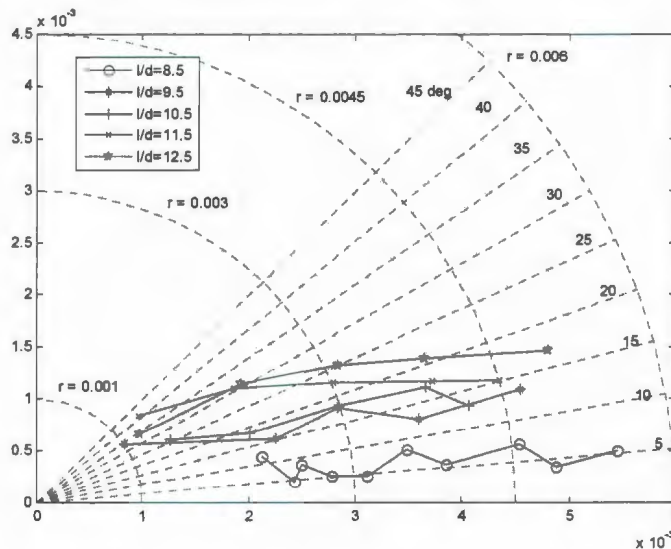
Fig. 4.14 Polar plot of the non-dimensional yaw moment amplitude for the

hull-series during pure yaw manoeuvres

95

4.4.4 Instantaneous variation of the hydrodynamic loads versus the model motions

Interesting observations were made by plotting the hydrodynamic loads versus the PMM state variables: PMM lateral velocity and yaw angle. As discussed, referring to (4-10) and (4-11), PMM lateral velocity and yaw angle theoretically have the same effect on the hydrodynamic loads in a pure yaw manoeuvre, and the experimental results, e.g. phase difference between the sway force and PMM lateral velocity compared to the phase difference between sway force and yaw angle, were only slightly different. Hence, the discussion is continued for the yaw angle. Figs. 4.15 and 4.16, for the vehicle with *LDR* 9.5, respectively show the instantaneous variation of sway force and yaw moment versus yaw angle. Different curves are the several runs with different sway motion amplitudes performed on the *LDR* 9.5 hull. These elliptical phase-plane trajectories with varying semi-axes length and orientation as shown in Figs. 4.15 and 4.16, represent the relations between the pure yaw manoeuvre input: yaw angle, and its outputs: hydrodynamic loads. Equation (4-11) for the yaw angle can be rewritten in the form:

$$f_1 = c_1 \sin(\omega t), \; f_1 = \beta, \; c_1 = \beta_0 \qquad (4\text{-}20)$$

Then the hydrodynamic loads: sway force and yawing moment, would be:

$$f_2 = c_2 \sin(\omega t - \varphi) \qquad (4\text{-}21)$$

where f_2 is either F_y or M_z, c_2 is either F_{y0} or M_{z0}, and φ is the phase difference between either sway force and yaw angle or yaw moment and yaw angular acceleration. In Figs. 4.15 and 4.16, f_2 was plotted against f_1. In the special case where $\varphi = 0°$, then using (4-21) it concludes: $\varphi = 0° \rightarrow f_2 = c_2 \sin(\omega t) = (c_2/c_1)f_1$; therefore, if there is no phase lag between f_1 and f_2 the phase-plane plot reduces to a line of slope c_2/c_1. For $\varphi = 180°$

96

we have: $\varphi = 180° \rightarrow f_2 = -c_2 \sin(\omega t) = -(c_2/c_1) f_1$; and for $\varphi = 90°$ it is: $\varphi = 90° \rightarrow f_2 = c_2 \sin(\omega t - \pi/2)$. After some algebra it reduces to $(f_1/c_1)^2 + (f_2/c_2)^2 = 1$ which is the equation for an ellipse of semi-axes c_1 and c_2 and no tilt angle.

In general, the phase lag φ and variables c_1 and c_2 are affecting the size and orientation of the ellipses. The ellipse equation in the general form is:

$$Af_1^2 + Bf_2^2 + Cf_1f_2 + Df_1 + Ef_2 + F = 0 \tag{4-22}$$

If the major axis of the ellipse has a tilt angle of θ it is calculated as:

$$\sin(2\theta) = -C/Q, \tag{4-23}$$

where:

$$Q = \sqrt{(A - B)^2 + C^2} \tag{4-24}$$

Also there are formulae to calculate the radii of the tilted ellipse based on the coefficients in (4-22) [Van Drent, webpage 2008]. With lengthy algebra on (4-20) and (4-21), one can find the ellipse coefficients in (4-22) based on f_1, f_2 and φ.
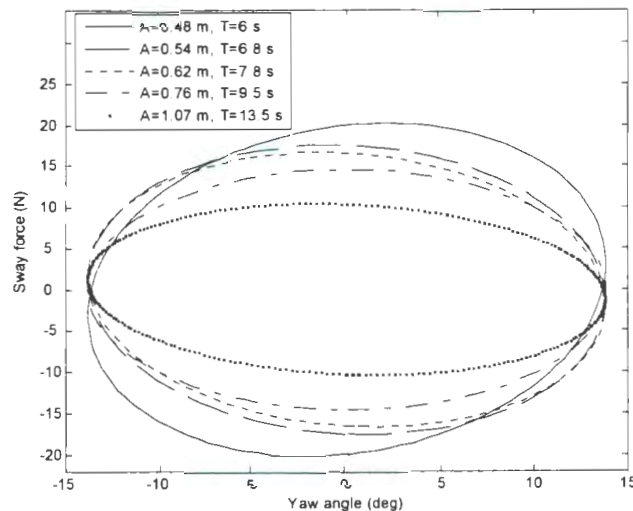
Fig. 4.15 Phase-plane plot of F_y versus β for LDR 9.5 during pure yaw manoeuvres

97
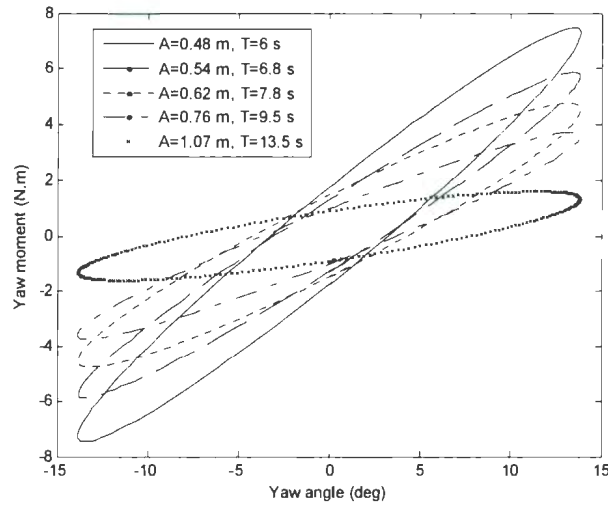
Fig. 4.16 Phase-plane plot of M_z vs. β for LDR 9.5 during pure yaw manoeuvres

Because the instantaneous yaw angle and PMM lateral velocity are in phase with each other, their derivatives are too. Thus the yaw rate of turning is in phase with the lateral acceleration of the PMM. Plotting the instantaneous variation of loads versus the yaw rate of turn, may further clarify the phenomena. In Figs. 4.17 to 4.19, the legend is the same as for Figs. 4.15 and 4.16. Fig. 4.17, for the vehicle with LDR 9.5, shows the instantaneous variation of yaw moment versus yaw rate of turn $\dot{\beta}$. Fig. 4.17 gives a more straightforward demonstration of the relation between yaw moment and manoeuvre characteristics. For a slow turn, e.g. $A = 1.07$ m and $T = 13.5$ s, the rate of turn is slow and therefore the yaw moment is small which results in the inner ellipse. Figs. 4.18 and 4.19 both for the vehicle with LDR 9.5 show the instantaneous variation of yaw moment versus yaw angle squared β^2 and yaw angle cubed β^3 respectively.
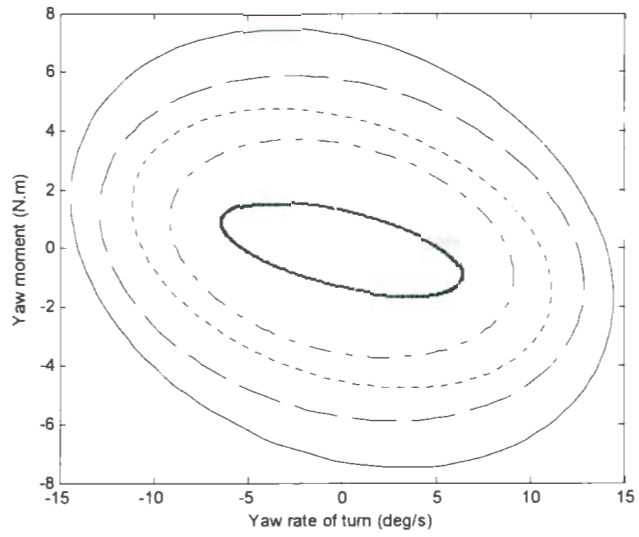
Fig. 4.17 Phase-plane plot of M_z vs. $\dot{\beta}$ for LDR 9.5 during pure yaw manoeuvres
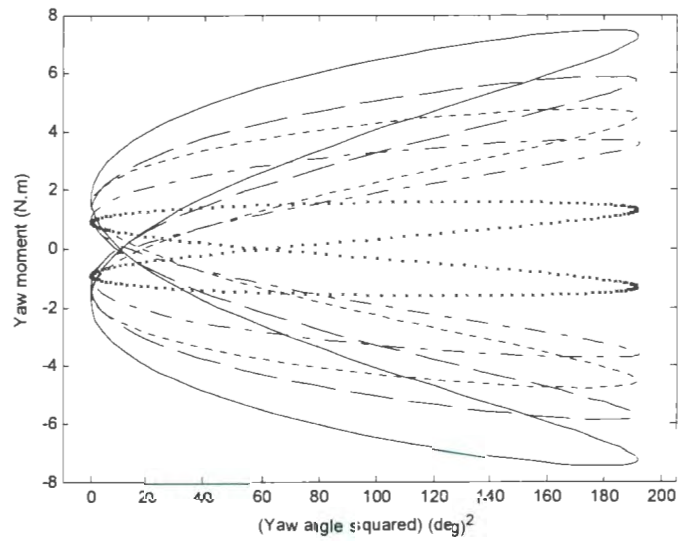
Fig. 4.18 Phase-plane plot of M_{z} vs. β^2 for LDR 9.5 during pure yaw manoeuvres
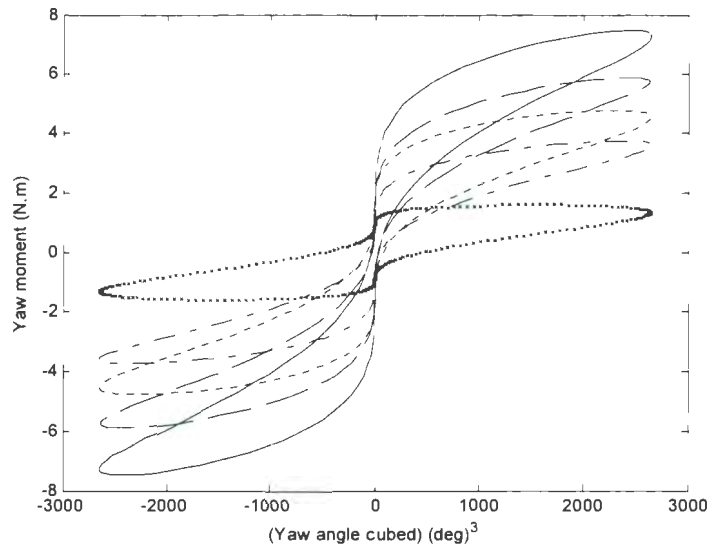
Fig. 4.19 Phase-plane plot of M_z vs. β^3 for LDR 9.5 during pure yaw manoeuvres

4.5 Response surface models for the pure yaw test results

As was demonstrated in chapter 2, section 2.4.4, a regression model for a response, which depends on two factors, is a surface in 3D space. The Response Surface Model (RSM) can be a first-order model if the response is a linear function of the factors. If the response has curvature, then a higher order polynomial should be used. A second-order (quadratic) model is often able to capture the curvature.

4.5.1 The mathematical model

A mathematical model for the experimental results of the pure yaw manoeuvres is desired. According to the previous section, the input signals for these pure yaw manoeuvres are the PMM lateral velocity and yaw angle, (4-10) and (4-11), repeated below:

$$v = v_0 \sin(\omega_v t), \beta = \beta_0 \sin(\omega_\beta t) \qquad (4\text{-}25)$$

100

where the amplitude of the PMM lateral velocity v_0 was 0.5 m/s, and the amplitude of yaw angle β_0 was 14 deg. The frequencies of the two motions, sway and yaw, must be identical, thus $\omega = \omega_v = \omega_\beta$, and in phase with each other. On the other hand, measurements reveal that the frequency of the hydrodynamic loads is the same as frequency of the input signals. Therefore the sway force and yaw moment are of the form:

$$F_y = F_{y0} \sin(\omega t - \varphi_F) \tag{4-26}$$

$$M_z = M_{z0} \sin(\omega t - \varphi_M) \tag{4-27}$$

The measured response sway force F_y in a captive pure yaw manoeuvre in towing tank, for a range of different hull lengths, can be written as:

$$F_y = f(u_{carriage}, v, \beta, \dot{\beta}, \tfrac{A}{d}, LDR) \tag{4-28}$$

According to (4-25), for constant amplitudes of PMM lateral velocity and yaw angle, equation (4-28) reduces to:

$$F_y = f(\omega, t, \tfrac{A}{d}, LDR) \tag{4-29}$$

On the other hand, these tests were performed under the constraint of equation (4-8), that is: $A/T = 0.08$; which imposed a linear relation between the manoeuvring frequency and amplitude during these pure yaw tests as was shown in Fig. 4.1. Hence, (4-29) can be further simplified to:

$$F_y = f(t, \tfrac{A}{d}, LDR) \tag{4-30}$$

These results show that in the steady portion of each pure yaw run, the complicated relation (4-28) reduces to the simpler relation (4-30) while the forward towing speed and

the amplitudes of the PMM lateral velocity and yaw angle are constant for all the runs.

The same observation applies to the yaw moment M_z, thus:

$$M_z = g(t, \tfrac{A}{d}, LDR) \tag{4-31}$$

Using (4-26) and (4-27), equations (4-30) and (4-31) decompose into the following set of equations which are time-independent:

$$F_{y0} = f_1(\tfrac{A}{d}, LDR), \varphi_F = f_2\left(\tfrac{A}{d}, LDR\right) \tag{4-32}$$

$$M_{z0} = g_1(\tfrac{A}{d}, LDR), \varphi_M = g_2\left(\tfrac{A}{d}, LDR\right) \tag{4-33}$$

This gives a mathematical model for the pure yaw tests under study; smooth expressions for f_1, f_2, g_1 and g_2 are being sought. It should be noted that the mathematical model is constrained by equation (4-8), namely $A/T \approx 0.08$ [m/s] or $A \cdot \omega \approx 0.5$ [m·rad/s].

4.5.2 Regression model for the non-dimensional sway force amplitude

For the non-dimensional sway force amplitude Fig. 4.20 shows quadratic curves fitted to the test data. The fitted curves are of the following quadratic regression form:

$$1000F'_{y0} = p_1(\tfrac{A}{d})^2 + p_2\left(\tfrac{A}{d}\right) + p_3 \tag{4-34}$$

Table 4.2 shows the regression coefficients for the five hull models. The quadratic curves in Fig. 4.20 have closely the same trend as each other, which means that there is only a small interaction effect in the response sway force amplitude between the two factors sway amplitude and vehicle length. That is, whether the vehicle length is large or small, the relationship between sway force amplitude and sway motion amplitude is almost the same only shifted vertically. Since the curves have approximately the same trend, an average quadratic curve is plotted with bold solid line in Fig. 4.20, the coefficients of

which are the average of the coefficients in Table 4.2 for the four longest models. The average curve is:

$$1000F'_{y0} = 0.7(\tfrac{A}{d})^2 - 9.75\left(\tfrac{A}{d}\right) + 44.9 \qquad (4\text{-}35)$$

where $2 < A/d < 6$. Or if written versus frequency it is:

$$1000F'_{y0} = 4.25(\tfrac{1}{\omega})^2 - 24\left(\tfrac{1}{\omega}\right) + 44.9 \qquad (4\text{-}36)$$

where $0.38 < \omega < 1.37$ [rad/s]. Now if (4-34), with coefficients in Table 4.2, is used to make a new plot of the non-dimensional sway force amplitude in which length-to-diameter ratio is on the x-axis, a plot as in Fig. 4.21 is obtained. Different markers represent different non-dimensional sway amplitude values from two to six. As can be observed the variation of the non-dimensional sway force amplitude versus length-to-diameter ratio is almost linear for all sway amplitudes. The average linear variation of sway force amplitude versus length-to-diameter ratio is shown by the bold solid line in Fig. 4.21, which has the following regression equation:

$$1000F'_{y0} = 0.73(LDR) + 10.45 \qquad (4\text{-}37)$$

where $8.5 < LDR < 12.5$.

Table 4.2 Regression coefficients for the five hull series for the quadratic fit in equation (4-34)

LDR	p_1	p_2	p_3	R-square
8.5	2.29	-18.5	52.07	0.933
9.5	0.61	-8.43	40.21	0.981
10.5	0.89	-11	46.77	0.991
11.5	0.76	-10.84	48.33	0.987
12.5	0.54	-8.71	44.46	0.95

103
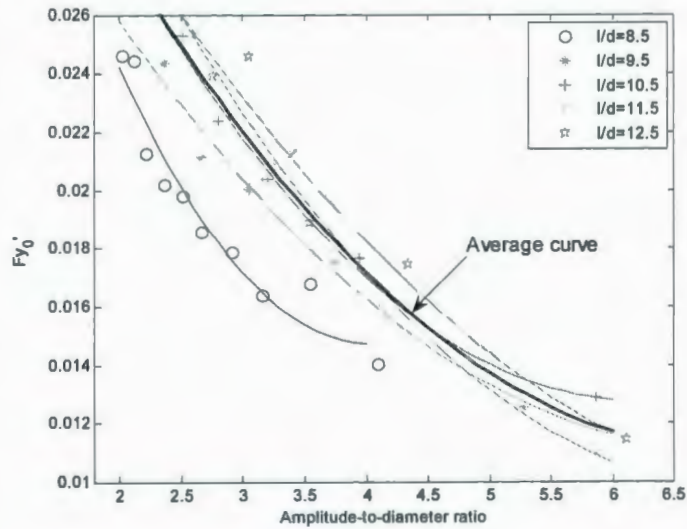
Fig. 4.20 Curve fits to the Non-dimensional sway force amplitude vs. A/d

during pure yaw manoeuvres

On the other hand, the lines in Fig. 4.21 are in closely the same trend, which again suggests that there is a small interaction effect on the response sway force amplitude between the factors sway amplitude and vehicle length. That is, whether the sway amplitude is large or small, the effect of vehicle length on the sway force amplitude is almost the same. For the sway force amplitude, combining (4-36) and (4-37), the following model is derived:

$$1000F'_{y0} = 0.7(\tfrac{A}{d})^2 - 9.75\left(\tfrac{A}{d}\right) + 0.73(LDR) + C \qquad (4\text{-}38)$$

where $2 < A/d < 6$ and $8.5 < LDR < 12.5$. Calibrating (4-38) with the experimental data in Table 4.1 at the end of this chapter results in a value of 36.80 for the intercept C. Note that the intercept value does not mean that the sway force for zero sway amplitude is non-zero; the RSM is not valid for extrapolation outside the range of variation of A/d as stated above.

104
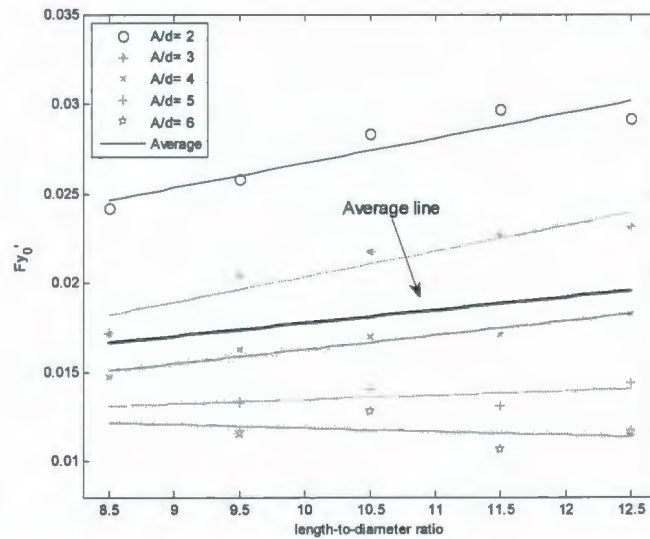
Fig. 4.21 Curve fits to the non-dimensional sway force amplitude vs. *LDR*

during pure yaw manoeuvres

It is convenient to convert the actual values of the two factors to coded levels. The coded factors are defined so as the low and high levels are minus one and plus one, respectively. It is easier to work with the data if they are scaled to have zero mean. Hence, if the coded factors A/d and LDR are named respectively X and Y varying from -1 to 1, as shown in Table 4.3, then (4-38) changes to:

$$1000F'_{y0} = 2.8\,X^2 - 8.3\,X + 1.46\,Y + C \qquad (4\text{-}39)$$

Note that the intercept C, in (4-38) and in (4-39) have different values; the intercept in (4-39) has the value 16.66. The advantage of working with the coded factors is that one can directly compare the regression coefficients to see which factor has a more significant effect on the response. According to (4-39), factor X, the sway amplitude, has a linear effect of about six times larger than the factor Y, the vehicle length, on the response sway force amplitude. Moreover, factor X is the source of curvature in the

105

response surface. The response surface for the sway force amplitude when plotted versus the coded factors is shown in Fig. 4.22. Note that the centre-point in Fig. 4.22, $(X, Y) = (0, 0)$ corresponds to the actual values $(A/d, LDR) = (4, 10.5)$. The largest force amplitude is at the corner: $(X, Y) = (-1, 1)$ which corresponds to $(A/d, LDR) = (2, 12.5)$, that is, the longest hull in its most rapid pure yaw manoeuvre experiences the largest force.

Table 4.3 Actual and coded factors for the pure yaw tests

A/d	2	3	4	5	6
X	-1	-0.5	0	0.5	1
LDR	8.5	9.5	10.5	11.5	12.5
Y	-1	-0.5	0	0.5	1
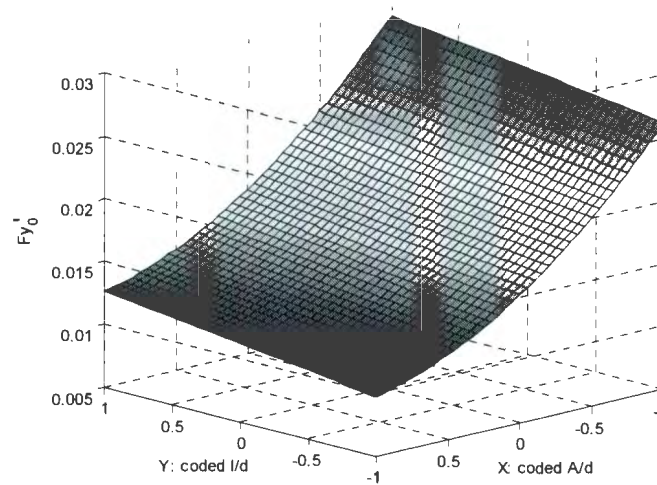
Fig. 4.22 Response surface for the non-dimensional sway force amplitude in pure yaw manoeuvres

4.5.3 Regression model for the non-dimensional yaw moment amplitude

Next the yaw moment amplitude in equation (4-33) is modeled through the same process as for the sway force. Therefore, first a quadratic regression is performed over the factor PMM sway amplitude A/d, which is followed by a linear regression over the

106

factor vehicle length-to-diameter ratio. The results are shown in Figs. 4.23 and 4.24. Again the average variation is shown with a bold solid line. The equations for the average quadratic curve in Fig. 4.23 and the average line in Fig. 4.24 are respectively:

$$1000M'_{z0} = 0.34(\tfrac{A}{d})^2 - 3.86\left(\tfrac{A}{d}\right) + 12.16, \text{ and} \tag{4-40}$$

$$1000M'_{z0} = 0.22(LDR) + 0.43 \tag{4-41}$$

which results in the following regression model for the yaw moment amplitude:

$$1000M'_{z0} = 0.34(\tfrac{A}{d})^2 - 3.86\left(\tfrac{A}{d}\right) + 0.22(LDR) + C \tag{4-42}$$

The test data provide a value of 9.9 in (4-42) for the intercept C. Also for the regression model of the yaw moment amplitude, equation (4-42), there is no term for the interaction effect of the two factors: PMM sway amplitude and vehicle length, which is reasonable due to the almost similar-trend curves in both Figs. 4.23 and 4.24. Physically it means that no matter what is the vehicle LDR, the non-dimensional PMM sway motion amplitude has approximately the same effect on the non-dimensional yaw moment amplitude, and vice versa. The regression model in (4-42) can be rewritten for the coded factors X and Y, as defined before in Table 4.3, hence:

$$1000M'_{z0} = 1.36\,X^2 - 2.28\,X + 0.44\,Y + C \tag{4-43}$$

The value for the intercept in the coded equation (4-43) is 2.21. As mentioned previously, the response model for the coded factors reveals the relative significance of the effect of each term. The linear effect of the PMM sway motion amplitude A/d on the yaw moment amplitude is about five times the effect of hull length LDR also the sway amplitude is the source of curvature in the response surface. The RSM is shown in Fig. 4.25.

107
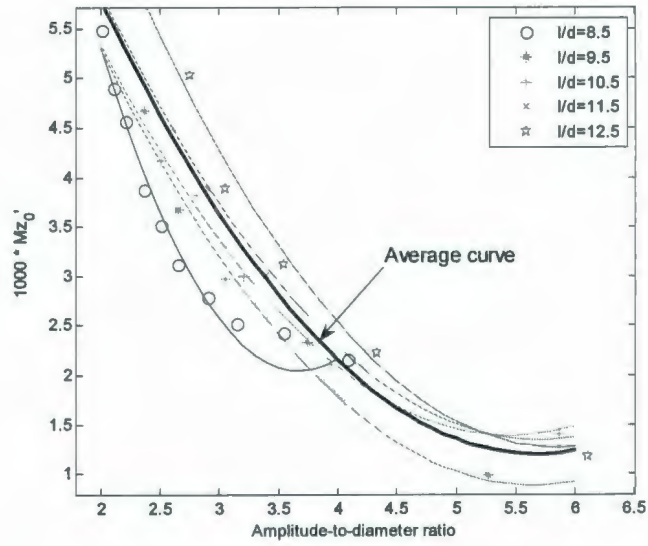
Fig. 4.23 Curve fits to the non-dimensional yaw moment amplitude vs. A/d
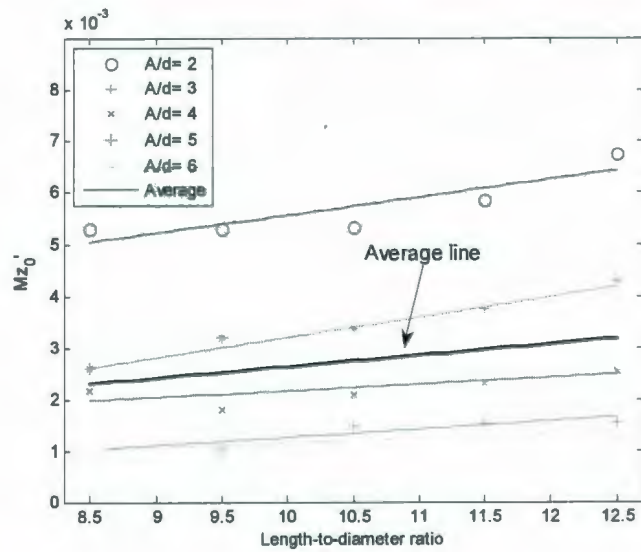
Fig. 4.24 Curve fits to the non-dimensional sway force amplitude vs. LDR
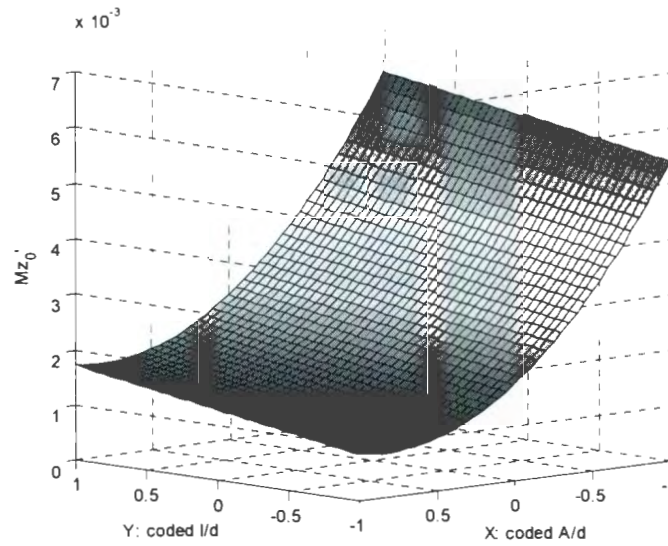
Fig. 4.25 Response surface for the non-dimensional yaw moment amplitude in pure yaw manoeuvres

4.5.4 The phase lag between manoeuvre inputs and hydrodynamic loads

It is more difficult to model the phase lags. The sinusoidal sway force is delayed by a phase angle φ_F of about $\pi/2$ radians relative to the sinusoidal yaw angle, and for the yaw moment the phase lag relative to the yaw angular acceleration φ_M is close to zero, though it gets as large as 0.7 radians for the long hulls in slow pure yaw manoeuvres. Figs. 4.26 and 4.27 show the experimental data for the hull-series for the sway force and yaw moment phase lags. Because of the scattered data the procedure that was used before to fit a response surface model does not work in this case. The curves fitted to the data only show the general trend for all hull series.
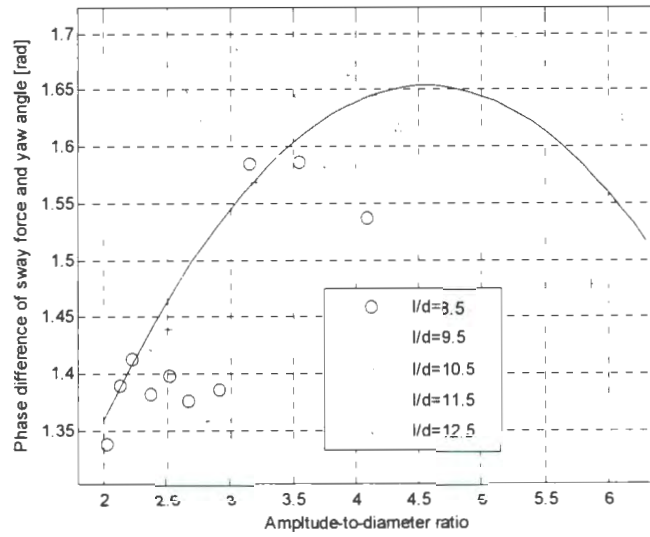
Fig. 4.26 Phase difference of F_y and β vs. A/d during pure yaw manoeuvres
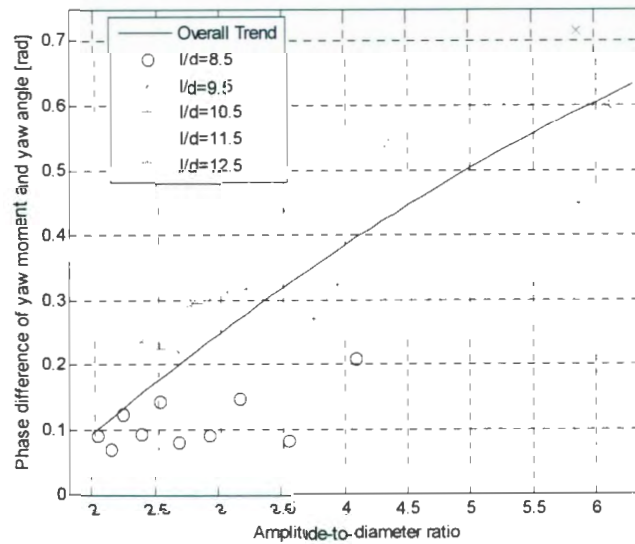
Fig. 4.27) Phase difference of M_z and $\ddot{\beta}$ vs. A/d during pure yaw manoeuvres

The fitted curves in Figs. 4.26 and 4.27 are the following quadratic equations respectively:

$$\varphi_F = -0.04(\tfrac{A}{d})^2 + 0.41 \left(\tfrac{A}{d}\right) + 0.7 \qquad (4\text{-}44)$$

$$\varphi_M = -0.01(\tfrac{A}{d})^2 + 0.19\left(\tfrac{A}{d}\right) - 0.26 \tag{4-45}$$

Or written versus the manoeuvring frequency the two fitting curves are:

$$\varphi_F = -0.1(\tfrac{1}{\omega})^2 + \left(\tfrac{1}{\omega}\right) + 0.7 \tag{4-46}$$

$$\varphi_M = -0.025(\tfrac{1}{\omega})^2 + 0.47\left(\tfrac{1}{\omega}\right) - 0.26 \tag{4-47}$$

The above assumption is not very realistic, because as can be seen from the experimental data the phase lag depends on the vehicle length-to-diameter ratio as well.

4.6 The application of the response surface models

4.6.1 The constraint

It should be recalled that the mathematical model used in this study and the response surface models based on that, are subject to a very important constraint, that is, equation (4-8): $A/T = 0.08$ [m/s]. This constraint says that the pure yaw tests of this study, are of relatively short period and abrupt. A zigzag manoeuvre run that was performed by the *MUN Explorer* underwater vehicle is used in order to clarify the applicability of the RSMs that were developed in this chapter. The *MUN Explorer* is a survey-class autonomous underwater vehicle (AUV) owned by Memorial University. It is 4.5 m in length with a maximum diameter of 0.69 m and is designed to go as deep as 3000 m with cruising speeds between 0.5 and 2.5 m/s.

In a series of free-running manoeuvring experiments that were performed by the *MUN Explorer* AUV in summer 2006 in the open ocean, there were some zigzag manoeuvres, both in horizontal and vertical planes. Reported by Issac et al. [2007a] is a horizontal zigzag manoeuvre, that is, a zigzag manoeuvre at a constant depth of about three metres

with commanded amplitude and cycle-length of 20 m and 80 m respectively, at a forward speed of 1.5 m/s. An overshoot of about eight metres in amplitude was observed, therefore the parameters for this zigzag are:

$$A = 28 \text{ [m]}, U = 1.5 \text{ [m/s]}, T = 80/1.5 = 53.3 \text{ [s]}, LDR = 6.5, A/d = 40.6 \qquad (4\text{-}48)$$

which results in:

$$A/T = 0.525 \text{ [m/s]} \qquad (4\text{-}49)$$

Note that the *LDR* ratio at about 6.5 for the *MUN Explorer* is outside the range of applicability $8.5 < LDR < 12.5$ of our response model. Similarly the value of A/d of 40.6 is outside the range of applicability of $2 < A/d < 6.1$ used in this study. It is postulated that the linear effects of length-to-diameter ratio will permit an extrapolation to 6.5 based on the validated range of 8.5 to 12.5. However, the quadratic effect of sway amplitude prevents extrapolation to A/d of 40.6 which is well beyond the validated range of two to six. Due to these considerations, these RSMs are not suitable for estimating the sway force and yaw moment exerted on the *MUN Explorer* in the above zigzag manoeuvre.

4.6.2 Sample application

For a sample application of the RSMs, imagine a zigzag manoeuvring mission to be performed by the *MUN Explorer* AUV defined as follows: commanded amplitude and cycle-length for the zigzag equal to 4 m and 50 m respectively with a forward speed of 1.0 m/s. Such an abrupt manoeuvre may occur, for example, during obstacle avoidance such as manoeuvring around a small iceberg. For this abrupt turn:

$$A = 4 \text{ m}, U = 1 \text{ m/s}, T = 50/1 = 50 \text{ s} \qquad (4\text{-}50)$$

In this case we have: $A/T = 0.08$ [m/s], which is the same as the mathematical model of this study. Converting the variables sway amplitude and vehicle length to their coded form, as was introduced in Table 4.3, result in:

$$LDR = 6.5 \rightarrow Y = -2, A/d = 5.8 \rightarrow X = 0.9 \qquad (4\text{-}51)$$

The coded factor Y is out of the original range $[-1, 1]$, but because its effect is linear it should predict the response closely. Inserting X and Y into (4-38) and (4-42) gives:

$$F'_{y0} = 8.5 * 10^{-3} \text{ and } M'_{z0} = 0.4 * 10^{-3} \qquad (4\text{-}52)$$

For the *MUN Explorer* the non-dimensionalizing factor is found to be:

$$\tfrac{1}{2}\rho U^2 A_p = \tfrac{1}{2} * 1025 * (1^2) * 4.5 * 0.69 = 1591.1 \text{ [N]} \qquad (4\text{-}53)$$

For the yaw moment, (4-53) should be multiplied by the length of the vehicle again. Therefore, the sway force and yaw moment amplitudes exerted on this AUV in such a manoeuvre are:

$$F_{y0} = 13.5 \text{ [N] and } M_{z0} = 2.84 \text{ [N.m]} \qquad (4\text{-}54)$$

The force and moment in (4-54) are estimates of the total hydrodynamic sway force and yaw moment that are exerted on the bare hull of this AUV in such a zigzag mission, considering that the bare hull of the *MUN Explorer* and the hull-series of this study are both streamlined and axisymmetric with similar shapes but different dimensions.

The yaw angle amplitude for this zigzag manoeuvre is derived using the approximation (4-6) as follows:

$$\beta_0 = 2\pi A/(T \cdot U) = 0.503 \text{ [rad]} = 28.8 \text{ [deg]} \qquad (4\text{-}55)$$

Hence, the maximum lateral speed, namely the amplitude of the PMM lateral velocity in the global coordinate system is:

113

$$v_0 = U \cdot \sin(\beta_0) = 0.72 \text{ [m/s]} \tag{4-56}$$

The phase lag between the yaw angle signal and hydrodynamic loads are estimated using (4-44) and (4-45) as follows:

$$\varphi_F = 90.7 \text{ [deg]}, \varphi_M = 33.5 \text{ [deg]} \tag{4-57}$$

The *MUN Explorer* AUV has two rudders with symmetric NACA 0024 profile, with chord, span and thickness of respectively:

$$c = 0.35 \text{ m}, b = 0.35 \text{ m}, t = 0.24 * c = 0.084 \text{ m} \tag{4-58}$$

The moment arm of the rudders (distance between centre of pressure of the rudders and centre of gravity of the vehicle) is about $x_{planes} = 1.36$ m. The total turning moment provided by the two rudders[5] is estimated to be given by

$$M_{z,planes} = 2 * (1/2)\rho U^2 \cdot b \cdot c \cdot C_L \cdot x_{planes} \tag{4-59}$$

Here the lift coefficient for NACA 0024 with an angle of attack relative to the local flow direction of α [deg] is approximately equal to[6]:

$$C_L = 0.03\alpha \tag{4-60}$$

Summarizing (4-58) to (4-60) it is estimated that:

$$M_{z,planes} = 5.12\alpha \text{ [N.m]} \tag{4-61}$$

Using (4-54) and (4-61), assuming that (4-54) is the total moment opposing the turn, results in:

$$I\ddot{\beta} = 5.12\alpha - 2.84 \tag{4-62}$$

---

[5] The AUV's stern-planes are in X-configuration, but here they were assumed in upright, cruciform: +, configuration.
[6] Lift coefficient of the *MUN Explorer* planes are derived in Chapter 5, section 5.4.1; see Fig. 5.8.

114

where α is in degrees. The moment of inertia of the flooded vehicle, denoted by I, is estimated about 3300 [kg.m^2], while the flooded vehicle, with the payload installed, weighs about 1450 kg[7]. The yaw angular acceleration in (4-62) is calculated:

$$\ddot{\beta} = -\beta \cdot \omega^2 \sin(\omega t) \qquad (4\text{-}63)$$

Fig. 4.28 shows the yaw angular acceleration and the yaw moment signals for this zigzag manoeuvre with the *MUN Explorer* AUV with a commanded amplitude and cycle-length for the zigzag equal to 4 m and 50 m respectively; forward speed 1 m/s.
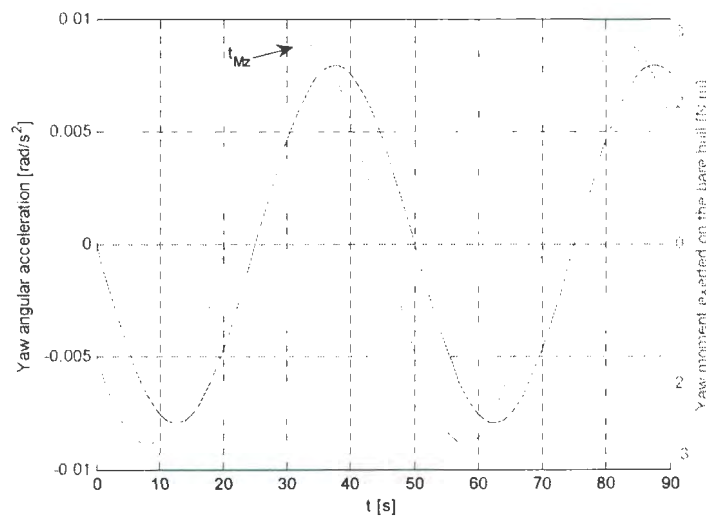
Fig. 4.28 Yaw moment and yaw angular acceleration signals for the zigzag manoeuvre with the *MUN Explorer* AUV

According to Fig. 4.28 when the yaw moment signal is maximum at time t_{Mz}, which is calculated at the first positive peak to be 32.86 s, the yaw angular acceleration $\ddot{\beta}$ is below its maximum value; therefore, the angular acceleration that should be substituted into (4-62) is read in Fig. 4.28 as follows:

---

[7] Derivation of the mass and moment of inertia of the *MUN Explorer* AUV is explained in more details in chapter 5, section 5.5.

$$\ddot{\beta} \text{ (at } t_{Mz} = 32.86 \text{ s)} = 6.63 * 10^{-3} \text{ [rad/s}^2] \qquad (4\text{-}64)$$

Substituting (4-64) and the estimated moment of inertia into (4-62) results in:

$$I\ddot{\beta} = 3300 * 6.63 * 10^{-3} = 5.12\,\delta - 2.84 \qquad (4\text{-}65)$$

This allows us to solve for the required deflection angle of the control planes δ for this zigzag manoeuvre, which is about 4.8 deg. Note that there is some efficiency lower than 100% for the rudders, and there is some extra opposing moment in addition to the bare hull moment evaluated by the RSMs here. In addition the assumption that the rudders are operating in a steady-flow regime, as would be experienced in a circular-arc turn at constant forward speed, during a zigzag manoeuvre where the instantaneous angle of attack and rudder deflection are changing continuously is not correct. Thus the deflection angle δ in (4-65) should properly account for the true local angle of attack while turning which is beyond the scope of this example application here.

4.7 Deriving the conventional yaw coefficients from PMM tests

Similar to section 3.8 that was presented for the sway coefficients, now the pure yaw test results are used for the derivation of the yaw coefficients. Fig. 4.29 illustrates the sway force and yaw moment vectors along with the vector of the heading angle of the PMM and its first and second derivatives which are respectively the rate of turn and the angular acceleration, and also the vector of lateral velocity and lateral acceleration of the PMM. The vectors in Fig. 4.29 are shown at the start of the motion and they turn in the plane at manoeuvring frequency of ω. The vector of sway force as was introduced before is φ_F radians behind the heading angle or the lateral velocity of the PMM, and the vector of

116

yawing moment as was introduced before is φ_M radians behind the angular acceleration of the PMM; the data for these phase angles are shown in Table 4.1 on page 124.
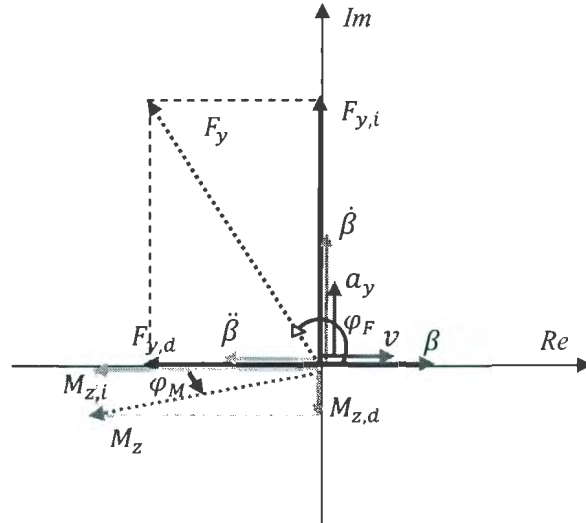
Fig. 4.29 Force and moment vectors illustrated along with the heading angle of the PMM

According to Bishop and Parkinson [1970, pages 54 and 55], the oscillatory yaw coefficients during these pure yaw manoeuvres can be calculated as follows:

$$\tilde{Y}_{\dot{r}} = F_{y0,d}/\ddot{\beta}_0, \ \tilde{Y}_r = mU - F_{y0,i}/\ddot{\beta}_0, \ \tilde{N}_{\dot{r}} = I_z - M_{z0,i}/\ddot{\beta}_0, \ \tilde{N}_r = -M_{z0,d}/\dot{\beta}_0 \qquad (4\text{-}66)$$

where the amplitudes of the rate of turn and angular acceleration of the PMM are respectively: $\dot{\beta}_0 = \beta_0 \omega$ and $\ddot{\beta}_0 = \beta_0 \omega^2$. The damping and inertia components of the sway force and yaw moment in equation (4-66) were illustrated in Fig. 4.29 which are calculated as follows:

$$F_{y0,d} = F_{y0} \sin(\varphi_F - \pi/2), \ F_{y0,i} = F_{y0} \cos(\varphi_F - \pi/2), \text{ and} \qquad (4\text{-}67)$$

$$M_{z0,i} = M_{z0} \cos(\varphi_M), \ M_{z0,d} = M_{z0} \sin(\varphi_M). \qquad (4\text{-}68)$$

where the force and moment amplitudes and their phase angles are reported for these pure yaw tests in Table 4.1 on page 124. As seen in Fig. 4.29, the inertia component of the

117

sway force is in phase with the lateral acceleration of the PMM, and its damping component is along the lateral velocity of the PMM; note that this damping force for most test runs is acting against the velocity but for some runs where the phase lag φ_F is smaller than $\pi/2$ it is acting in the same direction as the lateral velocity (see Table 4.1 on page 124). Also, the inertia component of the yaw moment is in phase with the angular acceleration of the PMM which is the same as the angular acceleration of the bare hull model, and the damping component of the yaw moment is in phase with the rate of turn acting in the negative direction.

The flooded mass and moment of inertia of the bare hull configurations, m and I_z in equation (4-66), were presented in Table 2.1, and the model speed tangent to its path during pure yaw manoeuvres is calculated as: $U^2 = u_{carriage}^2 + v_0^2$, then: $U = \sqrt{2^2 + 0.5^2} = 2.06$ m/s. The non-dimensional mass of the underwater bare hulls of LDR 8.5 to 12.5 dividing the flooded mass data in Table 2.1 by $\frac{1}{2}\rho l^3$ are respectively:

$$m' = 10^{-3} * [19.2, 15.4, 13.1, 11, 9.4]. \tag{4-69}$$

Similarly, the moment of inertia of the flooded hulls in Table 2.1 divided by $\frac{1}{2}\rho l^5$ results in the non-dimensional moment of inertia as follows:

$$I_z' = 10^{-4} * [11.5, 9.9, 7.6, 6.3, 6.15]. \tag{4-70}$$

Conveniently, the sway force hydrodynamic derivatives $\tilde{Y}_{\dot{r}}$ and $\tilde{Y}_r$ are non-dimensionalized respectively by $\frac{1}{2}\rho l^4$ and $\frac{1}{2}\rho U l^3$, and the yawing moment derivatives $\tilde{N}_{\dot{r}}$ and $\tilde{N}_r$ are non-dimensionalized respectively by $\frac{1}{2}\rho l^5$ and $\frac{1}{2}\rho U l^4$.

Using (4-66) the non-dimensional derivative $(m' - Y_r')$ is plotted against the manoeuvring frequency for the five hulls in Fig. 4.30. It is observed that the test data for each LDR are almost non-variant within the range of frequency $0.4 < \omega < 1.3$ rad/s, thus a constant average value is drawn in Fig. 4.30 for each LDR. Then substituting the non-dimensional mass values from (4-69) respectively result in the following values for the non-dimensional turning rate derivative of the sway force for LDR 8.5 to 12.5:

$$Y_r' = 10^{-3} * [6.7, 6.0, 5.7, 5.1, 4.6]. \tag{4-71}$$
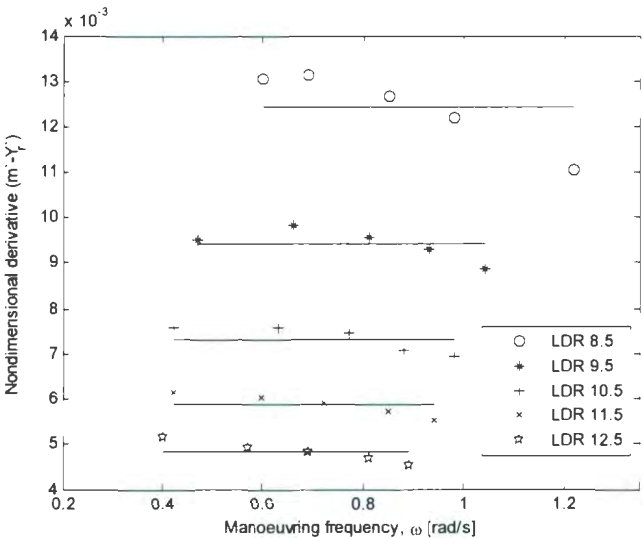
Fig. 4.30 Non-dimensional turning rate derivative of the sway force $(m' - Y_r')$ during pure yaw tests

A positive value for Y_r' means that the effect of stern is dominant, that is: when the vehicle turns in positive yaw direction a positive sway force is exerted on the stern and a negative sway force is exerted on the bow, sum of which gives the total sway force on the hull; thus positive Y_r' means that the effect of stern dominates. Also, note that according to (4-66), Y_r' –with a minus sign to show the opposing force– is in fact the non-

dimensional form of the cross-coupled added mass of water which accelerates in the lateral direction while the vehicle turns in the positive yaw direction.

Next, using (4-66) the non-dimensional derivative $(I'_z - N'_{\dot{r}})$ is plotted against the manoeuvring frequency for the five hulls in Fig. 4.31. Again, the test data for each *LDR* are approximated non-variant within this range of frequency $0.4 < \omega < 1.3$ rad/s, thus a constant average value is drawn in Fig. 4.31 for each *LDR*. Then substituting the non-dimensional values of the flooded moment of inertia from (4-70) respectively result in the following values for the angular acceleration derivative of the yaw moment for *LDR* 8.5 to 12.5:

$$N'_{\dot{r}} = -10^{-4} * [16.4, 11.0, 6.9, 8.0, 6.8]. \tag{4-72}$$
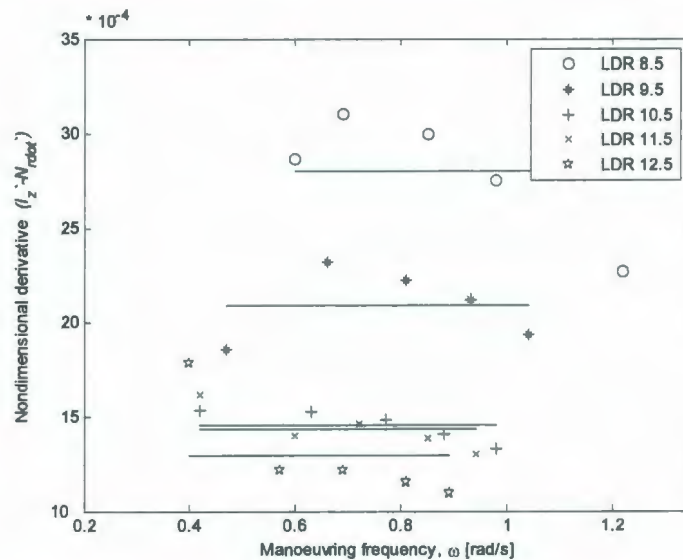
Fig. 4.31 Non-dimensional angular acceleration derivative of the yaw moment $(I'_z - N'_{\dot{r}})$

during pure yaw tests

Note that the term $M_{z0,i}/\ddot{\beta}_0$ in (4-66) is in fact the apparent moment of inertia of the vehicle-plus-water system. Then, $N'_{\dot{r}}$ is the non-dimensional form of the added moment of

inertia of the water with a minus sign, therefore it is opposing the rotational acceleration motion of the vehicle during these pure yaw manoeuvres. Also it is interesting to observe that the non-dimensional moment of inertia of the flooded hulls in (4-70) and the non-dimensional added moment of inertia in (4-72) are of about equal magnitude.

The other two derivatives: $Y_{\dot{r}}$ and N_r are less significant than the two above; because, as was illustrated in Fig. 4.29 and can be also followed in Table 4.1, the sway force and the yaw moment have small damping components that were recorded during these pure yaw manoeuvres. Using (4-66) the non-dimensional angular acceleration derivative of the sway force $Y_{\dot{r}}'$ and the non-dimensional turning rate derivative of the yaw moment N_r' are plotted versus the manoeuvring frequency in Figs. 4.32 and 4.33 respectively. The data in Figs. 4.32 and 4.33 are scattered and just the general trends were fitted by curves of respectively the forms: $a\sin(b\omega + c)$ and $a\omega + b$.
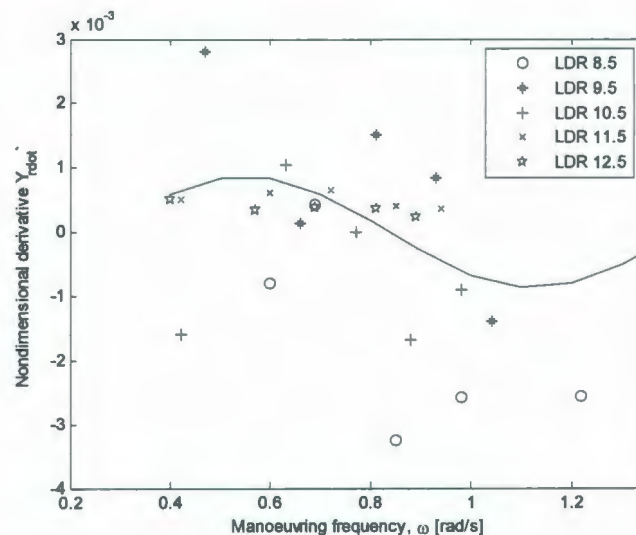
Fig. 4.32 Non-dimensional angular acceleration derivative of the sway force $Y_{\dot{r}}'$ during pure yaw tests

The data for Y_r' in Fig. 4.32 are mostly scattered about zero, but the data for N_r' in Fig. 4.33 have a small negative value which means that there is a moment opposing the turn due to the damping effects.
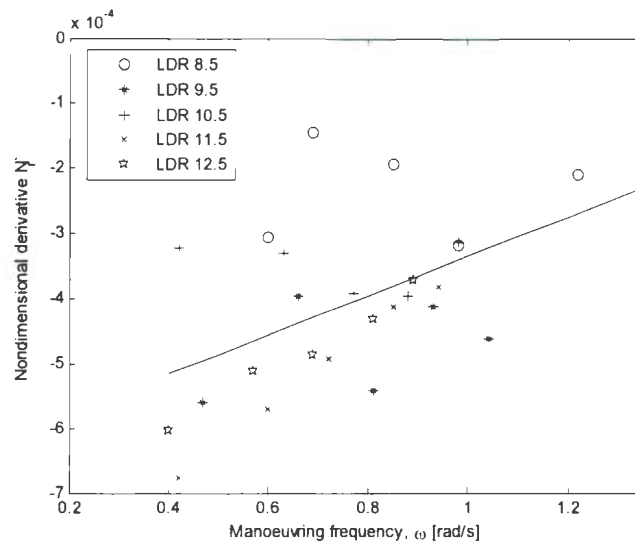
Fig. 4.33 Non-dimensional turning rate derivative of the yaw moment N_r' during pure yaw tests

Finally, it should be noted that the hydrodynamic yaw coefficients that were derived in this section using the conventional approach do not directly express the tests conditions. The approach that was used in the earlier sections of this chapter to analyze and model the test data was concerned with constructing a practical model to approximate the hydrodynamic loads that are exerted on the bare hull during zigzag manoeuvres for a free-running underwater vehicle, regarding that all the pure yaw runs in this study were subject to $A/T \approx 0.08$ m/s.

4.8 Summary

Results from towing tank experiments for pure yaw manoeuvres on the five axisymmetric hull forms for an underwater vehicle were reported. The coupled sway-yaw motion for pure yaw manoeuvres produced PMM sway amplitudes of up to about six diameters, maximum yaw angles of about 15 degrees, and, a maximum turning rate of 17 deg/s. Pure yaw manoeuvres with the small-sway-amplitudes and shorter periods and larger yaw rates produced larger non-dimensional hydrodynamic sway force and yaw moment. Next, the data from the pure yaw captive manoeuvring tests were used to develop regression equations in the form of Response Surface Models (RSMs) for the hydrodynamic loads versus manoeuvre inputs. A method was outlined for estimating the command signal required for the control surfaces in order to execute a zigzag manoeuvre by a self-propelled fully-submerged underwater vehicle. These set of pure yaw manoeuvres were of short period and abrupt, with a constant ratio of manoeuvre amplitude to its period $A/T = 0.08$ m/s. During a sample zigzag manoeuvre with the *MUN Explorer* AUV with commanded amplitude and cycle-length for the zigzag of respectively 4 m and 50 m with a forward speed of 1.0 m/s, the required rudder deflection angle was calculated to be about 4.8 degrees. In the last section of this chapter, the hydrodynamic yaw coefficients were also derived using the conventional approach to analyze the pure yaw test data. It was observed that the cross-coupled derivatives Y_r and $N_{\dot{r}}$ are of a significant magnitude during a pure yaw manoeuvre.

Table 4.1 Pure yaw test results for the five bare hull series

Model LDR	PMM sway amplitude [m]	PMM sway & yaw period [s]	Pure yaw frequency [rad/s]	PMM lateral velocity [m/s]	PMM lateral acceleration amplitude [m²/sec]	Approximate max PMM yaw rate [deg/sec]	Number of steady-state cycles in each run ≈	Sway force amplitude [N]	Phase lag between sway force and PMM lateral velocity [deg]	Yaw moment amplitude [N.m]	Phase lag between yaw moment and yaw angular acceleration [deg]
8.5	0.41	5.15	1.22	0.5	0.61	17.44	2.5	18.33	76.8	6.48	5.2
8.5	0.51	6.41	0.98	0.5	0.49	14.02	2	16.06	80.2	5.10	8.0
8.5	0.59	7.41	0.85	0.5	0.42	12.12	2	14.42	79.6	4.14	5.2
8.5	0.72	9.05	0.69	0.5	0.35	9.93	1.5	12.07	91.1	2.85	4.6
8.5	0.83	10.43	0.60	0.5	0.30	8.61	1	10.40	88.2	2.02	12.0
9.5	0.48	6.03	1.04	0.5	0.52	14.90	2	17.23	81.4	7.19	13.8
9.5	0.54	6.79	0.93	0.5	0.46	13.24	2	15.94	94.5	6.23	12.6
9.5	0.62	7.79	0.81	0.5	0.40	11.53	2	14.35	96.8	5.09	17.8
9.5	0.76	9.55	0.66	0.5	0.33	9.41	1.5	11.94	90.5	3.48	15.5
9.5	1.07	13.45	0.47	0.5	0.23	6.68	1	8.26	97.4	1.65	34.4
10.5	0.51	6.41	0.98	0.5	0.49	14.02	2	17.09	82.5	7.19	13.2
10.5	0.57	7.16	0.88	0.5	0.44	12.54	2	15.84	77.9	6.23	17.2
10.5	0.65	8.17	0.77	0.5	0.38	11.00	1.5	14.31	90.0	5.09	18.3
10.5	0.8	10.05	0.63	0.5	0.31	8.94	1.5	11.85	95.1	3.48	18.3
10.5	1.19	14.95	0.42	0.5	0.21	6.01	1	7.96	84.8	1.65	25.8
11.5	0.53	6.66	0.94	0.5	0.47	13.49	2	17.17	94.0	10.33	15.5
11.5	0.59	7.41	0.85	0.5	0.42	12.12	2	15.95	94.0	9.04	17.2
11.5	0.69	8.67	0.72	0.5	0.36	10.36	1.5	14.11	95.1	7.16	22.3
11.5	0.84	10.56	0.60	0.5	0.30	8.51	1.5	11.79	94.0	5.04	30.9
11.5	1.19	14.95	0.42	0.5	0.21	6.01	1	8.47	92.2	3.29	41.3
12.5	0.56	7.04	0.89	0.5	0.45	12.77	2	17.06	93.4	12.00	17.2
12.5	0.62	7.79	0.81	0.5	0.40	11.53	2	15.89	94.5	10.54	20.6
12.5	0.72	9.05	0.69	0.5	0.35	9.93	1.5	14.12	94.0	8.46	25.2
12.5	0.88	11.06	0.57	0.5	0.28	8.13	1	11.78	92.8	6.03	30.9
12.5	1.24	15.58	0.40	0.5	0.20	5.77	1	8.75	92.8	4.60	34.4

CHAPTER 5

MANOEUVRING SIMULATION OF THE *MUN EXPLORER* AUV BASED ON THE EMPIRICAL HYDRODYNAMICS OF AXISYMMETRIC BARE HULLS

5.1 Introduction

In a previous project that was reported by Azarsina et al. [2007a], manoeuvring of an underwater vehicle was studied under the action of its dynamic control systems. The equations of motion were solved numerically in the original state without any linearization or other simplification. The underwater vehicle was assumed to be a rigid body with six DoF (Degrees of Freedom) moving in calm water. The computer code developed, using MATLAB™7.1, could simulate various states of an underwater vehicle during manoeuvring. As an example, the turning manoeuvres were demonstrated in detail [Azarsina et al. 2007a]. Some major assumptions in that simulation code were: i) waves and underwater currents were not modeled; ii) the effects of internal moving masses, including ballast water with a free surface, were not modeled; iii) in the mass matrix calculation, mass and inertia of the hull were assumed to be dominant and the mass and inertia of the appendages were ignored; iv) the underwater vehicle was assumed to be neutrally buoyant with zero trim angle. More importantly, the hydrodynamics of that original code were fairly simple, since the main focus was to develop the motion simulation code and verify if it could properly respond to the manoeuvring mission, e.g. a

turning manoeuvre with a non-zero approach speed compared to a turning manoeuvre starting from a stationary state.

The purpose of the present study was to improve the previous simulation code. For this purpose, the hydrodynamics of the bare hull were developed in chapter 2, based on test results from captive tests that were performed on a series of bare hulls; and the control surfaces and the propeller were modeled for the *MUN Explorer* AUV (Autonomous Underwater Vehicle). The resulting upgraded code is useful to simulate several manoeuvring missions for the *MUN Explorer* AUV which is owned by the Memorial University as an active and valuable tool in the underwater research.

5.2 Dynamics of an underwater vehicle

The dynamics model to be used in this simulation has been introduced by Abkowitz [1969] and Fossen [1994]. The coordinate system is the same as was shown in chapter 2 shown again in Fig. 5.1: there is a global coordinate [X, Y, Z] in which the path and orientation of the vehicle was recorded, and a body-fixed coordinate system in which the velocities and forces were expressed.
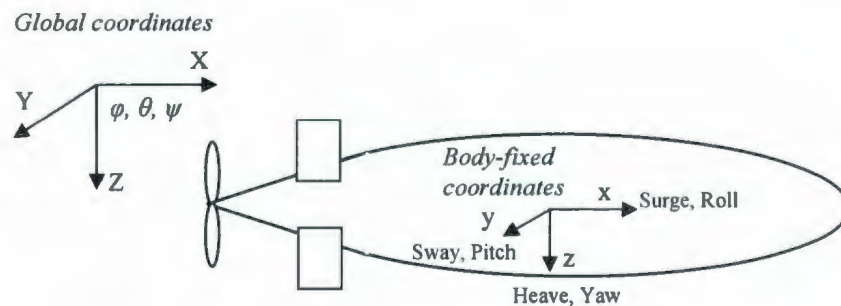
Fig. 5.1 Global and body-fixed coordinate systems for an underwater vehicle

The centre of gravity (*CG*) for the *MUN Explorer* is 2.44 m from the nose and about 40 mm below the longitudinal centreline; thus the *CG* is located about 20 cm aft of the vehicle mid-length; see section 5 in this chapter for more details. The origin used in this study is at the *CG* of the vehicle.

The dynamics of an underwater vehicle with six degrees of freedom can be represented by vectors: $\vec{\eta}$, $\vec{v}$ and $\vec{\tau}$, where $\vec{\eta}$ is the linear and angular displacement vector in global coordinates, $\vec{v}$ is the linear and angular velocity vector in body-fixed coordinates and $\vec{\tau}$ is the vector of forces and moments exerted on the underwater vehicle in the body-fixed coordinate system. Displacement, velocity and force vectors are defined as follow:

$$\vec{\eta} = [\vec{\eta}_1, \vec{\eta}_2] \tag{5-1}$$

$$\vec{v} = [\vec{v}_1, \vec{v}_2] \tag{5-2}$$

$$\vec{\tau} = [\vec{\tau}_1, \vec{\tau}_2] \tag{5-3}$$

where the linear and angular displacement, velocity and force vectors respectively are: $\vec{\eta}_1 = [x, y, z]$, $\vec{\eta}_2 = [\varphi, \theta, \psi]$, $\vec{v}_1 = [u, v, w]$, $\vec{v}_2 = [p, q, r]$, $\vec{\tau}_1 = [F_x, F_y, F_z]$ and $\vec{\tau}_2 = [M_x, M_y, M_z]$. The captive tests on the bare hull series were performed in the x-y plane. The hydrodynamic forces and moments which act in the horizontal and vertical planes on a body-of-revolution are the same. However, the *MUN Explorer* AUV has bow-planes, therefore in diving or surfacing it has a different performance than in a lateral-plane manoeuvre at constant depth. The simulation code in this study is programmed for the horizontal plane manoeuvres in which the force vectors have three elements: surge and sway forces along x and y-axes and yawing moment around z-axis in the body-fixed

coordinate system (see Fig. 5.1). In the planar manoeuvre with surge, sway and yaw degrees of freedom, the kinematics of motion simplify to the three equations as follow:

$$m[\dot{u} - vr - x_G r^2 - y_G \dot{r}] = F_x \tag{5-4}$$

$$m[\dot{v} + ur - y_G r^2 + x_G \dot{r}] = F_y \tag{5-5}$$

$$I_z \dot{r} + m[x_G(\dot{v} + ur) - y_G(\dot{u} - vr)] = M_z \tag{5-6}$$

In the above equations, m as will be explained later is the flooded mass of the underwater vehicle and I_z is the moment of inertia of the vehicle in the flooded state. The vertical axis around which the moment of inertia is calculated indicates the origin of the body-fixed coordinate system relative to which the centre of gravity may have non-zero offsets x_G and y_G. In this simulation, the origin of the body-fixed coordinate system is assumed to be at the mid-length of the vehicle.

The forces and moments exerted on the underwater vehicle are expressed as a function of velocity and acceleration vectors of the underwater vehicle, thus $\vec{\tau}$ is a function of time because both velocity and acceleration are variables of time. The underwater vehicle's acceleration at any instant t is obtained as the inverse of the mass matrix times the vector of forces and moments, that is:

$$\dot{\vec{v}}_{(t)} = M^{-1} \cdot \vec{\tau}_{(t)} \tag{5-7}$$

where M is the sum of the flooded vehicle mass matrix and the added mass matrix. Integration of the initial acceleration in the time interval δt gives the velocity vector at the next time-step. Integration of the initial velocity in the time interval δt gives the position vector at the next time-step. Finally, the position vector is transferred to the global coordinate system via the axes rotation which is defined by the Euler angles

$[\varphi, \theta, \psi]$. In order to make use of this procedure we must formulate $\vec{\tau}_{(t)}$ and the method chosen was to measure $\vec{\tau}$ experimentally for a typical underwater vehicle shape.

5.3 Bare hull hydrodynamics

Manoeuvring experiments were performed with a series of five slender axisymmetric bare hulls in November 2005 in the 90 m long, 12 m wide towing tank at the National Research Council Canada, Institute for Ocean Technology (NRC-IOT). Each of the five hulls used the same nose and tail sections, and varied only in the length of the constant-diameter mid-body section. The five bodies were mounted on a Planar Motion Mechanism (PMM) and the experimental conditions included straight-line runs, static yaw runs, dynamic sway and dynamic yaw manoeuvres. The hydrodynamic loads were measured with an internal three-component balance to record the axial force, lateral force and yaw moment. The recorded data have been extracted and analyzed as were presented in chapters 2, 3 and 4 of this thesis. The focus of the simulation results that are presented here is on the turning manoeuvres of a full-scale vehicle, the hydrodynamics of which are well-represented in a quasi-static sense for low yaw rates by measurements from static-yaw runs.

Using the fixed-attitude test results the following models for the drag, lift and moment coefficients were proposed in chapter 2:

$$1000 * C_D = 1.88\beta^2 + 11.7 LDR + 38 \tag{5-8}$$

$$1000 * C_L = (0.007 LDR + 0.011)\beta^3 + (4.87 LDR + 8.85)\beta \tag{5-9}$$

$$1000 * C_M = -0.01\beta^3 + 17.92\beta \tag{5-10}$$

The empirical formulae in (5-8) to (5-10) are valid over ranges of the factors: bare hull length-to-diameter ratio (LDR), yaw angle and forward speed of respectively: 8.5 to 12.5, -20 to 20 degrees and 1 to 4 m/s. Drag, lift and moment coefficients are substituted in the following relations to produce the drag and lift forces and the turning moment that are exerted on the bare hull of a torpedo-shape underwater vehicle:

$$D = C_D \cdot q \cdot A_f \tag{5-11}$$

$$L = C_L \cdot q \cdot A_f \tag{5-12}$$

$$M = C_M \cdot q \cdot A_f \cdot l \tag{5-13}$$

where $q = \frac{1}{2}\rho U^2$ is the dynamic pressure of the flow, $A_f = \pi d^2/4$ is the frontal area of the bare hull, and l is the overall length of the bare hull also denoted by LOA in this chapter. Forward speed of the vehicle relative to the flow is: $U^2 = u^2 + v^2$ where u and v as previously introduced are surge and sway velocity of the vehicle. If (5-8) to (5-10) are used to predict the drag and lift forces and the turning moment that are exerted on the bare hull of the *MUN Explorer* AUV, which is torpedo-shape with LDR 6.5, at various forward speeds within a range of -30 to 30 degrees of drift angle, the curves in Figs. 5.2 to 5.4 are produced. These curves suggest that the empirical formulae (5-8) to (5-10) also produce smooth variation outside the range of applicability.
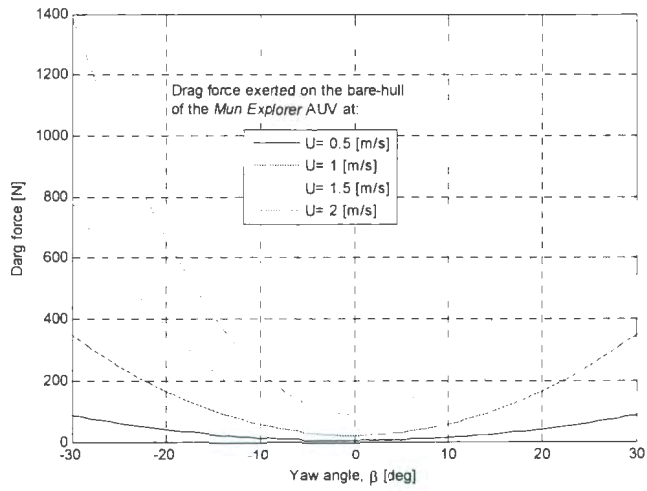
Fig. 5.2 Drag force exerted on the *MUN Explorer* AUV using empirical formulae (5-8)
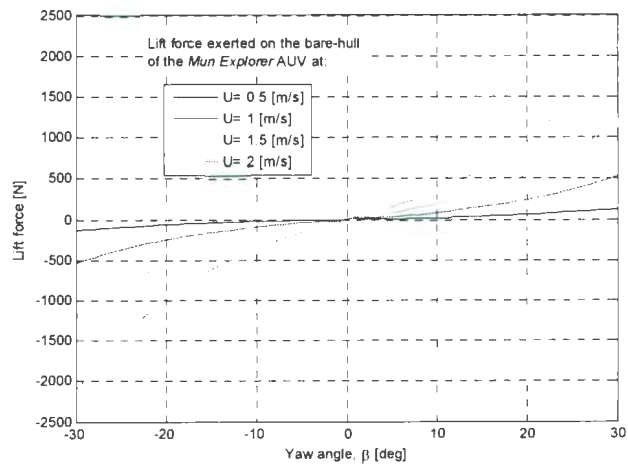
Fig. 5.3 Lift force exerted on the *MUN Explorer* AUV using empirical formulae (5-9)

131
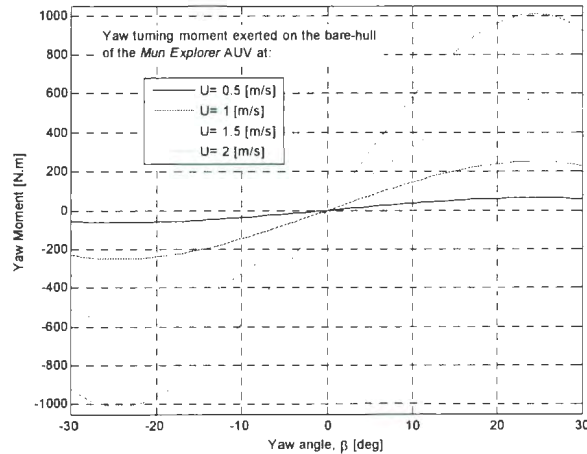
Fig. 5.4 Yaw turning moment exerted on the *MUN Explorer* AUV

using empirical formulae (5-10)

5.4. Dynamic control systems

5.4.1 Control surfaces

Fig. 5.5 shows the *MUN Explorer* AUV; its overall length is about 4.5 metres and it has a maximum diameter of about 0.69 m. A cylindrical main body is blended with an elliptical nose at its front and a tapered tail section at its rear. Manoeuvring of the vehicle is facilitated by four aft planes arranged in "X" configuration and two foreplanes which assist with precise depth and roll control. The vehicle yaw, pitch and roll motions can be independently controlled by the aft planes. With proper control of the vehicle pitch, the vehicle depth can also be controlled using only the aft planes. The planes have the symmetrical cross-section of NACA 0024. Each plane is controlled independently by a 24 Volt brushless DC motor that resides inside the plane body [Issac et al. 2007a]. *MUN*

Explorer's control planes are about 35 by 35 cm in chord and span, that is an aspect ratio of one[8].

In this simulation, which is to simulate the horizontal plane manoeuvres of the *MUN Explorer* AUV, the tail-planes are the active controllers. The bow-planes were modeled with zero deflection angles only to contribute to the axial force. This, of course, introduces some error in the simulation prediction, since the real vehicle even in a constant-depth manoeuvre operates with deflected bow-planes, which should be corrected in a later study. As was reported by Issac et al. [2007b], during a straight-ahead manoeuvre all six planes operate to bring the vehicle to a nose-up attitude, but the pitch attitude of the vehicle especially at lower forward speeds was observed to be negative; e.g. at 1 and 1.5 m/s forward speeds the vehicle had a negative pitch angle of respectively about 5 and 1.5 deg. This was explained by the fact that when the vehicle is at rest at the surface, it is normally trimmed to have the nose down trim so as to ensure that the antennas which are mounted on the communications mast on the vehicle tail are well out of the water thus providing a failsafe condition for communications. For the same reason the AUV has a positive buoyancy of about 8 kg. The bow-plane deflection angles that were recorded during some turning manoeuvres were reported by Issac et al. [2007b] which are reproduced later in this study.

---

[8] Each control plane consists of a stationary root-base of about 3 cm span which fairs to the hull and a moving main part of 35 cm span. Here, the root-base was not included in the modeling.
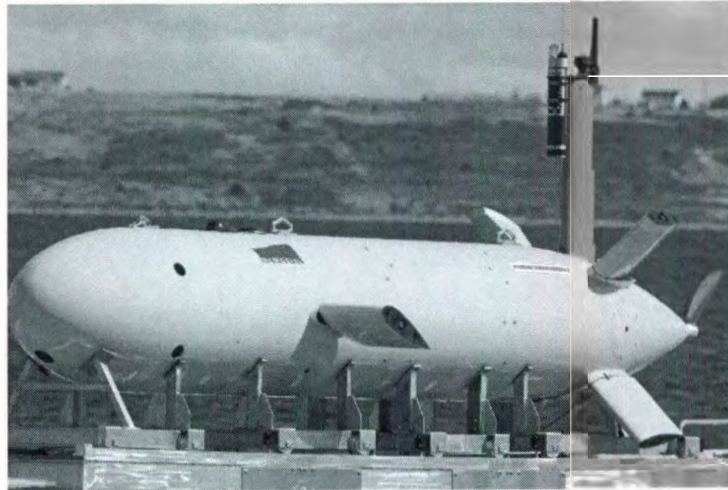
Fig. 5.5 *MUN Explorer* AUV [MERLIN 2009]

Numbering of the planes is compatible with the manufacturer's manual where the two bow-planes are number 1 and 2 and the stern-planes are number 3 and 4 on port-side and 5 and 6 on starboard-side. All planes have a positive deflection angle δ when the leading edge turns upward. Thus the lift force of each plane is positive upward. As shown in Fig. 5.5, the angle between the axis of rotation of each stern-plane and the horizontal, to be called the X-angle, was manufactured to be $\xi = 45$ deg.

The lift and drag coefficients for NACA 0024 planes are about the same as NACA 0025 for which extensive experimental results were reported in the NACA report No. 708 by Bullivant [1940]. The lift and drag coefficients versus angle of attack from that report were reproduced. The maximum lift coefficient is about one and occurs at about 20 deg, which corresponds to a drag coefficient of about 0.2. The pitching moment coefficient that was measured at an average Reynolds $3.2*10^6$ for NACA 0025 had a linear trend increasing from zero to about 0.05 at an AOA of 14 deg, and reducing back to zero at an

AOA of 24 deg. Fig. 5.6 shows the lift, drag and moment coefficients for NACA 0025 section of aspect ratio six reproduced from the NACA report.
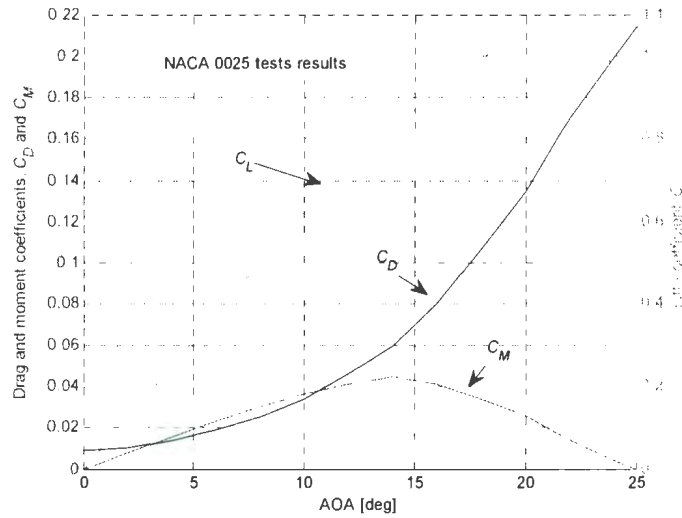
Fig. 5.6 Lift and drag coefficients for the control planes;

NACA 0025 airfoils of aspect ratio (AR) of six

The NACA tests were performed for airfoils of aspect ratio (AR) of six, while the *MUN Explorer* planes have an AR of one. For NACA 0015 profiles, in a study by Whicker and Fehlner [1958] the effect of aspect ratio was reported to be significant with higher lift-coefficient for larger aspect ratio. The following formulae [von Mises 1959, pp. 148 to 167] can be used to correct for the lift and drag coefficients of a 2D section to a 3D section:

$$C_{L(3D)} = C_{L(2D)} \cdot (AR/(AR + 2)) \qquad (5\text{-}14)$$

$$C_{D(3D)} = C_{D(2D)} + C_{L(2D)}{}^2/(\pi \cdot AR) \qquad (5\text{-}15)$$

Therefore:

$$C_{L(AR=6)} = C_{L(2D)} \cdot (6/8) \text{ and } C_{L(AR=1)} = C_{L(2D)} \cdot (1/3) \qquad (5\text{-}16)$$

$$C_{L(AR=1)} = C_{L(AR=6)} \cdot (8/6) \cdot (1/3) \qquad (5\text{-}17)$$

Note that the drag coefficient resulting from (5-15) for the 3D section is larger than a 2D section and it occurs at a higher actual angle of attack which is calculated as follows [Abbot and von Doenhoff, 1959]:

$$\alpha_{3D} = \alpha_{2D} + C_{L(2D)}/(\pi \cdot AR) \ [\text{rad}] \qquad (5\text{-}18)$$

The resulting drag and lift coefficients for NACA 0025 of $AR = 1$ were plotted versus the plane AOA in Fig. 5.7. According to (5-18), the curve of drag coefficient extends to larger AOAs.
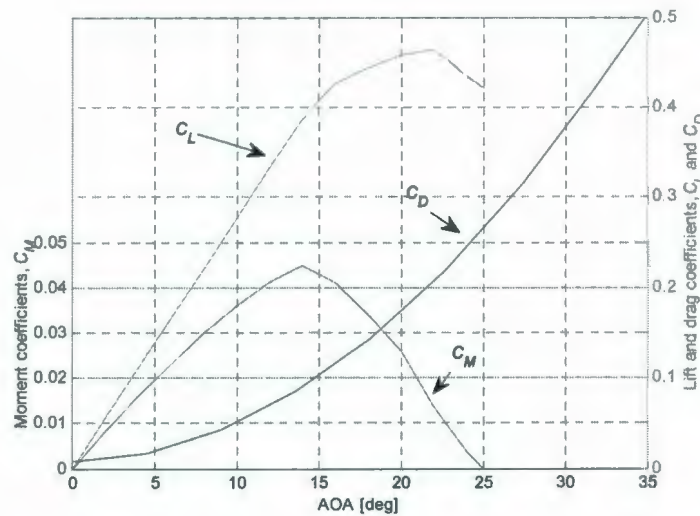
Fig. 5.7 Lift and drag coefficients for the control planes;

NACA 0025 airfoils corrected for $AR = 1$

The pitching moment about an axis through the quarter-chord point which is the center of pressure of the plane, that is at $c/4$ distance from the leading edge, is not influenced by the aspect ratio because the lift and drag forces are assumed to act at that location. Thus,

136

the NACA reported values for the pitching moment coefficient at $c/4$ for AR 6 are used for the *MUN Explorer* planes.

Fig. 5.8 is the view of stern-planes looking from behind while the vehicle has a surge velocity u, sway velocity v, and yaw rate of turn r. Also, the cut A-A in Fig. 5.8 is a top-view of plane number 3 while it is deflected by δ deg, during such a horizontal plane manoeuvre, as shown in Fig. 5.9(a). The resultant lateral velocity of the planes relative to flow which is corrected for the X-angle is as follows[9]:

$$v_{plane} = (v - r \cdot x_{plane}) \sin(\xi) \tag{5-19}$$

Then, the angle of incidence of the flow relative to plane number 3 as illustrated in Fig. 5.9(b) is:

$$\beta' = \tan^{-1}(-v_{plane}/u) \tag{5-20}$$

Then, the actual AOA for planes number 3 and 6 is as follows:

$$\alpha_{3,6} = \delta_{3,6} + \beta' \tag{5-21}$$

where δ is the controlled deflection angle of the plane relative to the hull which can reach a maximum of 25 degrees for the *MUN Explorer* AUV. Plane number 6 is the same as plane number 3 with the lower face facing the flow. For plane number 4 the angle of incidence of the flow relative to the plane is the same as (5-20) but is subtracted from the deflection angle of the plane, because in a positive starboard turn as illustrated in Fig. 5.8, the upper face of plane number 4 faces the flow. Therefore, the actual AOA of plane number 4 is:

$$\alpha_{4,5} = \delta_{4,5} - \beta' \tag{5-22}$$

---

[9] All four stern planes were assumed at the same longitudinal distance in the vehicle coordinate system.

Plane number 5 is the same as number 4 with the upper face facing the flow during a positive turn. Drag, lift and moment coefficients are derived for the actual AOA that are calculated in (5-21) and (5-22).
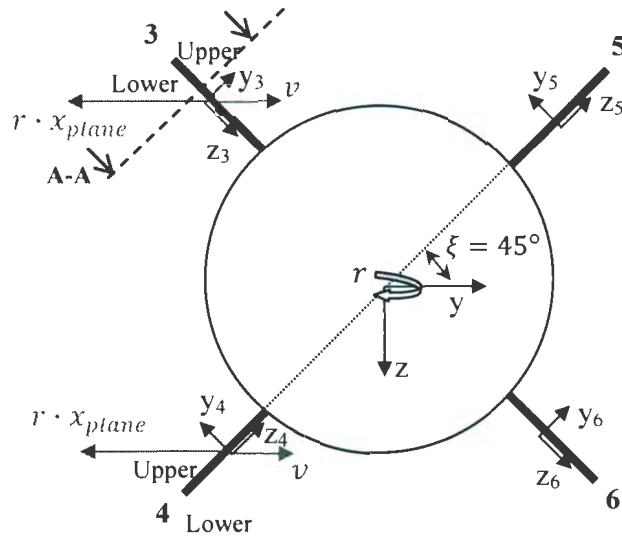
Fig. 5.8 View of the tail planes looking from behind: Illustration of the flow velocity relative to the stern-planes during a horizontal-plane manoeuvre
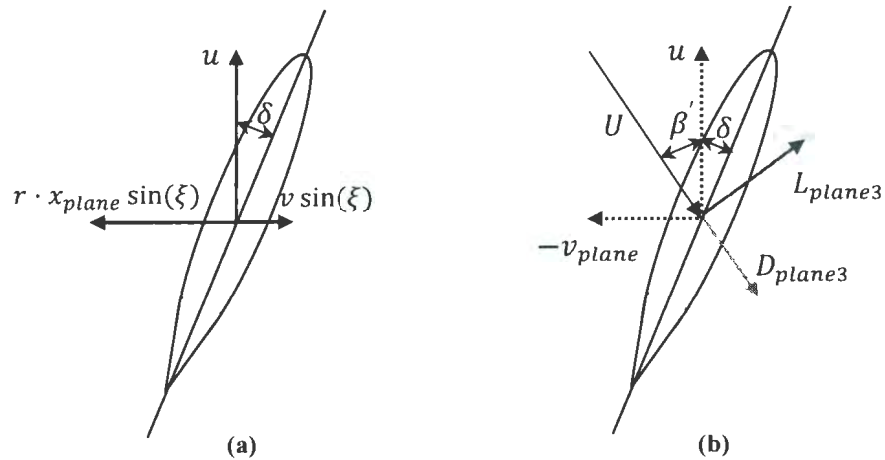
Fig. 5.9 Top view of plane 3 during a horizontal-plane manoeuvre: (a) the perpendicular cut A-A in Fig 5.8, (b) the resultant inflow velocity and drift angle

138

Note that the resultant lateral velocity was projected along the plane's perpendicular in (5-19). If the planes were in upright position: $\xi = 90$ deg for rudders and $\xi = 0$ deg for horizontal planes, then for the rudders $\sin(\xi)$ would reduce to unity and for the horizontal planes it would diminish. Also, note that the projected component of the resultant lateral velocity along the plane's parallel, which for $\xi = 45$ deg has equal magnitude as of (5-19), may introduce additional complexity into the hydrodynamic performance of the plane, however that effect is neglected here.

Therefore, in summary the lift and drag forces on each stern plane are as follow:

$$L = \frac{1}{2}\rho U^2 A_p C_L, \text{ and } D = \frac{1}{2}\rho U^2 A_p C_D \qquad (5\text{-}23)$$

where A_p is the planform area of each plane equal to chord-length, c, times span, b. The lift and drag coefficients in (5-23) are read from Fig. 5.7 at an actual angle of attack that is calculated by either (5-21) or (5-22) for planes number 3 to 6.

As shown in Fig. 5.9(b), the drag and lift forces should be projected along the x and y axes of the vehicle coordinate system to conclude the net axial force and sway force that are produced by the control planes. Thus, the sway force that is produced by plane number 3, along its y$_3$ axis that was shown in Fig. 5.8, is:

$$F_{y,plane3} = L_{plane3} \cos(\beta') + D_{plane3} \sin(\beta'), \qquad (5\text{-}24)$$

Then the net sway force of the four stern planes is calculated using the sway force of each plane similar to (5-24) and correcting them for the X-angle as follows:

$$F_{y,planes} = \left(F_{y,plane3} - F_{y,plane4} - F_{y,plane5} + F_{y,plane6}\right) \cdot \sin(\xi)$$

$$= \left[\left(L_{plane3} - L_{plane4} - L_{plane5} + L_{plane6}\right) \cdot \cos(\beta')\right.$$

$$+ \left.\left(D_{plane3} - D_{plane4} - D_{plane5} + D_{plane6}\right) \cdot \sin(\beta')\right] \cdot \sin(\xi)$$

$$= \frac{1}{2}\rho U^2 A_p \left[\left(C_{L,3} - C_{L,4} - C_{L,5} + C_{L,3}\right) \cdot \cos(\beta') + \left(C_{D,3} - C_{D,4} - C_{D,5} + C_{D,3}\right) \cdot\right.$$

$$\left.\sin(\beta')\right] \cdot \sin(\xi) \qquad\qquad (5\text{-}25)$$

Note that in (5-25), according to Fig. 5.8, the sway force of planes 3 and 6 are acting in the positive direction of the y-axis of the vehicle coordinate system, while the sway force of planes 4 and 5 are acting negative thus have a minus sign. The lift and drag coefficients for each plane depend on the actual AOA of that plane which itself is a variable of the vehicle velocity vector as was written in (5-19). During a simulation run, e.g. a turning manoeuvre, at the time instant t knowing the velocity vector of the vehicle, equation (5-25) is used to calculate for the net sway force of the stern-planes which is then added up with other forces that act in the sway direction, and the resultant force produces the sway acceleration vector at the next time instant. The sway acceleration vector is then integrated to produce the sway velocity vector from where the loop continues.

To turn the vehicle in positive yaw direction, to create a starboard turn, the vehicle tail should move in the negative y direction (to the portside), thus the resultant sway force in (5-25) should be negative. For that purpose, planes number 3 and 6 should have a negative deflection angle (LE down), and planes 4 and 5 should have a positive deflection angle (LE up). The yawing moment equals the net sway force that is produced

by the stern planes times the longitudinal distance of the centre of pressure of the stern planes from the body-fixed origin at the vehicle's mid-length, which was estimated about: $x_{plane} \approx 1.36$ m; so it follows:

$$M_{z,planes \text{ (due to the net sway force of the planes)}} = F_{y,planes} \cdot x_{plane} \qquad (5\text{-}26)$$

On the other hand, the pitching moment about an axis through the quarter-chord point, which is the center of pressure of the plane, is a vector acting in the coordinate system of each stern-plane in Fig. 5.8 along z_i-axis for the plane numbers: $i= 3$ to 6. Therefore, the pitching moment on the stern planes should be decomposed along y and z axes of the vehicle's coordinate system to produce respectively the pitching and yawing moments about the quarter-chord axes of the planes that act on the vehicle, as follows:

$$M_{y,planes \text{ (due to pitching moment on the stern planes)}} = \left(M_{z,plane3} + M_{z,plane4} + M_{z,plane5} + \right.$$
$$\left. M_{z,plane6} \right) \cdot \cos(\xi) \qquad (5\text{-}27)$$

$$M_{z,planes \text{ (due to pitching moment on the stern planes)}} = \left(M_{z,plane3} - M_{z,plane4} - M_{z,plane5} + \right.$$
$$\left. M_{z,plane6} \right) \cdot \sin(\xi) \qquad (5\text{-}28)$$

The yawing moment in (5-26) should be added to the yawing moment in (5-28) to conclude the total yawing moment that is produced by the stern planes. On the other hand, a net non-zero pitching moment on the vehicle in this simulation is undesired since the bow planes were not modeled as active actuators.

5.4.2 Propulsion

The AUV is propelled by a $d_p = 0.65$ m diameter high efficiency two-bladed propeller driven by a Hathaway 48 Volt DC brushless motor and can achieve a maximum speed of 2.5 m/s. The propeller is blended into the tail cone to maintain attached flow for better

hydrodynamics [Issac et al. 2007a]. The thrust coefficient K_T for the two-bladed propeller of *MUN Explorer* is unknown. However, straight-ahead trials were performed with the vehicle to attain the curve of the vehicle speed versus the propeller rpm [Issac et al., 2007b][10], as reproduced in Fig. 5.10 and Table 5.1. These data points were fitted with the following relation:

$$n = 109 * U \tag{5-29}$$

where U is the forward speed of the vehicle and n is the propeller speed of revolution in rpm. On the other hand, in a straight-ahead run, the propeller should produce a thrust approximately equal to the resistance force R plus the thrust deduction δT, that is: $T = R + \delta T$. For *MUN Explorer*, propeller diameter to hull diameter ratio is about $d_p/d \approx 1$, also referring to the test results reported for *C-SCOUT* by Thomas et al. [2003] thrust deduction fraction $\delta T/T$ may be estimated about $t^* \approx 0.1$. Also, the resistance force exerted on the vehicle R equals the bare hull resistance as was modeled by equation (5-8), plus the drag force on four stern-planes and two bow-planes all at zero deflection. Summing up the thrust force is as follows:

$$T \approx \left(\frac{1}{1 - t^*}\right)\left[\frac{1}{2}\rho U^2 (A_f C_{D,hull} + b \cdot c \cdot C_{D,planes})\right]$$

$$\text{where: } C_{D,hull} = 1.88\beta^2 + 11.7\, LDR + 38 \text{ and } C_{D,planes} \approx 0.01 \tag{5-30}$$

As mentioned before, it was also observed that the vehicle during a straight-line manoeuvre had non-zero pitch angles. To take that effect into account a pitch angle of about 5 deg is assumed for the vehicle and the control planes, and the drag coefficients in

---

[10] Those straight-ahead runs were performed in two phases: accelerating and decelerating as shown in Table 5.1. Thus, a total of eight data points for the vehicle speed versus propeller rpm were recorded. The average of the two phases is used as a single set of data in Fig. 5.10.

(5-30) were adjusted according to that[11]. Then substituting the forward speed from (5-29) into (5-30) and using the drag coefficients of the hull and control planes, provides an estimate of the propeller thrust versus its rpm which is the solid curve plotted in Fig. 5.11. Although, the test runs were performed over a range of 109 to 287 rpm which corresponded to forward speeds of 1 to 2.5 m/s, the curves in Figs. 5.10 and 5.11 were extrapolated to the range 10 to 287 rpm assuming that the propeller has a similar performance.

Table 5.1 *MUN Explorer*'s **forward speed versus propeller rpm**

during straight line tests [Issac et al., 2007b]

Acceleration phase	n [rpm]	109	155.8	210.8	263.2
	U [m/s]	1	1.5	2	2.5
deceleration phase	n [rpm]	287	223.9	173.4	125.5
	U [m/s]	2.5	2	1.5	1
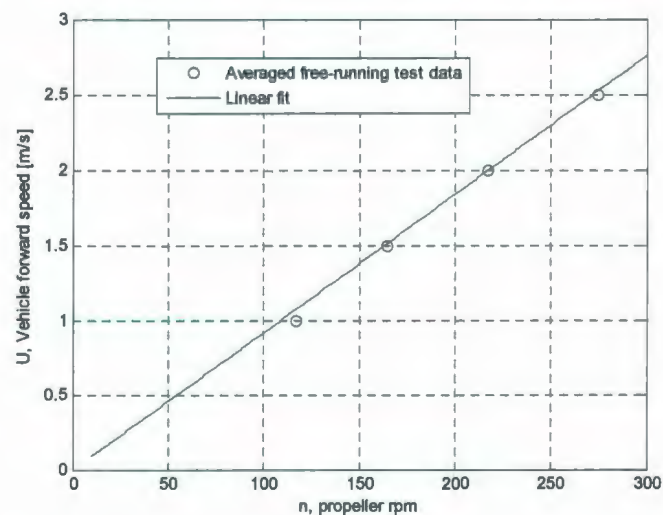
Fig. 5.10 *MUN Explorer*'s **forward speed vs. propeller rpm**

---

[11] Note that β in equation (5-30) is the yaw angle of the vehicle in degrees as was modelled using the static yaw test results. However, it is used to estimate the effect of pitch angle, although the *MUN Explorer* AUV has axisymmetric appendages in pitch direction.

143

In another approach, the propeller thrust coefficient can be estimated using the Wageningen propeller series [Kuiper 1992]. The resulting curve is shown as dashed curve in Fig. 5.11 which is obtained as is explained next.
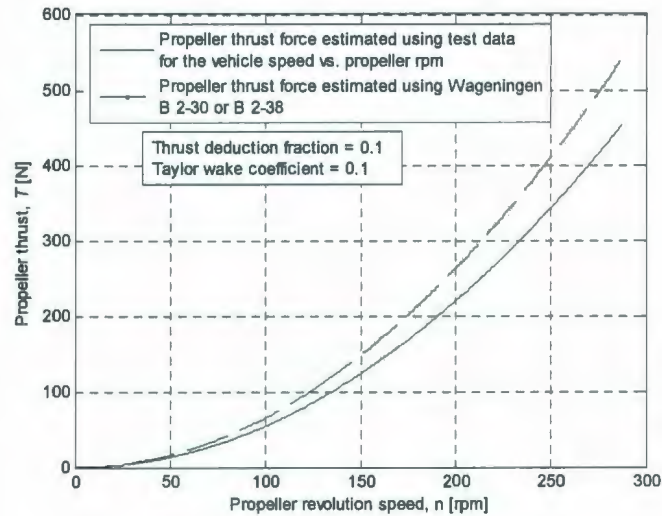
Fig. 5.11 Thrust vs. rpm for *MUN Explorer*'s propeller

Propeller pitch angle at 0.7 radius was measured by the author to be about 25 degrees which suggests a pitch P of about 0.69 m that is a propeller pitch-to-diameter ratio of: $0.69/0.65 = 1.06$. The advance ratio is defined as:

$$J = V_a/(N \cdot d_p), \tag{5-31}$$

where N is the propeller speed in revolutions-per-second and V_a is the flow speed through the propeller disc which is related to the vehicle forward speed by the following relation:

$$V_a = (1 - w)U \tag{5-32}$$

where w is the wake coefficient which is assumed to be about 0.1 here [Allmendinger 1990]. If the vehicle speed in (5-32) is substituted from (5-29), then the advance ratio in (5-31) – propeller speed in revolution per second – is calculated to be about 0.72. On the

144

other hand, for a pitch-to-diameter ratio of $P/d_p \approx 1$ as was calculated above, thrust coefficient of B 2-30, that is a two-blades propeller with a blade area ratio (BAR) of 0.3, and thrust coefficient of B 2-38 were reproduced as are shown in Fig. 5.12 [Kuiper 1992]. For an advance ratio of 0.72 either B 2-30 or B 2-38 has a thrust coefficient of 0.13.
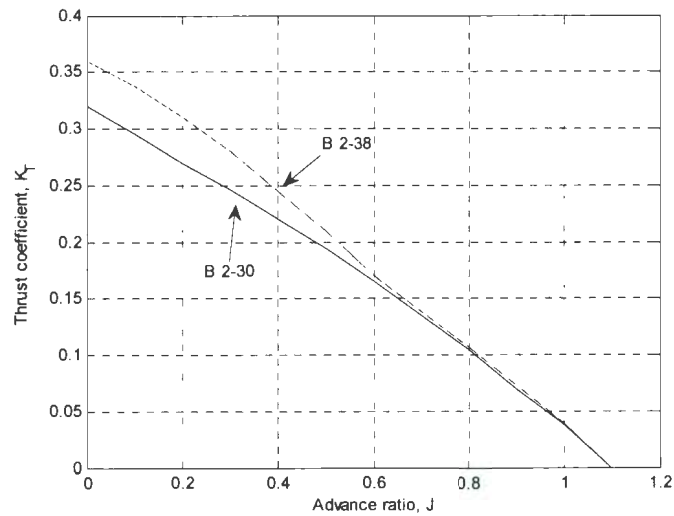
Fig. 5.12 Thrust coefficient for B 2-30 and B 2-38 for $P/d_p \approx 1$ reproduced from [Kuiper 1992]

Then the propeller thrust is calculated using:

$$T = \rho K_T \cdot N^2 \cdot d_p^4 \tag{5-33}$$

Equation (5-33), using the estimated value for the thrust coefficient for either B 2-30 or B 2-38, results in the curve of thrust force versus propeller speed as was shown by dashed curve in Fig. 5.11; the two curves are in good agreement, however, the curve which was obtained by the test data was used as the thrust force model in this simulation.

5.5 Vehicle mass and the added mass of water

5.5.1 The vehicle mass and moment of inertia

The dry mass of the *MUN Explorer* AUV was reported by Issac et al. [2007a] as 630 kg, which is the same amount as reported by the manufacturer and is the value used in this simulation. At the recovery stage of a sea-trial, an immediate reading of the weight scale indicated a total mass of about 1400 kg; a later calculation concluded a flooded mass of 1445 kg that is about 1445− 630 = 815 kg of floodwater mass.

The centre of gravity (*CG*) for *MUN Explorer* in the dry state is at 2.44 m from the front end and about 0.04 m below the centerline, but positioned on the centerline in the lateral plane. Thus, the *CG* of the dry vehicle is about 0.2 m rearwards of the vehicle mid-length, since most of the internal structure is placed within the pressure hull which is located in the rear half of the vehicle. The moment of inertia for *MUN Explorer* about a vertical axis through its *CG* was estimated by the author to be about $I_{CG} = 2454$ [kg.m^2]. However, the hydrodynamic forces which were modeled with the empirical formulae in this report used the test results that measured the yaw moment about a vertical axis located at the vehicle centre of buoyancy (*CB*) which can be assumed almost at the vehicle mid-length (see Table 2.2 for a comparison of the vehicle mid-length and longitudinal location of *CB* of the bare hull configurations). Hence, the moment of inertia for *MUN Explorer* should be shifted to the vertical axis through the origin of the body-fixed coordinate system at the vehicle mid-length, which results in a final value for the moment of inertia of the dry vehicle of 2475 [kg.m^2]. To this amount, the moment of inertia of the floodwater should be added. A rough estimate is to assume that the 815 kg of floodwater mass is evenly

distributed within an ellipsoid of the same length and diameter as the *MUN Explorer*[12], which results in a moment of inertia of 844 [kg.m^2] about the centre of volume of the ellipsoid, which is close enough to the vehicle mid-length. Thus, the moment of inertia of *MUN Explorer* in the flooded state to be used in this simulation code is estimated as $I_z = 2475 + 844 = 3319$ [kg.m^2]. Also the centre of gravity of the flooded vehicle is estimated as if the *CG* of the 815 kg floodwater is at the body-fixed origin (vehicle mid-length on the longitudinal axis), which results in a flooded *CG* 2.33 m from the bow end and 0.02 m below the centerline that is: $x_G = 2.25 - 2.33 = -0.08$ aft of mid-length, with $y_G = 0$ and $z_G = 0.02$ m below the longitudinal centerline of the hull.

5.5.2 Added mass and added moment of inertia

Assuming potential flow for an ellipsoid with a length of l and maximum diameter d, the first three significant terms: translation in surge and sway directions and rotation in yaw direction, for the added mass effect were studied by Lamb and the curves as are reproduced in Fig. 5.13 were proposed [Lamb, 1932]. The axial and lateral coefficients, K_1 and K_2, in Fig. 5.13 are respectively the ratio of the added mass of the ellipsoid in axial and lateral directions to its displaced mass, and the rotational coefficient, K', is the ratio of the added moment of inertia of the ellipsoid to the moment of inertia of its displaced volume of water about an axis through its mid-length.

For the forward acceleration state, the added mass according to the K_1 curve in Fig. 5.13, for the *MUN Explorer* AUV with *LDR* 6.5 is about 0.05. However, additional amount of

---

[12] Note that the enclosed volume of such an ellipsoid is smaller than the enclosed volume of *MUN Explorer*. Also note that assuming an even distribution of 815 kg floodwater within such an ellipsoid means that a density of about 726 [kg/m^3] is assumed for the water.

added mass is expected since the vehicle compared to an ellipsoid is more blunt, also it includes appendages. Thus the axial added mass was assumed to be one-tenth of the vehicle's flooded mass, i.e., one-tenth of 1445 kg. The lateral (sway) added mass and rotational (yaw) added moment of inertia coefficients for the ellipsoid of *LDR* 6.5 are respectively about: $K_2 = 0.92$ and $K' = 0.77$, where the lateral added mass is K_2 times the mass of the ellipsoid displaced volume and the added moment of inertia is K' times the moment of inertia of the displaced volume [Lamb 1932].
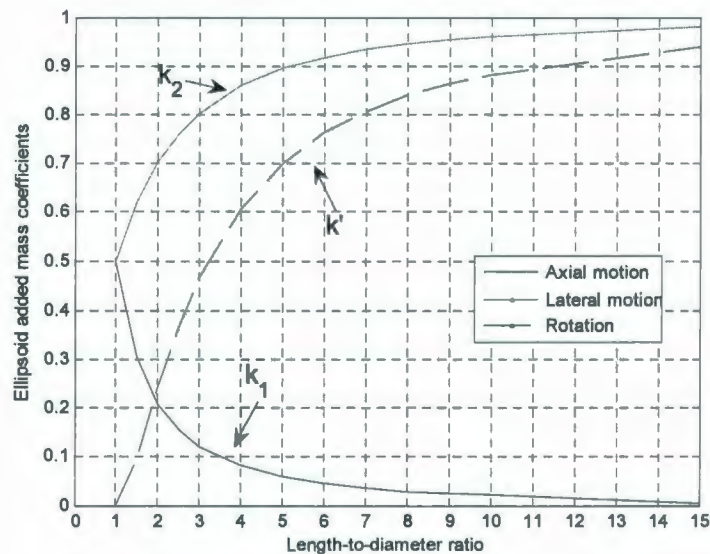
Fig. 5.13 Added mass and added moment of inertia for an ellipsoid [Lamb, 1932]

Resulting values for an ellipsoid equivalent to the bare hull of *MUN Explorer* are about 1057 kg for the added mass and 1191 [kg.m^2] for the added moment of inertia, derived for a sea-water density of 1025 [kg/m^3]. To estimate the added mass effect for the control planes it was noted that: the added mass magnitude of a rectangular plate of span b and chord length c accelerating normal to its face is:

$$\text{Lateral added mass of rectangle} = K_r \, \pi \rho b (c^2/4) \qquad (5\text{-}34)$$

148

where the coefficient K_r varies from 0.478 to one for span-to-chord ratios of one to infinity respectively [Brennen 1982]. Each of the four tail control planes of *MUN Explorer* are rectangles of equal span and chord length 35 by 35 cm (the root-base is ignored), for which the span-to-chord ratio is one and thus the added mass coefficient K_r is 0.478. Substituting this into (5-34) results in an added mass value of about 17.3 kg for each plane for acceleration normal to planform. Then, according to the orientation of the tail planes, if the deflection angle of the planes during a manoeuvre is ignored, each plane is accelerating 17.3 kg of surrounding water times the sine of the X-angle, $\xi = 45$ deg, in the lateral direction. Therefore, in a constant depth manoeuvre, the total lateral added mass due to the four tail planes is predicted as: $4 * 17.3 * \sin(\pi/4) = 49$ kg. Consequently, the added moment of inertia due to these stern planes is estimated as that amount of mass with the moment arm x_{planes} of about 1.36 m, i.e. $49 * 1.36^2 = 90$ [kg.m^2] of added moment of inertia about the z-axis through the origin of the body-fixed coordinate system.

5.6 Simulation results

The simulation code was developed and its convergence was verified by performing straight-ahead manoeuvres. The *MUN Explorer* AUV with an input propeller speed of 120 rpm starts to speed up under a thrust force of about 71 N and in about three minutes attains a steady forward speed of about 1.03 m/s. Changing the simulation time step slightly changes the response but it converges to about the same speed. For a larger simulation time-step, due to integration error, the distance travelled by the vehicle to reach a steady forward speed is shorter: e.g. at 120 rpm, simulation time-steps: $\delta t =$

0.01, 1 and 10 s respectively result in: 144.7, 143.2 and 130.8 m distance travelled until the vehicle reaches a steady speed of 1.03 m/s for all those time-steps. Figs. 5.14 and 5.15 respectively show the time-history of surge velocity and surge acceleration during a straight-line run for the above time-steps. All turning manoeuvres were simulated with a time-step of 0.01 s.
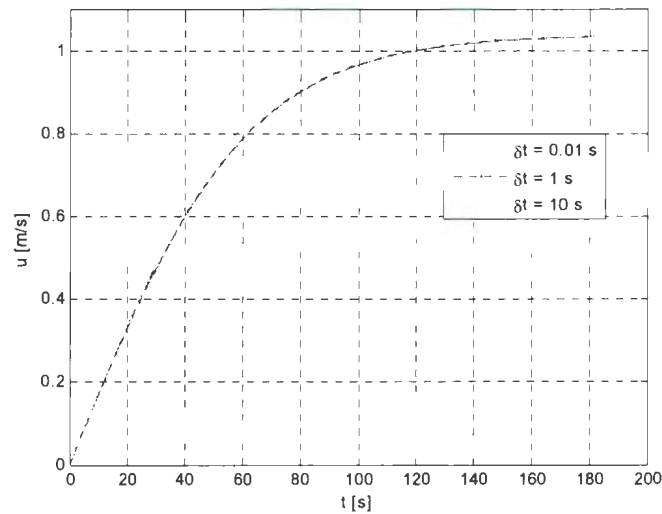
Fig. 5.14 Surge speed for the *MUN Explorer* AUV during a straight-line run at 120 rpm
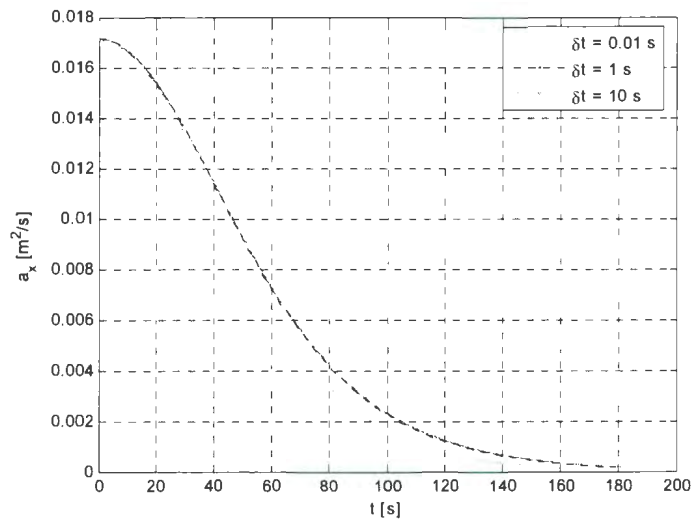
Fig. 5.15 Surge acceleration for the *MUN Explorer* AUV during a straight-line run at 120 rpm

5.6.1 Turning manoeuvres: calibrating the simulation code with the free-running test results

In August 2006, at Holyrood Harbour situated about 45 km south-west of St. John's, Newfoundland, a set of trials were performed with the *MUN Explorer* AUV, some of which were reported by Issac et al. [2007a] and Issac et al. [2007b]. Ten runs of turning circle manoeuvres with an approach speed of 1 m/s at a constant depth of 3 metres that were reported by Issac et al. [2007b] as are reproduced in Table 5.2 were used to evaluate and then calibrate the response of the simulation code. Note that to perform the turning manoeuvres with the AUV, the inputs to the software are the approach speed, the radius of turn and the centre-point around which it turns. Then, the vehicle path, its rate of turn, propeller rpm, forward speed and the controlled deflection of the six control planes are some of the recorded signals during each run. Each run is made of a straight-ahead phase until the vehicle attains the desired approach speed and then the control planes are deflected so as to turn the vehicle with the desired radius around the specified centre-point. The resulting radius of turn and its centre, even in calm water, may have minor errors relative to the commanded values.

The lower portion of Table 5.2 shows the reported results for the radius of turn, turning rate and forward speed for ten turning manoeuvre trials, indicated by "T" in parentheses, reproduced from [Issac et al., 2007b][13]. Indicated by "S" in parentheses are the respective simulation results. Note that for the simulation code, the tail plane deflection angles were set to the reported average value for the recorded signal of each plane during the trial as

---

[13] Rate of turn in [Issac et al. 2007b] was mistakenly reported as [rad/s]; the values were in [deg/s].

shown in Table 5.2: e.g. the first simulation run was performed with input deflections for the tail planes number 3 to 6 equal to −10.32, −0.1, −1.82, and −12.51 deg[14]. Note that for the approach speed of 1 m/s, the data from sea-trials as were shown in Table 5.2 are equivalent to an average deflection angle for the four planes calculated as: deflection (δ) of plane number 3 plus that of number 6 minus the δ of number 4 and 5; e.g. the average deflection angle for the first run is: $\delta = (-10.32 - 12.51 - (-0.1) - (-1.82))/4 = -5.23$ deg, which has about the same simulation result as a starboard turn of all four planes at 5.23 deg. This average δ is shown as the average plane angles in Table 5.2.

The simulation code operates the AUV straight-ahead under the thrust force at a propeller rpm of 120 until a steady forward speed of about 1 m/s is attained and the surge acceleration has been damped to zero, then at a rate of 1 deg/s the stern-planes are deflected up to the commanded values. The simulation time-step was 0.01 sec, therefore the deflection angles of the four control planes were changed by 0.01 deg during each computational loop, which means an effective rate of change of 1 deg/s. Relative errors for the radius of turn, if the test results are assumed to be the correct value, are defined as follows:

$$e_R = 100 * (R(S) - R(T))/R(T) \qquad (5\text{-}35)$$

Relative error between the test and simulation results in the radius of turn and the rate of turn for these ten runs are shown in Table 5.2 respectively by e_R and e_r which vary between 10 to 35 percent of error.

---

[14] The planes' deflection angle (δ) have different signs in [Issac et al., 2007b]; here all the stern planes have positive δ when the leading edge turns upward and thus provides upward lift force (also see Fig. 5.8).

Table 5.2 Simulation results for the turning manoeuvres at a constant depth with an approach speed of 1 m/s compared to trial results; T: tests, S: simulation

Run	Stern plane deflection angles [deg]				Average of stern-plane deflection angles [deg]	Bow-plane deflection angles [deg]	
	δ_3	δ_4	δ_5	δ_6	δ	δ_1	δ_2
1	-10.32	-0.1	-1.82	-12.51	-5.23	4.17	4.17
2	-10.54	0.01	-1.86	-12.52	-5.30	4.71	4.71
3	-10.19	-0.34	-2.38	-12.18	-4.91	5.23	5.29
4	-10.32	-0.39	-2.08	-12.26	-5.03	5.04	5.06
5	-10.17	-0.89	-2.43	-11.82	-4.67	5.12	5.11
6	-10.1	-0.97	-2.7	-11.54	-4.49	5.36	5.36
7	-9.87	-1.23	-2.77	-11.6	-4.37	5.28	5.28
8	-9.76	-1.6	-2.83	-11.31	-4.16	4.94	4.96
9	-9.66	-2.79	-3.53	-10.51	-3.46	5.42	5.51
10	-9.41	-2.77	-3.7	-10.34	-3.32	5.82	5.83

Run	$R(T)$	$R(S)$	$r(T)$	$r(S)$	$e_R\%$	$e_r\%$
1	22.51	15.4	2.560	2.070	-31.6	-19.1
2	23.8	15.3	2.413	2.090	-35.6	-13.4
3	25.02	16.9	2.304	1.960	-32.5	-14.9
4	25.09	16.4	2.296	2.000	-34.6	-12.9
5	26.58	18.2	2.180	1.880	-31.4	-13.8
6	27.97	19.3	2.053	1.82	-31.1	-11.3
7	28.11	20.0	2.070	1.78	-28.9	-14.0
8	29.65	21.4	1.954	1.71	-27.8	-12.5
9	33.44	27.0	1.695	1.45	-19.4	-14.5
10	37.54	28.3	1.531	1.41	-24.5	-7.9

Deflection angle of the two bow-planes as was reported by Issac et al. [2007b] is also shown in Table 5.2. Positive deflection angle means that the leading edge (LE) of the bow-planes turn upward during these starboard turns, thus they produce a net upward force, while the four stern-planes produce a net downward force. Therefore, the net vertical force is cancelled out, but a net positive pitching moment is produced. To find an explanation for this behaviour the 6 DOF equations of motion should be studied which is beyond the scope of this research. Again note that during a turning manoeuvre the radius

of turn and the centre-point are the inputs to the mission planning software of the actual AUV; but, for the simulation code the inputs are the propeller speed and the deflection angles of the control planes. The comparison of the prediction with the fullscale measurements is given in terms of the diameter of the circle and the vehicle speed around the circle.

Next, the simulation code was calibrated according to the test results so that the relative errors in the radius of turn and rate of turn were reduced. The simulation code results in smaller radius and also slower rate of turn. The reason is that: during the sea-trials, *MUN Explorer* was set on the autopilot thus the propeller speed was increased in order to keep the vehicle speed constant at 1 m/s. However, the simulation code operates at a constant propeller speed (120 rpm to reach an approach speed of 1.03 m/s), therefore there is a speed reduction within the steady phase of the turn, which means a slower rate of turn even though the radius of turn is smaller than the test data.

In section 5.1 the longitudinal location of CG was approximated: $x_G = -0.08$ m that is 8 cm rearward of the vehicle mid-length. For run numbers: 1, 6 and 10 in Table 5.2, where the average deflection angle of the stern-planes were respectively: 5.23, 4.49 and 3.32 deg, simulation was performed by changing the longitudinal location of the *CG* from minus 0.12 m to plus 0.08 m at a step of 0.04 m, that is from 12 cm aft of mid-length to 8 cm forward of mid-length. Variation of the relative error in the radius of turn as defined in (5-35) is plotted in Fig. 5.16 versus the longitudinal location of the *CG* for run numbers 1, 6 and 10. Note that the other runs in Table 5.2 have average deflection angles close to either run numbers 1, 6 or 10; therefore, these three runs represent the others too.
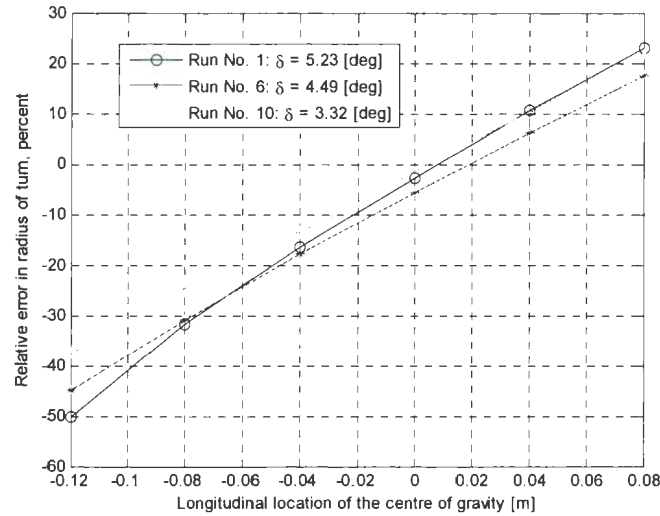
Fig. 5.16 Relative error in the radius of turns vs. longitudinal location of the *CG* of the vehicle

The trend is almost linear and if the centre of gravity for the simulation model coincides with the origin of the local coordinate system, as is seen in Fig 5.16, then the relative error in the radius of turn is less than 5 percent. Thus the model can be calibrated by moving the centre of gravity about 8 cm forward. For the reason explained above (no speed reduction during the sea-trials), rate of turn was not a good criterion to use for calibrating the code; the best correlation was obtained by using the radius of turn. The results presented after this were obtained by the calibrated simulation code. Also see Appendix A at the end of thesis for an uncertainty study of the simulation code.

5.6.2 Turning manoeuvres: radius of turn, turning rate, drift angle and speed reduction versus the stern-planes' deflection angle and the approach speed

The simulation code is a useful tool to study the variation of the indicators of turning manoeuvres such as: radius and rate of turn, drift angle and speed reduction versus the input factors: stern-planes' deflection angle and the approach speed. In the following simulations, the average plane angles were used for all four stern-planes. That is: planes

number 3 and 6 use $-\delta$ and planes 4 and 5 use δ to perform a starboard turn. Table 5.3 shows the resulting radius of turn, rate of turn, drift angle and surge velocity of the *MUN Explorer* AUV after it maintains a steady turn at propeller speeds of: 120, 174, 232 and 290 rpm which produce approach speeds of respectively: 1, 1.5, 2 and 2.5 m/s.

Table 5.3 Simulated radius of turn, turning rate, drift angle and surge velocity during a steady turning circle manoeuvre with *MUN Explorer* in constant depth vs. average deflection angle of the stern planes

120 rpm: 1.03 m/s						
δ [deg]	R [m]	r [deg/s]	Drift β [deg]	u [m/s]	U/R [deg/s]	$U_{turn}/U_{approach}$
1	131.4	0.44	1.3	1.02	0.44	0.99
2	64.8	0.88	2.6	1.00	0.88	0.97
3	42.2	1.23	4.0	0.90	1.23	0.88
4	30.6	1.56	5.3	0.83	1.56	0.81
5	23.6	1.85	6.6	0.76	1.85	0.74
6	18.8	2.10	8.0	0.68	2.10	0.67
7	15.1	2.31	9.4	0.60	2.31	0.59
8	12.6	2.58	10.8	0.56	2.58	0.55
9	10.54	2.74	12.2	0.49	2.74	0.49
10	8.93	2.98	13.5	0.45	2.98	0.45
11	7.83	3.09	14.9	0.41	3.09	0.41
12	6.64	3.38	16.1	0.38	3.38	0.38
13	5.83	3.54	17.3	0.34	3.54	0.35

174 rpm: 1.5 m/s						
δ [deg]	R [m]	r [deg/s]	Drift β [deg]	u [m/s]	U/R [deg/s]	$U_{turn}/U_{approach}$
1	131.4	0.65	1.3	1.48	0.65	0.99
2	64.8	1.29	2.6	1.45	1.29	0.97
3	42.2	1.79	4.0	1.32	1.79	0.88
4	30.6	2.28	5.3	1.21	2.28	0.81
5	23.6	2.69	6.6	1.10	2.69	0.74
6	18.8	3.06	8.0	1.00	3.06	0.67
7	15.1	3.36	9.4	0.87	3.36	0.59
8	12.6	3.75	10.8	0.81	3.75	0.55
9	10.5	4.00	12.2	0.72	4.00	0.49
10	8.9	4.33	13.5	0.66	4.33	0.45
11	7.8	4.50	14.9	0.59	4.50	0.41
12	6.6	4.92	16.1	0.55	4.92	0.38
13	5.8	5.16	17.3	0.50	5.16	0.35

14	5.2	5.47	18.5	0.47	5.47	0.33

232 rpm: 2 m/s

δ [deg]	R [m]	r [deg/s]	Drift β [deg]	u [m/s]	U/R [deg/s]	$U_{turn}/U_{approach}$
1	131.4	0.86	1.3	1.98	0.86	0.99
2	64.8	1.72	2.6	1.94	1.72	0.97
3	42.2	2.39	4.0	1.76	2.39	0.88
4	30.6	3.04	5.3	1.61	3.04	0.81
5	23.6	3.59	6.6	1.47	3.59	0.74
6	18.8	4.08	8.0	1.33	4.08	0.67
7	15.1	4.48	9.4	1.16	4.48	0.59
8	12.6	5.00	10.8	1.08	5.00	0.55
9	10.5	5.33	12.2	0.96	5.33	0.49
10	8.9	5.78	13.5	0.88	5.78	0.45
11	7.8	6.00	14.9	0.79	6.00	0.41
12	6.6	6.56	16.1	0.73	6.56	0.38
13	5.8	6.88	17.3	0.67	6.88	0.35
14	5.2	7.29	18.5	0.63	7.29	0.33
15	4.7	7.63	19.5	0.58	7.63	0.31

290 rpm: 2.5 m/s

δ [deg]	R [m]	r [deg/s]	Drift β [deg]	u [m/s]	U/R [deg/s]	$U_{turn}/U_{approach}$
1	131.4	1.08	1.3	2.47	1.08	0.99
1.5	87.2	1.59	2.0	2.42	1.59	0.97
2	64.8	2.09	2.6	2.36	2.09	0.94
2.5	51.3	2.55	3.3	2.28	2.55	0.91
3	42.2	2.99	4.0	2.20	2.99	0.88
4	30.6	3.78	5.3	2.02	3.80	0.81
5	23.6	4.47	6.6	1.83	4.47	0.74
6	18.8	5.08	8.0	1.65	5.08	0.67
6.5	16.9	5.37	8.7	1.56	5.35	0.63
7	15.1	5.65	9.4	1.48	5.69	0.60
8	12.6	6.18	10.8	1.34	6.20	0.55
8.5	11.5	6.44	11.5	1.27	6.46	0.52
9	10.5	6.70	12.2	1.20	6.67	0.49
10	8.9	7.2	13.5	1.09	7.20	0.45
11	7.8	7.69	14.9	0.99	7.49	0.41
12	6.6	8.17	16.1	0.91	8.17	0.38
13	5.8	8.63	17.3	0.84	8.65	0.35
14	5.2	9.08	18.5	0.78	9.09	0.33
15	4.7	9.52	19.5	0.73	9.53	0.31
16	4.2	9.93	20.5	0.69	10.00	0.29

The control planes can deflect up to maximum 25 degrees, however at an approach speed of 1 m/s if the average deflection angle is set above about 13 deg, the actual AOA of the planes relative to flow as calculated by equations (5-20) to (5-22), will exceed 25 degrees. Fig. 5.17 shows the time-history of the predicted AOA of plane number 3 during three turning manoeuvres at 290 rpm with commanded δ of respectively -7, -10 and -15 deg. After the vehicle obtains a steady forward speed, the plane starts to deflect at a rate of 1 deg/s, and the vehicle's tail turns in the positive yaw direction thus produces a negative sway velocity v and a positive $r \cdot x_{plane}$ velocity.
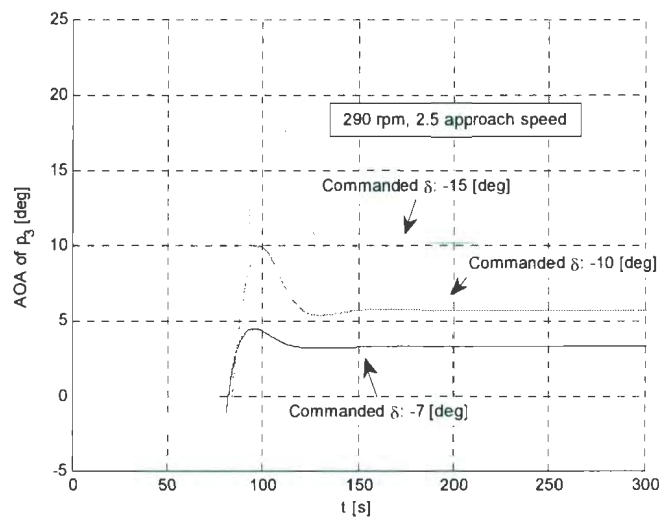
Fig. 5.17) Actual AOA of plane number 3 during turning manoeuvres at 290 rpm

with commanded deflection angles of respectively -7, -10 and -15 deg

As a result, the actual AOA of plane number 3, calculated by equation (5-21) becomes large positive as seen in Fig. 5.17. The actual AOA of plane number 6 has the same diagram as of Fig. 5.17, and the diagram of planes number 4 and 5 are mirrored vertically. According to Fig. 5.17 the actual AOA of the *MUN Explorer*'s planes, at an

approach speed of 2.5 m/s, will exceed 25 degrees for average deflection angles larger than about 16 deg.

Drift angle β, which is defined as the inverse tangent of the ratio of sway velocity to surge velocity of the vehicle with a minus sign, that is:

$$\beta = \tan^{-1}(-v/u), \qquad (5\text{-}36)$$

was shown in the fourth column in Table 5.3. For a starboard turn at 120 rpm, drift angle is in the positive yaw direction which means that the vehicle heads inside the circle. Drift angle increases for larger plane deflection angles. According to the data in Table 5.3, for a turning manoeuvre at 120 rpm with an average δ of about 4 degrees, the magnitude of drift angle is about 5.3 deg which is verified by the reported test results for the runs in Table 5.2 [Issac et al. 2007b, p. 7].

In Table 5.3, additional data-points were shown for the approach speed of 2.5 m/s (at 290 rpm). At higher approach speeds the AOA does not exceed 25 deg until larger deflection angles; i.e. at 2.5 m/s the average deflection angle of the control planes can be as large as 16 degrees which produces a minimum radius of turn about 4.2 m which is slightly smaller than the overall length of the vehicle 4.5 m. According the data in Table 5.3, radius of turn becomes smaller for larger deflection angles, but it does not depend on the approach speed. If the radius of turn is divided by the vehicle length to produce a non-dimensional radius of turn as follows:

$$R' = R/l, \qquad (5\text{-}37)$$

159

where l is the overall length of the vehicle, then the non-dimensional radius of turn versus the average δ of stern-planes for the *MUN Explorer* AUV is shown in Fig. 5.18. Simulation data were fitted with a rational curve as follows:

$$\frac{R}{l} = \frac{28.4}{\delta} \qquad (5\text{-}38)$$

where δ is the average deflection angle of the stern-planes in degrees. The rational curve is a good fit to the simulation data with an R-square value of about 0.99.
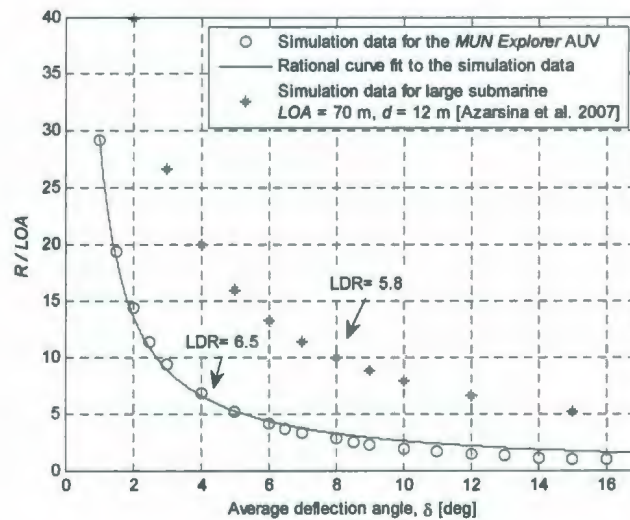
Fig. 5.18 Non-dimensional radius of turn; *MUN Explorer* simulation data compared to the data from the earlier version of the simulation code for a large submarine [Azarsina et al. 2007a]

The trend and also the magnitude of these data that were obtained for the *MUN Explorer* AUV are comparable to the simulation results for a large submarine of length 70 m and diameter 12 m as was presented by Azarsina et al. [2007a, p. 70] which are shown by asterisks in Fig. 5.18. Note that the *MUN Explorer* AUV has stern-planes in an X-

configuration, while the large submarine was modeled with two rudders and two horizontal planes in an upright configuration.

While the propeller rpm was maintained to a constant during the turns, the vehicle surge velocity notably decreased during the turn. The vehicle's total speed is the surge speed divided by the cosine of the drift angle, that is: $U = u/\cos(\beta)$. Rate of turn is equal to: the total speed of the vehicle after it maintains a steady speed during the turn, which is tangent to the vehicle path, divided by the steady radius of turn, that is: $r = U/R$. Rate of turn predicted by the simulation code is equal to the rate of turn that is calculated from the above formula as is shown in the second last column in Table 5.3. The data in Table 5.3 for the rate of turn at different approach speeds is plotted in Fig. 5.19.
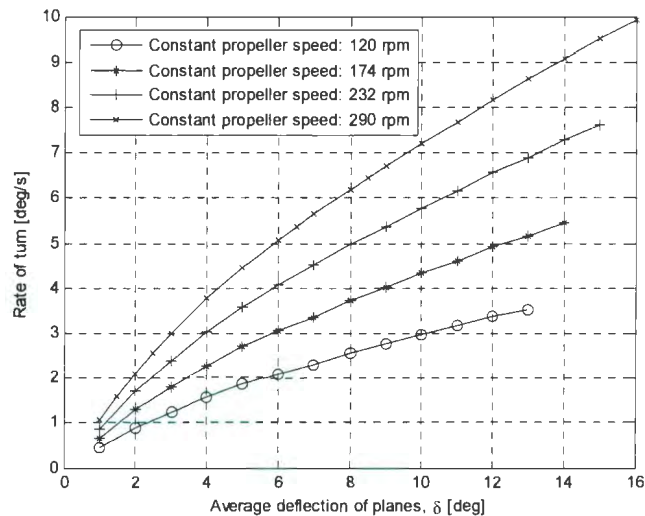
Fig. 5.19 Rate of turn versus stern-planes deflection angle for the *MUN Explorer* AUV

at the approach speeds: 1, 1.5, 2 and 2.5 m/s

Also the ratio of the steady speed of the vehicle during a turn to the approach speed was calculated and shown in the last column in Table 5.3. It is observed that this ratio has the

161

same variation versus the δ of the stern-planes regardless of the magnitude of the approach speed. Variation of the ratio: steady-turning-speed to approach speed versus the ratio: turning diameter to vehicle length based on empirical relationships was studied by Davidson [1944] and Shiba [1960] [PNA 1967, p. 488]. For the simulation data in Table 5.3 for *MUN Explorer* such a plot was produced as shown in Fig. 5.20. The trend is the same as of those empirical curves for ships; however, the simulation data for *MUN Explorer* demonstrate a rather large drop in the vehicle speed compared to the surface ships.
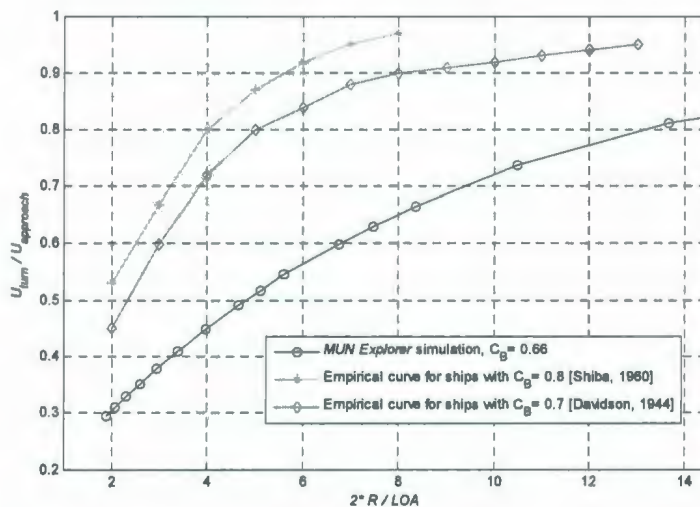
Fig. 5.20 Speed reduction as a function of non-dimensional turning diameter for

the *MUN Explorer* AUV compared with surface ships

Block coefficient for the surface ships is defined as the ratio of the submerged hull volume to the volume of a cube with dimensions: overall length by maximum breadth by ship draft. If block coefficient for an underwater vehicle in a similar way is defined as the ratio of the enclosed hull volume to a cube of volume: overall length times maximum

diameter squared, then for *MUN Explorer* it is: $C_B = 0.66$. Note that the curves by Shiba and Davidson were for ships with block coefficients C_B of respectively 0.8 and 0.7, and it can be concluded that a more slender body experiences a larger speed reduction during a turn. The abscissa in Fig. 5.20 for the *Explorer* data increases up to about $2 * \frac{R}{LOA} = 60$ and reaches an asymptotic trend at higher values, however only a part of the data were shown so as to be in range with the data for the surface ships.

5.6.3 Vehicle path, velocity and acceleration

The X-Y path of the vehicle at a propeller speed of 290 rpm turning with the stern-planes average δ of respectively −3, −6 and −9 deg are shown by black, blue and red curves in Fig. 5.21. Note that a starboard turn requires a negative average deflection angle and the turn is clockwise (Z-axis into the page; into the water depth). Clearly, a larger average δ produces a smaller radius of turn. At an average δ of 3 deg, the black curve, the turn is a circle which is initiated tangent to the X-axis. However, at 6 deg, the blue curve, the vehicle turns around and crosses the X-axis. Then, at an average δ of 9 deg, the red curve, the vehicle first turns in a smaller circle and then maintains a larger steady radius. Time-histories of the vehicle's position along X and Y axes are shown in Figs. 5.22 and 5.23. During the same length of time, with a larger δ, and same approach speed, the vehicle performs a larger number of turns.
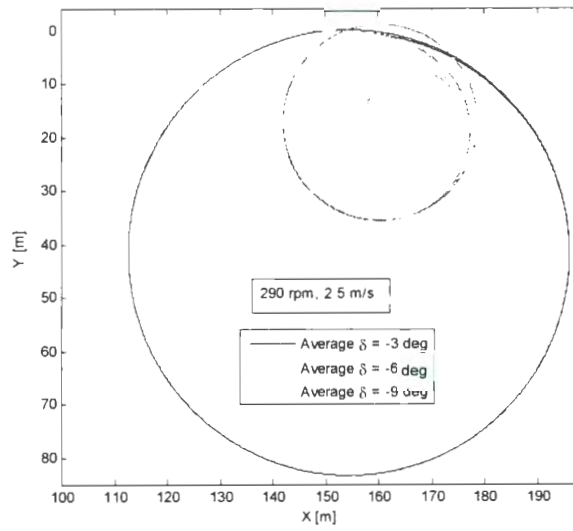
Fig. 5.21 Turning manoeuvres at 290 rpm with average AOAs of: 3, 6

and 9 degrees for the stern-planes
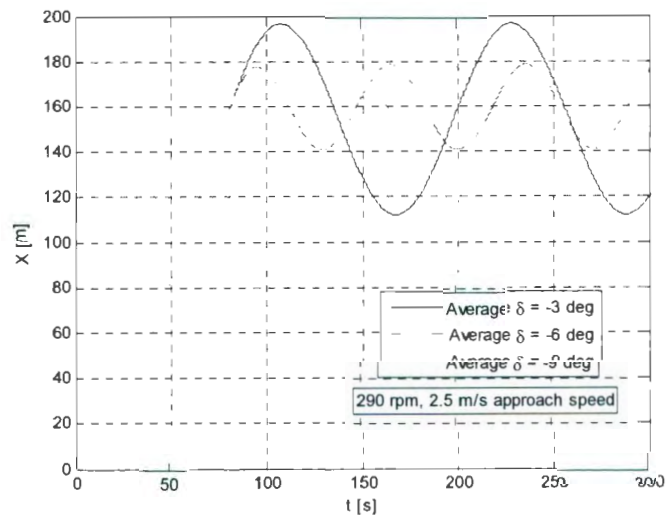
Fig. 5.22 Position of the vehicle along X-axis (global coordinates)

164
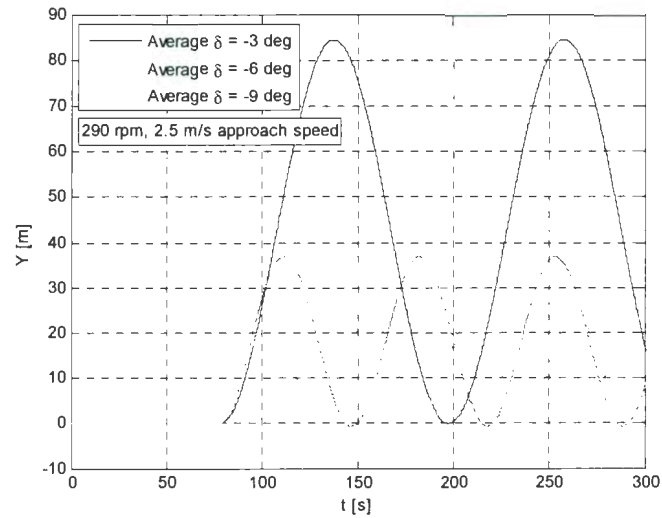
Fig. 5.23 Position of the vehicle along Y-axis (global coordinates)

Time-histories of the vehicle's surge and sway velocities are shown in Figs. 5.24 and 5.25. Yaw rate of turn is shown in Fig. 5.26. With increasing δ, nonlinear patterns occur. While the vehicle performs a starboard turn, it attains a steady sway velocity to the portside. In a starboard turn, the rate of turn is positive which is shown in rad/s in Fig. 5.26. Time-histories of the vehicle's surge and sway accelerations are shown in Figs. 5.27 and 5.28. As is observed in these velocity and acceleration curves, first the vehicle speeds up under the thrust force of the propeller until the axial forces are balanced. Then the stern-planes start to deflect which causes the vehicle to turn and therefore creates impulsive axial and lateral forces and also an impulsive yaw moment.

165
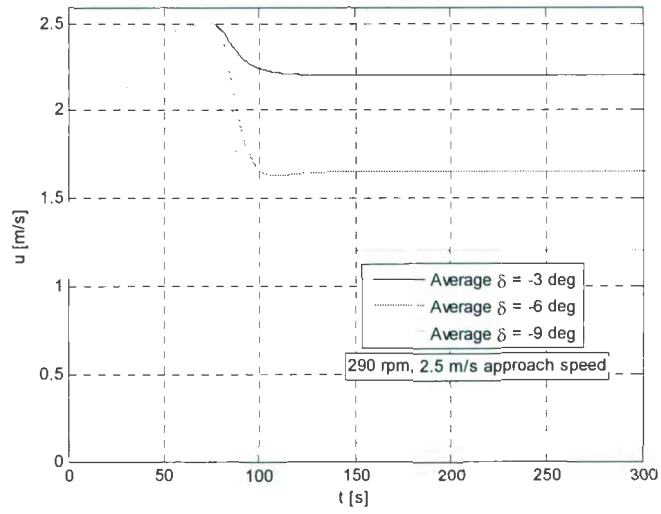
Fig. 5.24 Surge velocity of the vehicle during turns to starboard
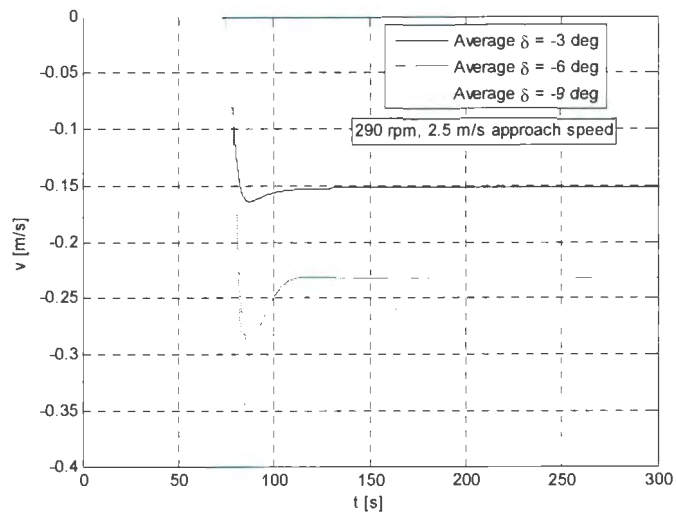
Fig. 5.25 Sway velocity of the vehicle during turns to starboard

166
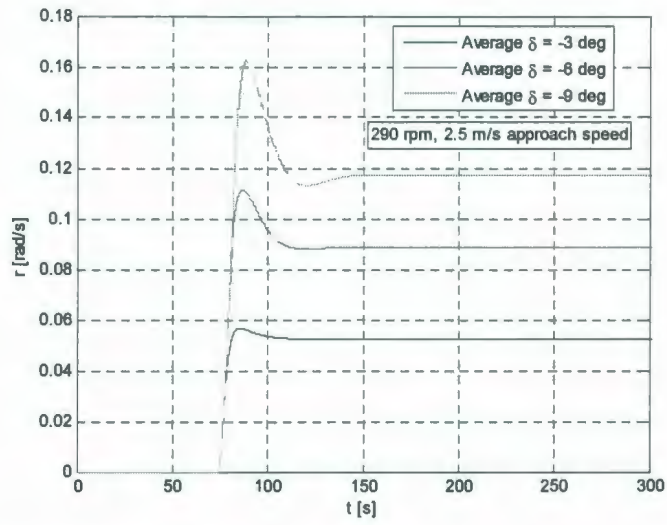
Fig. 5.26 Yaw rate of turn of the vehicle during turns to starboard
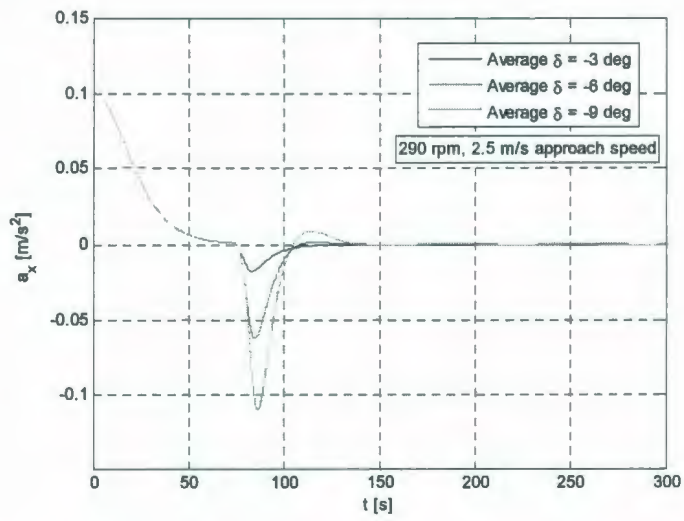
Fig. 5.27 Vehicle acceleration in the surge direction during turns to starboard

167
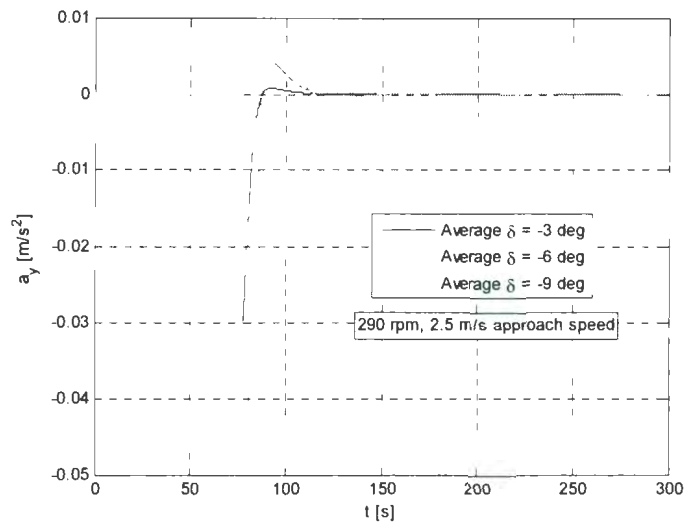
Fig. 5.28 Vehicle acceleration in the sway direction during turns to starboard

The predicted AOA of plane number 3 varies during the turns as is shown in Figure 5.29. Although it is commanded to deflect respectively 3, 6 and 9 deg in the negative direction (leading edge downward) the steady actual AOA is respectively about plus 1.1, 2.6 and 4.8 deg. As was shown in Fig. 5.21 the run with average deflection of 9 deg first turned in a smaller circle until it reached a steady radius. To check for the reason, the radius of curvature of the vehicle's path defined as the speed of the vehicle divided by its rate of turn, $R = U/r$, is plotted versus time during $t = 80$ to 200 seconds of the $\delta = -9$ deg manoeuvre in Fig. 5.30. Obviously, the radius of curvature is changing during the transient portion until the vehicle speed (see Figs. 5.24 and 5.25) and its turning rate (Fig. 5.26) reach to steady values and thus the radius of curvature reach a steady value of about 10.5 m. Note that the turn at $\delta = -9$ deg and 290 rpm initiates at $t = 73$ s, and the radius of curvature of the vehicle's path is of course infinite before it starts to turn.
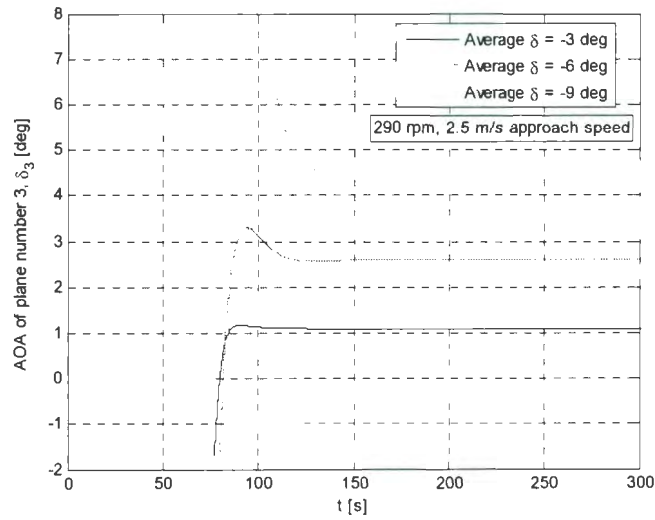
Fig. 5.29 Predicted AOA of plane number 3 during turns to starboard
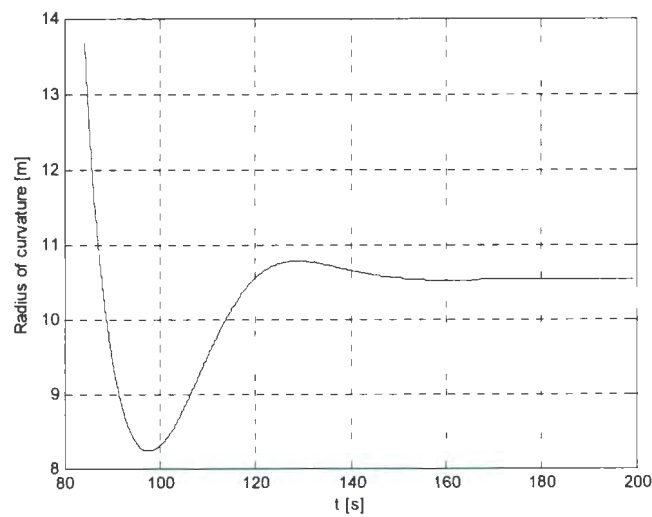
Fig. 5.30 Radius of curvature of the vehicle's path at average $\delta = -9$ deg, 290 rpm

The advantage of this simulation model is that the time histories of the force and moment

vectors for the bare hull and control planes can be traced independently. Time-histories of

the net sway force and the net yawing moment that were produced by the stern-planes

during these turns are shown in Figs. 5.31 and 5.32. To produce a starboard turn the

169

planes were deflected in order to produce a net sway force to portside (negative y-axis); the net sway force in the starting phase of turn with average δ of 9 deg reaches to a maximum of about 40 N towards port. However, as was described before and shown in Fig. 5.29 the actual AOA of planes due to the relative flow velocity change and thus the net sway force of the stern-planes during the steady phase of the turns is to starboard (Fig. 5.31). The net yawing moment of the stern-planes has the same variation but in the opposite direction: for a starboard turn first positive moment is produced, however the steady turning moment becomes negative due to the change in the actual incidence angle of the flow.
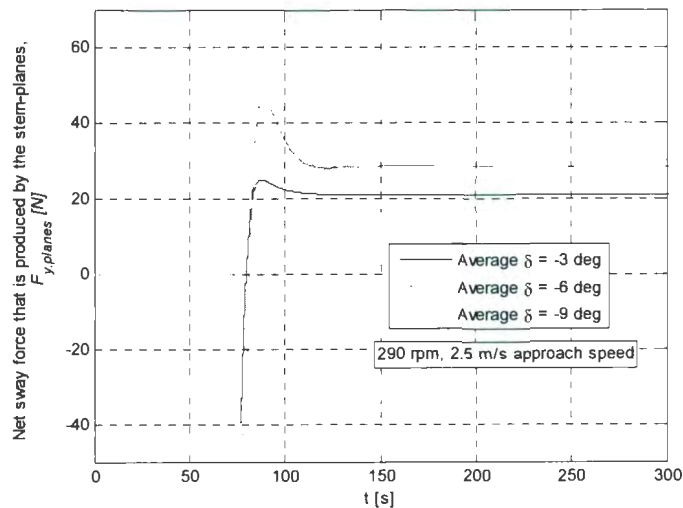
Fig. 5.31 Net sway force that is produced by the stern-planes during turns to starboard
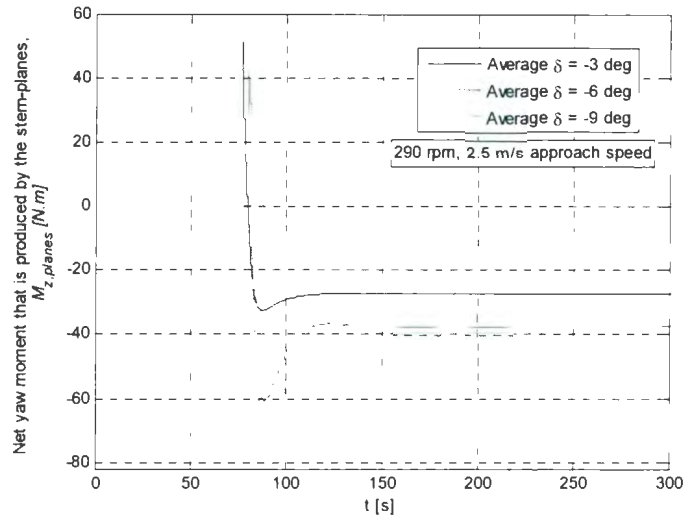
Fig. 5.32 Net yaw moment that is produced by the stern-planes during turns to starboard

The axial force that is exerted on the bare hull is shown in Fig. 5.33. At the start of the turn there is an impulsive increase in the axial force on the bare hull, but it decreases and reaches a steady value during the turn. The time-history of the sway force and the yaw moment that are exerted on the bare hull are shown in Figs. 5.34 and 5.35. The magnitudes of the overshoot in the vehicle response to rudder change, for larger δ are notable. According to Fig. 5.27, the time history of surge acceleration, at an average δ of 9 deg, at the start of the turn there is an impulsive deceleration which then causes a bounce back to acceleration; i.e., after the negative acceleration between about 70 to 100 s due to the rather large amount of deceleration the vehicle stores an inertia to bounce back to a forward acceleration phase (red curve in Fig. 5.27 between about 110 to 150 s) which finally is balanced to zero. This process results in the large reduction in the surge velocity as was shown in Fig. 5.24. Similar responses are also observable in the sway and yaw directions.

171
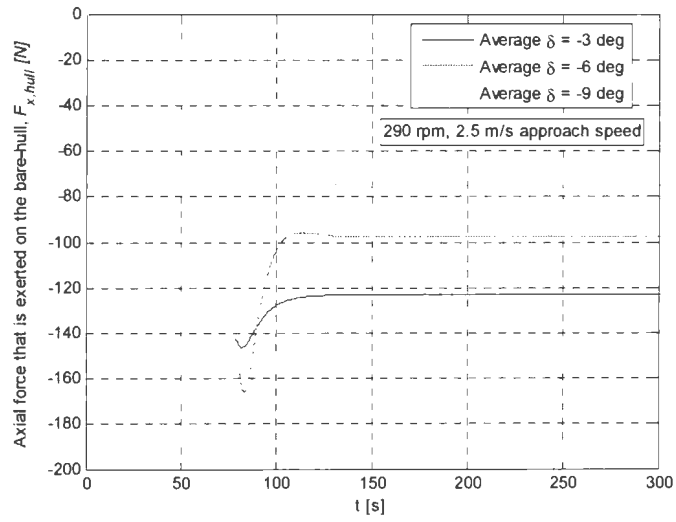
Fig. 5.33 Axial force that is exerted on the bare hull during turns to starboard
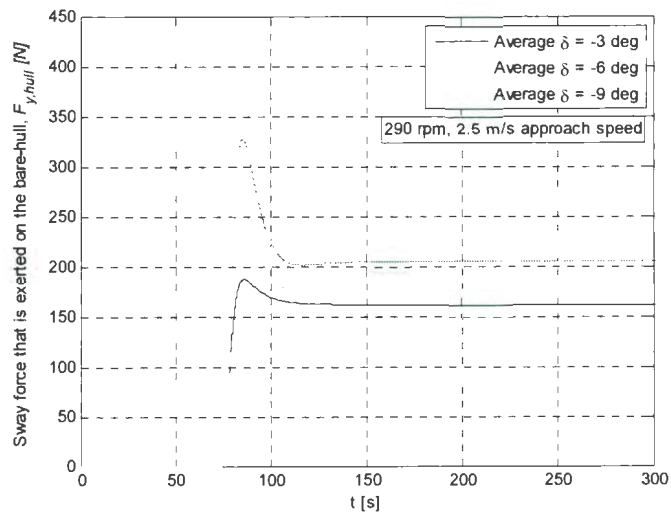
Fig. 5.34 Sway force that is exerted on the bare hull during turns to starboard
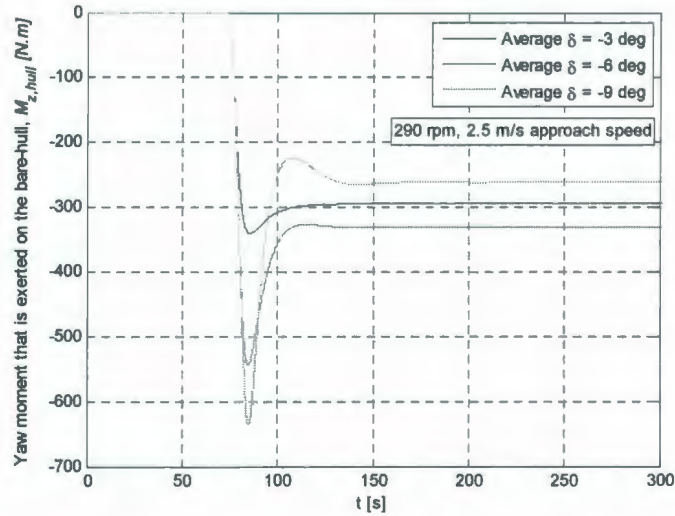
Fig. 5.35 Yaw moment that is exerted on the bare hull during turns to starboard

5.7 Verifying the simulation results with the theoretical formulae for turning manoeuvres

Solving the linearized equations of motion for a vessel during the steady phase of a turning manoeuvre, Mandel [PNA, Chapter VIII, p. 484] presented the following equations for the steady radius of turn and the steady drift angle:

$$R = \frac{-L}{\delta}\left[\frac{Y_v'(N_r'-m'x_G')-N_v'(Y_r'-m')}{Y_v'N_\delta'-N_v'Y_\delta'}\right] \tag{5-39}$$

$$\beta = -\delta\left[\frac{N_\delta'(Y_r'-m')-Y_\delta'(N_r'-m'x_G')}{Y_v'(N_r'-m'x_G')-N_v'(Y_r'-m')}\right] \tag{5-40}$$

Equations (5-39) and (5-40) have the following notation:

- R: steady radius of turn [m]

- β: steady drift angle during the turn [rad]

- L: overall length of the vehicle [m]; in this thesis: l

- δ: rudder deflection angle [rad]

173

- V: vehicle speed [m/s]; in this report: U, where $U^2 = u^2 + v^2$

- $Y_v' = Y_v/(\frac{1}{2}\rho L^2 V)$, where $Y_v = \partial Y/\partial v$, i.e. rate of change of sway force that is exerted on the vehicle with change in the sway velocity.

- $N_r' = N_r/(\frac{1}{2}\rho L^4 V)$, where $N_r = \partial N/\partial r$, i.e. rate of change of yaw moment that is exerted on the vehicle with change in the yaw rate of turn.

- $m' = m/(\frac{1}{2}\rho L^3)$, where m is the vehicle mass; m is the flooded mass for an underwater vehicle.

- $x_G' = x_G/L$, where x_G is the longitudinal location of CG (longitudinal distance from the origin of the coordinate system).

- Y_r' and N_v' are the nondimensional form of derivatives: $Y_r = \partial Y/\partial r$ (change in sway force relative to yaw rate of turn) and $N_v = \partial N/\partial v$ (change in yaw moment relative to sway velocity).

- $Y_\delta' = Y_\delta/(\frac{1}{2}\rho L^2 V^2)$, where $Y_\delta = \partial Y/\partial \delta$, i.e. rate of change of sway force that is produced by the rudder with change in the rudder deflection angle δ in radians.

- $N_\delta' = N_\delta/(\frac{1}{2}\rho L^3 V^2)$ where $N_\delta = \partial N/\partial \delta$, i.e. rate of change of yaw moment that is produced by the rudder with change in the rudder deflection angle δ in radians.

The contribution by the bare hull to the derivatives Y_v and N_v was estimated using the static yaw test results that were shown in Figs. 2.10 and 2.11 for the bare hull configurations in section 3.8 in equations (3-25) and (3-26). For the Phoenix bare hull with LDR 8.5 (Figs. 2.10 and 2.11) it was approximated: $Y_v' = -0.037$ and $N_v' = -0.011$. A negative value for the moment derivative N_v means that the effect of the bow

dominates. Converting the above non-dimensional derivatives to dimensional form for the *MUN Explorer* AUV with overall length $l = 4.5$ m at a forward speed $U = 2.5$ m/s, predicts: $Y_v \approx -958$ N/(m/s) and $N_v \approx -1363$ N.m/(m/s).

In a steady motion, for small sway velocity and small rate of turn, the sway force and yaw moment equations are:

$$Y = Y_v v + Y_r r \tag{5-41}$$

$$N = N_v v + N_r r \tag{5-42}$$

The derivatives: Y_r and N_r are still unknown. Sway force and yaw moment values during a turning manoeuvre for the *MUN Explorer* AUV are the outputs of the present simulation code as were shown in plots of section 5.6.3. At a propeller speed of 290 rpm: approach speed 2.5 m/s, the simulation code was performed for the average stern-planes' δ of 1 to 9 deg and the steady values of sway force and yaw moment that are exerted on the bare hull were recorded as are shown in Table 5.4. Variations of sway force versus sway velocity and yaw moment versus yaw rate of turn are respectively shown in Figs. 5.36 and 5.37 at approach speeds of 1, 1.5, 2 and 2.5 m/s. Also, in Table 5.4 values for the net steady sway force and yaw moment that were produced by the stern-planes during the steady phase of the turns at different δ are presented. Figs. 5.38 and 5.39 are plots of those values versus the average δ of stern planes at approach speeds of 1, 1.5, 2 and 2.5 m/s.

Table 5.4 Simulation results for the steady values of sway force and yaw moment that are exerted on the bare hull and produced by the stern-planes for the *MUN Explorer* AUV at 290 rpm: 2.5 m/s approach speed

δ [deg]	u [m/s]	v [m/s]	r [rad/s]	$F_{y,hull}$ [N]	$M_{z,hull}$ [N.m]	$F_{y,planes}$ [N]	$M_{z,planes}$ [N.m]
0	2.50	0	0	0	0	0	0
1	2.47	-0.057	0.019	65.6	-123.7	8.3	-10.8
2	2.36	-0.108	0.036	121.2	-225.6	15.49	-20.16
3	2.20	-0.152	0.052	161.6	-294.2	20.98	-27.29
4	2.02	-0.187	0.066	186.7	-329.8	24.75	-32.21
5	1.83	-0.213	0.078	199.5	-339.3	27.16	-35.34
6	1.65	-0.232	0.089	204.0	-331.1	28.6	-37.22
7	1.48	-0.246	0.099	203.1	-312.3	29.41	-38.29
8	1.34	-0.254	0.108	199.2	-288.1	29.83	-38.85
9	1.20	-0.26	0.117	193.7	-262.0	30.02	-39.12

Table 5.4 contd.

δ [deg]	$Y_v' * 10^3$	$N_r' * 10^3$	$Y_\delta' * 10^3$	$N_\delta' * 10^3$
0	—	—	—	—
1	-44.4	-12.4	7.33	-2.12
2	-42.0	-11.1	6.35	-1.84
3	-35.3	-8.27	4.85	-1.4
4	-27.6	-4.95	3.33	-0.97
5	-19.1	-1.49	2.13	-0.61
6	-9.03	1.46	1.27	-0.37
7	2.34	3.61	0.72	-0.21
8	18.9	4.91	0.37	-0.11
9	35.0	5.52	0.17	-0.05

In the second part of Table 5.4, the force and moment derivates were calculated using the following formulae:

$$Y_v = \partial F_{y,hull}/\partial v, \ N_r = \partial M_{z,hull}/\partial r, \ Y_\delta = \partial F_{y,planes}/\partial \delta, \ N_\delta = \partial M_{z,planes}/\partial \delta \ (5\text{-}43)$$

where δ is in radians. In (5-43) $\partial \delta$ is 1 deg $= \pi/180$ rad between successive rows, and all other parameters vary in part one of Table 5.4 between two successive rows.
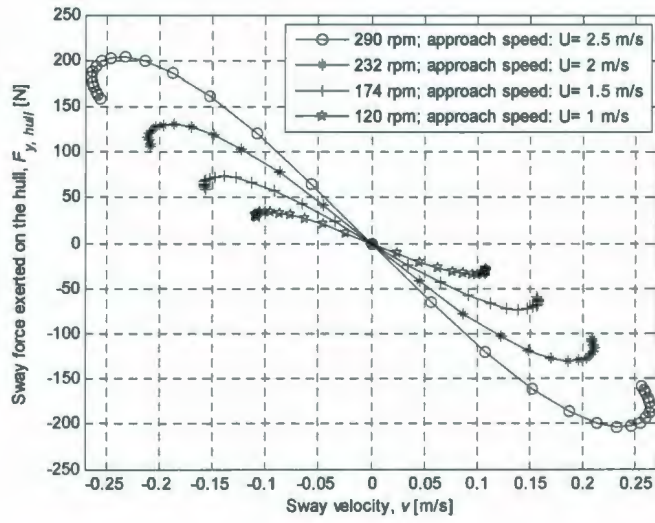
Fig. 5.36 Steady sway force exerted on the bare hull of *MUN Explorer*

during turning manoeuvres
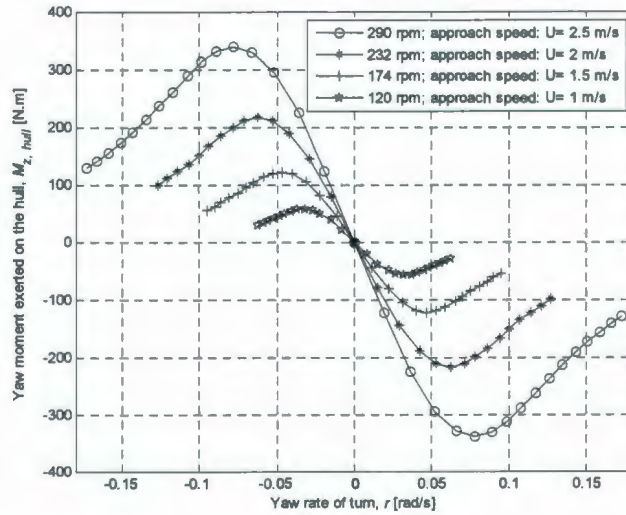
Fig. 5.37 Steady yaw moment exerted on the bare hull of *MUN Explorer*

during turning manoeuvres
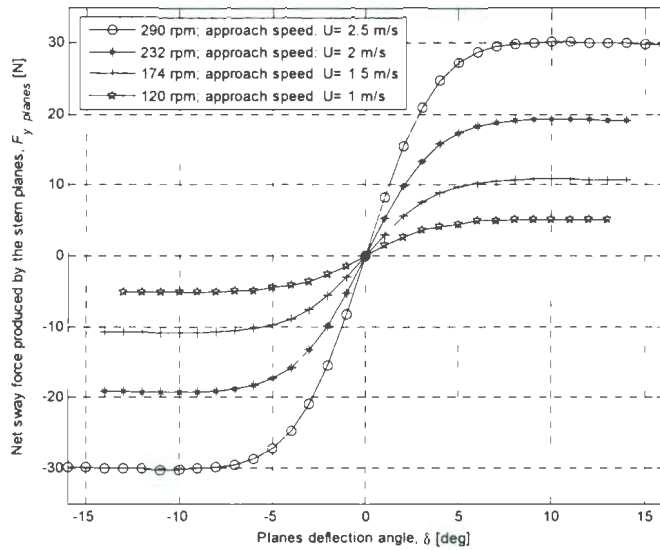
Fig. 5.38 Steady net sway force produced by the stern-planes of *MUN Explorer* **during**

turning manoeuvres
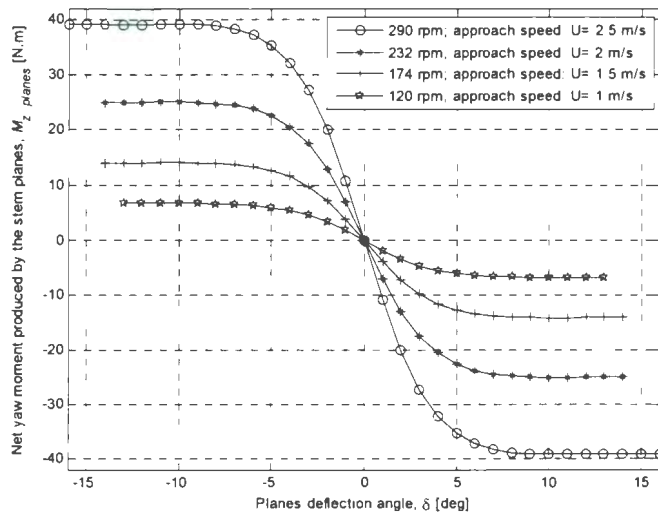
Fig. 5.39 Steady net yaw moment produced by the stern-planes of *MUN Explorer* **during**

turning manoeuvres

Hence, in the vicinity of zero δ where the variation of forces and moments as shown in

Figs. 5.36 to 5.39 are linear, if the first three values for the non-dimensional derivatives

in the second part of Table 5.4, i.e. at δ of 1, 2 and 3 deg, are averaged it indicates that:

$Y'_v = -40.6 * 10^{-3}$, $N'_r = -10.6 * 10^{-3}$, $Y'_\delta = 6.18 * 10^{-3}$, $N'_\delta = -1.79 * 10^{-3}$. Also it

is reminded that using the data in Fig. 2.10 for the bare hull with LDR 8.5 it was

estimated that: $Y'_v = -36.9 * 10^{-3}$ which is close to the value $-40.6 * 10^{-3}$ that is

derived above; the difference is because for the *MUN Explorer* AUV, the *LDR* is about

6.5 that is a less slender hull thus has a non-dimensional derivative of about 1.1 times

larger. Also using the static yaw test results for *LDR* 8.5 in Fig. 2.11 it was previously

estimated that: $N'_v = -11.7 * 10^{-3}$. If this derivative is also scaled by 1.1 then for the

MUN Explorer it is $N'_v = -12.8 * 10^{-3}$. The only remaining parameter to solve the

radius of turn and drift angle in (5-39) and (5-40) is Y'_r.

According the experimental and theoretical data for the non-dimensional derivatives for

the surface ships, with propellers and rudders and some without those, that were

presented by Mandel [PNA, 1967, pp. 526-540], Y'_r has a positive sign (which means that

the effect of stern is dominant, that is: when the vehicle turns in positive yaw direction a

positive sway force is exerted on the stern and a negative sway force is exerted on the

bow, sum of which gives the total sway force on the hull; thus positive Y'_r means that the

effect of stern dominates) and its average magnitude varies about 4 to 7 times smaller

than Y'_v. However, an underwater vehicle compared to a surface ship is more symmetrical

about yz-plane therefore may have a smaller cross-coupled derivative Y'_r. If Y'_r is assumed

between 7 to 10 times smaller than Y'_v, and all the non-dimensional derivates as were

calculated before are substituted in (5-39) and (5-40) the resulting curves compared to the

simulation results for the radius of turn and drift angle are shown in Figs. 5.40 and 5.41.

The values for derivatives are summarized within the plots; four different theoretical curves correspond to $|Y'_v/Y'_r| = 7$, 8, 9 and 10, with all other derivatives as were calculated above $Y'_v = -40.6 * 10^{-3}$, $N'_r = -10.6 * 10^{-3}$, $N'_v = -12.8 * 10^{-3}$, $Y'_\delta = 6.18 * 10^{-3}$, $N'_\delta = -1.79 * 10^{-3}$. The rational curve-fit in (5-38) is also shown in Fig. 5.40. Note that the minus signs in (5-39) and (5-40) mean that the average plane deflection angles for a starboard turn should be negative (that is: leading edge deflects to port). In this simulation for a starboard turn, planes number 3 and 6 are negative and planes number 4 and 5 are positive (Fig. 5.8). There is a good agreement between the simulation results and the theoretical curves. Non-dimensional radius of turn at $|Y'_v/Y'_r| = 10$, that is: $Y'_r = 4.1 * 10^{-3}$, is the closest to the simulation data.

Finally, note that the numerator in brackets on the right hand side of (5-39) indicates the directional stability of the vehicle. According to PNA [1967, page 475, equation (13m)], the vehicle is directionally stable if:

$$Y'_v(N'_r - m'x'_G) - N'_v(Y'_r - m') > 0 . \tag{5-44}$$

Substituting the above calculated values for the hydrodynamic derivatives $Y'_v = -40.6 * 10^{-3}$, $N'_r = -10.6 * 10^{-3}$, $Y'_r = 4.1 * 10^{-3}$, $N'_v = -12.8 * 10^{-3}$, and the non-dimensional mass equal to $m' = 0.031$ and $x'_G = 0$, it follows that:

$$Y'_v(N'_r - m'x'_G) - N'_v(Y'_r - m') = 8.6 * 10^{-5} > 0 . \tag{5-45}$$

Therefore the vehicle is directionally stable.
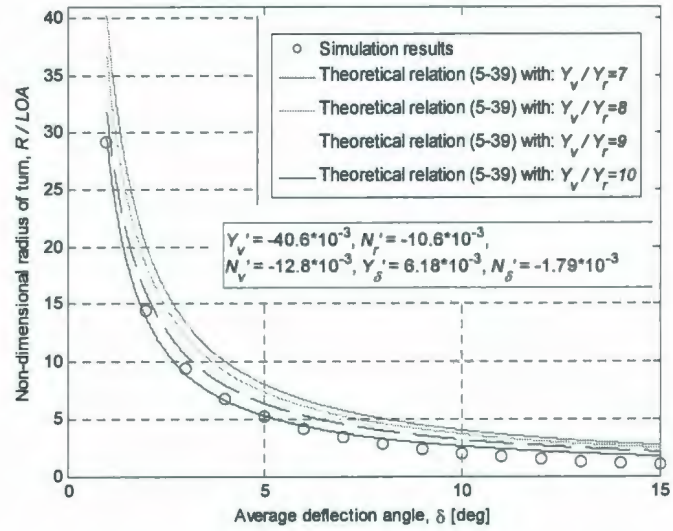
Fig. 5.40 Simulation results for the non-dimensional radius of turn compared to the theoretical

relation (5-39) [PNA 1967, p.485]
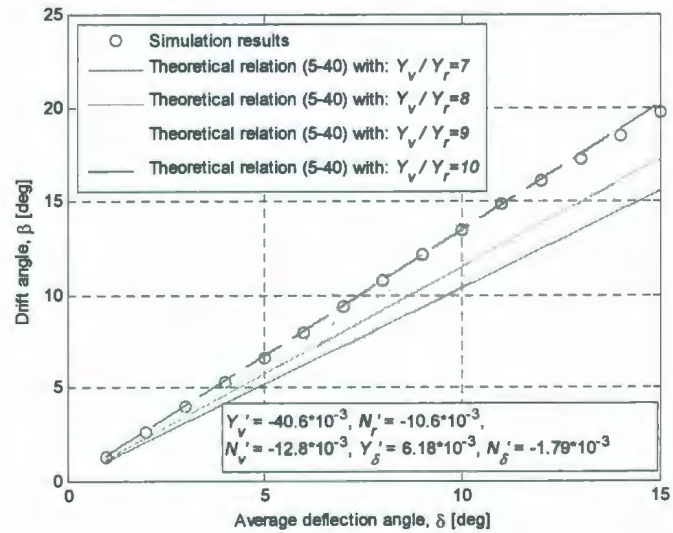
Fig. 5.41 Simulation results for the steady drift angle compared to the theoretical

relation (5-40) [PNA 1967, p.484]

5.8 Summary

In summary the following remarks are made:

1- Regression models for the hydrodynamic coefficients of the bare hull of a torpedo-shaped underwater vehicle that were developed in chapter 2, using the fixed-attitude test results, were usefully embedded within a simulation code to predict the manoeuvring behaviour of the *MUN Explorer* AUV.

2- Planar manoeuvres of the *MUN Explorer* AUV were studied; therefore, the stern-planes which are in an X-configuration were modeled to produce the required sway force and yawing moment for such constant-depth manoeuvres.

3- The propeller thrust force was modeled using the test results from straight-line sea-trials. Using the Wageningen B-series curves for the thrust coefficient produced slightly larger thrust force compared to the thrust force model based on the test results, however the model based on the test results was chosen for propulsion.

4- The simulation code could predict the full-scale experimental turning manoeuvres with a relative error of about 25% in the radius of turn compared to the test results for 10 turning circle sea-trials.

5- The simulation code was then calibrated within 5% relative error in the radius of turn compared to the test results, by changing the longitudinal location of the center of gravity (*CG*). The initial estimate for the longitudinal location of the *CG* was about 8 cm aft of the vehicle mid-length, which was then moved 8 cm forward so that to predict the radius of turn within 5% relative error.

6- The calibrated simulation code was then used to simulate turning manoeuvres for various approach speeds and various deflection angles of the stern-planes. It was observed that: i) radius of turn, drift angle and the speed reduction ratio (ratio of the forward speed of the vehicle within a steady turn to its approach speed) are independent of the approach speed, ii) the radius of turn has an inverse relation to the planes' deflection angle, iii) rate of turn is faster at higher approach speeds and higher deflection angles, iv) drift angle during a starboard turn is positive which means that the vehicle heading is inside the circle while it is turning; drift angle is larger at larger deflection angles, v) speed reduction ratio increases asymptotically to unity at higher radius of turns, i.e.: smaller deflection angles, vi) speed reduction during a turn is larger for more slender bodies, that is: bodies of smaller block coefficient.

7- The time-histories of path, velocity, acceleration and forces that are experienced by *MUN Explorer* during turning manoeuvres were also demonstrated. At larger deflection angles of stern-planes non-linear patterns in those signals are clearly observable.

8- The simulation code was finally checked with theoretical formulae for the radius of turn and drift angle based on the linearized equations of motion. Using the steady values for the sway force and yaw moment that were recorded for the bare hull and the stern-planes during the turns, non-dimensional force and moment derivatives were calculated and it was observed that the theoretical formulae

produced similar results for the radius of turn and drift angle as the simulation code.

The major restriction of the present simulation code is that it was modeled for the planar manoeuvres. To model the two bow-planes as active controllers which mainly affect the pitching and rolling behaviour of the vehicle, introduces a higher level of complexity into the simulation code.

CHAPTER 6

PRESSURE MEASUREMENT EXPERIMENTS ON AN

UNDERWATER VEHICLE

6.1 Introduction

From 1929 to 1932, a series of very extensive and valuable experiments were performed in the wind tunnel of the U.S. National Advisory Committee for Aeronautics (NACA) on some airship models, including a 1/40-scale model of the U.S. Airship "Akron". One set of experiments, [Freeman 1932a], on the Akron airship was designed to determine the drag force, lift force and pitching moment on the bare hull and hull with appendages. In another set of experiments, [Freeman 1932b], a 1/40-scale model of the ZRS-4 airship was used to study pressure distributions. The Akron airship model had a length of 5.98 m (19.62 ft) and had a maximum diameter of 1 m (3.32 ft); therefore the model had a length-to-diameter ratio (*LDR*) of 5.9. Pressure data were recorded for a nominal air speed of 100 mph equivalent to 44.7 m/s in the 20-foot (6 metres) propeller-research wind tunnel of the National Advisory Committee for Aeronautics and were completed in July 1931 [Freeman 1932b].

This chapter is an introduction on how to use this re-analysis of the old experiment data to plan pressure-measurement experiments on an underwater vehicle. Up-to-date numerical methods and tools were used to re-analyze the data from the "Akron" pressure experiment. The data extracted from NACA report No. 443 included the geometrical shape of the bare hull and the variation of the pressures measured on the surface of the

bare hull at about 400 locations and at eight pitch angles. The geometric data includes the shape of the bare hull, that is, the variation of the hull radius over its length. The pressure data included the ratio p/q_0, where p is the dynamic pressure measured at each orifice, and q_0 is the dynamic pressure of the free stream:

$$q_0 = \frac{1}{2}\rho U^2 \qquad (6\text{-}1)$$

where ρ is the air mass density and U is the free stream velocity.

In this study, in order to integrate the measured normal pressures over the surface of the bare hull of the airship, it was meshed by panels. Normal pressure integration results in the pressure drag only, however about 80 percent of the drag force is due to the viscous effects. Viscous properties of the flow from another set of experiments on the 1/40-scale model of the airship Akron were observed and reported [Freeman 1932c].

6.2 Fitting curves to the experimental data

6.2.1 Airship geometry and arrangement of the orifices

About 400 pressure orifices, distributed longitudinally over 26 transverse stations, on the port half of each station simultaneously recorded the local pressure on the airship hull both with and without control surfaces fitted to the model. Eight angles of pitch θ of the bare hull of 0, 3, 6, 9, 12, 15, 18 and 20 degrees and two air speeds of about 70 and 100 mph (31.3 and 44.7 m/s) were used. In these experiments the model angle of attack was restricted to variations of the pitch angle only; the effects of changes in yaw or roll attitude were not investigated. Table 6.1 and Fig. 6.1 show the location of stations along the airship model, and Fig. 6.2 shows the location of the orifices around each station.
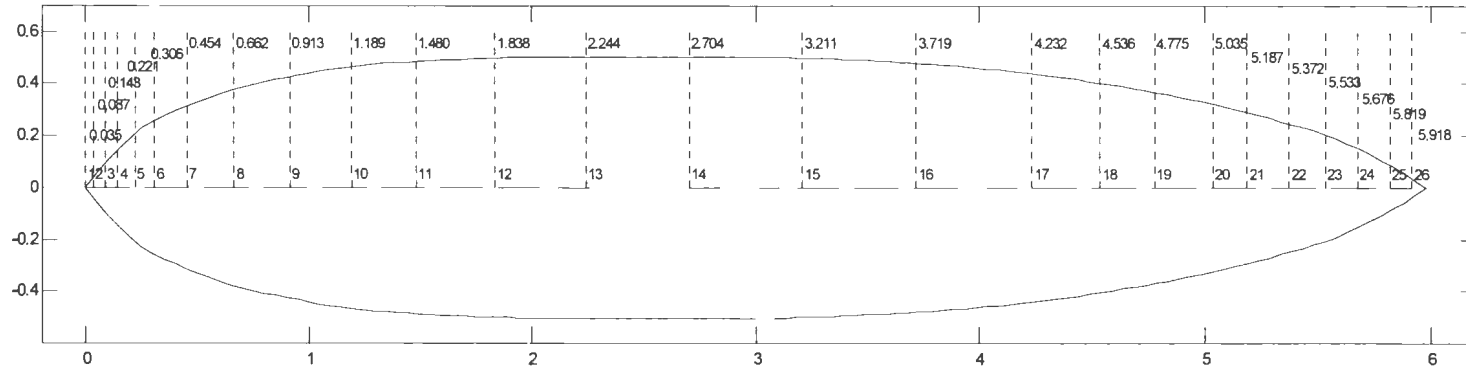
Fig. 6.1 Location of measurement stations in metres reproduced from [Freeman 1932b]

Table 6.1 Measurement stations and their axial location

Station No.	1	2	3	4	5	6	7	8	9
Axial location [m]	0	0.035	0.087	0.143	0.221	0.306	0.454	0.662	0.913
x/l	0	0.006	0.015	0.024	0.037	0.051	0.076	0.111	0.153

Contd.

10	11	12	13	14	15	16	17
1.189	1.480	1.838	2.244	2.704	3.211	3.719	4.232
0.199	0.248	0.307	0.375	0.452	0.537	0.622	0.708

Contd.

18	19	20	21	22	23	24	25	26
4.536	4.775	5.035	5.187	5.372	5.533	5.676	5.819	5.918
0.759	0.798	0.842	0.867	0.898	0.925	0.949	0.973	0.990

187
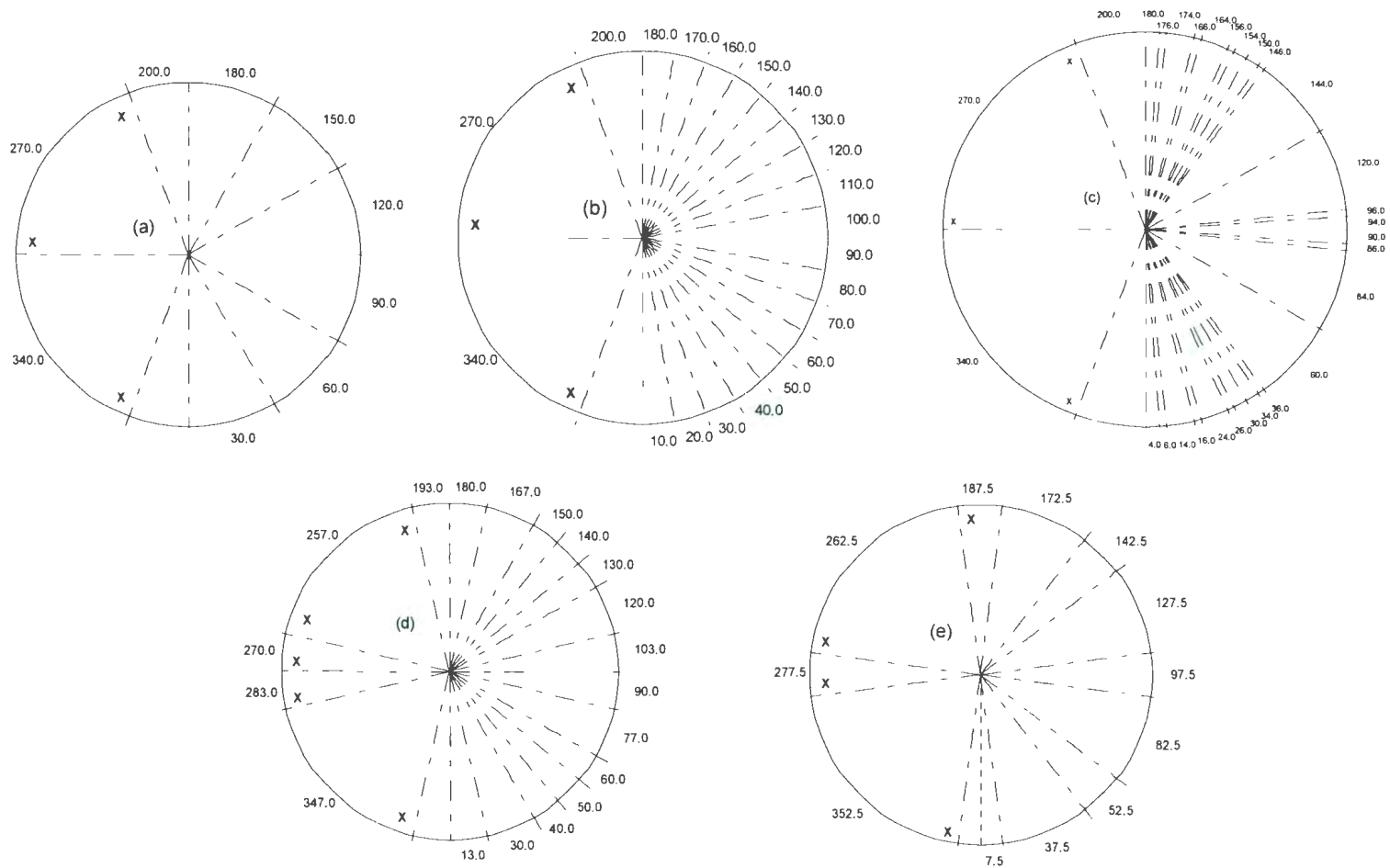
Fig. 6.2 Angular position of the orifices at different transverse stations; all views looking aftward (locations marked "X" are orifices to check the flow symmetry): (a) Stations 2, 3, 4, 6, 10, 14 and 16; (b) stations 5, 7, 9, 11, 13, 15 and 17; (c) stations 8 and 12; (d) Stations 18 to 21 inclusive; (e) stations 22 to 26 inclusive [reproduced from Freeman 1932b]

The different front views shown in Fig. 6.2 are due to the different arrangement of the orifices at different stations. Some stations in each group include the orifices marked "X" so as to check for the equality of pressures on the port and starboard sides. The orifices were 0.8 mm (1/32 inch) in diameter.

6.2.2 Fitting curves to the data around each station

As mentioned p/q_0 the ratio of dynamic pressure measured at each orifice to the dynamic pressure of the free stream was the main measured data in the "Akron" tests. Fig. 6.3 (a) to (c) show the variation of the recorded data p/q_0 versus angular position of the orifices, namely the azimuth angle ω for stations number 8, 14 (mid-body), and 25 (in the stern). The azimuth angle varies from zero at the airship keel, to 180 degrees at the airship top-line. Measured data are marked according to the legend for different pitch angles. The curves fitted are all of the form:

$$\text{Fit} = A + B \cos(\omega) + C \left[\cos(\omega)\right]^2 + D\left[\cos(\omega)\right]^3 \qquad (6\text{-}2)$$

The fitted curves in Fig. 6.3(a) match the data very closely. The data in Fig. 6.3(b) show that at large pitch angles there are some discrepancies between the fitted curves and the experimental data. In Fig. 6.3(c) further back towards the stern where the level of flow turbulence is high, the fitted curves intersect each other and get somewhat disordered for larger pitch angles. However, this fitting equation has good correlation with the experimental data for all stations. Fig. 6.4 shows the average correlation coefficient for the fitted curves over eight pitch angles for stations 2 to 26.
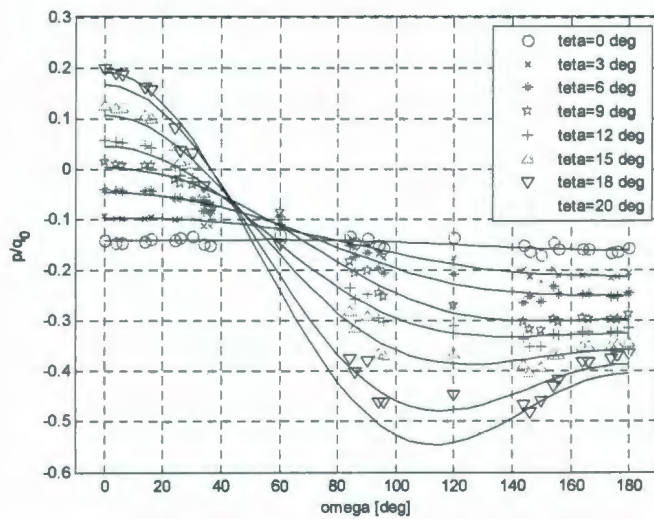
Fig. 6.3(a) Variation of the recorded data p/q_0

versus angular position of the orifices, at station 8
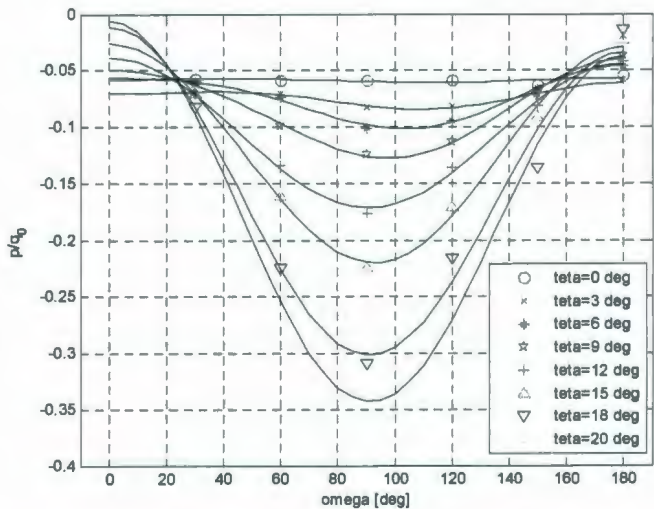
Fig. 6.3(b) Variation of the recorded data p/q_0

versus angular position of the orifices, at station 14

190
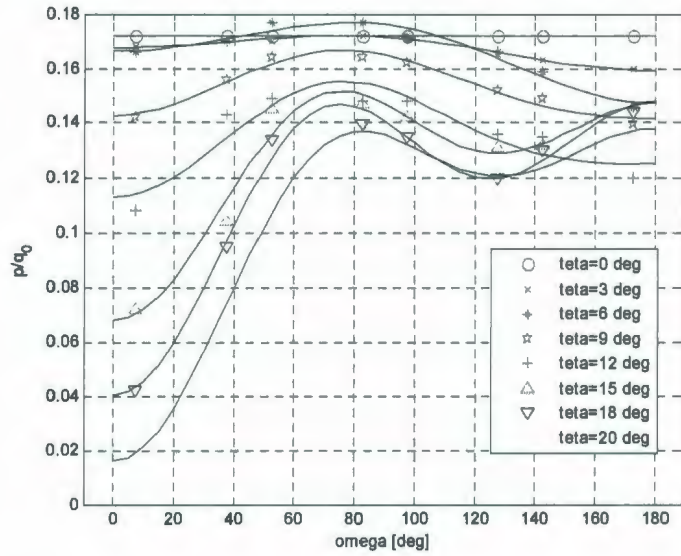
Fig. 6.3(c) Variation of the recorded data p/q_0

versus angular position of the orifices, at station 25
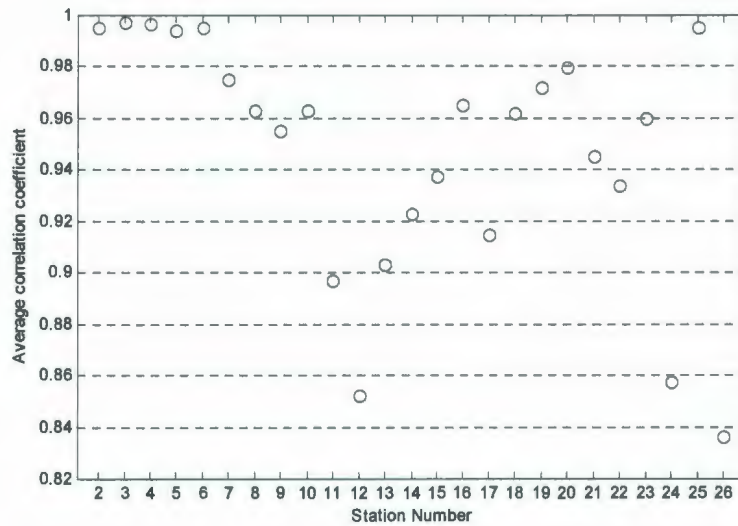
Fig. 6.4 Average correlation coefficient for the fitted curves by equation (6-2)

over eight pitch angles for each station

Next the fitted curves were used to develop curves of the variation of pressure along generator lines along the surface of the hull. A generator line should be a smooth curve

191

along the hull showing the variation of p/q_0. Having the coefficients of the fitted curves from equation (6-2) for stations 2 to 26 for eight pitch angles, fitted values of p/q_0 could be calculated for any desired value of the circumferential angle. At this point, it had to be decided what angular increment $\Delta\omega$ was desired. Fitted values of p/q_0 for a pitch angle of 15 degrees and an azimuth angle of 180 degrees are shown in Fig. 6.5. Fitted values are marked by asterisks and experimental data by circles.
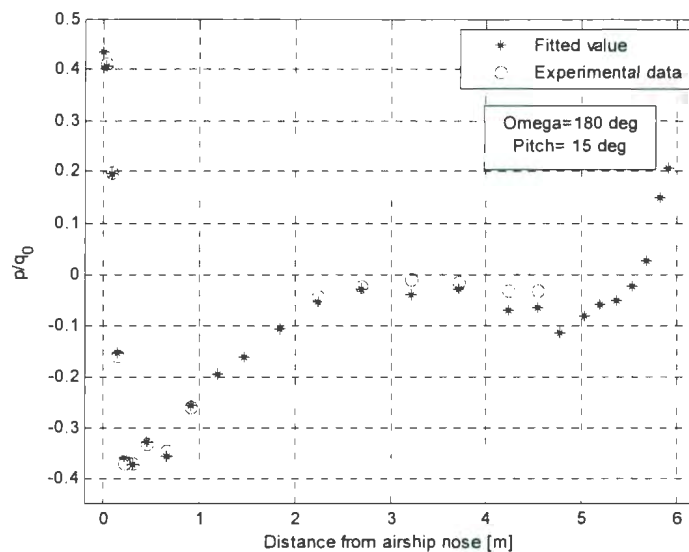
Fig. 6.5 Fitted values of p/q_0 along the hull compared to the

Experimental data; $\theta = 15°$ and $\omega = 180°$

Experimental data were not available for every azimuth angle, e.g. for $\Delta\omega = 5$ deg and $\omega = 45$ deg no measurements were taken but still equation (6-2) fits values to p/q_0. Only for station number 1, that is at the airship nose, is the fitted value the same as the experimental data. Table 6.2 shows the experimental measurements at the airship nose, station number 1, for all pitch angles. The method of reporting the experimental data included subtraction of the static pressure which was measured at each station along the

centerline of the wind-tunnel without the model in the test section; see Fig. 6.6 and Table 6.3. Thus the tabulated values for p/q_0 were corrected for the effects of the longitudinal gradient of static pressure. The result is that the ratio p/q_0 at the airship nose is unity at a pitch angle of zero as shown in Table 6.2.

Table 6.2 Dynamic pressure measured at the airship nose for eight pitch angles

Pitch angle [deg]	0	3	6	9	12	15	18	20
p/q_0	1.000	0.967	0.900	0.785	0.682	0.434	0.098	-0.132

Table 6.3 Static pressure distribution along the longitudinal centreline of the test section in the absence of the airship

x/l	0	0.1	0.2	0.3	0.4	0.5	0.6	0.7	0.8	0.9	1.0
p_s/q_0	0.032	0.025	0.020	0.017	0.015	0.013	0.011	0.010	0.010	0.011	0.013
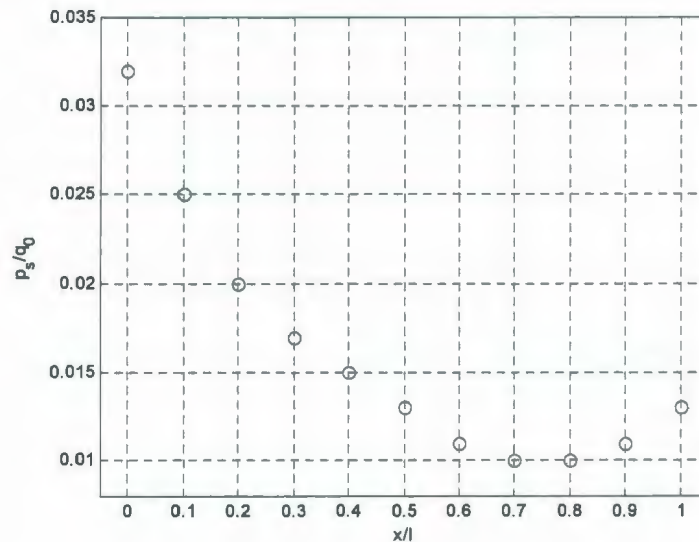
Fig. 6.6 Variation of the static pressure in the test section

without the model present

6.2.3 Fitting 9th order polynomials to the pressure data along the airship hull

Now smooth generator curves can be fitted to the discrete fitted values that were obtained at each station by fitting equation (6-2) to the experiments data; these points are shown by asterisks in Fig. 6.5. Polynomials of 9th order were used to fit the values of p/q_0, which were themselves fitted values to the experimental data. The 9th order polynomial fit is the final pressure generator equation to be used for integration[15]. The polynomial curve itself is a discrete series of values fitted over the longitudinal coordinate x by an increment of Δx. For example, the polynomial representation is shown in Fig. 6.7 for a pitch angle of zero and azimuth angle of 90 degrees, and in Fig. 6.8 for a pitch angle of 15 degrees and azimuth angle 180 degrees. Note that due to the high order of the polynomial, care must be taken not to use this to predict pressures outside of the range of the input data.
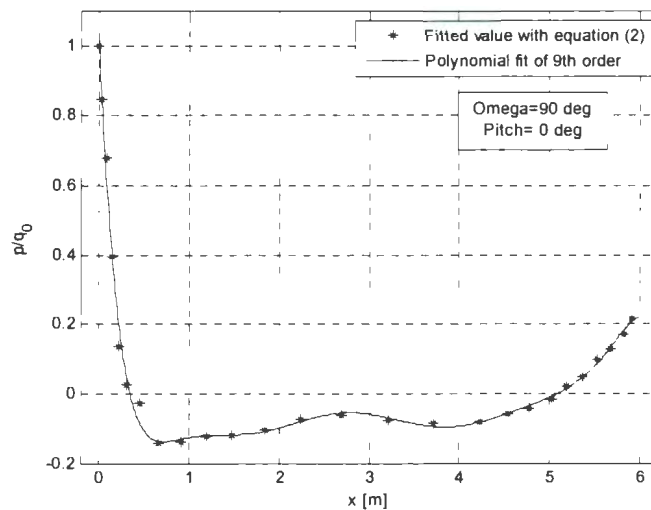
Fig. 6.7 Polynomials of 9th order (solid line) fitted to the p/q_0 values (asterisks)

Fitted by equation (6-2); $\theta = 0°$ and $\omega = 90°$

---

[15] These curve-fit coefficients are available from the author upon request.
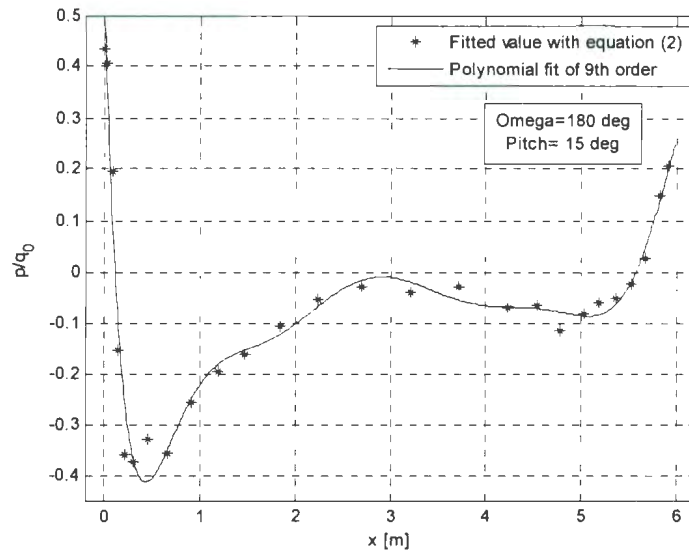
Fig. 6.8 Polynomials of 9th order (solid line) fitted to the p/q_0 values (asterisks)

Fitted by equation (6-2); $\theta = 15°$ and $\omega = 180°$

6.2.4 Geometry of the panels

The angular increment from which the generator curves were produced, determines the size of one side of the surface panels, and the increment Δx by which the polynomial curve was defined, determines the size of the other side of the panels. Thus one side is of dimension $r \cdot \Delta \omega$, where r is the radius of the hull cross-section, and, the second side is of dimension $\Delta x / \cos(\varphi)$, where φ is the angle between the tangent line to the surface of the hull and the longitudinal axis. The meshed surface obtained using the surface-panel method is shown in Fig. 6.9. A tangent to the meshed surface at the bow end should have a 90 degree slope, whereas a curve fitted to the as-constructed shape has a slope of about 0.9 radian (52°) at the bow end. Fig. 6.9 shows the 3D view of the meshed airship for longitudinal increment of 0.1 m and angular increment of 10°. In this study the x-axis is positive toward the stern, the y-axis is positive to starboard and the z-axis is positive

195

upward; these axes do not follow the SNAME convention for underwater vehicles [SNAME 1950].

In summary, the area of each panel is derived as

$$\Delta A = (\Delta x / \cos(\varphi)) \cdot (r \cdot \Delta \omega) \qquad (6\text{-}3)$$

where $\varphi = \varphi(x)$ and $r = r(x)$ hence:

$$\Delta A = \Delta A(x) \qquad (6\text{-}4)$$

According to equation (6-4) the panel size depends only on the longitudinal distance from the airship nose. In equation (6-3), the longitudinal side of each panel, $\Delta x / \cos(\varphi)$, is approximated as a straight line; hence, the error in calculating ΔA increases as the incremental value of Δx increases, but the incremental value of $\Delta \omega$ does not affect the surface area value, because $r \cdot \Delta \omega$ is the exact arc length of the lateral side of each panel.
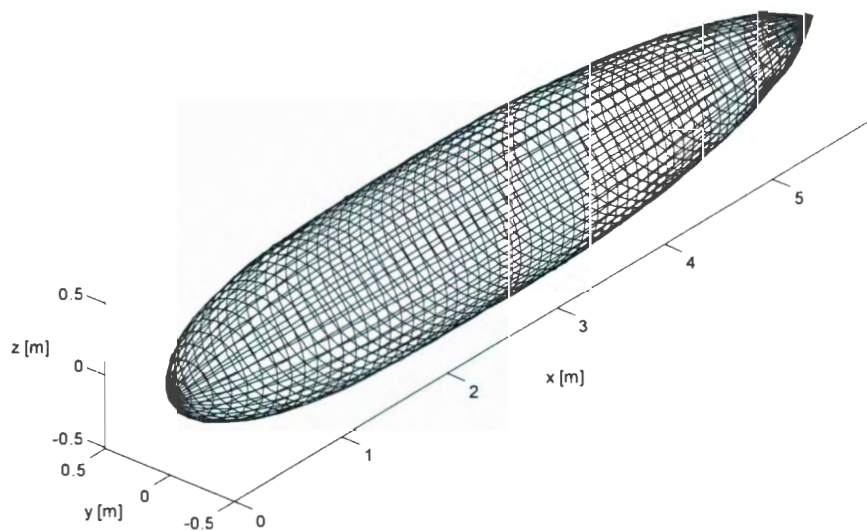
Fig. 6.9 Isometric view of the "Akron" airship hull meshed according to

$$\Delta \omega = 10 \text{ deg and } \Delta x = 0.1 \text{ m}$$

6.3 Pressure surface illustration

The pressure data can be illustrated by surfaces as in Figs. 6.10 and 6.11 on axes of azimuth angle ω and the longitudinal distance from the airship nose x. Fig. 6.10 is the pressure surface for a pitch angle of nine degrees and Fig. 6.11 is the pressure surface for a pitch angle of 20 deg. The magnitude of the maximum and minimum pressures for pitch angles nine and 20 degrees are shown within the plots. There is not a significant change in maximum pressure between these two pitch angles, however the minimum pressure is considerably lower (larger vacuum) for the larger pitch angle.

In this re-analysis, the dry air density was assumed to be 1.168 kg/m^3 for a temperature of 25 C$^\circ$ and barometric pressure of 100 kPa, hence for the air speed of 100 mph the free stream dynamic pressure is:

$$q_0 = \frac{1}{2}\rho U^2 = \frac{1}{2} * 1.168 * (100 * 0.44704)^2 = 1167 \qquad (6\text{-}5)$$

The maximum pressure for zero pitch angle is exactly equal to the dynamic pressure in equation (6-5) and for the other pitch angles it is close to that value. Table 6.4 shows the maximum and minimum pressures for the eight different pitch angles tested. The longitudinal location and azimuth angle of the minimum and maximum pressures are included in Table 6.4; however, the pressure surface interpolation is not accurate up to three decimals as is shown for the maximum pressure location. Pressure contours give a better illustration of the pressure variation along and around the airship hull. Fig. 6.12(a) shows the pressure contours on axes of azimuth angle and the longitudinal distance from the airship nose for a pitch angle of 15 degrees.

197
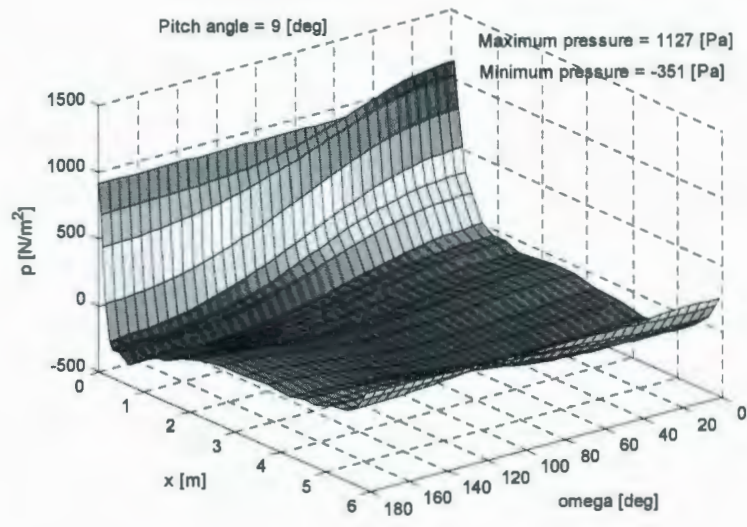
Fig. 6.10 Pressure distribution over the bare hull of

The "Akron" airship for a pitch angle of 9 deg
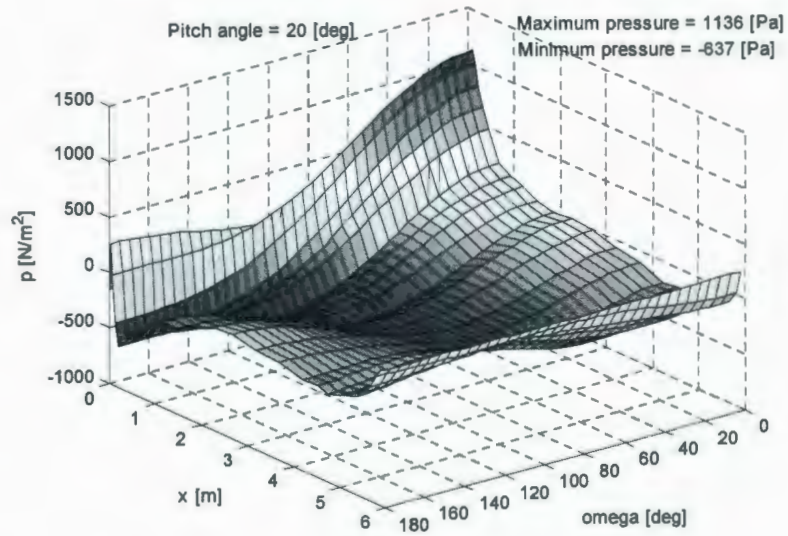
Fig. 6.11 Pressure distribution over the bare hull of

The "Akron" airship for a pitch angle of 20 deg

Table 6.4 Maximum and minimum pressures for different pitch angles for the Akron model at a

windspeed of 44.7 m/s

Pitch angle [deg]	0	3	6	9	12	15	18	20
Max pressure [N/m²]	1167	1129	1109	1127	1132	1138	1132	1136
ω for max [deg]	–	0	0	0	0	0	0	0
x/l for max	0	0.004	0.005	0.006	0.007	0.008	0.01	0.013
Min pressure [N/m²]	-187	-247	-291	-351	-387	-451	-559	-637
ω for min [deg]	–	170	160	150	140	130	120	115
x/l for min	0.12	0.12	0.12	0.11	0.11	0.11	0.1	0.1
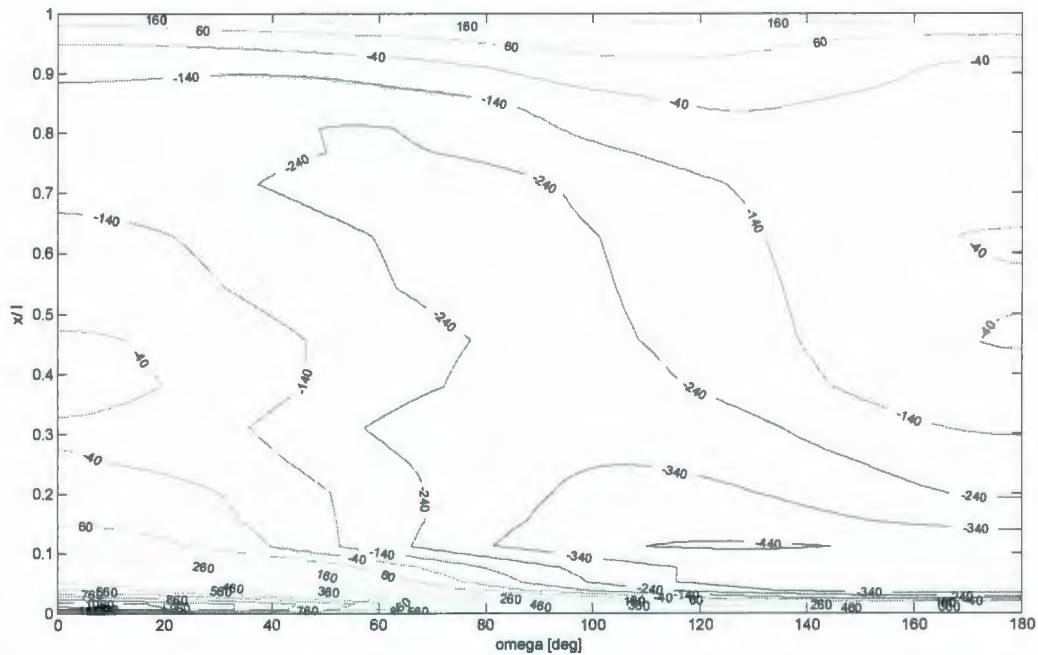
Fig. 6.12(a) Pressure contours over the bare hull of the Akron airship for a pitch angle of 15 deg

In Fig. 6.12(a), the high-pressure zone at the airship nose is magnified and shown in Fig. 6.12(b). The highest-pressure contour, shown in the zoom-in, is 1120 Pa, and the maximum pressure for the pitch angle of 15 degrees, according to Table 6.4, is 1138 Pa which should be a point inside the contour of 1120 Pa.
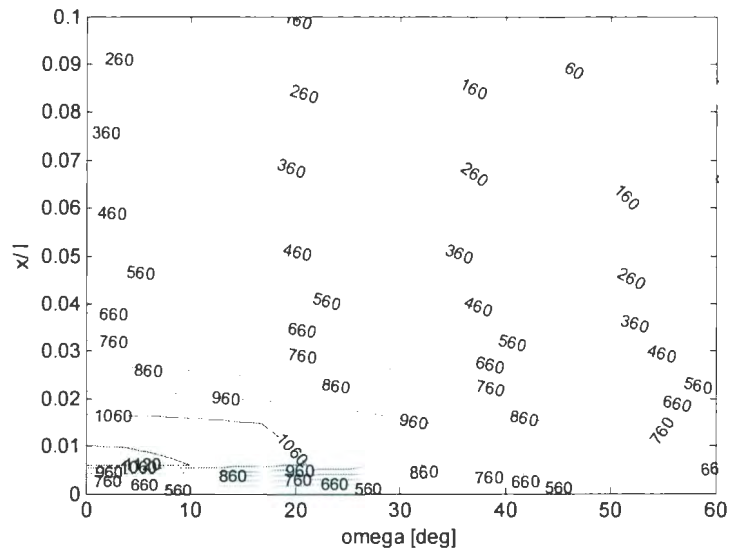
Fig. 6.12(b) Magnified region near the nose for a pitch angle of 15 deg

The pressure distribution over the bare hull of an underwater vehicle should have the same pattern and same variation with pitch or yaw angle as for the airship for the same hull shape (if it is a body of revolution the effect of pitch and yaw attitude changes are the same). The pressures for an underwater vehicle that is towed at a speed of 3 m/s in fresh water are scaled relative to the "Akron" airship surface pressures according to:

Underwater vehicle normal stresses/Airship normal stresses=

$$(\rho_{water}U_{water}^2)/(\rho_{air}U_{air}^2) = (1000 * 3^2)/(1.168 * 44.7^2) = 3.86 \qquad (6\text{-}6)$$

Therefore the maximum and minimum pressures occurring on the surface of the hull of an underwater vehicle (which has the same shape as the "Akron" airship) at a towing speed of 3 m/s are roughly four times the values in Table 6.4.

6.4 Pressure integration over the 3D meshed model

The fitted pressures were integrated over the meshed surface of the hull. For an arbitrary circumferential angle along the airship the differential normal force on each panel is:

200

$$\Delta F(x, \omega) = (p/q_0) \cdot \Delta A(x) \cdot q_0 \tag{6-7}$$

The first term in parentheses on the RHS of equation (6-7) is read from the polynomials of 9th order. The elemental force resulting from equation (6-7) is perpendicular to the panel and should be projected in the directions parallel and perpendicular to the longitudinal axis of the hull. This is illustrated in Fig. 6.13(a); therefore, the radial and axial components of the differential force are as follows:

$$\Delta F_x = \Delta F \cdot \sin(\varphi) \tag{6-8}$$

$$\Delta F_r = \Delta F \cdot \cos(\varphi) \tag{6-9}$$

The component of force in the radial direction ΔF_r should be projected into the lateral and vertical directions, as illustrated in Fig. 6.13(b). Hence, using equation (6-9) results in:

$$\Delta F_y = \Delta F_r \cdot \sin(\omega) = \Delta F(x, \omega) \cdot \cos(\varphi) \cdot \sin(\omega) \tag{6-10}$$

$$\Delta F_z = \Delta F_r \cdot \cos(\omega) = \Delta F(x, \omega) \cdot \cos(\varphi) \cdot \cos(\omega) \tag{6-11}$$
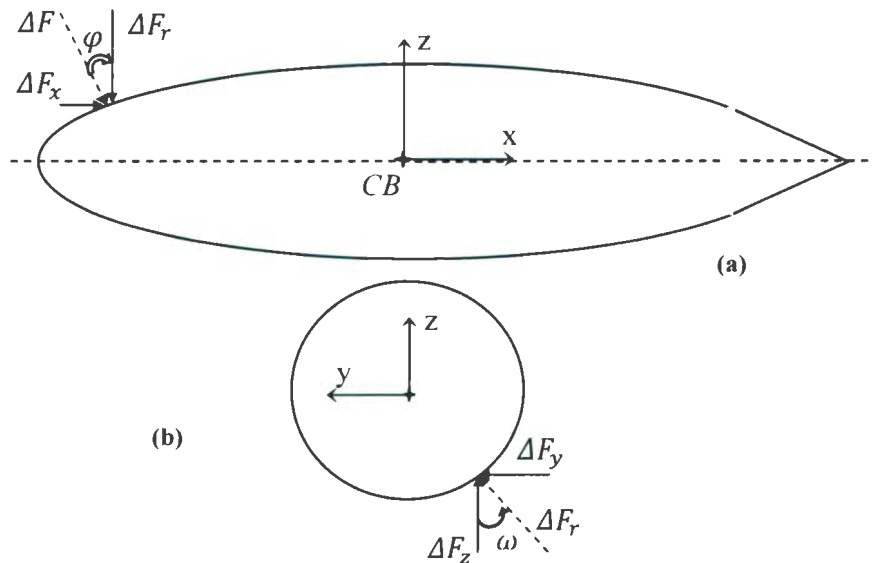
Fig. 6.13 Arbitrary elemental forces illustrated in: (a) side-view and (b) front view looking aftward (x-axis goes into the sheet)

201

Equation (6-8) gives the elemental axial force; the integration of $\Delta F_x(x, \omega)$ over both Δx and $\Delta \omega$ will give the total axial force acting on the hull, which is expected to be zero for a pitch angle of zero. Equation (6-10) gives the elemental lateral force; the integration of $\Delta F_y(x, \omega)$ over both Δx and $\Delta \omega$ will give the total lateral force acting on the hull, which is expected to be zero for any pitch angle as long as the yaw angle is zero, since the flow is assumed to be symmetric on the port and starboard sides. Equation (6-11) gives the elemental normal force; the integration of $\Delta F_z(x, \omega)$ over both Δx and $\Delta \omega$ will give the total normal force acting on the hull, which is expected to be zero for a pitch angle of zero.

As illustrated in Fig. 6.14, relations between the axial and normal forces which give the drag and lift forces for a pitch angle of θ are:

$$D = F_x \cdot \cos(\theta) + F_z \cdot \sin(\theta) \tag{6-12}$$

$$L = F_z \cdot \cos(\theta) - F_x \cdot \sin(\theta) \tag{6-13}$$

The pitching moment was calculated about the centre of buoyancy (CB). The differential force on each panel creates a moment; the axial component of the differential force has a moment arm equal to:

$$d_x = r \cdot \cos(\omega) \tag{6-14}$$

and the vertical component of the differential force has a moment arm equal to:

$$d_z = x_{CB} - x \tag{6-15}$$

where the longitudinal location of the CB, according to [Freeman 1932b] is: $x_{CB} = 0.464 * l = 2.77$ m. The differential moment due to one panel is:

$$\Delta M_y = -\Delta F_x \cdot dx + \Delta F_z \cdot dz \tag{6-16}$$

Note that the directions of the positive axes are required to interpret the minus sign in (6-16). The circumferential angle ω is zero at the keel and positive counterclockwise in a front view when looking aftward.
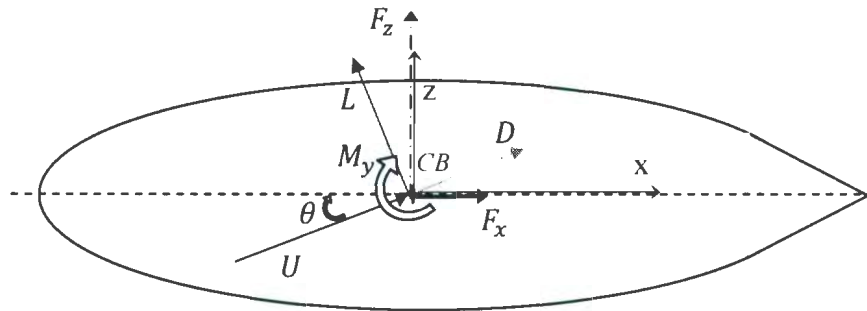
Fig. 6.14 Axial and normal forces and drag and lift forces illustrated

Figs. 6.15 to 6.19, respectively, show the axial force F_x (positive aftward), normal force (positive away from the keel), drag force (positive downwind), lift force (positive upward), and pitching moment (positive nose upward). Each figure has been plotted for several mesh-sizes with the smallest and largest increments for Δx and $\Delta \omega$ of respectively: 0.01 and 0.2 m, and 1 and 30 degrees. The mesh-size $(\Delta x, \Delta \omega)$ of (0.01 m, 1 deg) is an extremely fine mesh for a hull which is almost 6 m long. For the axial force, normal force and pitching moment the reported results from [Freeman 1932b] are also shown with square markers. For the axial force F_x the NACA reported result found from a 2D integration has large errors compared to the 3D panel method used here. In the NACA report, no values were reported for pitch angles of 18 and 20 degrees; interpolated results are now available for these two pitch angles. The integrated values for the axial force with fine mesh sizes for a zero pitch angle converge to a value of 6.5 [N]. This axial force is the pressure-drag as can be observed in Fig. 6.17 for pitch angle of zero. Up to a

203

pitch angle of 15 deg the axial force is about the same value; however, decreases from there to negative values for the larger pitch angles. For the pitch angle of 20 degrees the integrated axial force is about −16.5 [N].

Except for the axial force results, the other forces resulting from the 3D fine mesh size integration approach the reported NACA results, even though the latter used the relatively simple 2D integration methods. As can be observed, there are large differences between the computed forces and moments for the fine mesh size with $(\Delta x, \Delta \omega)$ of [0.01 m, 1 deg], and for the coarse mesh size with $(\Delta x, \Delta \omega)$ of [0.2 m, 30 deg].
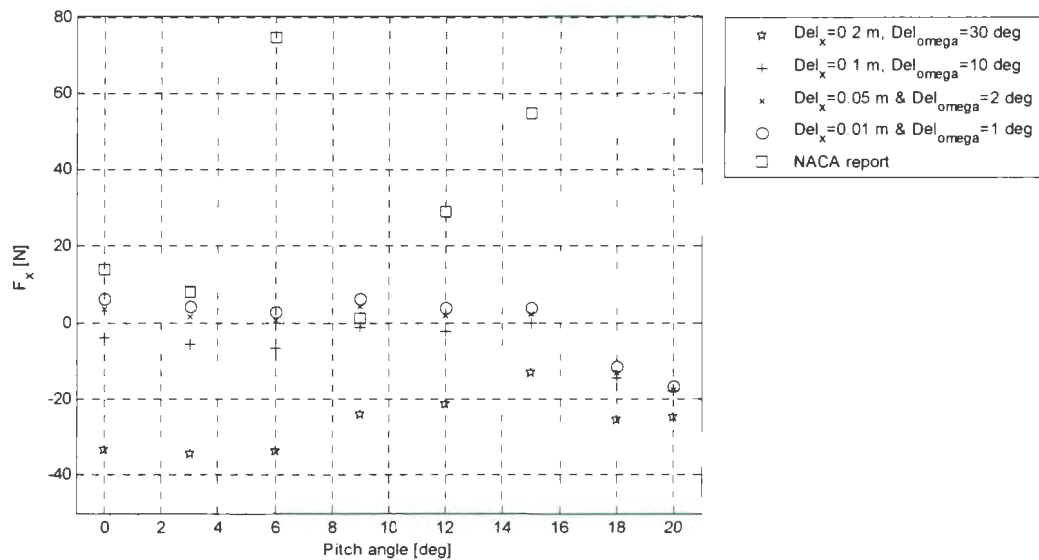
Fig. 6.15 Axial force vs. pitch angle for various mesh sizes compared to NACA report
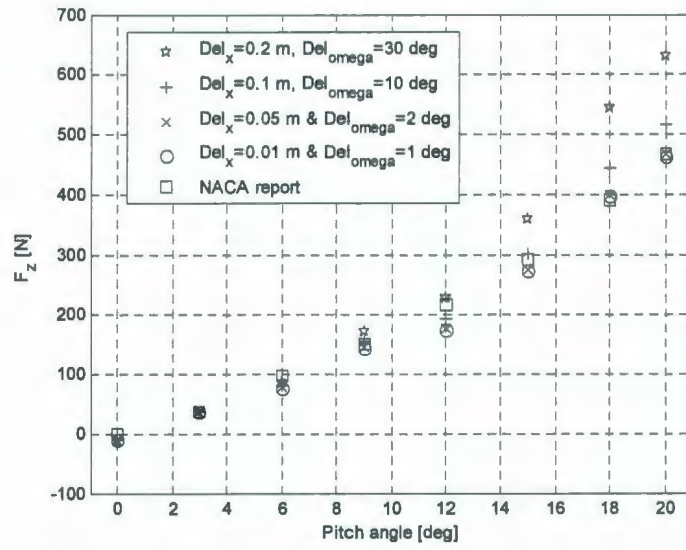
Fig. 6.16 Normal force vs. pitch angle for various mesh sizes compared to NACA report
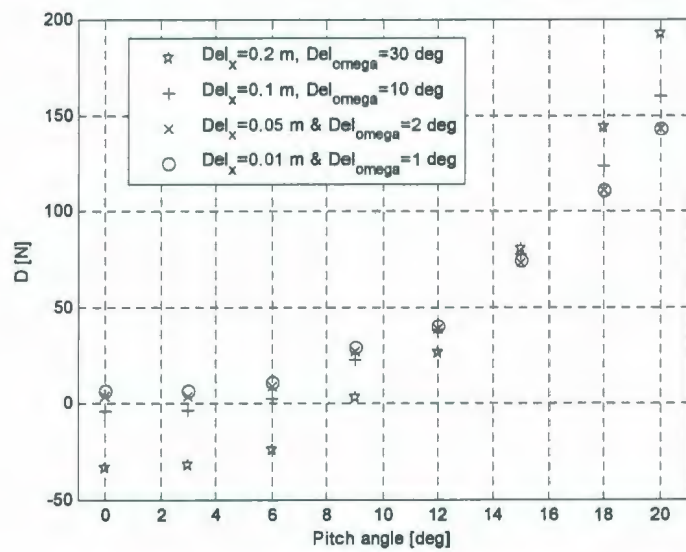
Fig. 6.17 Drag force vs. pitch angle for various mesh sizes

205
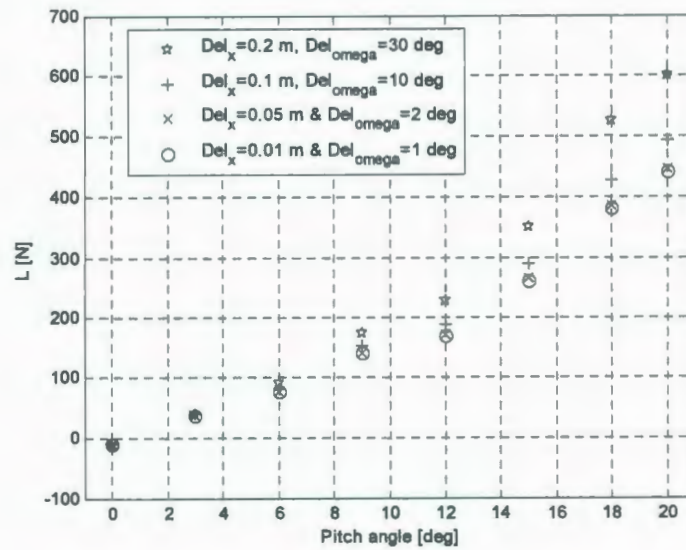
Fig. 6.18 Lift force vs. pitch angle for various mesh sizes
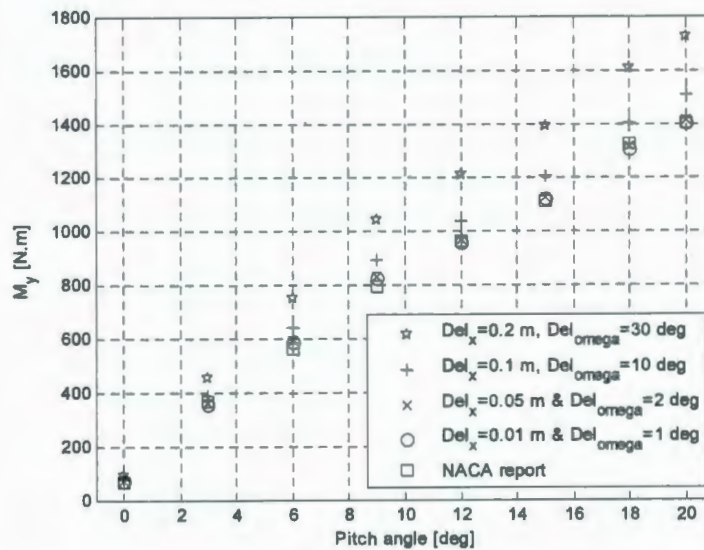
Fig. 6.19 Pitching moment vs. pitch angle for various mesh sizes compared to NACA report

6.5 Pressure measurements on a manoeuvring underwater vehicle

In this study of the hydrodynamics of Autonomous Underwater Vehicles (AUVs), employing mostly experimental methods, a method to extract the dependence of the hydrodynamic loads on the vehicle characteristics and the manoeuvring parameters is

desired. In addition to the fixed-attitude manoeuvres as in the "Akron" experiments, variable-attitude manoeuvres with underwater vehicles including high-amplitude, high-rate manoeuvres, such as those which occur during obstacle avoidance, have to be performed. Measurements of the overall hydrodynamic loads with an internal balance have already been performed and some results were presented in chapters: two to four. The main motivations for pressure measurements are:

1) To know the pressure distribution over the underwater vehicle. Pressure distribution information will result in knowledge of the locations of the maximum and minimum pressures, the pressure gradients, and locations of flow separation.

2) To evaluate the hydrodynamic loads by integrating the pressures. Pressure transducers only measure the normal pressure; therefore, the viscous effect that results from the shearing stresses is not taken into account in the integration. The differences between the hydrodynamic loads resulting from direct load measurement and from pressure tests will clarify the contribution of viscous shearing effects. Note that there is a viscous pressure axial force as was shown in Fig. 6.15.

The first stages in these measurements are the straight-line towing and static yaw tests, which are very similar to the "Akron" tests. One major difference is that the airship was tested in a wind tunnel with the fluid passing over it; however, in these tests it will be necessary to tow the vehicle through stationary fluid.

6.6 Summary

For the study of AUVs (Autonomous Underwater Vehicles) at the NRC-IOT (Institute for Ocean Technology, National Research Council, Canada) pressure measurements over the bare hull of an AUV model towed with a variable attitude apparatus (Planar Motion Mechanism) in the calm towing tank water is recommended. To approximate the distribution and magnitude of pressures over the bare hull of an AUV and the resulting forces and moment, the best available resource is the pressure data from the US airship "Akron" tested by the NACA in 1932.

A re-analysis of the Akron pressure data utilizing modern numerical tools concluded:

a- Plots of pressure distribution versus the azimuth angle and the longitudinal distance from the airship nose. Hence, one can know where the maximum and minimum pressures occur for each pitch angle. Also these data will be useful for those people who wish to validate their CFD predictions using experimental results.

b- Drag and lift forces and pitching moment show nonlinear variations versus pitch angle resulting from the measured normal stresses. This can be compared to the total forces and moment including shear stresses.

With this basic knowledge the design of the pressure-measurement experiments for an AUV is recommended.

CHAPTER 7

CONCLUSIONS AND RECOMMENDATIONS

In this research, the main goal was to find the correct form of the physically-based expressions for the hydrodynamic loads that are exerted on completely-submerged underwater vehicles during various manoeuvres. It was noted that for high-amplitude, high-rate manoeuvres, first-order Taylor-series expansion is insufficient to capture the higher-order non-linear dependence of the loads on the flow angle and the vehicle turning rate. Therefore, experiments to measure the hydrodynamic loads that are exerted on the bare hull of a slender torpedo-shaped underwater vehicle during manoeuvres with large angles of attack and large rates of turn were performed.

The fixed-attitude (resistance and static yaw) test results were analyzed and regression models for drag, lift and moment coefficients of the bare hull were obtained versus the experiment factors: bare hull length-to-diameter ratio (LDR), forward speed and yaw angle. These regression models were later embedded within a simulation code to predict the manoeuvring behaviour of the *MUN Explorer* AUV. Also, the concept of statistical design of experiment was introduced and its possible application to design experiments for the study of underwater vehicle hydrodynamics was discussed.

The variable-attitude pure sway tests were also performed on the five bare hull configurations. To model the sway force that is exerted on the bare hull of a slender underwater vehicle during lateral accelerations, the recorded test data were decomposed into an inertial and a damping force component. Study of the inertial force component, revealed that the apparent mass of the submerged body depends on the manoeuvring

frequency and amplitude; although, the magnitude of the apparent mass during lateral acceleration manoeuvres is conventionally, in a potential flow, assumed to depend only on the body geometry. Moreover, a study of the apparent drift angle and the resulting apparent drag and lift forces, that are exerted on the bare hull models during these pure sway manoeuvres, revealed that the resultant lateral force due to the apparent drag and lift forces does not notably vary with the manoeuvring frequency; hence, the variation of the recorded sway force over manoeuvring frequency is due to the added mass phenomena. Eventually, using the conventional approach to find the hydrodynamic derivatives showed that again there is a difference between the resulting values for the same derivatives obtained from the static and dynamic tests.

Pure yaw tests were also performed on the same bare hull configurations and the test results, which all had sway amplitude to cycle period ratio of $A/T \approx 0.08$ [m/s], thus fulfilled the requirement of rapid turning manoeuvres, were reported. First, observations on the magnitude and phase of the hydrodynamic loads: sway force and yaw moment as well as their instantaneous variation during these pure yaw manoeuvres were reported, and then response surface models were constructed to capture the test results. A sample application of these models to predict the required deflection angle of the control planes to perform a zigzag manoeuvre with the *MUN Explorer* AUV was illustrated. Finally, the conventional hydrodynamic yaw coefficients were obtained using these test results. It was observed that the lateral force derivative with respect to the rate of turn and the yaw moment derivative with respect to the angular acceleration of the model are significantly large during a pure yaw manoeuvre.

Next, a simulation code to predict the manoeuvring behaviour of the *MUN Explorer* AUV was developed. The empirical formulae for the drag, lift and moment coefficients for the slender torpedo-shaped bare hull of an underwater vehicle, were used in the simulation code. Stern-planes of *MUN Explorer* which are in an X-configuration were modeled as the active actuators to navigate the vehicle in a constant-depth planar manoeuvre. The propeller thrust force was modeled using the test results from straight-line sea-trials. Simulation results for turning manoeuvres clearly proved that at higher stern-plane deflection angles which result in higher sway velocity and higher rate of turn, the hydrodynamic loads have non-linear variation.

Finally, an initial step towards the aim of performing pressure measurement experiments over the surface of an underwater vehicle was presented. The integration code that was developed to predict the axial and normal forces and the turning moment due to the normal pressures can be used for future test data from underwater pressure measurement experiments. Also, this re-analysis of the old airship data provided an estimate of the magnitude of the normal pressures that may be experienced by an underwater vehicle during manoeuvres; therefore, the required test apparatus can be either designed or purchased.

In summary, the following items are recommended for future research:

1. To perform a statistically designed set of tests for lateral acceleration manoeuvres (as was proposed in Table 3.2 on page 61).

2. To develop a numerical simulation code with its bare hull hydrodynamics based on the empirical formulae for high-amplitude high-rate-of-turn manoeuvres, which is then capable of simulating abrupt high-rate-of-turn manoeuvres.

3. To measure the pressure distribution on the bare hull of an axisymmetric underwater vehicle during both static and dynamic captive tests. The pressure test results will provide new information for the hydrodynamics of underwater vehicles.

Bibliography in alphabetic order

24th ITTC, 2005, Testing and Extrapolation Methods, Manoeuvrability Captive Model Test Procedures, ITTC Quality Manual, 7.5 – 02 – 06 – 02.2

Aage, C., and Smitt, L.W., "Hydrodynamic Manoeuvrability Data of a Flatfish Type AUV", IEEE Proceedings, Oceans'94, Vol.3, pp. 425-430, 1994

Abbott, I.H. and Von Doenhoff, A.E., Theory of Wing Sections, Dover Publications, New York, 1959

Abkowitz, M.A., Stability and Motion Control of Ocean Vehicles, The MIT Press, 1969

Allmendinger, E.E., Underwater Vehicle Systems Design, Written by a Group of Authorities, The Society of Naval Architects and Marine Engineers, 1990

Azarsina, F., Williams, C.D., Lye, L.M., "Resistance and Static Yaw Experiments on the Underwater Vehicle *Phoenix*; Modeling and Analysis, Utilizing Statistical Design of Experiments Methodology", OCEANS'06 MTS/IEEE-Boston Conference, September 18 to 21, 2006

Azarsina, F., Bose, N., Seif, M.S., 2007a, "An Underwater Vehicle Manoeuvring Simulation; Focus on Turning Manoeuvres", The Journal of Ocean Technology, Volume II, Number I, winter 2007

Azarsina, F., Williams, C.D., Issac, M.T., 2007b, "Pure Yaw Experiments on a Series of Hull Forms for an Underwater Vehicle: Hydrodynamic Observations and Analysis", International Symposium on Underwater Technology, Tokyo, Japan, April 17-20, 2007

Azarsina, F., Williams, C.D., Bachmayer, R., 2007c, "Response Surface Models for the Hydrodynamic Loads Measured on Slender Underwater Vehicles During Pure Yaw Manoeuvres", 15th Symposium UUST, Durham, New Hampshire, August 19th- 22nd, 2007

Barth, T., "A Brief Overview of Uncertainty Quantification and Error Estimation in Numerical Simulation", Exploration Systems Directorate, NASA Ames Research Center, PowerPoint presentation searched online October 2008

Bishop, R.E.D., and Parkinson, A.G., "On the Planar Motion Mechanism used in ship model testing", Philosophical Transactions of the Royal Society of London, Series A, Mathematical and Physical Sciences, Volume 266, Issue 1171, pp. 35-61

Boger, D.A., Dreyer, J.J., "Prediction of Hydrodynamic Forces and Moments for Underwater Vehicles Using Overset Grids", 44th AIAA Aerospace Sciences Meeting and Exhibit, 9 to 12 January 2006, Reno, Nevada

Brayshaw, I., "Hydrodynamic Coefficients of Underwater Vehicles", Maritime Platform Division, Aeronautical and Maritime Research Labs, DSTO, Melbourne, 1999

Brennen, C. E., "A Review of Added Mass and Fluid Inertial Forces", Department of the Navy, Naval Civil Engineering Laboratory, Port Hueneme, California, Report No. CR. 82.010, January 1982

Bullivant, W.K., "Tests of the NACA 0025 and 0035 Airfoils in the Full-Scale Wind Tunnel", NACA Report No. 708, Langley Field, 1940

Chung, J.H., Kwon, J., Lee, S.G., "Application of Design of Experiment Methodology to the UNDEX Whole Ship Shock Modeling & Simulation", The 76th Shock & Vibration Symposium, Destin, FL, October 30 to November 3, 2005

Curtis, T.L., "The Design, Construction, Outfitting and Preliminary Testing of the *C-SCOUT* Autonomous Underwater Vehicle (AUV)", M.Eng. Thesis, Memorial University of Newfoundland, October 2001

Davidson, K.S.M., "On the Turning and Steering of Ships", Trans. SNAME, 1944

Dering, J. (ed.), A code of practice for the operation of Autonomous Underwater Vehicles, Society for Underwater Technology, London, 2000

Finck, R.D. "USAF Stability and Control Data Compendium", (DATCOM), Air Force Flight Dynamics Laboratory, Wright Patterson Air Force Base, April, 1976

Fossen, T.I., Guidance and Control of Ocean Vehicles, John Wiley & Sons Ltd., 1994

Freeman, H.B., 1932a, "Force measurements on a 1/40-scale model of the U.S. Airship *Akron*", Report No. 432, N.A.C.A, 1932

Freeman, H.B., 1932b, "Pressure-distribution measurements on the hull and fins of a 1/40-scale model of the U.S. Airship *Akron*", Report No. 443, N.A.C.A, 1932

Freeman, H.B., 1932c, "Measurement of flow in the boundary layer of a 1/40-scale model of the U.S. Airship *Akron*", Report No. 430, N.A.C.A, 1932

Goodman, A., "Experimental techniques and methods of analysis used in submerged body research", Proc. 3rd Symposium on Naval Hydrodynamics, September 19 to 22, 1960, Scheveningen, Netherlands

Hewitt, G. and Waterman, E., "Phoenix Model Measurement and Bifilar Swinging", NRC-IOT Report SR-2005-29, December 2005

Hochbaum, A. C., "Virtual PMM Tests for Manoeuvring Prediction", 26th Symposium on Naval Hydrodynamics, Rome, Italy, 17-22 September 2006, Vol. I, pp. 31-41

Issac, M.T., Adams, S., Moqin, H., Bose, N., Williams, C.D., Bachmayer, R., 2007a, "Manoeuvring Experiments Using the *MUN Explorer* AUV", International Symposium on Underwater Technology, Tokyo, Japan, April 17-20, 2007

Issac, M.T., Adams, S., Moqin, H., Bose, N., Williams, C.D., Bachmayer, R., Crees, T., 2007b, "Manoeuvring Trials with the *MUN Explorer* AUV: Data Analysis and Observations", OCEANS'07 MTS/IEEE-Vancouver Conference, September 29 to October 4, 2007

Jones, D.A., Clarke, D.B., Brayshaw, I.B., Barillon, J.L., Anderson, B., "The calculation of hydrodynamic coefficients for underwater vehicles", Maritime Platform Division, DSTO-TR-1329, July 2002

Kowalski, S.M., and Potcner, K.J., "How to Recognize a Split-Plot Experiment", Quality Progress, November 2003

Kuiper G., The Wageningen Propeller Series, MARIN Publication, 1992

Lamb, H., Hydrodynamics, Dover Publication, 6th edition, 1932

Mackay, M., Bohlmann, H.J. and Watt, G.D., "Modeling Submarine Tailplane Efficiency", Proceedings of the NATO RTO SCI Symposium on "Challenges in Dynamics, System Identification, Control and Handling Qualities for Land, Air, Sea and Space Vehicles", May 2002, Berlin

MERLIN (Marine Environmental Research Laboratory for Intelligent Vehicles), *MUN Explorer* AUV, URL: http://www.mun.ca/creait/MERLIN/auv.php, visited on March 2009

Montgomery, D.G., Design and Analysis of Experiments, 5th Edition, John Wiley & Sons, 2001

Morelli, E.A., Deloach, R., "Wind Tunnel Database Development Using Modern Experiment Design and Multivariate Orthogonal Functions", 41st AIAA Aerospace Sciences Meeting and Exhibit, January 6-9, 2003, Reno, NV

Myers, R. H. and Montgomery, D. C., Response Surface Methodology; Process and product optimization using designed experiments, John Wiley, 1995

Nahon, M., "Determination of Undersea Vehicle Hydrodynamic Derivatives Using the USAF DATCOM", Proceedings IEEE OCEANS'93 conference, pp. 283 to 288

Peterson, R. S., "Evaluation of semi-empirical methods for predicting linear static and rotary hydrodynamic coefficients", NCSC TM 291-80

Potcner, K.J., and Kowalski, S.M., "How to Analyze a Split-Plot Experiment", Quality Progress, Vol. 37, No. 12, December 2004, pp. 67-74

PNA, Comstock, J.P., 1967 version all in one volume, Chapter VIII Ship Maneuvering and Control

Shiba, H., "Model Experiments about the Manoeuvrability and Turning of Ships", First Symposium on Ship Manoeuvrability, DTMB Report, 1461, October 1960

SNAME 1950, The society of naval architects and marine engineers. Nomenclature for Treating the Motion of a Submerged Body through a Fluid, Technical and Research Bulletin, No. 1-5

Statease website, URL: http://www.statease.com/articles.html, last visited June 2008

Sutulo, S., and Guedes Soares, C., "An Algorithm for Optimized Design of Manoeuvring Experiments", Journal of Ship Research, Vol. 46, No. 3, Sept. 2002, pp. 214–227

Thomas, R., "Performance Evaluation of the Propulsion System for the Autonomous Underwater Vehicle *C-SCOUT*", M.Eng. Thesis, Memorial University of Newfoundland, August 2003

Thomas, R., Bose, N., Williams, C.D., "Propulsive Performance of the Autonomous Underwater Vehicle *C-SCOUT*", OCEANS 2003, 22 to 26 September, San Diego, California

Van Drent, W., Digital Measurement Division, ADE Technologies, Inc. Newton, MA, webpage: http://home.att.net/~numericana/answer/geometry.htm#ellipticarc, visited on July 2008

Van Leeuwen, G., "The Lateral Damping and Added Mass of an Oscillating Shipmodel", 1964 Publ. Shipbuilding Lab. Univ. Tech. Delft. No. 23

Von Mises, R., Theory of Flight, Dover, 1959, pp. 148 to 167

Whicker, L. Folger and Fehlner, Leo F., "Free-Stream Characteristics of a Family of Low-Aspect-Ratio All-Movable Control Surfaces for Application to Ship Design", David Taylor Model Basin, AD- A014 272, 1958

Williams, C.D., Mackay, M., Perron, C., and Muselet, C., "Physical Modelling of Vehicle Performance in High-Amplitude and High-Rate Manoeuvres", Proceedings of the NATO RTO SCI Symposium on "Challenges in Dynamics, System Identification, Control and Handling Qualities for Land, Air, Sea and Space Vehicles", May 2002, Berlin

Williams, C.D., Curtis, T.L., Doucet, J.M., Issac, M.T., Azarsina, F., "Effects of Hull Length on the Manoeuvring Characteristics of a Slender Underwater Vehicle", Proceedings of OCEANS'06 MTS/IEEE-Boston Conference, September 18 to 21, 2006

Appendix A: Uncertainty study for the simulation code

A.1 Introduction

The sources of uncertainty in a numerical simulation were named as follow by Barth [2008]:

1. Geometric uncertainty: to check if the geometry is exactly known.

2. Initial and boundary data uncertainty: to check if the initial or boundary conditions are precisely known.

3. Structural uncertainty: to check if the physics is modeled correctly with the equations, e.g. in: turbulence models, combustion models or in the present study the equations of motion.

4. Parametric uncertainty: to check if the parameters of the model were measured or estimated accurately, e.g. in the present study: the mass and moment of inertia of the underwater vehicle.

The first two sources are not applicable to the present study; those are in fact more related to CFD (Computational Fluid Dynamics) studies where the fluid field geometry should be defined and meshed and initial/ boundary conditions should be set. The third source is assumed to be 100% certain in the present study; that is, the equations of motion were written in their original form which provides the exact state of the vehicle's motion in the x-y plane. Therefore, the only source of uncertainty is the uncertainty in the model parameters. In the following, a study of the effect of uncertainty in the model parameters on the simulation response is presented. The approach was to vary the model parameters: the mass and moment of inertia of the vehicle within a confidence interval e.g. ±10% and

run the simulation code for turning manoeuvres at several deflection angles of the stern-planes to observe the variation in the manoeuvre outputs such as: radius of turn, drift angle, speed reduction and the steady values of the loads. Thus, the presented uncertainty study is only for the turning manoeuvres which were all preformed at a propeller speed of 290 rpm: 2.5 m/s approach speed and at average stern-plane deflection angles of 1, 3, 6, 9, 12, 14 and 16 degrees.

A.2 Uncertainty in the model mass

In chapter 5, the vehicle mass (dry mass of the vehicle plus floodwater mass) was estimated 1445 kg. If this value is ±10% uncertain then the resulting uncertainty for the radius of turn, drift angle, speed reduction ratio and sway force and yaw moment that are exerted on the bare hull are presented in Table A.1. The uncertainty is defined as the relative error in the simulation response if the vehicle mass is ±10% uncertain; e.g. the uncertainty in the radius of turn is:

$$U_{R,\{m\}\pm 10\%} = 100 * (R - R_{\{m\},\pm 10\%})/R \qquad \text{(A-1)}$$

Similarly, the uncertainty in the simulation response for e.g. the steady drift angle during a turn due to uncertainty in the vehicle mass is denoted by $U_{\beta,\{m\}\pm 10\%}$, and so on. Comparing the second and third parts of Table A.1 it is observed that the effect of ±10% uncertainty in the vehicle mass is not symmetric on the simulation response. In either case: mass underestimated or overestimated, the errors in simulation response are mostly within a 10% range.

Table A.1 Uncertainty in the steady values of turning manoeuvres due to ±10% uncertainty in the mass of the vehicle; approach speed 2.5 m/s

Simulation response for the originally estimated vehicle mass of 1445 kg:

δ [deg]	R [m]	β [deg]	$U_{turn}/U_{approach}$	$F_{y,hull}$ [N]	$M_{z,hull}$ [N.m]
1	131.1	1.3	0.99	65.6	-123.7
3	42.26	4.0	0.88	161.6	-294.2
6	18.79	8.0	0.67	204.0	-331.1
9	10.50	12.2	0.49	193.7	-262.0
12	6.64	16.1	0.38	176.1	-191.0
14	5.19	18.5	0.33	166.6	-156.0
16	4.25	20.5	0.30	159.1	-129.8

If the vehicle mass was originally 10% overestimated then the percentage errors are:

δ [deg]	$U_{R,\{m\}-10\%}$	$U_{\beta,\{m\}-10\%}$	$U_{speed\ reduction,\ \{m\}-10\%}$	$U_{Fy,\{m\}-10\%}$	$U_{Mz,\{m\}-10\%}$
1	4.9	3.1	-0.2	3.9	3.9
3	4.9	4.3	-0.9	3.0	2.7
6	3.4	4.8	-1.5	1.3	0.0
9	0.6	5.5	-1.8	0.1	-3.3
12	-1.0	5.9	-1.3	-0.6	-6.4
14	-1.7	5.9	-0.9	-0.7	-7.9
16	-1.2	5.8	1.0	-0.6	-8.9

If the vehicle mass was originally 10% underestimated then the percentage errors are:

δ [deg]	$U_{R,\{m\}+10\%}$	$U_{\beta,\{m\}+10\%}$	$U_{speed\ reduction,\ \{m\}+10\%}$	$U_{Fy,\{m\}+10\%}$	$U_{Mz,\{m\}+10\%}$
1	-5.5	-4.6	-0.2	-3.5	-3.4
3	-4.6	-3.8	1.1	-2.6	-2.3
6	-3.2	-5.0	3.9	-1.0	0.3
9	-1.0	-5.2	5.5	0.1	3.5
12	1.6	-6.0	9.2	0.7	6.3
14	2.2	-5.7	11.2	0.8	7.5
16	2.8	-5.5	11.9	0.8	8.2

Fig. A.1 is the plot of radius of turn versus stern-planes average deflection angle with error-bars according to the data in Table A.1 about the original simulation results. In order that the error-bars are observable only data above 6 deg deflection angle were shown in Fig. A.1
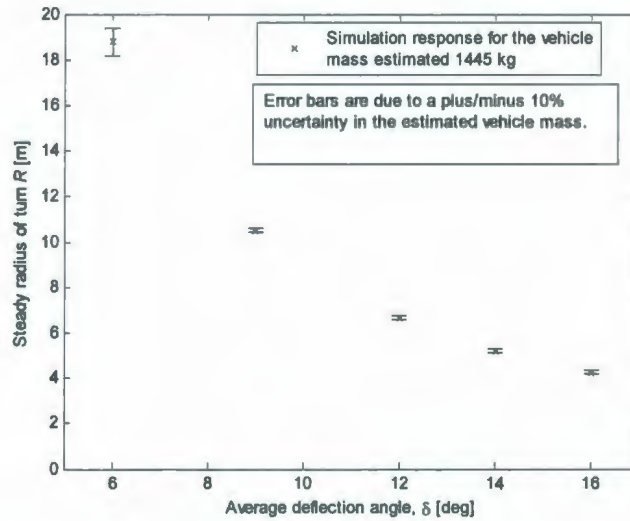
Fig. A.1 Radius of turn with error-bars according to the data in Table A.1

A.3 Uncertainty in the model moment of inertia

Next, if the estimated value for the moment of inertia of the vehicle (moment of inertia of the dry vehicle plus that of the floodwater about an axis through the mid-length of the vehicle) which was 3319 kg.m^2 has an uncertainty of $\pm 10\%$, the uncertainty in simulation outputs during turning manoeuvres were studied. It was observed that the 10% level uncertainty in the moment of inertia does not have an observable effect on the steady simulation response during the turning manoeuvres. However, the time-history of the response in sway and yaw directions are slightly different if the moment of inertia is $\pm 10\%$ uncertain. Fig. A.2 is the plot of time-history of the sway force that is produced by the stern-planes at an average deflection angle of 12 deg; it is observed that although the steady value of the force does not vary due to this level of uncertainty in the moment of inertia, the maximum and minimum values are different (see the peak region enlarged in Fig. A.2). Table A.2 shows the uncertainty in the peak values of the sway force and

yawing moment that are exerted on the bare hull and produced by the stern-planes during turning manoeuvres due to ±10% uncertainty in the moment of inertia of the vehicle. These uncertainties are within 5% calculated by the same notation as in equation (A-1) and is denoted by $U_{loads,\{I_z\}\pm10\%}$
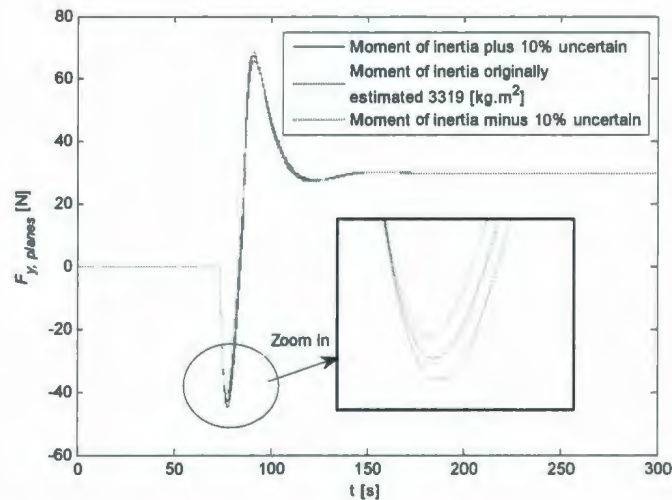
Fig. A.2 Net sway force that is produced by the stern-planes during turning manoeuvres at an average deflection angle of $\delta = 12$ deg; studying the effect of uncertainty in the moment of inertia

Table A.2 Uncertainty in the peak values of hydrodynamic loads due to uncertainty in the moment of inertia of the vehicle

Peak value of:	$I_z - 10\%$	I_z	$I_z + 10\%$	$U_{loads,\{I_z\}+10\%}$	$U_{loads,\{I_z\}-10\%}$
$F_{y,hull}$	478.9 [N]	474.8 [N]	470.6 [N]	-0.9	0.9
$M_{z,hull}$	-657.8 [N.m]	-654.8 [N.m]	-651.5 [N.m]	-0.5	0.5
$F_{y,planes}$	-40.79 [N]	-42.84 [N]	-44.85 [N]	4.8	-4.7
$M_{z,planes}$	52.96 [N.m]	55.64 [N.m]	58.24 [N.m]	4.8	-4.7

Appendix B: Contribution of the skin friction and form drag

in the total resistance force[16]

From Allmendinger [1990, page 253], first equation 64 from the ITTC for the skin friction coefficient is:

$$C_f = 0.075/\{[log_{10}(RN) - 2]^2\} \tag{B-1}$$

And then equation 65 from Hoerner for the total resistance coefficient is stated as:

$$C_t = C_f * [1 + 1.5(d/l)^{1.5} + 7(d/l)^3] \tag{B-2}$$

Then the resistance force on the bare hull of the underwater vehicle is:

$$R = \frac{1}{2}\rho(\text{WSA}) \cdot U^2 \cdot C_t \tag{B-3}$$

where WSA is the wetted surface area of the hull. For the five bare hull configurations the wetted surface areas were reported in Table 2.2 that were:

$$\text{WSA} = [0.9511 \quad 1.0806 \quad 1.2100 \quad 1.3395 \quad 1.4690] \text{ m}^2. \tag{B-4}$$

Then at forward speeds U of 1 to 4 m/s, using (B-1) to (B-4) in a water density of 1000 kg/m^3, the values in Table B.1 are obtained for the five bare hull configurations.

It is inferred from (B-2) that the contribution of the skin friction in the total resistance is measured by C_f, and the expression in brackets in (B-2) is the contribution of the form drag to the total resistance coefficient. Note that these two contributions are not additive but rather are multiplicative. The contribution of the skin friction in the total resistance is calculated as $(C_f/C_t)\%$ which is shown in the second last column in Table B.1; the rest

---

[16] This appendix was created mainly on the basis of an email sent by Dr. Chris Williams to the author.

of it is obviously the contribution of the form drag as shown in the last column in Table

B.1. It is observed that more than 90% of the resistance force is due to the skin friction.

Table B.1 Resistance force calculated by the skin friction and form drag method

U [m/s]	LDR	$RN * 10^{-6}$	C_f	C_t	R [N]	Skin friction %	Form drag %
1	8.5	1.726	0.0042	0.0045	2.13	93.3	6.7
1	9.5	1.929	0.0041	0.0043	2.34	94.4	5.6
1	10.5	2.132	0.0040	0.0042	2.54	95.2	4.8
1	11.5	2.335	0.0039	0.0041	2.75	95.9	4.1
1	12.5	2.538	0.0039	0.0040	2.95	96.4	3.6
2	8.5	3.451	0.0036	0.0039	7.43	93.3	6.7
2	9.5	3.857	0.0036	0.0038	8.16	94.4	5.6
2	10.5	4.263	0.0035	0.0037	8.89	95.2	4.8
2	11.5	4.669	0.0034	0.0036	9.61	95.9	4.1
2	12.5	5.075	0.0034	0.0035	10.33	96.4	3.6
3	8.5	5.177	0.0034	0.0036	15.48	93.3	6.7
3	9.5	5.786	0.0033	0.0035	17.04	94.4	5.6
3	10.5	6.395	0.0032	0.0034	18.57	95.2	4.8
3	11.5	7.004	0.0032	0.0033	20.09	95.9	4.1
3	12.5	7.613	0.0031	0.0033	21.59	96.4	3.6
4	8.5	6.902	0.0032	0.0034	26.12	93.3	6.7
4	9.5	7.714	0.0031	0.0033	28.76	94.4	5.6
4	10.5	8.526	0.0031	0.0032	31.36	95.2	4.8
4	11.5	9.338	0.0030	0.0032	33.94	95.9	4.1
4	12.5	10.150	0.0030	0.0031	36.48	96.4	3.6

The curves of resistance force for the five bare hulls are plotted in Fig. B.1 using the

calculated values in Table B.1 column#8 based on the skin friction and form drag

contributions. Also the measured test data for the axial force during the resistance runs

are shown in Fig. B.1. It is observed that the estimated values using the skin friction and

form drag in equation (B-3) are in closer agreement with the test data at lower forward

speeds, however at larger speeds the measured test data for the resistance force is larger than the estimated values by (B-3).
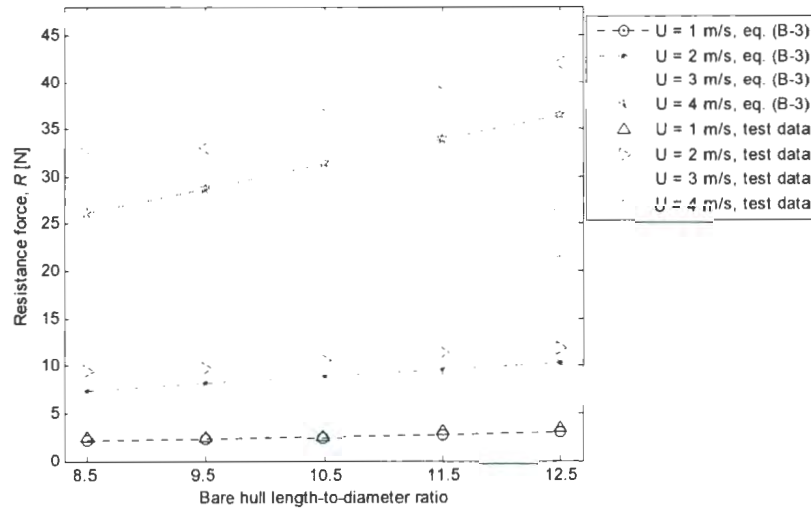
Fig. B.1 Comparison of the resistance force estimated using the skin friction and form drag with the test data for the five bare hull configurations at forward speeds of 1 to 4 m/s

For the *MUN Explorer* with length 4.5 m and diameter 69 cm, the *LDR* is 6.5 so using (B-2) it is concluded that the skin friction contributes close to 90% of the total resistance and the form drag contributes 10%. Of course those estimates are valid only for:

(i)   the same Reynolds Number based on length,

(ii)   the same surface roughness on the *Explorer* as on the *Phoenix* models, and,

(iii)   it assumes that the *Explorer* has the same axisymmetric shape of the Phoenix models.

So this prediction method for any other full-scale bare-hull axisymmetric shape can be used by:

(i)   scaling the results by the ratio of the constants in equation (B-1) to represent the surface roughness on the vehicle,

(ii)   scaling to a longer or shorter vehicle using the appropriate WSA, and,

(iii)   scaling to a different LDR via the expression in the square brackets in (B-2).

Also if the forward speed is different the Reynolds Numbers will be different at model-scale and full-scale so that scaling should be performed by using ratio of RN factors in (B-1).

MEMORIAL
UNIVERSITY

FINAL ORAL EXAMINATION FOR THE DEGREE OF
DOCTOR OF PHILOSOPHY

In accordance with the regulations governing the degree of Doctor of Philosophy, candidates are examined by an officially appointed Examination Board. The examinations are public, and are chaired by the Dean of Graduate Studies or her delegate.

CANDIDATE:	Farhood Azarsina, B.Sc., M.Sc.
DISCIPLINE:	Ocean & Naval Architecture Engineering
THESIS TITLE:	Experimental Hydrodynamics and Simulation of Manoeuvring of an Axisymmetric Underwater Vehicle
EXTERNAL EXAMINER:	Dr. Martin Robert Renilson Australian Maritime College University of Tasmania Tasmania, Australia
INTERNAL EXAMINERS:	Dr. Don Bass Faculty of Engineering Memorial University
	Dr. Heather Peng Faculty of Engineering Memorial University
SUPERVISORS:	Dr. Ralf Bachmayer Faculty of Engineering & Applied Science Memorial University
	Dr. Neil Bose Faculty of Engineering & Applied Science Memorial University
	Dr. Christopher Williams Faculty of Engineering & Applied Science Memorial University
DATE:	Tuesday, December 16, 2008
TIME:	5:30 p.m.
PLACE:	Room EN-4002, S.J. Carew Building

School of
S G S
Graduate Studies